Conception et synthèse de matériaux bioactifs par polymérisation à deux photons basés sur la chimie click thiol-ène et les protéines

Xingming Ju

PSL UNIVERSITÉ PARIS

THÈSE DE DOCTORAT
DE L'UNIVERSITÉ PSL

Préparée à l'École Nationale Supérieure de Chimie de Paris (ENSCP)

Design and Synthesis of Bioactive Material by Two-photon Polymerization based on Thiol-ene Click Chemistry and Proteins

Soutenue par
Xingming JU
Le 17 novembre 2023

Ecole doctorale n° 406
Chimie Moléculaire de Paris Centre

Spécialité
Chimie Moléculaire

Composition du jury :

Valérie MARVAUD *Présidente*
Directrice de Recherche CNRS
Institut Parisien de Chimie Moléculaire
Sorbonne Université

Olivier STEPHAN *Rapporteur*
Maître de conférences
Laboratoire Interdisciplinaire de Physique
Université Grenoble Alpes

Lydie PLOUX *Rapportrice*
Directrice de Recherche CNRS
U1121 INSERM, Université de Strasbourg

Ferdinando Tristán LOPEZ *Examinateur*
Professor
Institut Technologique de Celaya

Anouk GALTAYRIES *Examinatrice*
Maître de conférences
Institut de Recherche de Chimie Paris
Chimie ParisTech, Université Paris Science et Lettres

Vincent SEMETEY *Directeur de thèse*
Directeur de Recherche CNRS
Institut de Recherche de Chimie Paris
Chimie ParisTech, Université Paris Science et Lettres

Chimie Paris ParisTech | PSL

Acknowledgments

Time flies, as always.

In Paris for four years, I've been shaped by this city to be what a man of this city should be, whether studying or living. Looking back over the years, I have so many people to thank.

Firstly, I would like to express my heartfelt thanks to my two supervisors, Dr. Vincent SEMETEY and Dr. Sylvie COSCOY. Four years ago, I was so excited when I got the offer to work on an amazing project in Chimie ParisTech, PSL University and Institut Curie. When I arrived, Vincent and Sylvie opened a totally new door for me. This discipline project is quite challenging for me. During the four years, Vincent was always there to discuss the experiment, help me analyze the results and guide me to the next step. Sometimes I was lost but Vincent was always very patient to talk with me and drag me back on the right path. He always reminded me to be logical and accurate during our research process. He has been teaching me how to be a scientific researcher through his actions. Vincent told me that his work is to keep pushing me forward. I am very grateful that he never gave up on me when I failed again and again and even stagnated. At the same time, I got lots of help from Sylvie. I knew nothing about cell biology when I started this project. Sylvie was very patient to teach me from the beginning. Every time I needed help, she was always there to discuss and sometimes to do experiments together with me. When I met problems with scientific writing, she was there every day to read and correct my paragraphs to help me improve my writing. Her rigorous academic attitude deeply influenced me. When I faced complex problems, her calmness and kind help released me a lot. Sylvie also showed me lots of French culture which is totally new to me. Vincent and Sylvie, I am really very happy to work with you two. Thanks again!

Secondly, I would like to express my great thanks to my Comité de Suivi, Prof. Thibaut CORADIN and Prof. Valerie MARVAUD. They were always there to talk about my project and my daily life every year. I met a big problem after the covid, we had several meetings together. I got lots of support and suggestions from them. Ph.D. is not only about science but also about life.

During my work in the lab, I received lots of help from collaborators. Great thanks also go to Prof. Gilles Gasser, we started a side project at the beginning of my thesis. Even though we did not finish the project, I learned a lot from the talk with him. I would like to thank Prof. Catherine MONNOT. I learned a lot from the work with her. I would like to thank Dr. Fun SUN. He trained me on how to perform SEM images. I used the SEM a lot during my thesis, and he was very patient to answer my questions and help me solve the problem. I would like to thank Mme. Fanny TABARIN. She gave me lots of support on cell

culture. I would also like to thank Mme. Chloe GUEDJ for your help with spinning disk confocal microscopy. I would like to thank Mme. Anouk GALTAYRIES for her help with the XPS analysis.

Besides, I would also like to thank my colleagues in Chimie ParisTech, Liang, Guivanni, Mohhedine, Pedro, Natacha, Elnaz, Ana, Patricia Prof. Ferdinando, Prof. Min-hui LI, Nian, Hui, Bin, Zhihua, Gaoyu, Yakui, Yandong, Morvan, Irène, Merino. In Institut Curie, there are also lots of excellent colleagues in Silberzan/Buguin team. They are Pierre, Hsiang, Nolan, Quentin, Caroline, Flavia, Brice, Nasstasia, Mathilde, Artem, Bart, Thibaut, Trinish, and Thomas, Prof. Pascal SILBERZAN, Porf. Isabelle BONNET, Prof. Axel BUGUIN. I had a great time working with you.

I would like to thank my friend, Yufeng LI. During the hard time, you are always there to drag me out of the darkness.

I would like to thank Mme. Ikame BENKADDOUR for her support with the lab management. I would also like to thank Mme. Irène RASOARINORO from ED 406 Sorbonne for help with the registration affair.

Special thanks go to Mme. Jennifer OBROVAC. I am very happy to be your colleague. Thank you, Mom Jenni. You are always there to take care of your lab kids, surely including me, haha.

I acknowledge the Guangzhou Elite Project for financial support. Special thanks to Mme. Huiting MAI and the service team in Guangzhou.

Especially, I would like to thank my fiancée, Qidian LI (李奇点). The first time we met was more than ten years ago. Thanks for your support and love for the past years. This thesis is also a gift for you, the hexagonal Bee-My-Love.

Finally, I would like to thank my family. Mom (德芝) and Dad (水元), you are always behind me to give me endless love. You sent me to the school when I was two years old. As far back as I can remember, you have always been working hard. You've always been role models in my life.

Now, Paris, the same as the cities Beijing and Guangzhou where I finished my bachelor’s and master’s degrees, is inside me. I learned a lot from this thesis. Perseverance and advancing bravely will lead us to a beautiful life.

Contents

Abbreviations

ECM	extracellular matrix
3D	three-dimensional
TPP	two-photon polymerization
OSTE	off stoichiometry thiol-ene
BSA	bovine serum albumin
PEG	polyethylene glycol
PI	photoinitiator
UV	ultraviolet
OPP	one-photon polymerization
OPA	one-photon Absorption
TPA	two-photon Absorption
GM	Göppert-Mayer
CCD	charged-coupled device
NA	numerical aperture
TPP-3DP	two-photon polymerization-3D printing
LSR	lateral spatial resolution
SEM	scanning electronic microscope
ITC	intramolecular charge transfer
WLC	white-light continuum
Ts	toluenesulfonyl
PEI	poly(ethylene imine)
PEGMEM	poly(ethylene glycol) methyl ether methacrylate
TPO	2,4,6-trimethylbenzoyl-diphenylphosphine oxide
FMN	flavin mononucleotide
FAD	flavin adenine dinucleotide
BSA	bovine serum albumin
bBSA	biotinylated bovine serum albumin
MB	methylene blue
BPD	benzophenone dimer
MBS	sodium 4-[2-(4-morpholino)benzoyl-2-dimethylamino]butylbenzenesulfonate
DBMP	2,6-di-tert-butyl-4-methylphenol
PGMEA	propylene glycol monomethyl ether acetate

HOIP	Hybrid Organic-Inorganic Photopolymers
Ormocil	organically modified silica
NOA61	Norland Optical Adhesive 61
PETA	pentaerythritol triacrylate
PETTA	pentaerythirol tetraacryalte
TPETA	trimethylolpropane ethoxylate triacrylate
TE	thiol-ene
STE	stoichiometric thiol-ene
OSTE+	off-stoichiometry thiol-ene-epoxy
HEK293A	human embryonic kidney cells 293-A type
TPO-L	ethyl (2,4,6-trimethylbenzoyl) phenylphosphinate
XTT	2,3-bis(2-methoxy-4-nitro-5-sulfophenyl)-5-carboxanilide-2H-tetrazolium
DBN	1,5-diazabicyclo[4.3.0]non-5-ene
GC-MS	gas chromatography-mass spectroscopy
LC-MS	liquid chromatography-mass spectroscopy
MTT	3-(4,5-dimethylthiazol-2-yl)-2,5-diphenyltetrazolium bromide
PEG	polyethylene glycol
Cys	cysteine
IgG	immunoglobulin G antibody
hIgG	half-antibodies
TCEP	tris(2-carboxyethyl)phosphine
PETMP	pentaerythritol tetrakis (3-mercaptopropionate)
Di-TMPTTA	di-trimethylolpropane tetraacrylate
DMSO	dimethyl sulfoxide
RB	Rose Bengal
RhB	rhodamine B
R6G	rhodamine 6 G
PBS	phosphate-buffered saline
HEPES	4-(2-hydroxyethyl)-1-piperazineethanesulfonic acid
PPII	polyproline II-type
Gly	glycine
PEO	polyethylene oxide
NHS	N-Hydroxysuccinimide
OEG	oligomer ethylene glycol

PLL-g-PEG	poly-L-Lysine grafted PEG
DA	dopamine
SI-ARTP	surface-initiated atom transfer radical polymerization
PDMS	polydimethylsiloxane
HAS	Human Serum Albumin
APTES	aminopropyl-triethoxysilane
MSCs	Mesenchymal Stem Cells
TPO-Li	lithium phenyl-2,4,6- trimethylbenzoylphosphinate
RCP	recombinant peptide
hMSCs	human mesenchymal stem cells
CEFs	chicken embryonic fibroblasts
PS	phenacyl sulfide methacrylate
PE	photoenol methacrylate
FN	fibronectin
Bt	biotin
Bt-VN	biotinylated vitronectin
A549	lung epithelial cells
Av	avidin
3T3	mouse embryonic fibroblasts
AFM	atomic force microscopy
ATR-FTIR	total reflectance-Fourier transform infrared
XPS X-ray	photoelectron spectrometry
SALDI	surface assisted laser desorption ionization
P/S	penicillin/streptomycin
GFP	green fluorescent protein
E. coli	*Escherichia coli*
Tg	glass transition temperature
LG	laser gain
ET	exposure time
MDCK	Madin-Darby canine kidney
PFA	paraformaldehyde
CP	cloud point
PLGA	poly(lactic-co-glycolic acid
HUVEC	Human Umbilical Vein Endothelial cells

SEM	scanning electron microscope
VEGF	vascular endothelial growth factor
UV	ultraviolet
THF	tetrahydrofuran
BDAB	bis(diethylamino)benzophenone
PEGDA	poly(ethylene glycol) diacrylate
ppm	parts per million
EHT	electron high tension
mIMCD3	mouse Inner Medullary Collecting Duct cells
WT	wild-type
MDA-MB-231	breast adenocarcinoma cells
pI	isoelectric point
BDB	*N*-(4-benzoylbenzyl)-*N*,*N*-dimethylethanaminium bromide

Résumé de Thèse en Français

Conception et synthèse de matériaux bioactifs par polymérisation à deux photons basés sur la chimie click thiol-ène et les protéines

Xingming JU[1,2] sous la direction de Vincent SEMETEY[1] et Sylvie COSCOY[2]

[1] Institut de Recherche de Chimie ParisTech (UMR 8247 CNRS/Chimie ParisTech), Chimie ParisTech-PSL, 11 rue Pierre et Marie Curie, 75005 Paris, France

[2] Laboratoire de Physicochimie Curie (UMR 168 CNRS/Institut Curie), Institut Curie, 11 rue Pierre et Marie Curie, 75005 Paris, France

Le microenvironnement cellulaire joue un rôle majeur en biologie et apparaît comme un déterminant clé du comportement et des fonctions des cellules dans de nombreux processus biologiques. La matrice extracellulaire (MEC) dans le microenvironnement cellulaire constitue une base structurelle pour les cellules, mais aussi une source de facteurs biochimiques et biophysiques tridimensionnels (3D) qui déclenchent et régulent les comportements cellulaires. De plus en plus d'éléments suggèrent que le caractère tridimensionnel du microenvironnement est impliqué dans le développement de nombreuses réponses cellulaires critiques observées *in vivo*, d'où l'importance du développement de matériaux fonctionnels et biomimétiques pour l'ingénierie du microenvironnement cellulaire tridimensionnel.

L'ingénierie tissulaire permet de construire des échafaudages contrôlés à l'échelle de la cellule. En particulier, des technologies telles que la polymérisation à deux photons (TPP) permettent la microfabrication à une échelle inférieure au micromètre avec des applications non seulement dans le domaine médical des bio-implants, mais aussi dans celui de la biologie cellulaire fondamentale. De nombreuses études ont démontré l'influence des microtopographies sur le comportement des cellules de mammifères. Des comportements cellulaires tels que la polarisation, la prolifération, la différenciation, la migration et l'alignement ont été déclenchés par des microtopographies 3D spécifiques. Un autre aspect central régissant le comportement des cellules est la chimie de l'échafaudage, qui donne accès à des surfaces chimiques spécifiques (répulsives ou adhésives pour les cellules, surfaces sélectives pour certaines cellules). Cependant, la manière dont la combinaison de la topographie et de la chimie de surface influence le comportement des cellules n'est pas bien comprise. **Ce travail vise à tirer parti de la chimie et de la TPP pour construire des microstructures 3D avec un contrôle précis des chimies locales et, par conséquent, des propriétés des échafaudages générés, en tant qu'outil pour la biologie cellulaire**.

Dans cette thèse, nous nous sommes concentrés sur un matériau synthétique, les résines thiol-ène hors stoechiométrie (OSTE), et sur un matériau naturel, les protéines. Les résines thiol-ène ont été utilisées par de nombreux chercheurs pour fabriquer des structures 3D en raison de leurs bonnes propriétés mécaniques. Avec la TPP, les structures 3D peuvent être fabriquées facilement. En changeant le ratio de deux groupes fonctionnels (thiols et alcènes), nous pouvons obtenir des surfaces avec des groupes thiol ou alcène en excès, ce qui offre des opportunités considérables pour le post-traitement après la fabrication. Nous avons spécifiquement étudié le greffage des PEG (polyéthylène glycol) *via* une réaction thiol-ène sur les surfaces OSTE pour leur conférer des propriétés anti-adhésives. Les protéines sont également d'excellents candidats pour la formation d'un microenvironnement 3D en raison de leur biocompatibilité. Nous avons en particulier fabriqué des structures 3D complexes avec de l'albumine de sérum de bovin (BSA). Le matériau synthétique OSTE et le matériau naturel BSA offrent tous deux la possibilité de développer de nouveaux outils en biologie cellulaire.

Cette thèse comprend six chapitres. Le chapitre I est une introduction générale présentant les objectifs de la thèse et l'état de l'art associé. Le chapitre II porte sur les résines OSTE et les modifications de la surface en 2D. Le chapitre III est dédié à des structures tridimensionnelles (3D) à base de résine OSTE pour la biologie cellulaire. Le chapitre IV traite de la polymérisation à deux photons des protéines. Le chapitre V reprend les principaux résultats des travaux de thèse et expose les perspectives de ces travaux. Le chapitre VI clôture le mémoire avec la partie expérimentale.

Chapitre I : Introduction

La principale technique utilisée dans notre thèse est la polymérisation à deux photons (TPP). Nous avons tout d'abord comparé les mécanismes de l'absorption à un photon (OTA) et de l'absorption à deux photons (TPA).

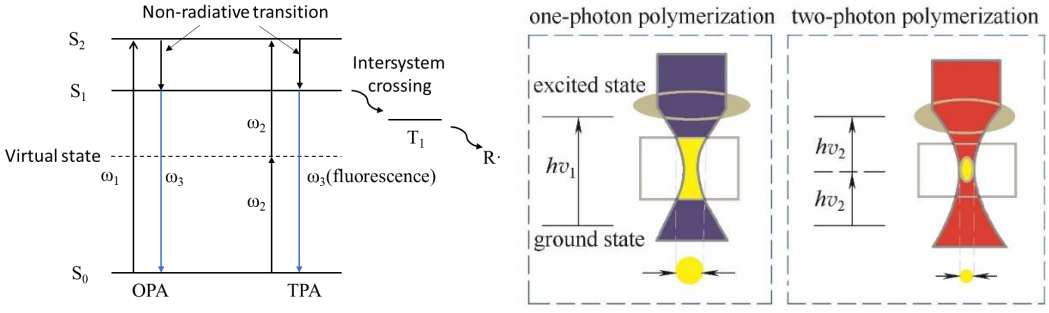

Figure 1. Diagramme énergétique schématique pour l'OPA et le processus TPA dégénéré (à gauche). S0 est l'état singulet fondamental, S_1 et S_2 sont des états singulet excités ; ω_1 et ω_2 sont les fréquences de la lumière incidente et ω_3 est la fréquence d'émission de la fluorescence; T_1 est l'état triplet ; $R^{\bullet}$ est le radical.
Distribution de l'intensité lumineuse dans le foyer laser d'un faisceau gaussien (à droite)

Pour l'OPA, l'absorption est linéaire alors que pour le TPA, deux photons doivent être présents quasi-instantanément au même endroit (**Figure 1**, gauche). Ainsi, la zone polymérisée de TPP est restreinte au voxel, tandis que la polymérisation à un photon (PPO) produit une grande zone polymérisée (**Figure 1**, droite). La haute résolution de la TPP (jusqu'à 100 nm) nous permet de fabriquer des microstructures précises.

La résolution de la TPP peut être ajustée à partir de l'instrument lui-même (longueur d'onde du laser et ouverture numérique (NA)), des paramètres d'entrée (intensité du laser et temps d'exposition) et de la composition du prépolymère (type de prépolymère, photo-initiateur et inhibiteur de radicaux). La plus petite unité de la TPP est le voxel, et la **Figure 2** montre la forme et la résolution du voxel. En analysant les résultats expérimentaux de la littérature, nous arrivons aux conclusions suivantes. Premièrement, une longueur d'onde plus courte induit une meilleure résolution. A puissance identique, augmenter l'ouverture numérique permet de diminuer le rapport d'aspect du voxel (c'est-à-dire le ratio taille verticale sur taille latérale). Des temps d'exposition plus longs et des puissances laser plus élevées produisent des voxels plus grands. Le choix du photo-initiateur est lié à la longueur d'onde du laser, et il convient de sélectionner des photo-initiateurs ayant une grande efficacité d'absorption à deux photons aux longueurs d'onde utilisées. Des 'quenchers' de radicaux peuvent aider à obtenir une résolution optimale. Après la fabrication au laser, le post-traitement permet d'améliorer la stabilité des microstructures 3D.

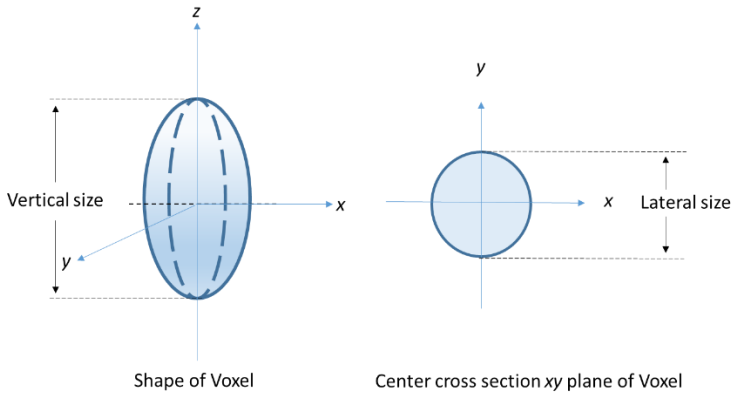

Figure 2. Forme du voxel dans les plans *xz* et *xy*

Les matériaux de polymérisation à deux photons peuvent être grossièrement divisés en deux catégories principales : les polymères synthétiques tels que les photorésines à base d'époxy, les résines à base de (méth)acrylate, les résines à base de thiol-ène … et les polymères naturels comme les protéines. Notre objectif est de trouver un matériau qui puisse être utilisé avec les cellules et qui puisse également être modifié en surface pour apporter une fonctionnalité anti-adhésives. Il ressort de notre étude bibliographique que les matériaux à base de thiol-ène sont un excellent choix en raison

de leurs excellentes propriétés mécaniques et de la possibilité de modifier leur surface. Ils sont de plus non toxiques. Dans la littérature, le PEG est couramment utilisé comme molécule pour conférer des propriétés anti-adhésives. Les rapports de la littérature montrent que le PEG5000 à longue chaîne mais aussi des oligo éthylène glycol à courte chaîne (6 unités d'oligo éthylène glycol) se sont avérés être des molécules efficaces pour conférer des propriétés anti-adhésives.

Enfin le Chapitre I recense les travaux dans la littérature utilisant des microstructures 3D fabriquées par TPP à partir de matériaux synthétiques ou protéiques comme outil en biologie cellulaire.

Chapitre II. Résine OSTE et modification de la surface en 2D

Basée sur la chimie des résines thiol-ène, la résine OSTE a été initialement utilisée dans le domaine de la microfluidique. Avec une bonne biocompatibilité et des propriétés mécaniques ajustables, l'OSTE a été utilisé avec succès comme biomatériau en plus du PDMS et de la résine photorésistante SU8. Il existe un large éventail de monomères à base de thiols et d'alcènes pouvant être utilisés. En ajustant le rapport thiol-ène, nous pouvons obtenir des surfaces avec un excès de groupes thiol ou alcène. La résine OSTE repose sur la chimie click thiol-ène (**Figure 3 (A)**). Le photo-initiateur produit des radicaux sous illumination UV. Les radicaux réagissent avec le groupe thiol, ce qui induit une propagation avec les alcènes. Lorsque le nombre total de groupes thiol est égal à celui des groupes alcène, il ne reste plus aucun groupe fonctionnel après la réaction complète dans le cas d'une composition stœchiométrique. Dans le cas contraire, il restera des groupes thiol ou alcène après la polymérisation avec une composition non stœchiométrique (**Figure 3 (B)**). Le rapport hors stœchiométrie offre la possibilité d'une post-modification. Les surfaces excédentaires en thiol et en alcène peuvent être modifiées avec des groupes fonctionnels cibles aux propriétés particulières. Avec différents rapports de groupes thiol et alcène, la rigidité du matériau final varie également.

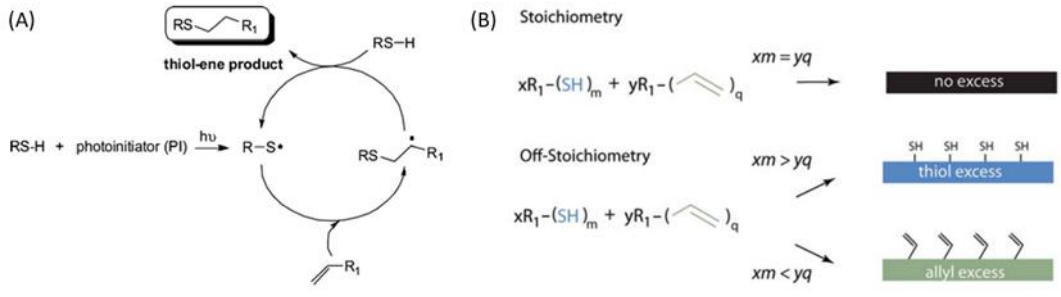

Figure 3. (A) Mécanisme de la réaction click thiol-ène et (B) résine OSTE.[1,2]

Un monomère tétrathiolé (pentaerythritol tetrakis(3-mercatopropionate)) a été choisi pour sa structure souple et associé à un monomère comportant trois alcènes (tris(prop-2-en-1-yloxy)-1,3,5-triazine) choisi pour sa rigidité. Pour caractériser analytiquement les propriétés de surface de la résine

polymérisée, nous avons utilisé l'infrarouge à transformée de Fourier en mode réflectance totale atténuée (ATR-FTIR) pour l'analyse qualitative et quantitative (**Figure 4**). L'ATR-FTIR permet également de connaître la composition moléculaire à la surface du matériau.

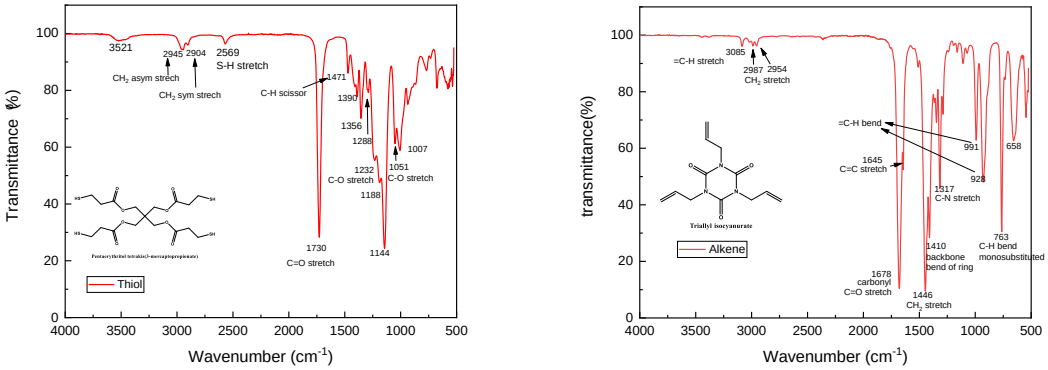

Figure 4. ATR-FTIR du thiol pentaerythritol tetrakis(3-mercatopropionate) et de la tris(prop-2-en-1-yloxy)-1,3,5-triazine (trialcène) (trialcène).

L'OSTE peut être polymérisé avec ou sans photo-initiateur. Nous avons utilisé deux formulations, l'une sans photo-initiateur et l'autre avec 2 w/w% d'Irgacure 651 comme photo-initiateur. Pour trouver la meilleure formulation, nous avons suivi la cinétique de durcissement traduisant l'avancée de la polymérisation des deux formulations. Toutes les polymérisations ont été effectués avec une source UV de 7.2 mW/cm^{-2} à 254 nm. Après avoir suivi la cinétique de durcissement, nous avons constaté que l'OSTE avec 2 % en poids d'Irgacure 651 comme photo-initiateur était le composant le plus efficace et que le meilleur temps de durcissement était de 10 minutes.

Nous avons par ailleurs étudié la polymérisation via le durcissement des résines OSTE en fonction du rapport thiol:ène. La plage d'utilisation des résines OSTE était comprise entre 4:1 et 1:5 en polymérisation à un photons, entre 5 :1 et 1 :5 à deux photons (**Figure 5**).

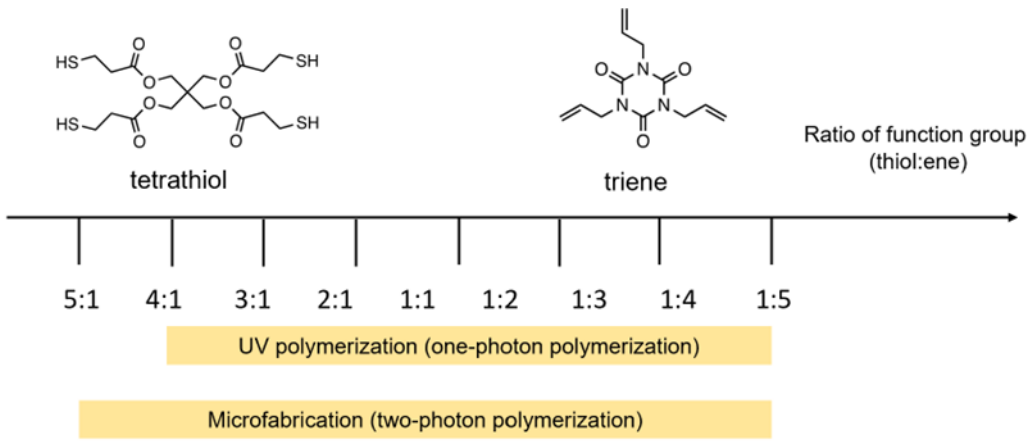

Figure 5. Polymérisation de la résine OSTE en polymérisation à un photon et à deux photons.

La biocompatibilité est un point crucial pour les biomatériaux. En testant la viabilité des cellules de rein canin de Madin-Darby (MDCK), nous avons constaté que la résine OSTE en excès d'alcène n'était pas toxique, tandis que la surface en excès de thiol engendrait une faible viabilité des cellules MDCK en raison du relargage des petites molécules n'ayant pas réagi. Dans le reste de nos travaux, nous nous sommes concentrés uniquement sur la surface en excès d'alcène.

Angle de contact. Les résines OSTE ont été caractérisées par la mesure des angles de contact. Le tableau 1 montre les angles de contact statiques et dynamiques de la résine thiol-ène avec différents rapports entiers de 1:1 à 1:5. L'angle de contact statique augmente avec l'augmentation du composant alcène. Le groupe alcène est un groupe fonctionnel ayant un effet hydrophobe. La même tendance s'applique à l'avancée et au retrait de l'angle de contact.

Tableau 1. Angle de contact avec l'eau de la résine thiol-ène pour différents ratios. Chaque échantillon a été testé 3 fois et la déviation standard a été calculée.

Rapport thiol-ène	1:1	1:2	1:3	1:4	1:5
Angle de contact statique	53±1	60±2	61±3	68±1	70±1
Angle de contact à l'avancée	57±1	63±1	68±1	69±1	*Note*
Angle de contact au retrait	17±1	27±1	28±2	34±1	*Note*

Note : L'angle de contact à l'avancée et au retrait du thiol:ene =1:5 varie de manière très irrégulière. Et la variance était très importante (plus de 10 degrés). Les valeurs n'étaient pas comparables aux valeurs de l'angle de contact dynamique d'autres surfaces. C'est pourquoi les valeurs n'ont pas été indiquées ici.

ATR-FTIR

Nous avons suivi l'ATR-FTIR des résines thiol-ène avec des rapports entiers confirmés allant de 5:1 à 1:5 avant et après un durcissement de 10 minutes avec 7.2 mW/cm^{-2} 254 nm UV. Pour toutes les formules, 2 % en poids d'Irgacure 651 ont été ajoutés comme photo-initiateur. La **Figure 6** montre l'ATR-FTIR de la résine avant polymérisation. Avec l'augmentation du composant alcène, l'absorption à 1645 cm^{-1} augmente progressivement avec l'augmentation de la proportion d'alcène. Après polymérisation, la résine OSTE en excès d'alcène présente toujours un signal fort à 3085 cm^{-1}, qui provient du =C-H, tandis que la résine OSTE en excès de thiol présente un pic à 2570 cm^{-1} qui provient du S-H (**Figure 7**).

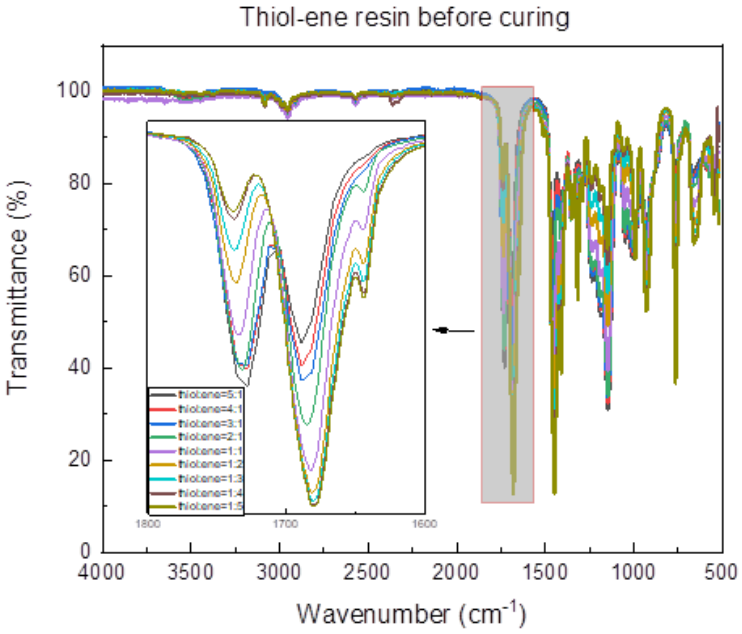

Figure 6. ATR-FTIR de toutes les résines thiol-ène à rapports entiers avant polymérisation, toutes les formulations contiennent 2 % en poids d'Irgacure 651 comme photo-initiateur.

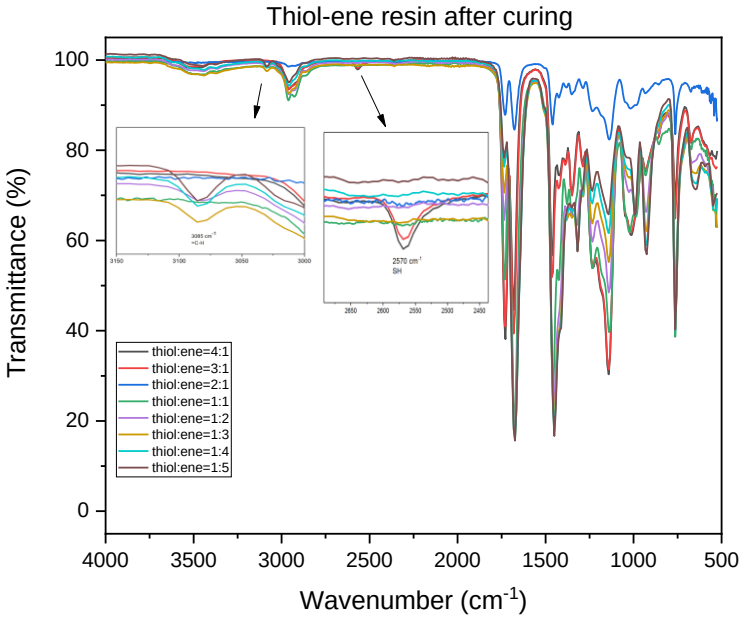

Figure 7. ATR-FTIR de tous les rapports entiers de la résine thiol-ène après durcissement sous une illumination de 7.2 mW/cm^{-2}, 254 nm UV. Toutes les formulations contiennent 2 % en poids d'Irgacure 651 comme photo-initiateur.

Pour mieux comprendre les propriétés de bio-adhésion de la résine OSTE, nous avons incubé les surfaces avec des bactéries *Escherichia coli* exprimant la protéine fluorescente verte (*E. coli* MG1655) pendant 1 heure. Les bactéries flottantes ont ensuite été éliminées par lavage. La **Figure 8** montre le nombre de bactéries ayant adhéré en fonction des différents ratios des résines OSTE. La densité des bactéries augmente légèrement avec l'augmentation du composant 'ène' plus hydrophobe ; ceci est en accord avec la littérature.

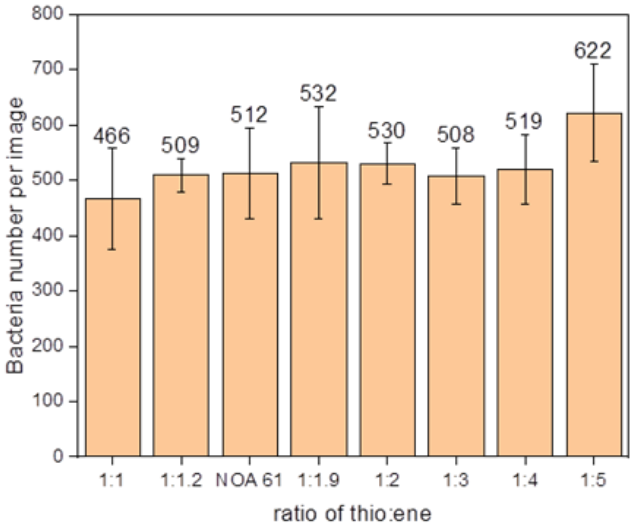

Figure 8. Nombre de bactéries adhésives par image (0.0015 cm^{-2}) pour différents ratios de résine thiol:ene. La barre d'erreur représente l'écart-type. Une série d'expériences, valeur moyenne de 10 images pour chaque échantillon.

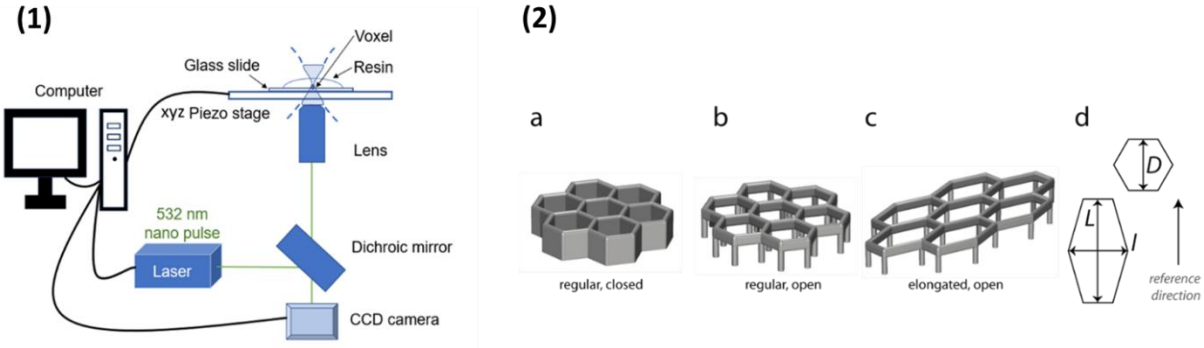

Figure 9. (1) Configuration de notre équipement de polymérisation à deux photons. (2) Structures conçues pour la TPP. (a) Structure hexagonale fermée régulière, *D8K1H5-fermée*. (b) *D8K1H5-ouverte* (c) *l7L14H7-ouverte.*

Nous avons utilisé brièvement trois types de microstructures : 1) La **Figure 9** (2a) représente une structure hexagonale régulière fermée que nous nommons d'après ses paramètres géométriques

D8K1H5-ouverte. *D* est le diamètre en µm du cercle inscrit et *D8* signifie que ce diamètre est de 8 µm. *K* représente le nombre de couches d'hexagones qui entourent la structure centrale et *K1* signifie qu'il n'y a qu'une seule couche. *H* est la hauteur de la structure hexagonale et *H5* signifie que la hauteur est de 5 µm. 2) La **Figure 9** (2b) représente une structure hexagonale ouverte régulière, dénommée *D8K1H5-ouverte* car seule la partie supérieure est connectée. Cette structure hexagonale supérieure est soutenue par des piliers. 3) La **Figure 9** (2c) représente une structure ouverte allongée *l7L14H7-ouverte*. Comme l'explique la **Figure 9** (2d), *L* est la longueur de la direction allongée basée sur *D*, tandis que *l* est la distance entre deux sommets dans la direction perpendiculaire à la direction d'étirement.

Pour explorer la possibilité d'une TPP de la résine OSTE, nous avons testé trois photoinitiateurs, Irgacure 369, Irgacure 651 et Irgacure 2959. Nous avons constaté que la résine OSTE avec Irgacure 651 ou Irgacure 2959 sont toutes deux correctes pour la PPT. La **Figure 10** montre le test des paramètres de fabrication *D8K1H5-ouverte* de la résine thiol:ene = 1:1 avec 0.5 % en poids d'Irgacure 651. Lorsque le gain laser était de 0,15, nous avons obtenu des microstructures stables avec une bonne résolution. En transférant le paramètre à la structure allongée *l7L14H7-ouverte,* nous avons constaté que la structure était plus stable sur la lame silanisée, permettant un meilleur ancrage de la microstructure sur la surface de verre (**Figure 10 B**(b)) que sur la lame non silanisée (**Figure 10 B**(a)). Nous en avons conclu que la résine OSTE avec 0.5 % en poids d'Irgacure 651 est l'une des meilleures options de formulation pour d'autres expériences, et que nous devrions fabriquer nos structures allongées sur des lames de verre silanisées.

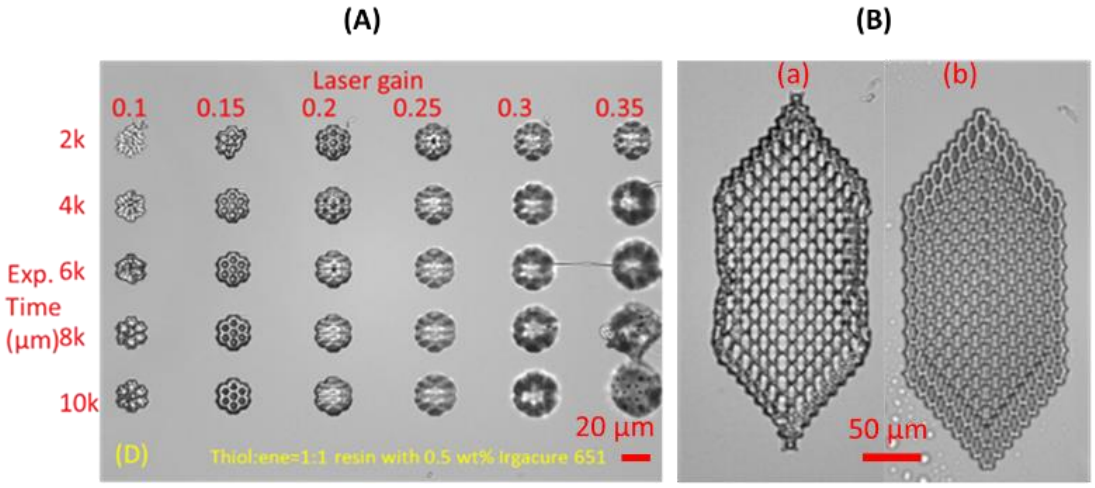

Figure 10. Images de la matrice du test des paramètres de polymérisation à deux photons avec la résine thiol:ène =1:1 contenant 0.5 % en poids d'Irgacure 651 comme photo-initiateur. (A) Petite structure hexagonale *D8K1H5-open*, barre d'échelle 20 µm ; (B) structures hexagonales ouvertes allongées *l7L14H7-ouvertes* sur (a) lame de verre non silanisée ou (b) silanisée, barre d'échelle 50 µm. Paramètres de fabrication gain laser/temps d'exposition : 0,15/2000 µs.

Modification de la surface avec Me-PEG-SH

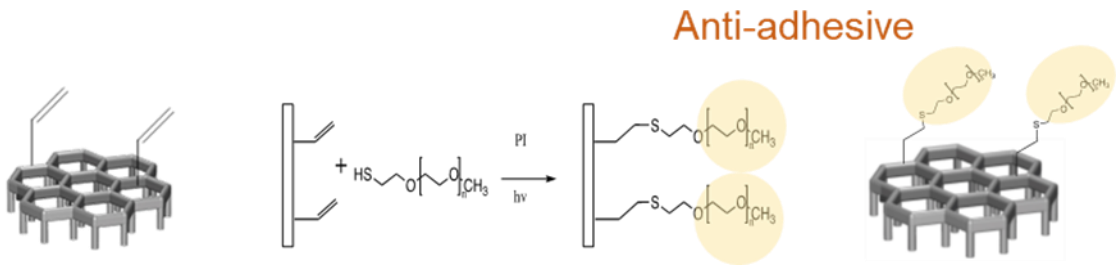

Figure 11. Stratégie "Grafting to" de modification de la surface de l'excès d'alcène de la résine OSTE avec Me-PEG-SH par chimie click thiol-ène.

Pour obtenir des propriétés anti-adhésives, nous avons essayé de modifier la surface de résines OSTE présentant un excès d'alcène avec du Me-PEG-SH (**Figure 11**). Quatre longueurs différentes de Me-PEG-SH (Me-PEG308-SH, Me-PEG750-SH, Me-PEG2000-SH, Me-PEG5000-SH) ont été testées.

Dans la littérature, les surfaces modifiées par PEG5000 ont largement démontré leurs propriétés anti-adhésives. Ici, nous avons commencé par le greffage de Me-PEG5000-SH sur la surface thiol:ene = 1:1.9. Nous avons conçu une série d'expériences pour valider les meilleurs paramètres de greffage, y compris le temps de greffage UV, la concentration de Me-PEG5000-SH et le photo-initiateur. Nous avons conclu que 40 mg/ml de Me-PEG5000-SH avec 5 w/w% d'Irgacure 651 comme photo-initiateur, 10 minutes de temps de greffage UV comme paramètres pour l'expérience ultérieure.

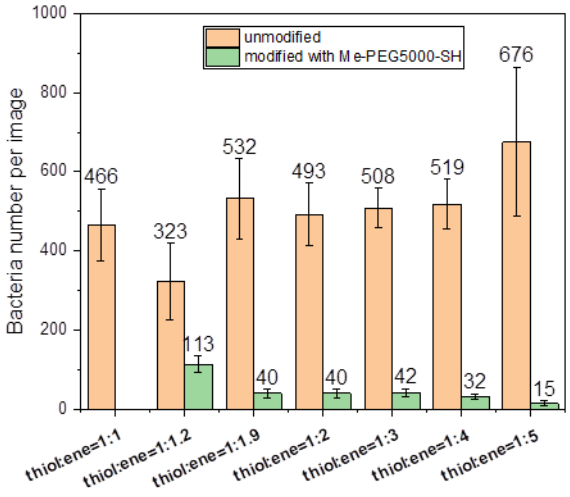

Figure 12. Nombre moyen par image (0,0015 cm^{-2}) de E. coli MG1655 sur des surfaces OSTE modifiées et non modifiées avec différents rapports thiol:ene. 40 mg/ml ($8x10^{-3}$ mmol/ml) de Me-PEG5000-SH avec 5 w/w% d'Irgacure 651 comme photo-initiateur dans du méthanol. Le temps de greffage était de 10 minutes. La barre d'erreur correspond à la déviation standard. Une série d'expériences, valeur moyenne de 10 images pour chaque échantillon.

Après le greffage avec le Me-PEG5000-SH, le nombre moyen de bactéries a diminué avec l'augmentation des proportions d'alcènes, ce qui explique la densité de greffage plus élevée du Me-PEG5000-SH avec l'augmentation de la densité d'alcènes (**Figure 11**).

Lorsque nous greffons la même surface thiol:ene =1 : 5 avec la même concentration de PEG308 ($8x10^{-3}$ mmol/ml). Nous avons constaté que le nombre de bactéries sur la surface modifiée par le PEG308 était 12 fois plus élevé que sur la surface modifiée par le PEG5000. Le PEG308 est plus court que le PEG5000. Pour former une surface entièrement recouverte, nous devons greffer plus de PEG308 sur la surface. Nous avons validé la méthode de greffage avec une concentration élevée de PEG308 dans le glycérol.
Nous avons constaté que le Me-PEG308-SH/glycérol/Irgacure 651 était le meilleur pour produire une surface repoussant les bactéries et les cellules. Le protocole optimisé de greffage est le suivant : le Me-PEG308-SH et le photoinitiateur Irgacure 651 ont été dissous dans du glycérol à une concentration finale respective 1.5 mmol/ml. et 20 mM). Le greffage a été effectué sous une illumination UV de 7.2 mW/cm^{-2} à 254 nm pendant 10 minutes sous une lamelle de quartz. Ce protocole est appelé système Me-PEG308-SH/glycérol/Irgacure 651.

La **Figure 12** montre l'ATR-FTIR de la résine OSTE en excès d'alcène non modifiée et modifiée par Me-PEG308-SH/glycérol/Irgacure 651. Après modification avec Me-PEG308-SH, le signal à 2869 cm^{-1} augmente, ce qui correspond à la bande d'étirement de la chaîne répétée $-CH_2-CH_2-O-$ du Me-PEG308-SH. Ce signal, de plus, augmente avec la proportion de groupes alcènes sur la surface. Pour confirmer le greffage, nous avons analysé la surface à l'aide d'un spectromètre photoélectronique à rayons X (XPS). Nous avons constaté que le pic à 286.6 eV (C-O) augmentait en raison du greffage du Me-PEG308-SH (**Figure 13**). Les résultats XPS concordent avec les résultats obtenus en ATR-FTIR.

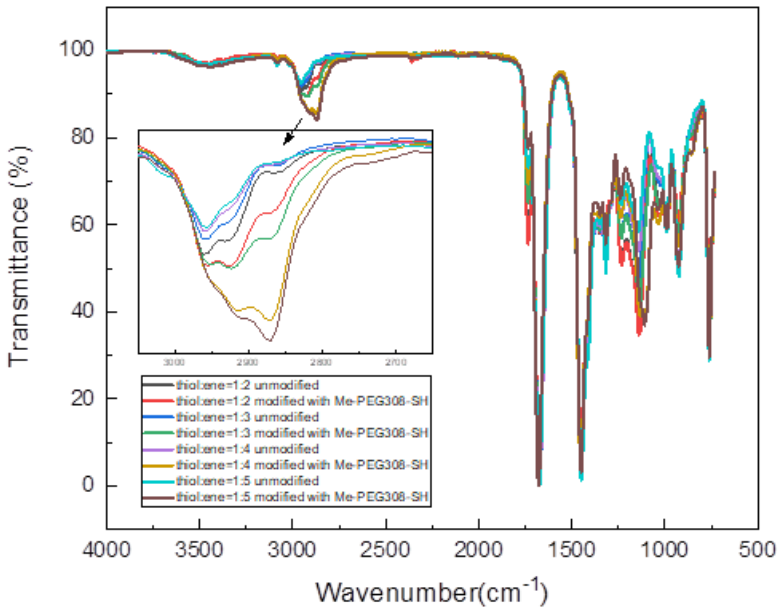

Figure 12. ATR-FTIR de la résine thiol:ene non modifiée et modifiée par Me-PEG308-SH en excès d'alcène de 1:2 à 1:5. La modification de la surface a été réalisée avec le système Me-PEG308-SH/glycérol/Irgacure 651. Le greffage a été effectué sous une illumination de 7.2 mW/cm^{-2} 254 nm UV pendant 10 minutes.

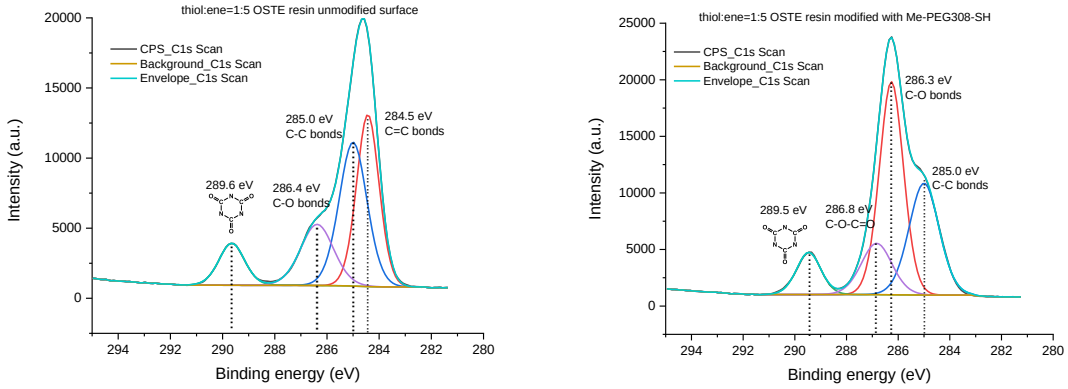

Figure 13. Spectre XPS de surfaces de résine OSTE non modifiées (à gauche) et modifiées par Me-PEG308-SH (à droite) thiol:ene = 1:5.

Comportement des cellules MDCK sur la surface modifiée Me-PEG308-SH.

Surface polymérisée à un photon modifiée par greffage à un photon. Notre objectif est de produire une surface qui repousse les cellules. Nous avons donc réalisé des expériences d'adhésion de MDCK avec des surfaces OSTE non modifiées et modifiées par du Me-PEG308-SH/glycérol/Irgacure 651.

La **Figure 14** montre que le nombre de cellules adhérentes a tendance à diminuer avec l'augmentation du composant alcène, de thiol:ène = 1:2 à thiol:ène = 1:5. Une raison possible est qu'à mesure que le composant alcène augmente, la résistance mécanique du substrat durci diminue et le substrat devient de plus en plus mou.

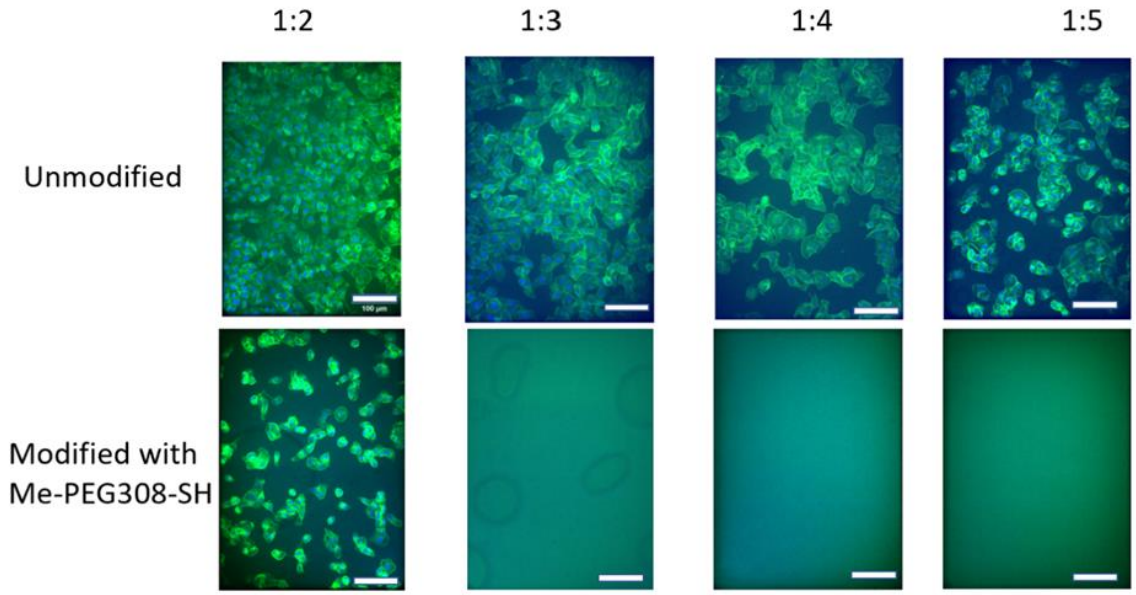

Figure 14. Images confocales de cellules MDCK sur une surface OSTE non modifiée et modifiée par du Me-PEG308-SH/glycérol/Irgacure 651 avec différents rapports entiers thiol:ene. En bleu, les noyaux. Vert, F-actine. Barre d'échelle 100 µm.

Surface polymérisée à deux photons modifiés par greffage à deux photons. Pour transférer les résultats de la polymérisation et du greffage à un photon à la polymérisation et au greffage à deux photons, nous avons conçu un tapis pour tester la répulsion des cellules MDCK.

Comme le montre la **Figure 15**, une goutte de résine OSTE a été déposée sur une lame silanisée. Ensuite, un grand tapis (280 *µm* x 280 *µm*) a d'abord été fabriqué (bleu). La résine OSTE non polymérisée a été lavée par un écoulement rapide d'acétone. Ensuite, une autre goutte de mélange de Me-PEG308-SH, glycérol et d'Irgacure 651 a été déposée sur le grand tapis pour réaliser le greffage *via* le balayage du voxel en suivant une trajectoire composée de réseaux de petits carrés (40 *µm* x 40 *µm*) au niveau du grand tapis. Après la fabrication, le glycérol restant a été éliminé par un lavage rapide à l'acétone. Ainsi, nous avons obtenu un grand tapis carré avec une alternance de petits carrés non modifiés (bleu) et de petits carrés modifiés par Me-PEG308-SH (orange).

Figure 15. Processus de fabrication de tapis par (A) polymérisation à deux photons et greffage à deux photons (B) polymérisation à deux photons et greffage à un photon.

Les cellules MDCK ont été ensemencées sur le tapis stérilisé. Après 2 heures d'ensemencement, les cellules MDCK ont été fixées et marquées. La **Figure 16** (B) montre que les cellules MDCK se trouvent uniquement sur les petits carrés non modifiés de la surface 2D, ce qui démontre l'efficacité de la stratégie poursuivie.

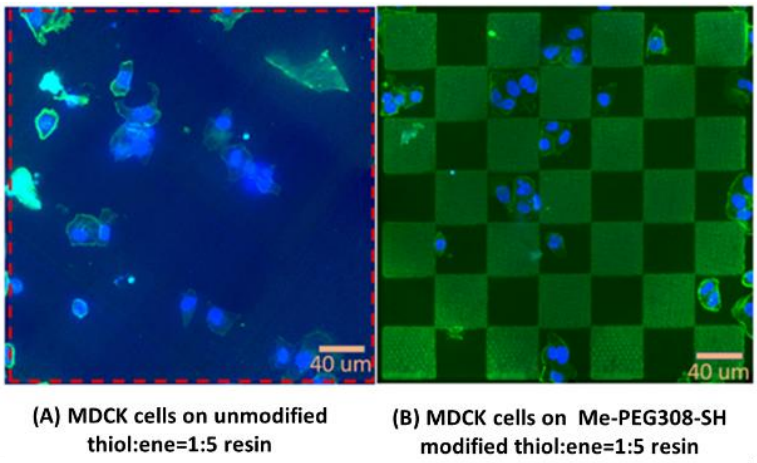

Figure 16. Cellules MDCK sur une résine non modifiée (A) et modifiée par Me-PEG308-SH (B) thiol:ene = 1:5 par polymérisation à deux photons et greffage à deux photons. La ligne pointillée rouge sur (A) est le bord du tapis. Bleu : noyaux. Vert : F-actine. Barre d'échelle 40 μm.

Dans ce chapitre, nous avons mis au point la formulation de la résine OSTE pour la polymérisation à un et deux photons. Pour obtenir une fonction anti-adhésive, différents types de Me-PEG-SH avec différentes longueurs de chaîne PEG ont été greffés sur la surface par greffage à un photon. Les modifications avec le Me-PEG308-SH plus court ont apporté une excellente anti-adhésion à la fois pour *E. coli* et les cellules MDCK. En combinant la polymérisation à un et deux photons et le greffage, des motifs antiadhésifs à l'échelle cellulaire ont été construits avec succès sur la surface 2D.
L'un des grands avantages du greffage photodirigé à deux photons est la possibilité d'effectuer des modifications locales. La modification en 2D est une étape préalable à la modification en 3D. En se basant sur les résultats de l'anti-adhésion sur la surface 2D à l'échelle cellulaire, nous pouvons prévoir que les résultats sur 2D pourraient être transférés à des microstructures 3D en adaptant la trajectoire du laser.

Chapitre III. Structure tridimensionnelle (3D) de la résine OSTE pour la biologie cellulaire

Dans ce chapitre, nous avons fabriqué plusieurs types de structures hexagonales (Figure 5) avec du NOA 61 (une résine OSTE commerciale) et nous nous sommes concentrés sur les microtopographies 3D induisant des protrusions endothéliales, les filopodes, caractéristiques de l'initiation de l'angiogenèse. Ensuite, nous avons transféré les meilleures conditions de greffage thiol-ène pour obtenir des propriétés anti-adhésives d'une surface 2D à des structures/échafaudages 3D avec nos résines OSTE décrites au chapitre II. Une surface 3D modifiée a été réalisée pour explorer le comportement des cellules sur une surface anti-adsorption.

Contrôle de l'élongation des cellules en monocouche.

Nous avons observé la disposition des cellules endothéliales (HUVEC) sur des structures ouvertes normales et allongées par microscopie confocale. Les résultats ont montré la présence de cellules confluentes en monocouche sur les structures normales *D10-ouvertes* (**Figure 17 b**) et sur les structures allongées *l7L14-ouvertes* (**Figure 17 a**). L'élongation ou non de la structure n'a pas eu d'influence sur la colonisation cellulaire avec le type d'ensemencement cellulaire utilisé (au-dessus de la structure). Mais si l'on considère l'orientation des cellules, des différences claires sont apparues entre les structures régulières et les structures allongées.

L'élongation ne se produit que sur les structures allongées, qu'elles soient fermées ou ouvertes (**Figure 17 c** et **d**). En comparant les angles moyens des cellules sur les structures allongées et normales, nous pouvons conclure que l'allongement horizontal des structures hexagonales pourrait contrôler la direction d'élongation des cellules, ce qui est en accord avec la littérature qui montre que les cellules et les noyaux s'allongent dans la même direction.

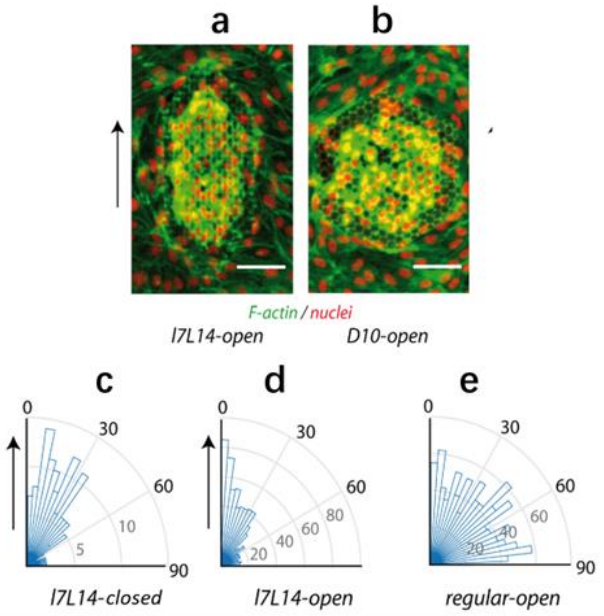

Figure 17. Organisation cellulaire dans la monocouche supérieure. (a, b) Couverture globale des HUVECs des microstructures (a) *l7L14-ouverte* et (b) *D10-ouverte*. rouge : noyaux, vert : F-actine, barre d'échelle 50 μm. (c-e) Histogrammes des orientations des noyaux dans la couche supérieure des microstructures. (c) *l7L14-fermée* (127 noyaux dans 7 structures) (d) *l7L14-ouverte* (700 noyaux dans 15 structures) (e) microstructures *D4.5*, *D6.6*, *D8.8*, *D10*, et *D13.5-ouvertes* (1051 noyaux dans 23 structures). La flèche verticale en (a) représente l'axe de référence pour la structure allongée. Pour les structures régulières, l'axe de référence a été choisi perpendiculairement à un côté de l'hexagone**.**

Piliers verticaux - engagement contrôlé de la monocouche.

Outre l'allongement des cellules, nous avons également constaté que l'engagement de la cellule dans la direction verticale était différent. En nous concentrant uniquement sur les structures *l7L14*, nous avons comparé les structures *l7L14-fermées* et *l7L14-ouvertes*. Pour les structures *l7L14-fermées*, les cellules ne s'engagent que sur la partie supérieure des structures. Il n'y avait pas d'engagement significatif au bas de la structure (**Figure 18 a**). En revanche, les cellules s'engageaient verticalement jusqu'au fond (lamelle de verre) dans les structures *l7L14-ouvertes*, tout en conservant une organisation en monocouche au-dessus de la structure (**Figure 18 b** et **c**).

La **Figure 18 a** et **b** montre que des filopodes endothéliaux se forment dans une structure hexagonale ouverte, alors que ces filopodes ne sont pas observés dans des cultures 2D et sont caractéristiques *in vivo* de l'initiation de l'angiogenèse (filopodes exploratoires des cellules 'tip cells'). Mais une faible concentration de facteur de croissance de l'endothélium vasculaire (VEGF) de 0.5 ng/ml était présente dans le milieu endothélial basal, une concentration insuffisante pour déclencher l'angiogenèse 3D. Cependant, pour vérifier la dépendance possible au VEGF, nous avons ensemencé des cellules HUVEC sur des microstructures ouvertes *l7L14* avec différentes concentrations de ce facteur de croissance. Nous avons constaté que toutes les concentrations de VEGF induisaient la

formation de filopode, et que les filopodes étaient générés dans les structures même sans VEGF (**Figure 18 c**). Nous pouvons conclure que la formation des filopodes est indépendante du VEGF, ce qui signifie que la micro-géométrie seule de nos microstructures ouvertes en *l7L14* peut déclencher la formation de filopodes. Enfin, nous avons observé que les filopodes induits avaient une orientation préférentielle dans les structures allongées, ce qui confirme l'importance de la géométrie du substrat pour la génération et le maintien des filopodes.

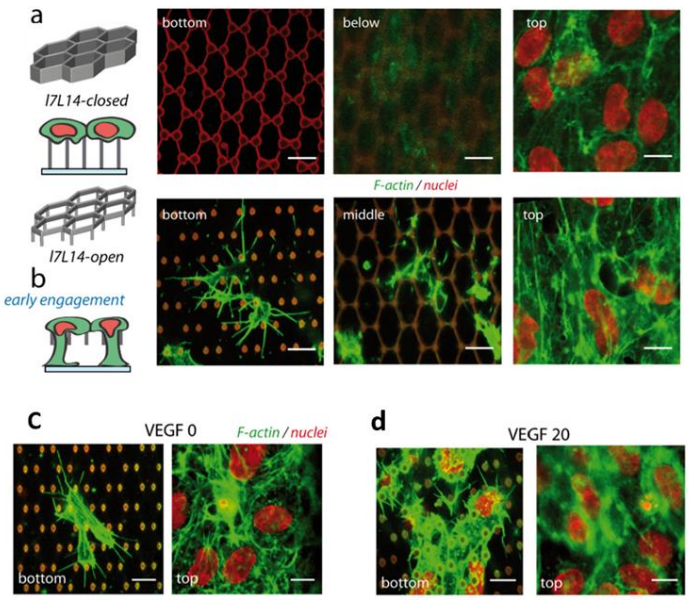

Figure 18. Schéma récapitulatif du comportement global des cellules dans les microstructures (Haut) Organisation des HUVEC endothéliales en fonction de l'allongement des hexagones et de la nature ouverte ou fermée de la microstructure. Ces deux caractéristiques modulent l'orientation de la monocouche supérieure, l'engagement vertical.

La **Figure 19** résume le rôle des microstructures sur le comportement des cellules endothéliales. Avec la TPP de la résine NOA61 à base d'OSTE, nous avons fabriqué des structures fermées et ouvertes, régulières et allongées. Les structures allongées ont pu induire l'élongation des cellules sur la monocouche supérieure. Lorsque les structures étaient ouvertes, qu'elles soient régulières ou allongées, l'engagement vertical sur les structures était déclenché. Les microstructures pouvaient induire la formation de filopodes, même en l'absence du VEGF qui la déclenche *in vivo* dans la première étape de l'angiogenèse.

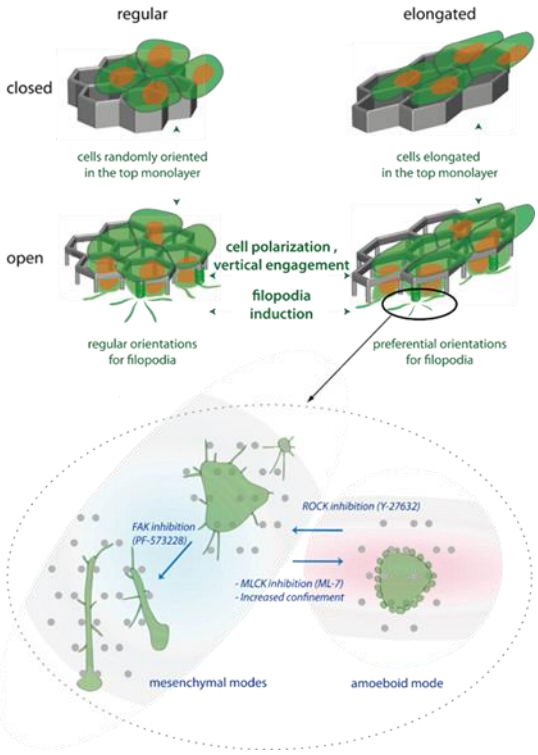

Figure 19. Schéma récapitulatif du comportement global des cellules dans les microstructures (Haut) Organisation des HUVEC endothéliales en fonction de l'allongement des hexagones et de la nature ouverte ou fermée de la microstructure. Ces deux caractéristiques modulent l'orientation de la monocouche supérieure, l'engagement vertical et l'induction des filopodes, ainsi que l'orientation des filopodes. (Bas) Zoom des différents modes protrusifs présents dans le plan inférieur (piliers) des structures allongées ouvertes, et des transitions entre eux : de gauche à droite, dactylopodes et filopodes dans le mode mésenchymateux, et blebs membranaires dans le mode amiboïde**.**

Structures 3D OSTE entièrement modifiées

Grâce aux expériences d'anti-adhésion sur les surfaces 2D du chapitre II, nous savons que les surfaces modifiées avec le Me-PEG308-SH peuvent apporter des propriétés totalement anti-adhésives pour *E. coli* et les cellules MDCK, pour les surfaces à fort ratio d'excès d'alcène OSTE. Nous avons donc transféré cette stratégie aux surfaces 3D. Nous avons choisi la structure c de la **Figure 7** pour l'expérience d'adhésion cellulaire. Nous avons utilisé la résine OSTE thiol:ène = 1:5 avec 0.5 w/w % Irgacure 651 pour fabriquer la structure *l7L14-ouverte* avec une hauteur de 7µm. Après la fabrication, la structure a été rincée avec de l'acétone pour éliminer la partie non polymérisée. Pour une modification complète, une goutte de Me-PEG308-SH/Glycérol/Irgacure 651 a été déposée sur la structure et éclairée sous une lumière UV de 254 nm (7.2 mW/cm^2) pendant 10 minutes. Après le greffage, la structure a été placée dans du méthanol pendant 3 fois, 5 minutes à chaque fois. Nous avons ensuite ensemencé des cellules MDCK pendant 2 heures pour observer la situation des colonies sur les structures non modifiées et modifiées. La **Figure 20** montre les résultats de l'adhésion des cellules MDCK. La structure non modifiée a été entièrement colonisée par les cellules MDCK, alors qu'il n'y avait pas de cellules sur la structure modifiée Me-PEG308-SH et que toutes les cellules étaient autour.

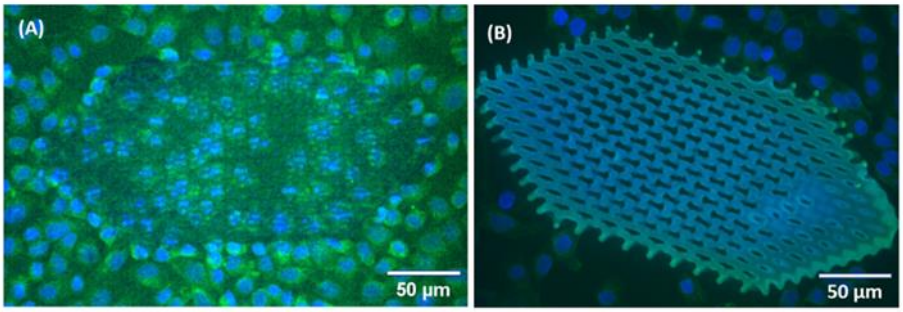

Figure 20. Images de cellules MDCK au microscope confocal sur des structures 3D non modifiées et modifiées. (A) structure non modifiée *l7L14-ouverte* avec thiol:ene = 1:5 résine OSTE, h = 7µm (B) structure modifiée par le Me-PEG308-SH *l7L14-ouverte* avec thiol:ene = 1:5 résine OSTE, h = 7µm. Bleu : noyaux. Vert : F-actine. Barre d'échelle 50 µm.

Dans ce chapitre, nous avons exploré la possibilité d'utiliser la résine OSTE pour générer des échafaudages en tant qu'outils pour la biologie cellulaire fondamentale. Les structures ouvertes fabriquées avec la résine OSTE commerciale (NOA 61) ont induit l'engagement de la monocouche endothéliale, avec la génération de nombreux filopodes associés à un phénotype évocateur d'initiation d'angiogenèse. Ce processus était indépendant du facteur de croissance de l'endothélium vasculaire (VEGF), suggérant que les filopodes endothéliaux, non observés classiquement dans les

cultures 2D, pouvaient être déclenchés par la seule microtopographie. Ensuite, pour combiner la microtopographie et la chimie de surface contrôlée, nous avons utilisé notre propre résine OSTE. Lorsque le rapport de la résine OSTE était de 1:5, nous avons obtenu une surface répulsive pour les cellules en greffant du Me-PEG308-SH. Par greffage à un photon, la structure entièrement modifiée était totalement répulsive pour les cellules. Les prochaines étapes consisteront à effectuer des modifications locales de la surface par polymérisation à deux photons, ce qui permettra un positionnement spatial 3D précis, y compris dans la direction Z, des zones anti-adhésives. Cela fournira un nouvel outil pour le contrôle de l'adhésion locale.

Chapitre IV. Polymérisation à deux photons des protéines

Parmi les matériaux pour la polymérisation à deux photons, outre les polymères synthétiques, les protéines naturelles constituent également une classe de matériaux très importante.
La matrice extracellulaire (MEC) est une structure complexe entourant la cellule et composée d'un groupe de molécules telles que des protéines, des polysaccharides, des facteurs de croissance et d'autres biomolécules. La matrice extracellulaire joue une variété de rôles importants dans les tissus et les organes. En utilisant des protéines comme matériau de départ pour la 2PP, les échafaudages cellulaires préparés peuvent mimer la MEC dans les tissus, fournissant un environnement propice à l'attachement, à la prolifération et à la différenciation des cellules. Les protéines, telles que le collagène, l'élastine ou la fibronectine, sont des composants majeurs de la matrice extracellulaire et jouent un rôle clé dans le comportement des cellules et le développement des tissus. L'utilisation de protéines comme matière première pour la préparation d'échafaudages cellulaires à partir de 2PP permet de recréer la structure et la composition de la matrice extracellulaire naturelle.
La sélection des photo-initiateurs est l'un des points centraux de la polymérisation des protéines, nous avons choisi cinq photoinitiateurs possibles pour tester la polymérisation de la BSA. Bengale rose, mononucléotide de flavine (FMN), Irgacure 2959, sel de benzophénone auto-synthétisé et sel de TPO-Li.

Choix du photo-initiateur

Nous avons testé les cinq photo-initiateurs dans la **Figure 21**. En comparant tous les résultats, nous avons constaté que 25 mg/ml de BSA et 0.5 mg/ml de Rose Bengale (BSA25/RB0.5) dans l'eau constituaient une bonne formulation de la solution protéique pour la polymérisation à deux photons. Pour obtenir la meilleure structure, nous avons réduit le gain laser de 0.3 à 0.4. Après la fabrication, les microstructures ont été placées dans un bain d'eau pour être lavées, puis transférées dans un bain

d'eau pour être visualisées. La **Figure 22** montre les microstructures BSA obtenues dans cette gamme étroite.

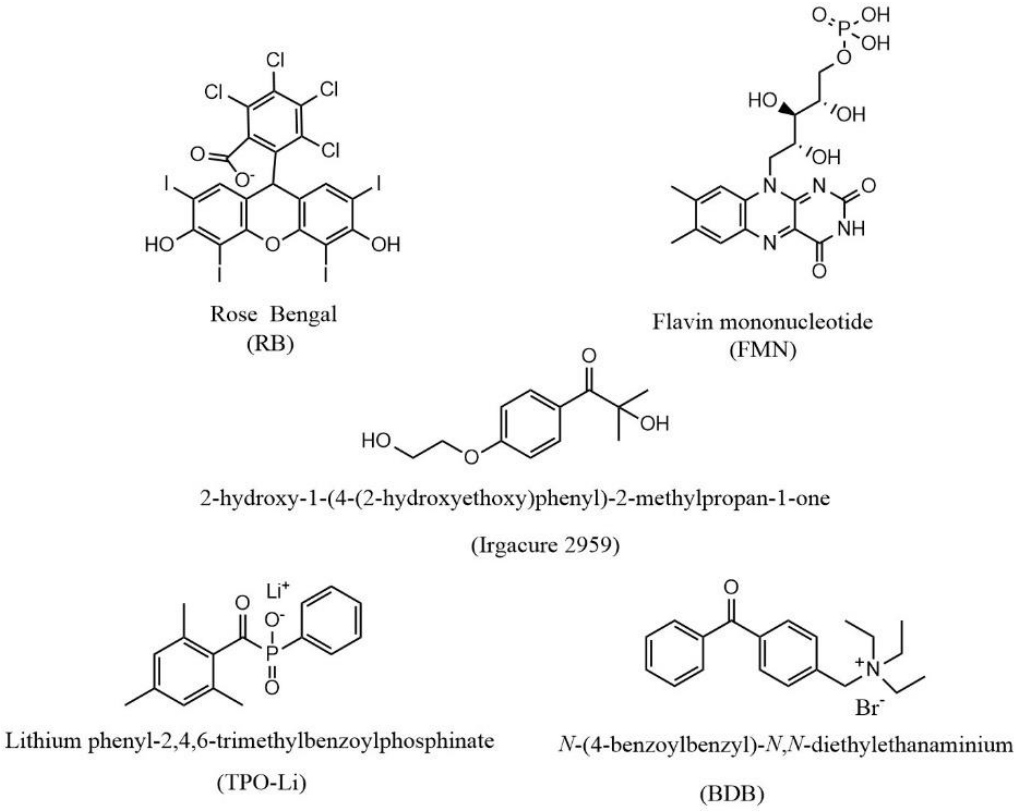

Figure 21. Structures chimiques des photo-initiateurs pour la TPP de la BSA

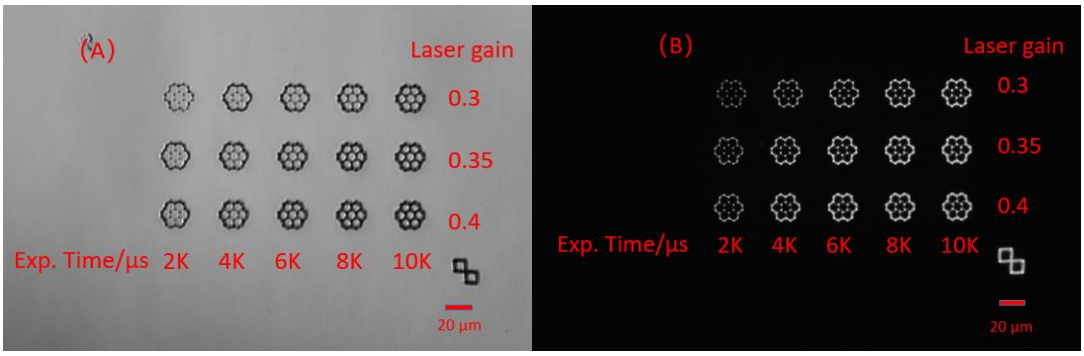

Figure 22. Matrice de structure TPP de BSA25/RB0.5 dans l'eau (A) image de champ de lumière blanche (B) images de fluorescence acquises avec le filtre de canal GFP. Barre d'échelle 20 µm.

Nous avons essayé de sécher les microstructures en BSA directement à l'air pour les observer au microscope électronique à balayage (MEB). Mais toutes les structures BSA se sont effondrées. Les structures BSA ne peuvent pas conserver leur stabilité après avoir été séchées directement à l'air. Le glutaraldéhyde a été utilisé en post-traitement pour réticuler les protéines et les stabiliser. La **Figure 23** montre le mécanisme de réaction du glutaraldéhyde avec les protéines. La **Figure 24** montre les

images des microstructures BSA obtenues avec différents paramètres observées microscope électronique à balayage (MEB). La structure avec LG0.35/Exp8000 avait une partie supérieure très fine. La structure avec LG 0.35/Exp10000 a conservé sa forme 3D. Nous avons conclu que BSA25/RB0.5 était la meilleure formule de polymérisation parmi les solutions testées, et que LG 0.35/Exp10000 était le meilleur paramètre pour leur fabrication à deux photons.

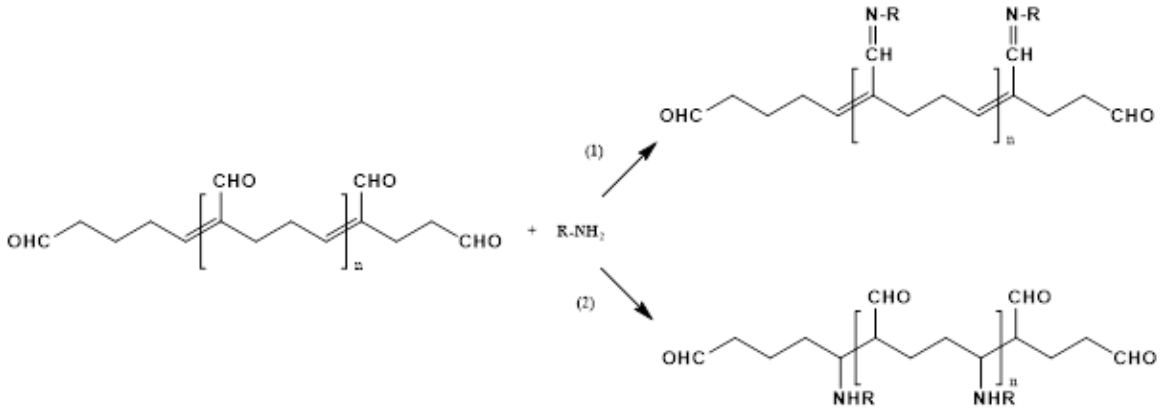

Figure 23. Réactions du glutaraldéhyde avec des protéines *via* (1) la base de Schiff (2) l'addition de Michael.[3]

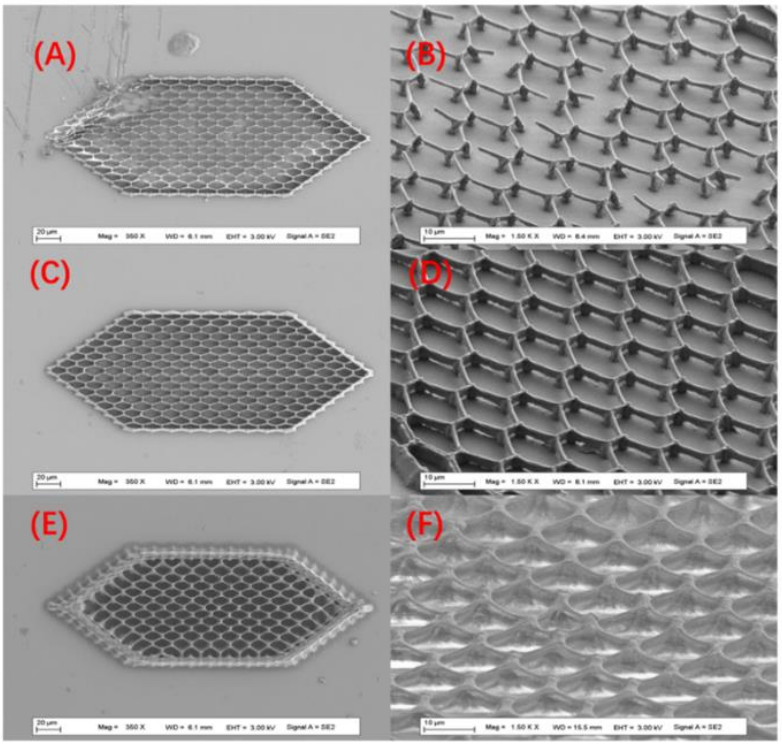

Figure 24. Images SEM de la structure hexagonale ouverte allongée avec BSA. Paramètres de gain laser/temps d'exposition (µs) : (A) LG0,35/Exp8000, (B) zoom de (A). (C) LG0.35/Exp8000, (D) zoom de (C). (E) LG0.35/Exp10000, (F) zoom de (E). Barre d'échelle, 20 µm pour (A), (C) et (E), 10 µm pour (B), (D) et (F).

Comportement des cellules MDCK sur les structures BSA non fixées

La **Figure 25 (A)** montre l'évolution des structures BSA non fixées après l'ensemencement des cellules. Après 1 jour d'incubation, les cellules ont colonisé les trois structures. La **Figure 25 (C)** montre clairement que seule la zone colonisée par les cellules MDCK de la structure avec LG0.35/Exp8000 s'est effondrée. En revanche, aucune déformation ou une déformation minime a été observée dans les zones colonisées par les cellules de la structure LG0.35/Exp10000. Après deux jours d'incubation, les cellules MDCK ont partiellement détruit toutes les structures BSA. En particulier pour la structure avec LG0.35/Exp8000 (**Figure 25 (D)**), la couronne supérieure a disparu, et les piliers intérieurs et la paroi extérieure se sont tous effondrés (**Figure 25 (E)**). Pour les structures construites avec des temps d'exposition plus élevés, les piliers des structures avec LG0.35/Exp10000 (**Figure 25 (F)**) et LG0.4/Exp8000 se sont effondrés et ont partiellement disparu. Après trois jours d'incubation, les structures LG0.35/Exp10000 ont presque disparu alors que les deux autres structures n'ont conservé que la couche externe. Après sept jours d'incubation, la structure LG0.35/Exp8000 ne pouvait plus être trouvée. Les deux autres structures ne conservaient qu'une partie de la paroi externe. Nous avons testé deux autres types cellulaires sur des structures BSA, et nous avons obtenu des résultats similaires.

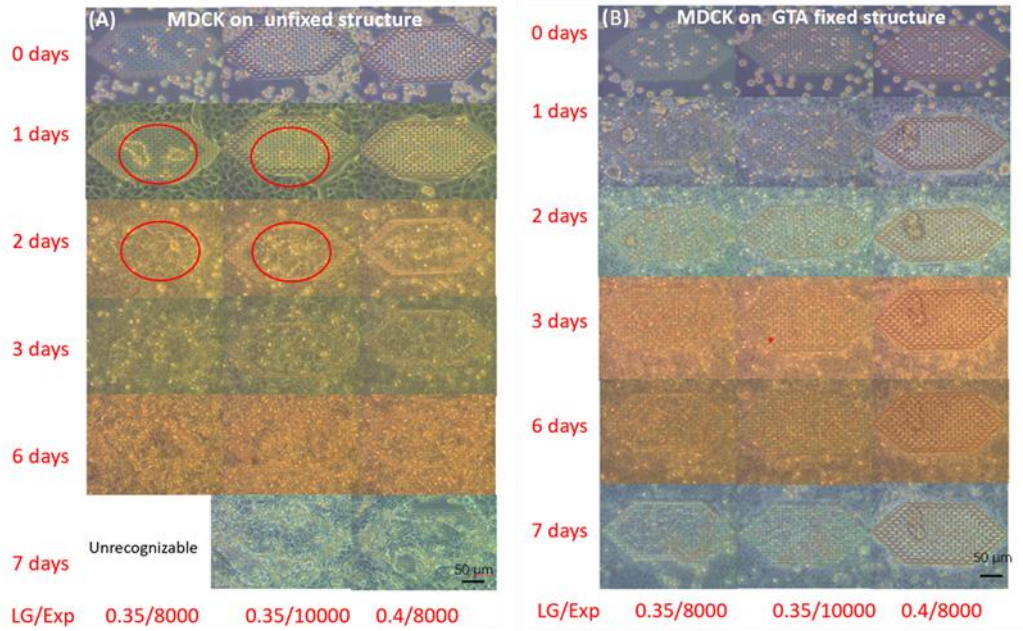

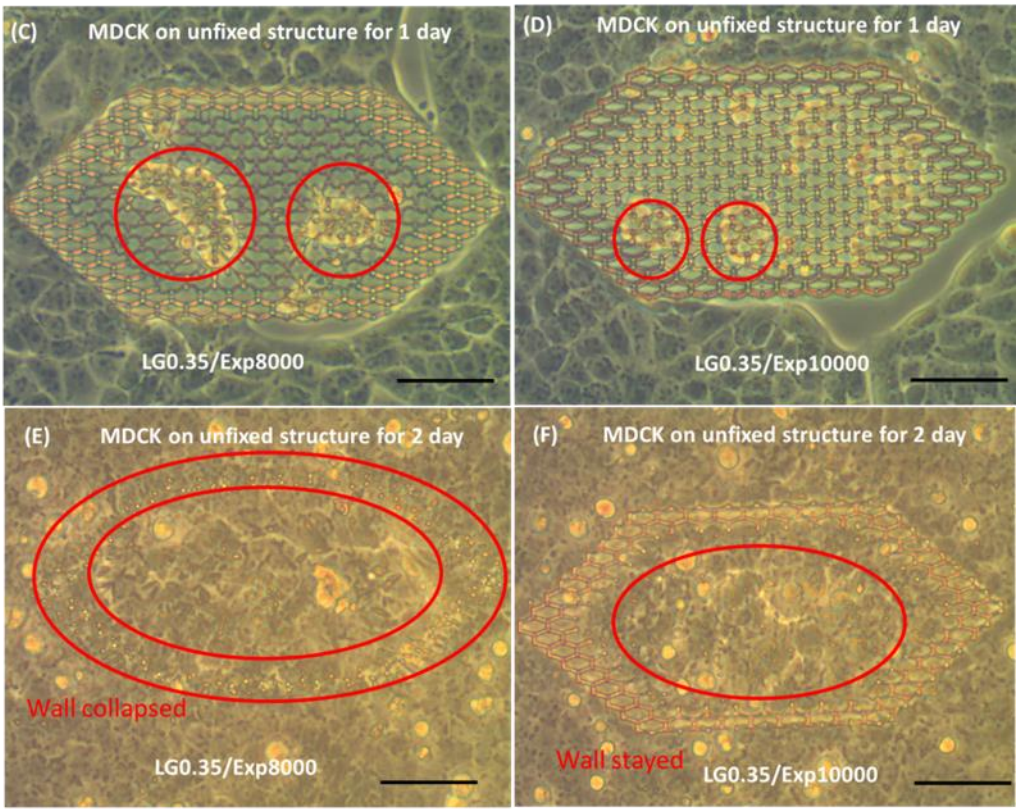

Figure 25. Cellules MDCK sur des structures BSA non fixées (A) et des structures BSA fixées au glutaraldéhyde (B). (C, D, E, F) zoom arrière de (A). Barre d'échelle 50 µm. Résultats similaires obtenus à partir de trois expériences. Images au microscope confocal (canal DAPI) d'une structure BSA incubée avec le surnageant de cellules MDA-MB-231 (Lifeact-mCherry) pendant 3 jours. L'image de gauche représente le bas et l'image de droite le haut de la structure BSA. Paramètres de fabrication, LG0.35/Exp8000. Barre d'échelle 50 µm.

Deux raisons peuvent expliquer la disparition des structures BSA. L'une d'entre elles provient des forces mécaniques et de l'étirement exercés par les cellules. La stabilité mécanique des structures BSA est relativement faible, et les cellules MDCK qui y sont attachées se déplacent d'une manière qui arrache directement la structure. Une autre raison peut être la biodégradation enzymatique qui fragilise les microstructures. En effet, les cellules MDCK sécrètent des protéines hydrolases (protéases) au cours de leur croissance, qui pourraient directement décomposer l'échafaudage protéique.

La structure BSA obtenue par TPP avec BSA25/RB0.5 peut être utilisée comme microstructure pour la culture d'une variété de types cellulaires. Les premières expériences avec différentes lignées de cellules épithéliales, cancéreuses ou non (cellules MDCK, cellules IMCD et cellules MDA-MB-231), ont suggéré que les cellules pouvaient détruire les échafaudages de BSA en quelques jours. Ce phénomène peut être évité par un prétraitement impliquant une réticulation des échafaudages BSA par le glutaraldéhyde. Les mécanismes sous-jacents peuvent impliquer à la fois l'action des protéases cellulaires et la déformation des structures par les forces mécaniques exercées par les cellules. Des

expériences préliminaires de digestion des structures par le surnageant cellulaire ont suggéré une contribution importante des protéases sécrétées. Les expériences futures pourraient viser à préciser les protéases impliquées, par exemple par des études avec des inhibiteurs pharmacologiques, et les forces cellulaires en jeu.

Chapitre V. Résumé général et perspectives

Cette thèse décrit le développement de matériaux bioactifs par polymérisation à deux photons avec une résine thiol-ène hors stœchiométrie (OSTE) et avec des protéines, en se concentrant sur l'albumine sérique bovine (BSA). Avec la résine OSTE en excès d'alcène et la modification de sa surface, nous avons obtenu un substrat repoussant les cellules à l'échelle cellulaire. Il s'agit d'un résultat important, car la technique développée permettra théoriquement de réaliser des greffes de surface localisées ou des parties anti-adhésives dans tout type d'architecture 3D. La résine OSTE pourrait également être utilisée pour fabriquer des structures tridimensionnelles (3D) et pour étudier la réponse des cellules aux microtopographies ; ici, nous avons identifié des géométries spécifiques capables de déclencher la formation de filopodes endothéliaux. En ce qui concerne la TPP des protéines, nous avons identifié des conditions permettant d'obtenir de bonnes résolutions pour les structures BSA et nous avons caractérisé leur évolution lors de l'ensemencement des cellules, en mettant en évidence un comportement de biodégradation intéressant.

Pour la résine OSTE, la modification de surface a été réalisée sur des structures 2D avec du Me-PEG308-SH en premier lieu, et nous avons également réalisé une modification anti-adhésive complète sur des structures TPP 3D. Dans la littérature, la plupart des travaux visant à contrôler les comportements d'adhésion des cellules en 3D ont été réalisés par le biais d'une fabrication par étapes avec la combinaison de différents matériaux. Cette méthode ne permet pas de réaliser un contrôle local de structures complexes en 3D et dans la direction verticale *z*. Cependant, notre succès dans le contrôle de la surface 2D par modification à deux photons peut être transféré pour résoudre les difficultés liées aux modifications locales de structures 3D complexes.

Pour le matériau BSA, le mécanisme même de dégradation de la structure BSA par les cellules doit encore être mieux caractérisé, avec l'utilisation éventuelle d'inhibiteurs ciblant des protéases spécifiques, et l'acquisition d'expériences plus résolues spatiotemporellement afin d'estimer la contribution des forces cellulaires et des déformations de la structure qui en résultent dans le processus. Outre la BSA, de nombreuses protéines peuvent encore être utilisées pour remplacer la BSA, en particulier le collagène I. L'étude de l'application du collagène I, composant majeur de la matrice extracellulaire, dans la TPP sera un sujet important à explorer à l'avenir.

References

(1) Lowe, A. B. Thiol-Ene "Click" Reactions and Recent Applications in Polymer and Materials Synthesis. *Polym. Chem.* **2010**, *1* (1), 17–36. https://doi.org/10.1039/b9py00216b.

(2) Carlborg, C. F.; Haraldsson, T.; Öberg, K.; Malkoch, M.; Van Der Wijngaart, W. Beyond PDMS: Off-Stoichiometry Thiol-Ene (OSTE) Based Soft Lithography for Rapid Prototyping of Microfluidic Devices. *Lab Chip* **2011**, *11* (18), 3136–3147. https://doi.org/10.1039/c1lc20388f.

(3) Migneault, I.; Dartiguenave, C.; Bertrand, M. J.; Waldron, K. C. Glutaraldehyde: Behavior in Aqueous Solution, Reaction with Proteins, and Application to Enzyme Crosslinking. *Biotechniques* **2004**, *37* (5), 790–802. https://doi.org/10.2144/04375RV01.

Chapter I. Introduction

In recent years, the demand for biomaterials has sharply increased. The development of biomaterials has been a long and continuously evolving process, which is now in strong expansion with a large set of new interdisciplinary approaches making possible new applications, and the definition itself of biomaterials has evolved during the development of the field. While the goal of biomaterials has always been to improve the life quality of human beings, the preliminary definitions in 1967 and 1974 both emphasized the inert material for implantation.[1,2] The early requirement for biomaterials appeared quite simple and focused on good biocompatibility.

Nowadays, researchers pay growing attention to designing bioactive materials. Bioactive material means there is a specific biological response arising from its interaction with the biological system.[3] For tissues, the aims are to restore and repair the original function of organs. This is based on responses at the cellular level that can include polarization, proliferation, differentiation, etc. For bacteria, the functions targeted when building biomaterials can be anti-fouling or bacteria-killing. More special developments like biodegradation and biomimicry are on the road to meet the need for smart materials.

The cell microenvironment plays a major role in biology and emerges as a key determinant of cell behavior and cell functions in many biological processes. The extracellular matrix (ECM) within the cell microenvironment constitutes a structural foundation for cells, but also a source of three-dimensional (3D) biochemical and biophysical cues that trigger and regulate cell behaviors. Increasing evidence suggests that the 3D character of the microenvironment is involved in the development of many critical cell responses observed *in vivo*, requiring the development of functional and biomimetic materials for engineering the 3D cell microenvironment.[4]

Precise tissue engineering allows us to build controlled scaffolds as the cell scale. In particular, technologies like two-photon polymerization (TPP) give rise to microfabrication at a submicrometer scale. This has applications not only for the medical field of bioimplants but also in the field of fundamental cell biology. Many researches have shown the effect of microtopographies on the behavior of mammalian cells. [5,6] Cell behaviors like polarization[7], proliferation, differentiation[8,9], migration[10] or alignment[11] were triggered out by the generation of specific 3D microtopographies. Another central aspect governing cell behavior is the chemistry of the scaffold, giving access to specific chemical surfaces (cell repellent or cell adhesive, cell selective surfaces) and participating in the definition of their mechanical properties. But how the combination of both topography and surface chemistry will influence the cell behavior is not well-understood and is still under dynamic development. The aim of this work is to take advantage of both chemistry and TPP to build real 3D microstructures with the

precise control of the local chemistries, and consequently to control the properties of the scaffolds generated as a tool for cell biology. And also, it could be also used in the field of bioimplants in the future.

In this introductive chapter, first, we will give an overview of the principles of TPP from theory and experimental processes, which builds the fundamental stage for the 3D microstructure fabrication. The first sub-section is mainly about the mechanism of TPP, equipment set-up, parameters setting of the equipment, selection of the photoinitiators, and post-process after fabrication. The mechanism of TPP and equipment set-up will help us to determine how best to realize TPP. Having a good understanding of the TPP theory and instrumentation, we will shift our focus to the composition of the materials. The photoinitiator is an important component of the materials. A fixed laser wavelength is imposed in our set-up; the selection of a photoinitiator that is compatible with the given wavelength is an important part of the development of materials for TPP. The choice of photoinitiator deeply affects the resolution of fabrication, which means the accuracy of the 3D microstructure. Here we will describe the principles of photoinitiators for TPP, the commonly used photoinitiators and how chemists can design efficient photoinitiators to meet their needs based on the principles of molecular structures. The development of post-process is the last step of fabrication to obtain a stable 3D structure with nice resolution.

For the second sub-section, we will introduce the materials that can be used for TPP. There are many commercially available resists nowadays. Besides, we will focus more specifically in this PhD on a synthetic material, off stoichiometry thiol-ene (OSTE) resin, and a natural material, proteins. Thiol-ene resin has been used by many researchers to fabricate 3D structures due to its good mechanical properties. By TPP, 3D structures can be fabricated easily and by changing the ratio of two functional groups, surfaces with excess of thiol or alkene groups bring considerable opportunities for post-process after fabrication. Proteins are, as well, excellent candidates for the formation of 3D microenvironment. Proteins have been used to fabricate pH sensitive structures, optical microdevices and polymer-protein hybrid structures. Here we will introduce the commonly used proteins for microfabrication, especially bovine serum albumin (BSA), collagen I.

Equipment and materials enable us to fabricate desired structures. Further functionalization brings more opportunities for the application of the structure fabricated by TPP. In a third sub-section of this introduction, we will present tools to perform surface modifications of TPP structures. We will specifically address the acquisition of anti-adhesive properties by PEG (polyethylene glycol), which will be used further in our work for the grafting of OSTE surfaces.

Finally, we will introduce the applications of microfabrication in cell biology. The development of materials enriches the toolbox for biology. Many researchers have used microstructures to study basic cell biology. Both the synthetic material OSTE and the natural material BSA will give us opportunities to explore new tools in this field.

1.1 Introduction of Two-Photon Polymerization (TPP)

3D microstructures have become more and more important in many fields, such as microfluidics[12,13], medical devices[14,15,16] or tissue engineering[17,18]. To meet the growing demand, techniques like 3D printing[12,13,17,], microstereolithography[19], NanoImprint Lithography[20], electron beam lithography[21] or electrospinning[22] are developed to manufacture structures for different situations. Among these methods, TPP is a voxel-by-voxel technique that allows to build microstructures with resolutions down to 100 nm. In this chapter, we will first remind the basic mechanisms of TPP, second detail the important optical parameters to be optimized to produce the microstructures, and then the way to improve the accuracy of two-photon polymerization.

1.1.1 Mechanism of TPP

1.1.1.1 Photopolymerization

Photopolymerization is a reaction initiated by light absorption, in which a liquid or gel monomer is polymerized into a solid structure. It involves the creation of radicals by light from photoinitiators. A photopolymerization process consists of three steps, the initiation step, the propagation step and the termination step. In the initiation step, equation (1), photoinitiators (PIs) reach to the excited state (PI*) by light absorption and decompose to radicals (R•). *x* is the number of photon (*hv*) that the PI absorbs. In the propagation step, equation (2), the radicals combine with monomers (M) to produce monomer radicals (RM_n•). In the termination step, equation (3), two monomer radicals recombine, which increase the chain length, and the photopolymerization process is terminated.

$$PI + x\,hv \rightarrow PI^* \rightarrow R\bullet + R\bullet \quad (1)$$

$$R\bullet + M \xrightarrow{M} RM\bullet \xrightarrow{M} RMM\bullet \xrightarrow{M} \dots \xrightarrow{M} RM_n\bullet \quad (2)$$

$$RM_n\bullet + RM_m\bullet \rightarrow RM_{(n+m)}R \quad (3)$$

Typical photopolymerization is realized by ultraviolet (UV) light and involves classical processes of one-photon absorption for step (1). Traditional UV light polymerization is also used to fabricate bulk 3D tablets by injection.[23] But when the size of the 3D structure to be produced goes to cell scale, traditional polymerization realized by UV, one-photon polymerization (OPP), cannot realized the target any more. TPP is in need to meet the demand of increased 3D resolution.

1.1.1.2 One-Photon Absorption (OPA) and Two-Photon Absorption (TPA)

Photopolymerization is triggered by radicals produced from photon absorption of a photoinitiator. Photon absorption is the first process when incident light penetrates the atmosphere of interacting molecule. Electronic transition occurs when molecules absorb photons. The electronic system transfers

from the lowest-energy ground state (S_0) to an electronically excited higher-energy state (Sn, in which n = 1, 2 and so on).[24] Exited molecule can produce radicals like equation (1) in part 1.1 or return to ground state by emission fluorescence. The ability to absorb photon of a molecule depends on the molecule itself and on the wavelength of the incident light. Depending on the number of photons that the molecule absorbs, photon absorption can be classified into OPA and multiple-photon absorption. For multiple photon absorption, all the photons must be present quasi-instantaneous and at the same location. The absorption probability therefore scales as the light intensity to the power of the number of photons triggering the absorption event (typically two, but in some cases three or more).[25] Here, we are mainly talking about one-photon and two-photon absorptions. **Figure 1.1** reveals the energy level transitions for OPA and TPA.

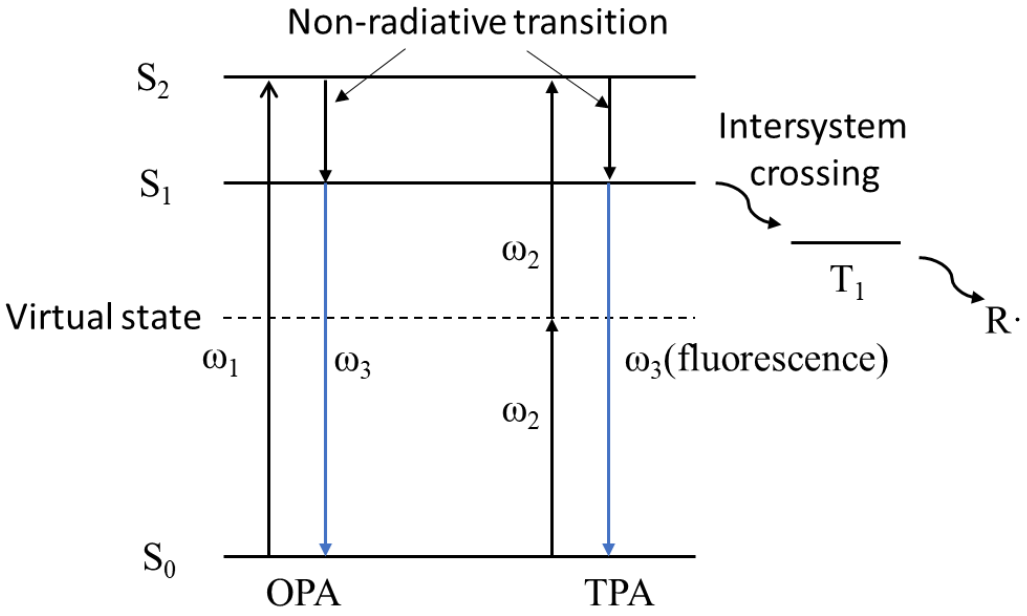

Figure 1.1 The schematic energy diagram for OPA and degenerate TPA process. S_0 is the ground singlet state, S_1, and S_2 are excited singlet states; ω_1 and ω_2 are incident light frequencies and ω_3 is fluorescent emission frequency; T_1 is the triplet state; $R^{\cdot}$ is radical.

TPA, consisting in quasi-simultaneous absorption of two photons by a chromophore, was first proposed theoretically by Maria Göppert-Mayer in 1931.[26] In 1961, TPA was experimentally observed by W. Kaiser and C. G. B. Garrett.[27] TPA is a non-linear process, meaning that the absorption coefficient depends on the optical intensity.

The probability of TPA is proportional to the square of the light intensity. Thus the confocal volume of TPA aggregates to a volume small enough to bring a series of advantages like reduced out-of-focus photobleaching, reduced autofluorescence and intrinsically high three-dimensional resolution.[24] In order

to achieve high photon density in the light beam to induce simultaneous absorption of several photons by one molecule, specialized lasers are used, which will be described in detail in the following part.

The primary quantity used to describe a molecule's ability to absorb a photon of a particular wavelength and polarization is the absorption cross-section, which has units of area (e.g.: cm^2). In memory of the contribution of Maria Göppert-Mayer, the unit for TPA cross-section is named the "GM". One GM is 10^{-50} cm^4 s $photon^{-1}$. The absorption cross-section for TPA is far lower than that for OPA. As Figure 1.1 shows, radicals are produced only when electron transfers from singlet state to triplet state after TPA, while fluorescence is also produced with a certain probability from S_1 singlet state to S_0 singlet state.

1.1.1.3 Specificities of TPP

TPP is a photochemical process initiated by a laser beam focused tightly into the volume of the photosensitive materials. It is realized through TPA of the photoinitiator or photosensitizer, with photochemical reactions described in 1.1.1.

By moving the focus following the designed trajectory, a three-dimensional structure with a specified shape can be processed. The elementary photopolymerized area is called voxel, and its size is a measurement of TPP processing resolution.

Fourkas *et al.*[25] gave a model to calculate the distribution of excited molecules. If we ignore the depletion of beam intensity in *z* direction, the total number of molecules *Ne(z)* excited in a light beam is independent from the height of light beam *z* in one photon absorption but inversely proportional to the area of the plane of the beam *A* in two-photon absorption. Thus, the probability of exciting molecules with TPA is much greater at the laser focus than in any other region of the beam.[28] More intuitively, the shape of the excitation profile explains that the spatial resolution of TPP is higher than that of one-photon polymerization (OPP), not only in the vertical direction, but also in the lateral one (**Figure 1.2**)[29]. The high spatial resolution makes it possible to fabricate subcellular-scale microstructures for cell behavior research. The polymerization only begins when there are enough radicals to reach out the threshold (**Figure 1.3**)[30], with the following difference between OPP and TPP.

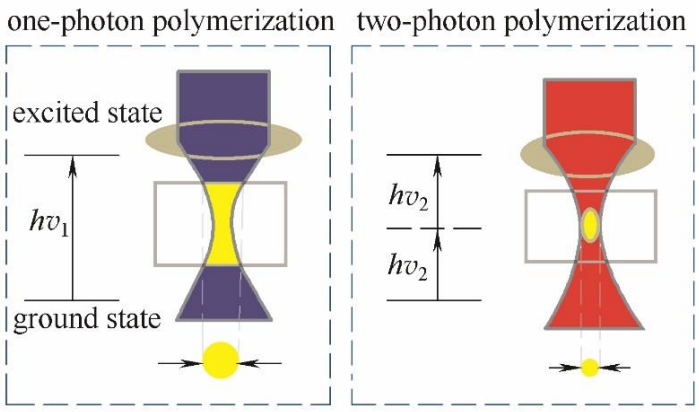

Figure 1.2 Region of OPA and TPP

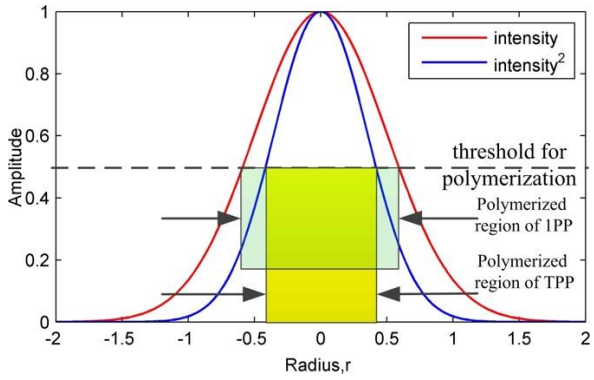

Figure 1.3 Distribution of light intensity in the laser focus of a Gaussian beam: $I(r) = I_0\exp(-2r^2/\omega_0{}^2)$, where the beam waist is $\omega_0 = 1$ and the light intensity at the focus is $I_0 = 1$ (dimensionless for clarity). The intensity (red) and the squared intensity (blue) of laser focus. The photopolymerization process takes place at the region where the light intensity reaches the threshold for polymerization.[30]

1.1.2 Equipment and parameters for TPP

1.1.2.1 Equipment set-up for TPP.

A typical experiment set-up for TPP is divided into three parts, laser source, microscope with laser path and control system. The laser from the source reaches the microscope through a series of focuses and reflections in the optical path. A computer controls the whole process by shutter, attenuator, and piezo stage. With a charged-coupled device (CCD) camera, the operator can capture in time the image of the manufacturing process(**Figure 1.4**).

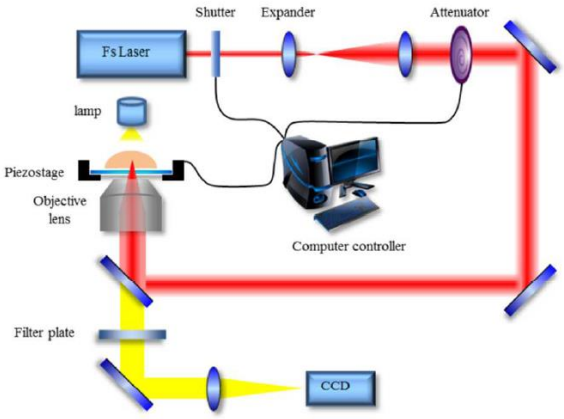

Figure 1.4 Typical experiment set-up for TPP[29]

For the choices of laser source, there are three kinds of laser sources for TPP, femtosecond, picosecond and nanosecond lasers. [14,31]

For the optical system, the microscope and laser path can vary. The objective lens, which gathers the incident light to a focus point to meet the needed light intensity, is a central element in the optical system.

For the control system, the piezo stage is a key element to realize 3D designs. The laser source is fixed. So, the fabrication trajectory is traversed by changing the relative position of the resin to the laser. The shutter in the control system is used to control the exposure time. With the demand for large area fabrication, 3D control systems like 3D linear motor-driven stages are developed to enlarge the size of the microstructures produced.

The typical equipment set-up above uses a single laser beam. The TPP process goes along with the movement of the laser focus, so that it takes time to fabricate a large area structure. Gittard *et al.*[32] developed a new method to fast the manufacturing process. As shown in **Figure 1.5**, a computer-generated hologram pattern technology was used to generate multiple laser beams in controlled positions from a single laser. These multiple beams were then used to simultaneously produce multiple microstructures by TPP. Arrays of micro-Venus structures (the world-wide famous sculpture in Louvre *Venus de Milo*), tissue engineering scaffolds, and microneedle arrays were successfully produced by this technique of multifocus TPP.

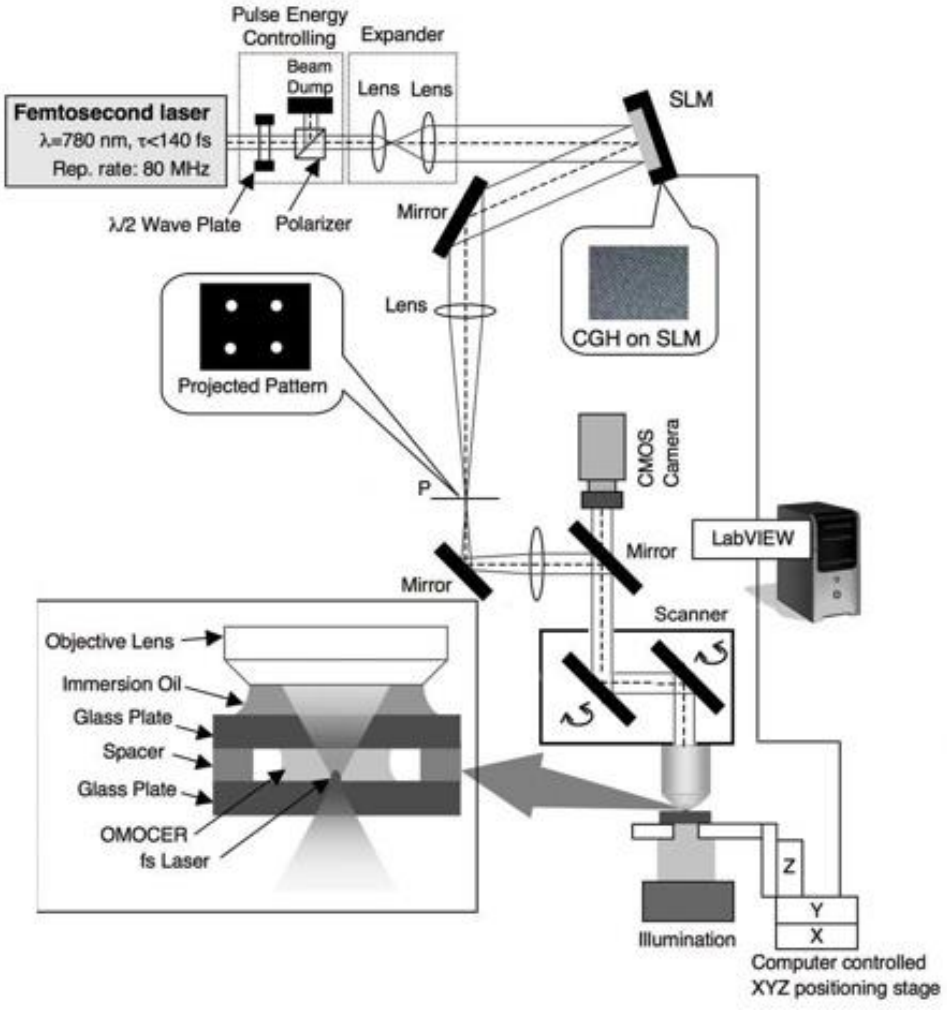

Figure 1.5 Diagram of the multi focus laser system.[32]

1.1.2.2 Parameters of the TPP system.

The main parameters characterizing a pulsed laser are the wavelength (nm), the pulse width (ms, μs, ns, ps, fs), the pulse energy (J), the peak power (W), the average power (W), and the repetition rate or frequency (Hz). The pulsed laser usually refers to the laser devices that produce pulses between 0.5 and 500 ns. When the pulse width is below 100 ps, we usually name them with ultrafast laser. (**Figure 1.6**)[33]

The most used laser for TPP in the literature is the femtosecond pulse laser. Most common commercial microfabrication systems are from Nanoscribe (https://www.nanoscribe.com , Karlsruhe, Germany). The wavelength used in this system is always 780 or 800 nm. The wavelengths of the commonly used picosecond and nanosecond pulse lasers are both 532 nm (see Microlight3D, https://www.microlight3d.com, France). The laser wavelength needs to be chosen according to the two-photon absorption characteristics of the photoinitiator and the resin.

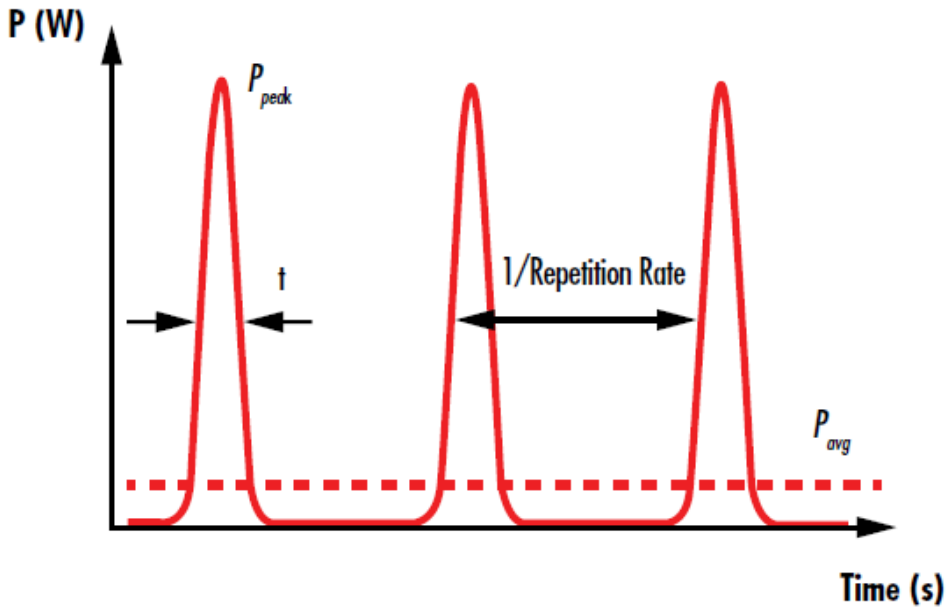

Figure 1.6 The pulses of a pulsed laser are temporally separated by the inverse of the repetition rate.[33]

During the controlling by computer, the manufacturing parameters are the laser power, and the exposure time which controls the shutter speed. An important optical parameter for the microscope is the Numerical Aperture (*NA*) of the lens. The refractive index (*n*) of the medium in which the lens is placed determines the light-gathering ability. (**Figure 1.7**)

$$NA = n \cdot \sin\theta \quad (4)$$

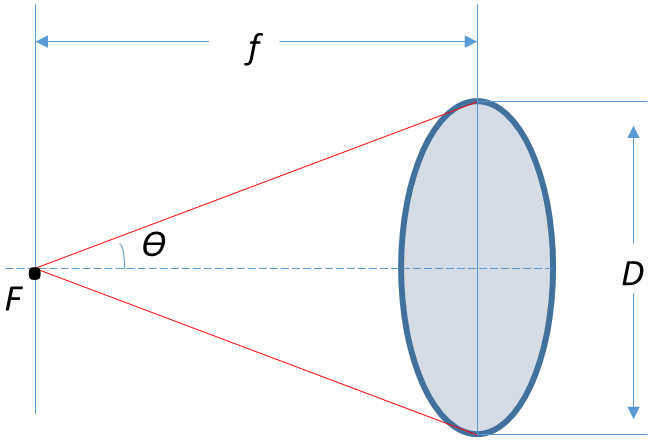

Figure 1.7 Numeral aperture of optical lens

In general, the refractive index *n* varies according to the medium, 1.00 for air, 1.33 for pure water, and typically 1.52 for immersion oil. The larger the value is, the stronger the light gathering ability of the microscope

1.1.3 Influence of parameters for the resolution of fabrication

1.1.3.1 Basic concepts

In 2001, the "micro-bull" proposed by Kawata *et al.*[34] was a milestone in the development of two-photon polymerization-3D printing (TPP-3DP) technology. The authors used SCR500 photosensitive resin, a femtosecond laser with a wavelength of 780 nm and a pulse width of 150 fs to process a bull model of 10 μm long and 7 μm high (**Figure 1.8**). The size of red blood cells is around 7~8 μm. So, the TPP construction can theoretically flow in the finest capillaries in the human body, showing the potential application value of TPP-3DP technology in the medical field. The microstructures created were thinner than the diffraction limit determined by the Rayleigh criterion. The Rayleigh criterion for the diffraction limit to resolution states that two images are just resolvable when the center of the diffraction pattern of one is directly over the first minimum of the diffraction pattern of the other. Hence the Rayleigh criterion will influence the size in lateral direction. In this work, the lateral spatial resolution (LSR) is as small as 120 nm. The results beyond the diffraction limit are attributed to the threshold of TPP, because the laser intensity of the focal point is spatially Gaussian, with the highest intensity in the center of the focal spot.

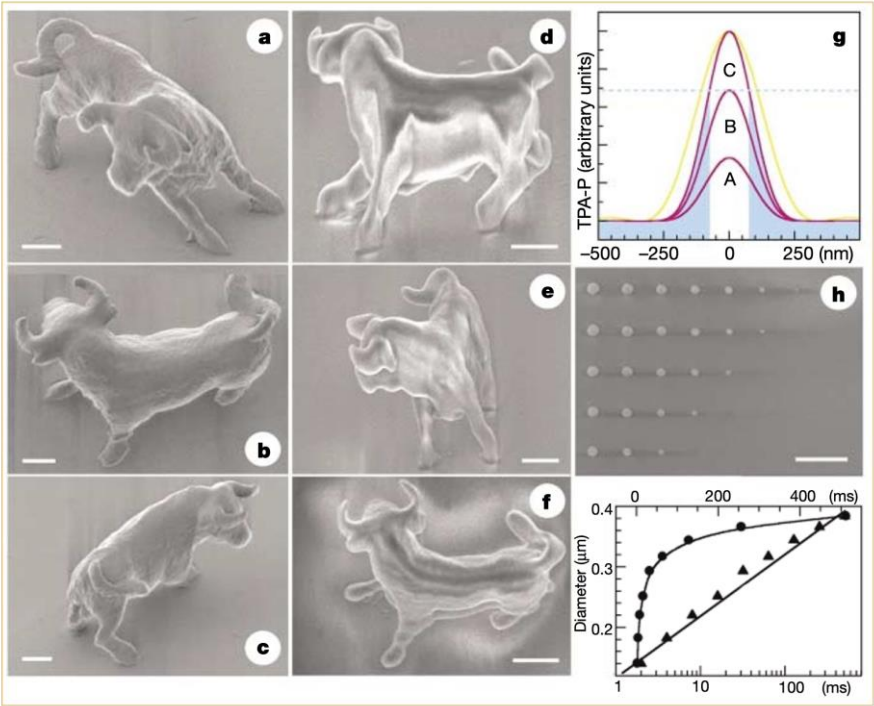

Figure 1.8 Microfabrication and nanofabrication at subdiffraction-limit resolution[34].

To better understand the fabrication process of TPP, it is very important to figure out the resolution and fabrication accuracy. Resolution refers to the minimal unit size of the fabrication. For pinpoint scanning model laser source, the resolution refers to the size of an individual voxel. For continuing scanning

model, the resolution refers to the width of the lines. Fabrication accuracy relies on voxels and the overlapping of voxels. For example, tight overlapping of voxels generates structures with smoother edges (more accurate) than loose overlapping. The accuracy of process lies in the size, shape, surface roughness and overlapping of isolated voxels. Hence how to control the voxel is the key point to realize accurate fabrication. A voxel is characterized by its dimensions in the horizontal plane (*xy* plane), named the lateral spatial resolution (LSR), and in the *z* plane, named the vertical resolution.(**Figure 1.9**) The voxel size depends on the laser gain and exposure time. When laser gain is fixed, longer exposure time brings bigger voxel. While exposure time is still, higher laser gain brings bigger voxel. The overall control of voxel size needs the combination of laser gain and exposure time at the same time.

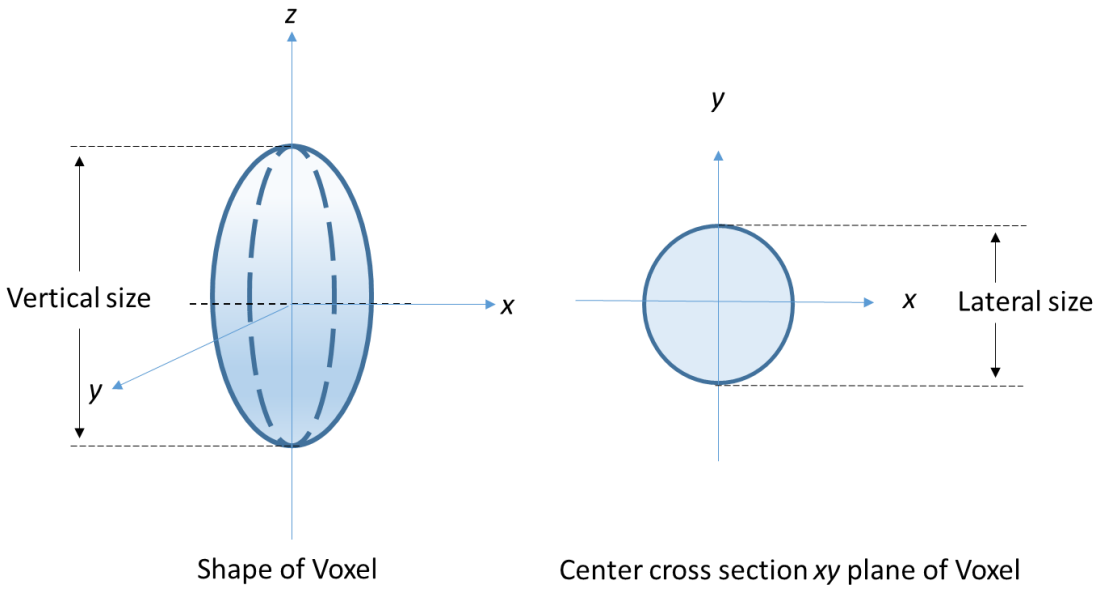

Figure 1.9 The shape of voxel in the *xz* and in the *xy* planes

For TPP, the first step is to choose the laser. Stankevičius *et al.*[31] compared the differences by using nanosecond (35 ns) and picosecond (300 ps) pulsed lasers to form pillars. The structure fabricated by 35 ns pulse laser was around 1-2 times taller and wider compared to the structures produced using the 300 ps-laser pulses, even when the peak intensity of the ps pulses was 3.5 times larger than that of the ns pulses. Results showed that the resolution of nanosecond laser pulse was easily influenced by thermal accumulation and oxygen diffusion.

Also, Stankevičius *et al.*[31] explored the effect of the repetition rate. For 300 ps laser pulse with the same peak intensity, two pulse repetition rates (1 kHz and 500 Hz) were tested. The results revealed that higher repetition rate also produced bigger size in both lateral and vertical direction. Influence of resolution from thermal accumulation and oxygen diffusion for ps pulse laser starts to matter when the repetition rates are higher than 1kHz.

Besides the laser and repetition rate and pulse width, the wavelength of the beam is also a key role that influences the accuracy of manufacturing.

According to the calculation of Zhou *et al.*[30], the length of voxel is expressed as follows,

$$l(P,t) = \frac{2\lambda\left(n_{oil}^2 - NA^2\right)^{1/2}}{\pi NA}\left[\left(\frac{\delta_e I_0^2 n\tau}{C}\right)^{1/2} - 1\right]^{1/2} \quad (5)$$

in which,

$$I_0 = \frac{2.3P\lambda}{\pi\omega_0^2\tau f h C} \quad (6)$$

$$n = ft \quad (7)$$

and C is defined as

$$C = \ln\left[\rho_0/(\rho_0 - \rho_{th})\right] \quad (8)$$

where $P, \lambda, n_{oil}, NA, n, \delta, \omega_0, \tau, f, h, t, c$ and ρ denote the basic concepts (**Table 1.1**).

Table 1.1 Basic concepts used in the calculation of length of the voxel.[30]

average power	P
wavelength of laser beam	l
refractive index of the immersion oil	n_{oil}
numerical aperture	NA
number of the pulse	n
effective two-photon cross section	δ_e
beam waist	w_0
pulse width	t
repetition frequency	f
Planck constant	h
total processing-irradiation time	t
speed of light	c
initiator particle density	ρ_0

Taking equations (6), (7), (8) into (5), we can know that the length of voxel l is proportional to the wavelength of laser beam (λ) to the power of 1.5 equation (9). Hence, a shorter wavelength induces a smaller resolution.

$$l \propto \lambda^{1.5} \quad (9)$$

When the laser intensity is lower than the TPP threshold, no polymerization reaction occurs at the focal point; when the laser intensity reaches the TPP threshold, TPP will occur in the center of the focal point. As the laser intensity increases, a larger area in the focal point will polymerize. Although the Rayleigh criterion indicates that TPP has a theoretical diffraction limit, the actual aggregate size can break through the diffraction limit determined by the Rayleigh criterion due to the existence of the TPP threshold. Adjusting the TPP threshold can change its resolution.

1.1.3.2 Exposure time and laser power

The exposure time and the laser power also influence the shape of isolated voxel. Sun *et al.*[35] found that in TPP, the influences of power change and exposure time tuning obey different rules. If μ is defined as the ratio of vertical size to lateral size (**Figure 1.9**), the results show that the ratio μ grows faster with increasing laser power than with increasing exposure time. With an increase of power, the intensity of radicals grows by the square of the light density in vertical direction (**Figure 1.10** a). Whereas the radical change caused by exposure time change depends on the diffusion towards all directions (**Figure 1.10** b). This model shows that low power combined with long exposure time favors the formation of low μ voxel, which brings high quality fabrication at the end.

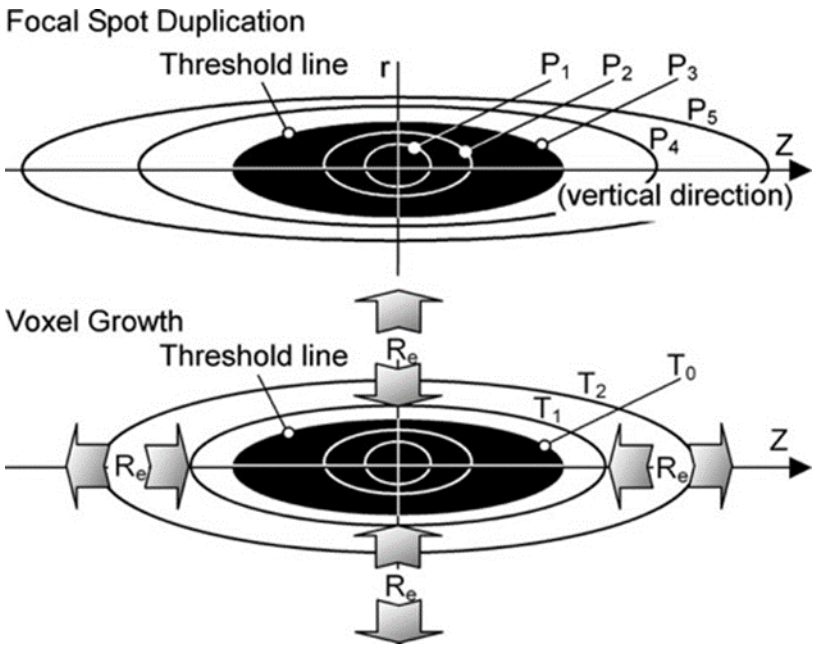

Figure 1.10 Models for initial voxels formation and growth. a) Focal spot duplication, which is responsible for rapid increase of aspect ratio in P scheme and b) voxel growth. The arrows represent the radical (Re) diffusion directions.[35]

The size and shape of individual voxels were studied in Sun's work[36]. **Figure 1.11** shows the top and side views of the scanning electronic microscope (SEM) images of an isolated voxel. We can see that

with the increase of exposure time, the longitudinal (vertical) size increased while the lateral size reached a plateau very soon.

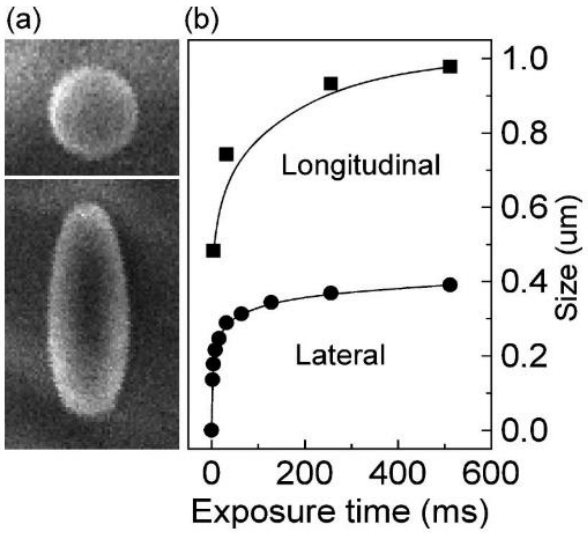

Figure 1.11 (a) SEM images of an isolated complete voxel, top and side views. (b) The voxel size changes with the exposure time.[36]

1.1.3.3 Numeral Aperture (*NA*)

Further research was done about isolated voxels with another important aspect. Sun *et al*.[37] also tried different lenses with varied numeral apertures, 0.88, 1.12, 1.35 and 1.40. The different *NA*s were realized by a variable pinhole. The change in *NA* redistributes the photon energy in the focal volume. It was very clear that, for a fixed laser power, a higher *NA* gave a smaller vertical voxel size but a bigger lateral size (**Figure 1.12**). For example, the lateral size of the voxel is 350 nm with a lens of *NA* 0.88, while with the same focal power a lens of *NA* 1.4 induced a voxel with 460 nm lateral size when exposure time was around 200 ms. But one more thing should be paid attention to, when the laser power is optimized for each *NA*, the smallest visible voxels with a lower *NA* (260 nm at *NA* 0.88) is bigger than that with a higher *NA* (120 nm at *NA* 1.4).

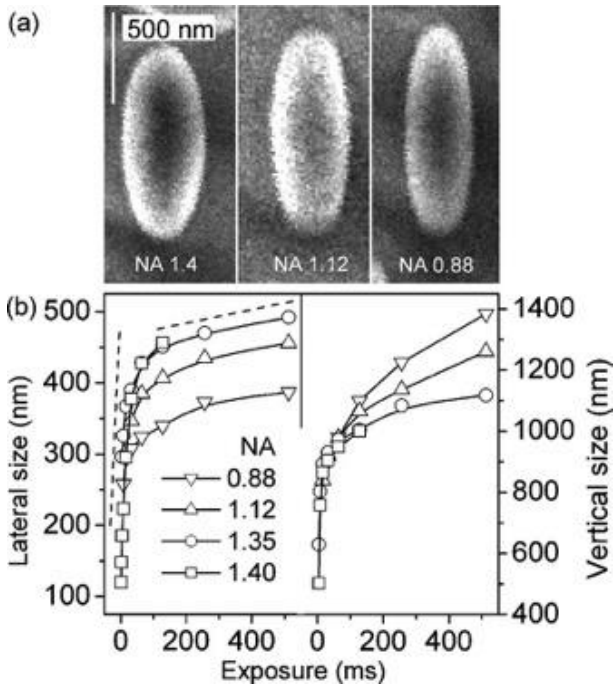

Figure 1.12 *NA*-dependent voxels. a) Side-view SEM images of voxels formed with identical focal spot laser power. b) Exposure time-dependent voxel size in both lateral and longitudinal directions under different *NA*s [37]

Altogether, the size of the voxel can be controlled by changing the repetition rate, the pulse width, the wavelength of the laser, and the numerical aperture, the exposure time and the laser power. Shorter wavelength gives a higher resolution.

According to the results, we can conclude as follows. When the focal spot power is identical, the lateral size of the voxel produced with a lower *NA* is smaller than the one produced with a higher *NA*. For the vertical size of voxel, the result is inversed. Longer exposure times and higher laser powers produce bigger voxels. Those rules are just instructions for TPP fabrication. Every new material needs to be tested to find the exact parameters according to the rules.

1.1.3.4 Overlap and trajectory

Two-photon polymerization is a step-by-step method to fabricate 3D structures. Overlap of single voxel is the basic step. For varied shapes, the trajectory will also differ. The pillars are voxel spiraling stacks. Fibers are made of voxel stacked in parallel. The wall consists of parallel stacks of fiber in longitudinal direction. Step stack distance influence the roughness and stiffness of the final shapes. As the overlap step distance decreases, the surface roughness decreases and becomes constant.

1.1.4 Photoinitiators for TPP

Research by Katawa *et al.*[34] showed that the lower the threshold, the higher the TPP resolution. The use of high-activity initiators can effectively lower the TPP threshold. Laser energy and exposure time are

two key factors that determine LSR. The laser energy determines the initial area of free radicals generated by the initiator, and the exposure time will affect the number of free radicals generated by the initiator. A low threshold can reduce the area where free radicals are generated, and a short exposure time can reduce the number of free radicals and the diffusion of free radicals. Therefore, it is possible to control the TPP area by controlling the above two factors. At the same time, the photoinitiator also plays an important role in the control of the voxel. To obtain a high LSR, highly sensitive and efficient photoinitiators can be used and also, contribute to low threshold and short exposure time, which reduces the size of the region where radicals are initially generated and decrease the number and diffusion of radicals, respectively. Therefore, it can be helpful to develop a more effective photoinitiator.

TPA cross section (δ_{TPA}) is proportional to the amount of intramolecular charge transfer (ITC). In photochemistry, ITC means that charges transfer from a donor (D) to an acceptor (A). Methods such as extending the length of the molecular conjugate chain[38], introducing strong electron-donating or electron-withdrawing groups on the molecule, and increasing the molecular dimension can all increase ITC, thereby increasing the δ_{TPA} of the molecule.

As mentioned in the former part, TPP is realized by TPA of the photoinitiators. The efficiency of TPA and the quantum yield of radicals are two key factors of an efficient photoinitiator. To optimize the choice of photoinitiators for a given application, it is of great significance to grasp the basic principles of how photoinitiators work.

A photoinitiator is a molecule that produces active moieties that induce photopolymerization. According to the photolysis mechanism, photoinitiators are divided into two categories, radical polymerization photoinitiators and cationic polymerization photoinitiators, among which the free radical photoinitiators are the most widely used ones. Furthermore, free radical photoinitiators can be divided into cracking photoinitiators (type I) and hydrogen abstraction photoinitiators (type II) based on the mechanism of free radical generation.[39] For type I photoinitiators, molecules crack into free radicals after absorbing light and initiate polymerization. Most of type I photoinitiators have an aromatic alkyl ketone structure.[40] While for type II, they cannot generate active free radicals through single molecule reaction. Another molecule needs to be combined to form a multicomponent photoinitiator system. Type II photoinitiators are mainly aromatic ketone compounds or dyes together with an electron donor or acceptor, for example tertiary amines.[41] **Figure 1.13** shows the mechanisms of two types of free radical photoinitiators.

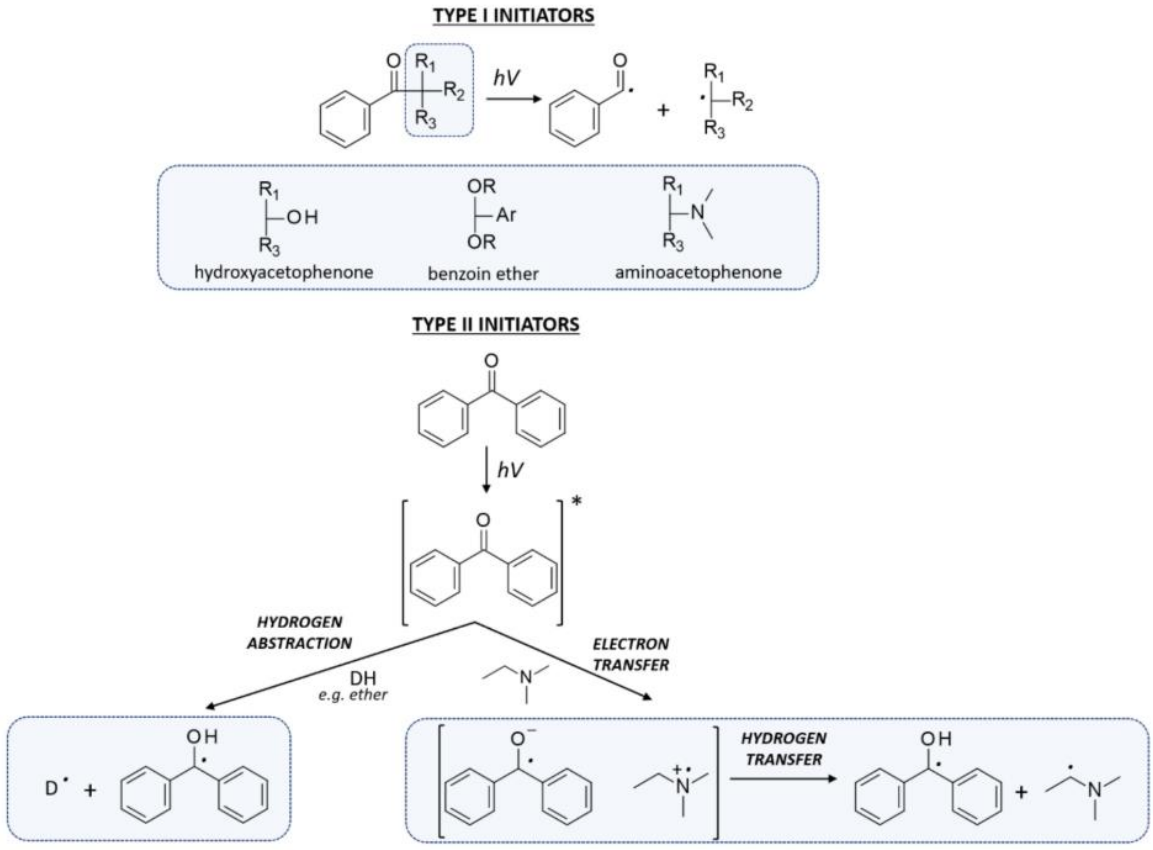

Figure 1.13 Representative examples of the two types of photoinitiators: type I photoinitiator radical form and type II initiator cationic form.[39]

Representative examples of the two types of photoinitiators: type I photoinitiator radical form and type II initiator cationic form.[39]

The classification of photoinitiators depends on how radicals are produced. The process of photon absorption separates OPA from TPA. As formerly described, photoinitiators must absorb two photons in quasi-instantaneous for TPP. But not all the photoinitiators are efficient enough to induce TPP. Choosing highly efficient photoinitiator is very important for TPP.

1.1.4.1 Traditional commercially available photoinitiators for TPP

In the beginning, most commercially available photoinitiators (**Figure 1.14**) were designed for OPA but they always had a relatively lower two-photon cross-section. The most used commercial photoinitiators are the Irgacure series photoinitiators from the famous chemical company BASF. Schafer *et al.*[42] tested the two-photon cross section of the most common photoinitiators by two methods, white-light continuum (WLC) method and Z-scan method. WLC pump-probe method is a technique that uses femtosecond pump-probe spectroscopy with WLC pulse.[43] While Z-scan relies on the transformation of phase distortion into amplitude distortion during beam propagation through a nonlinear medium.[44]

Those two methods are widely used for TPA cross section test. **Table 1.2** shows the TPA cross section of the photoinitiators shown in **Figure 1.14**.

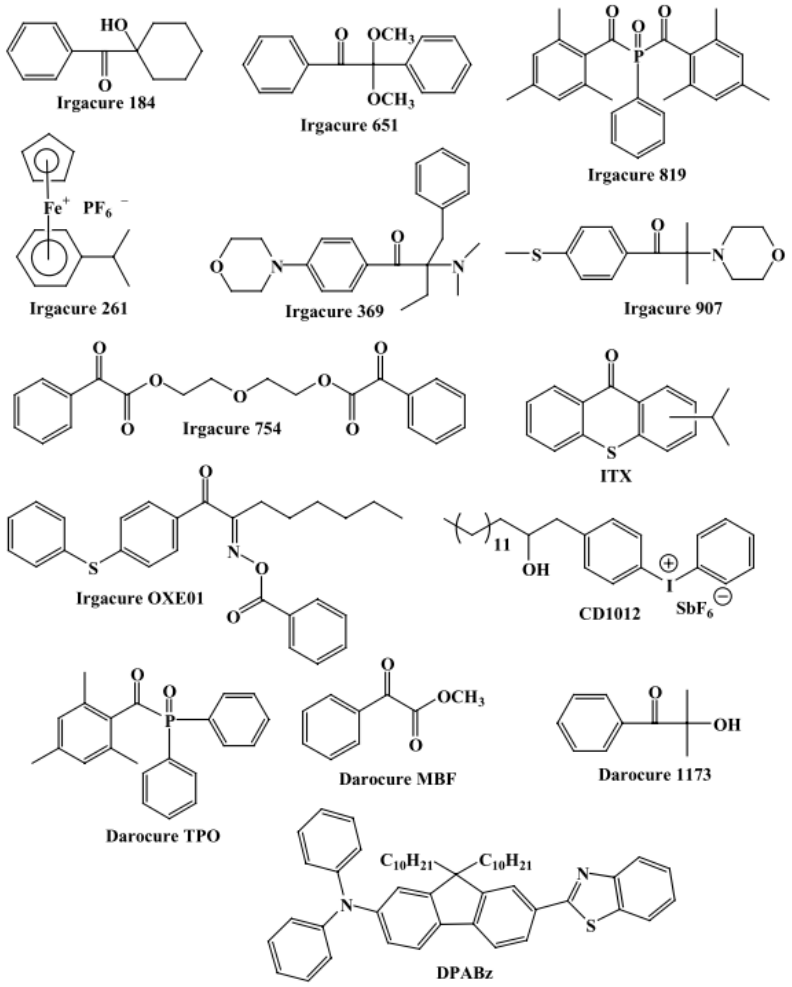

Figure 1.14 Structures of most commercially available photoinitiators [42]

Table 1.2 Peak TPA cross-sections for photoinitiators, determined using Z-scan and WLC methods[42]. λ_{max} means the one-photon absorption peak. $\lambda^{(2)}_{max}$ is the two-photon absorption peak. δ_{meas} represents the two-photon absorption cross section, while GM is the unit.

Compound	λ_{max} (nm)	Z-scan		WLC-2PA	
		$\lambda^{(2)}_{max}$	δ_{meas} (GM)	$\lambda^{(2)}_{max}$	δ_{meas} (GM)
Irgacure 261	242	265	<20	250	<20
Darocure 1173	244	265	<20	250	<20
Irgacure 184	246	265	23	250	<20
CD1012	247	265	16	273	14
Irgacure 754	253	265	21	250	10
Irgacure 651	254	265	28	250	<20

Darocure MBF	255	265	27	250	<20
Irgacure 819	295	300	<4	300	<5
Darocure TPO	299	300	<4	300	<5
Irgacure 907	306	300	4	300	<5
Irgacure 369	324	335	7	318	27
Irgacure OXE01	328	330	31	330	38
ITX	382	380	5	377	4
DPABz	390	390	100 (THF)[q]	388	120 (THF)

Note, (1) All the photoinitiator rank along the $\lambda_{max.}$ (2) DPABz was tested in tetrahydrofuran (THF).

1.1.4.2 Specially designed photoinitiators for TPP

Due to the existence of two-photon absorption threshold, and the fact that traditional commercial photoinitiators have a relatively lower two-photon cross-section, molecules with high two-photon cross-section are needed to be specially designed to improve the efficiency of TPP. The basic rule is that structure determines function.

Design Principles

Torgersen *et al.*[45] pointed out that the ability to separate the charge of molecule is the direction to increase the probability of TPA. A typical molecule structure is described as D–π –A–π–D symmetric molecule where D means π-electron donor and A represents π-electron acceptor Big π conjugation separates the charge homogeneously. Furthermore, Dudek *et al.* [46] summarized the basic combinations between D and A (**Figure 1.15**).

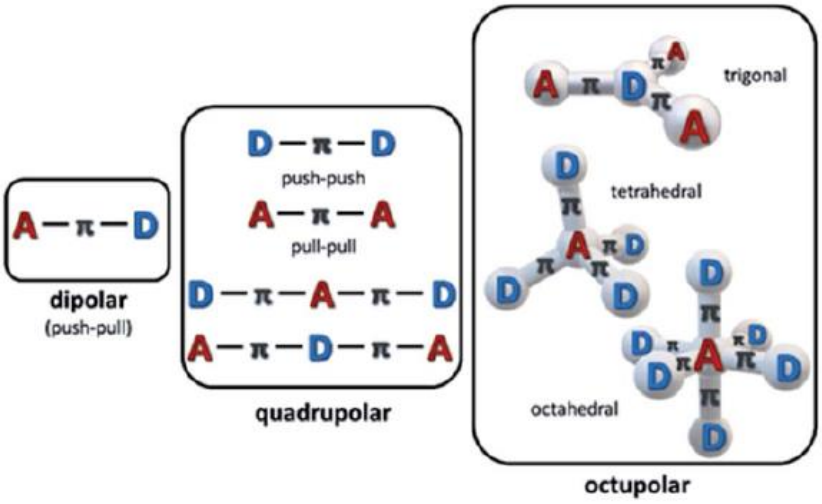

Figure 1.15 Structure designs of different combinations of π-electron donor and acceptor for TPA[46]

Separated charges of molecule bring higher two-photon cross-section. But a high two-photon cross-section is only the first demand for structure design. The total efficiency of a photoinitiator equals the product of efficiencies of photon absorption, radical generation and reactivity of radicals. Electrons in an excited state induced by two-photon absorption can also return to ground state by emitting fluorescence. Albota *et al.*[47] designed a series of chromophores based on *E*-stilbene. By introducing di-*n*-butylamino at both ends and inserting phenylene relatives to elongate the length of conjugation, a D-A-D type molecule was established. A very high two-photon cross-section (> 900 GM) was obtained, moreover also with high fluorescence yield (>0.88). Radicals are only produced from triplet state. Hence how to minimize the fluorescence quantum yield and increase the possibility of intersystem crossing from single state from triplet state is another key point of structure design.[48] At the same time, chromophores with large two-photon cross-section and high fluorescence quantum yield are used for two-photon microscope, tracers and sensors.[49]

Some designed photoinitiators for TPP

Benzophenones are the most widely used initial molecule to design D–π –A–π–D chromophores. Bis(diethylamino)benzophenone (BDAB) meets the demands perfectly. **Figure 1.16** gives some examples of molecules containing the D–π –A–π–D structure. As Li *et al*.[50] pointed out, fluorescence lifetime and quantum yield strongly depend on polarity. Long conjugation length and good coplanarity make a huge contribution to their large two-photon cross-section. Strong fluorescence can be transferred into lower fluorescence by intersystem crossing. Benzophenone provides a longer conjugation than simple ketone. Fluorenone and anthraquinone contribute not only to good coplanarity but also to longer π conjugated system with stronger electron acceptor. As a result, all the newly designed photoinitiators reveal more than 200 GM two-photon cross-section at 800 nm. B3FL series are successfully used to fabricate complex 3D structures.

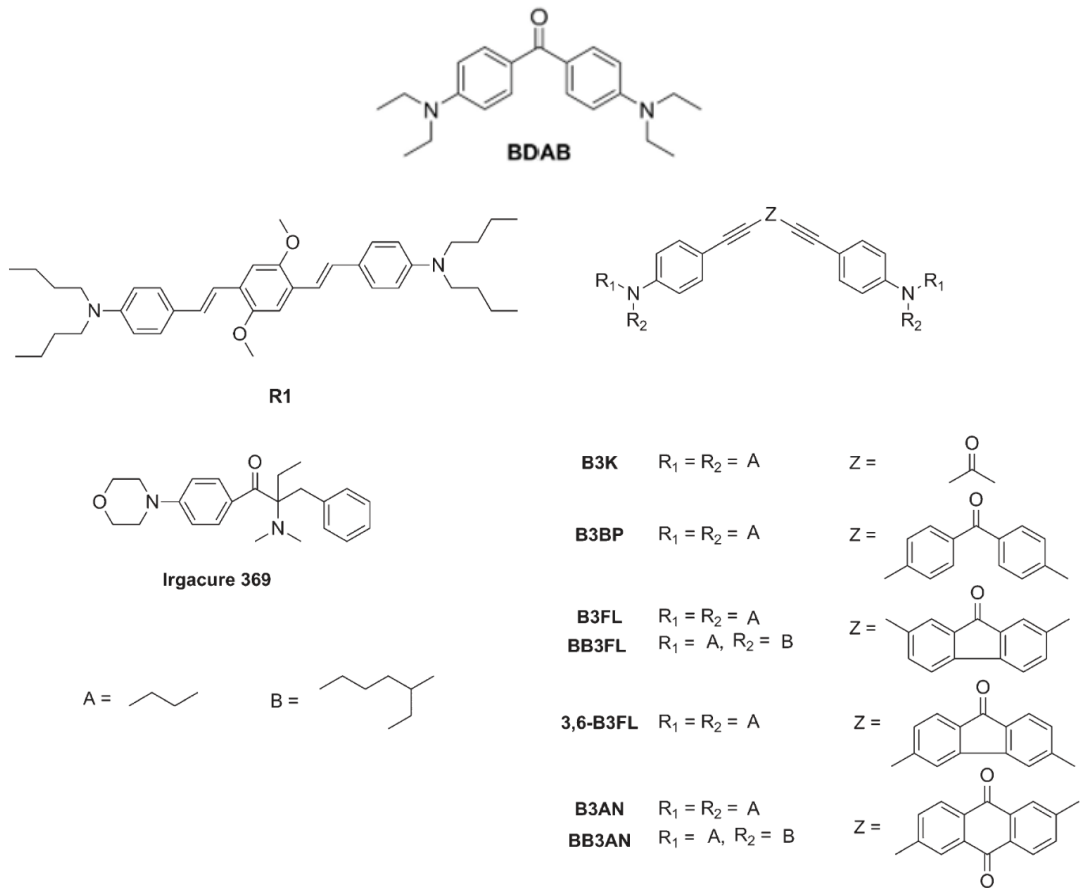

Figure 1.16 Chemical structure of BDAB and of another centrosymmetric designed molecule as photoinitiators for TPP.[50]

Even though specially designed centrosymmetric molecules have very large two-photon cross-sections, their OPA is not large enough to induce polymerization due to the select rules. There are two kinds of states, gerade state (or even state) and degenerate state (odd state). Only when the two states have the same parity, both gerade states (g) or both ungerade states (u), the TPA transition between them is allowed. The transition between g and u states is not allowed. For one-photon absorption, only transition between different parities is allowed. **Figure 1.17** shows the rate equations and the selection rules of OPA and TPA of centrosymmetric molecules. Hence the high TPA cross-section of this kind of molecule is not related to its OPA cross-section to the same extent. The energy level of one photon allowed odd symmetry excited $1B_u$ state is slightly higher than that of the lowest two-photon-allowed even symmetry excited $2A_g$ state in some series linear polyenes. By structure design, Rumi *et al.*[51] showed that the energy level of $1B_u$ state can be also lower than that of $2A_g$ in bis-doner substitute molecules.

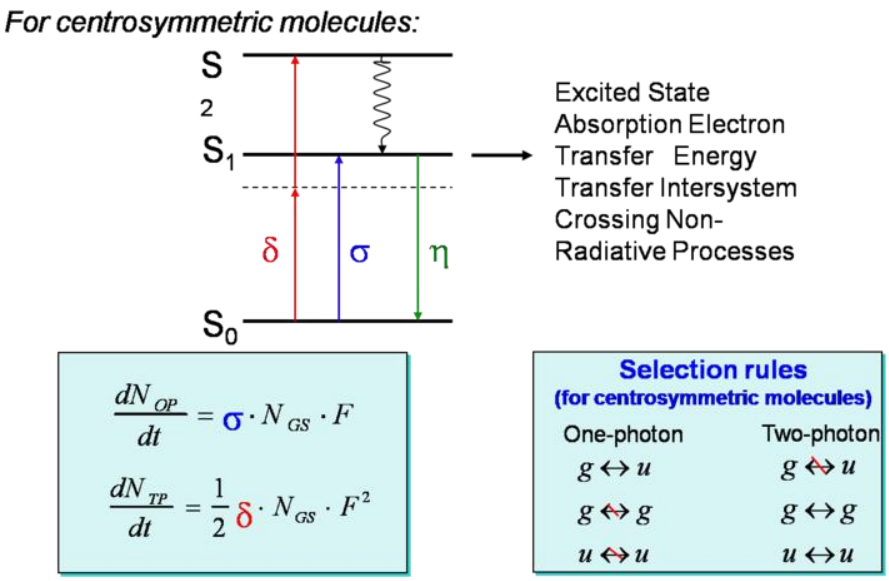

Figure 1.17 Rate equations and selection rules for two-photon and one-photon absorption. N is the number of molecules per unit volume. F is the photon flux (number of photons per unit area and time).[52]

1.1.4.3 Photoinitiators used in TPP for biological applications

Water-insoluble photoinitiators

The most used commercial photoinitiators listed in Table 3.1 are water-insoluble ones. They are used together with organic resins for TPP in the biological field. Ovsianikov *et al.* [14] successfully used Irgacure 369 together with Ormocomp (a commercial resin), poly(ethylene glycol) diacrylate (PEGDA) and ethoxylated trimethylolpropane triacrylate (SR499), to fabricate a wide range of microneedle arrays for drug delivery. Irgacure 369 was also used to fabricate 3D microscaffolds for cell biology studies.[53,54] Irgacure 651 was also tested by Jhaveri *et al.*,[55] together with AF 240 and pluronic F127, to construct 3D hydrogels. An important point that cannot be ignored is the cytotoxicity of water-insoluble photoinitiators. Williams *et al.*[56] tested the cytocompatibility of Irgacure 184, Irgacure 651 and Irgacure 2959 on six cell lines. The results showed that water insoluble Irgacure 184 and Irgacure 651 are more toxic than Irgacure 2959 for cells, which limited their use in biological applications.

Water-soluble photoinitiators

The typical photoinitiators mentioned in Table 3.1 are water-insoluble except Irgacure 2959 (2-hydroxy-1-[4-(2-hydroxyethoxy) phenyl]-2-methyl-1-propanone). But the solubility of Irgacure 2959 in water is relatively limited, about 1 wt%. As type I photoinitiator, Irgacure 2959 is widely used for hydrogel preparation. In order to improve the solubility but keep the good reactivity of Irgacure 2959, Eren *et al.* [57] linked Irgacure 2959 (I2959) with toluenesulfonyl (Ts) forming toluenesulfonate ester (Ts-I2959)[58]

first and then Ts-I2959 was linked with hyperbranched poly(ethylene imine) (PEI) and by electrophiles substitution reaction between secondary amine and toluenesulfonate ester. Two new water-soluble photoinitiators PEI-I2959 (water solubility 35-45 mg/ml) and PEI-I2959-Ts (salt) were designed and prepared. Both were successfully used to induce photopolymerization of (meth)acrylates with very high conversions of 90-100% of carbon-carbon double bond. Concerning cytotoxicity, PEI-I2959-Ts is not toxic while PEI-I2959 is biocompatible at lower dosage (<1 μg/ml).

A similar strategy was also used to modify bisacylphosphine (BAP-H). Wang *et al.*[59] modified BAP-H with poly(ethylene glycol) methyl ether methacrylate (PEGMEM) by phospha-Micheal addition[60] and then oxidates it with H_2O_2, forming PEG-BAPO. PEG-BAPO reveals good water solubility, while BAPO is not water-soluble at all. With water-soluble PEG-BAPO, a gyroid shape hydrogel structure was successfully fabricated by 3D printing.

Besides modifying the aromatic photoinitiators with water-soluble polymer, ionization is also an efficient direction to increase the solubility. **Figure 1.18** shows several typical water-soluble photoinitiators obtained from water-insoluble ones. BAPO-OLi and BAPO-ONa were synthetized to improve the solubility of BAPO, and 2,4,6-trimethylbenzoyl-diphenylphosphine oxide (TPO) was also transferred into TPO-Na and TPO-Li.[61] Le *et al.*[62] also used a similar strategy to improve the water solubility of (2,6-dimethyl- 4-dimethylaminobenzoyl) diphenylphosphine oxide (MAPO-1). Triflate (MAPO-3) was used to prepare polyacrylate hydrogel. With respect to cytotoxicity, MAPO-3 behaves better than the reference phenol in MTT assays. Until 1 mM, MAPO-3 still shows the same level cell viability (around 100%) as the non-treated control, while phenol shows less than 70% cell viability.

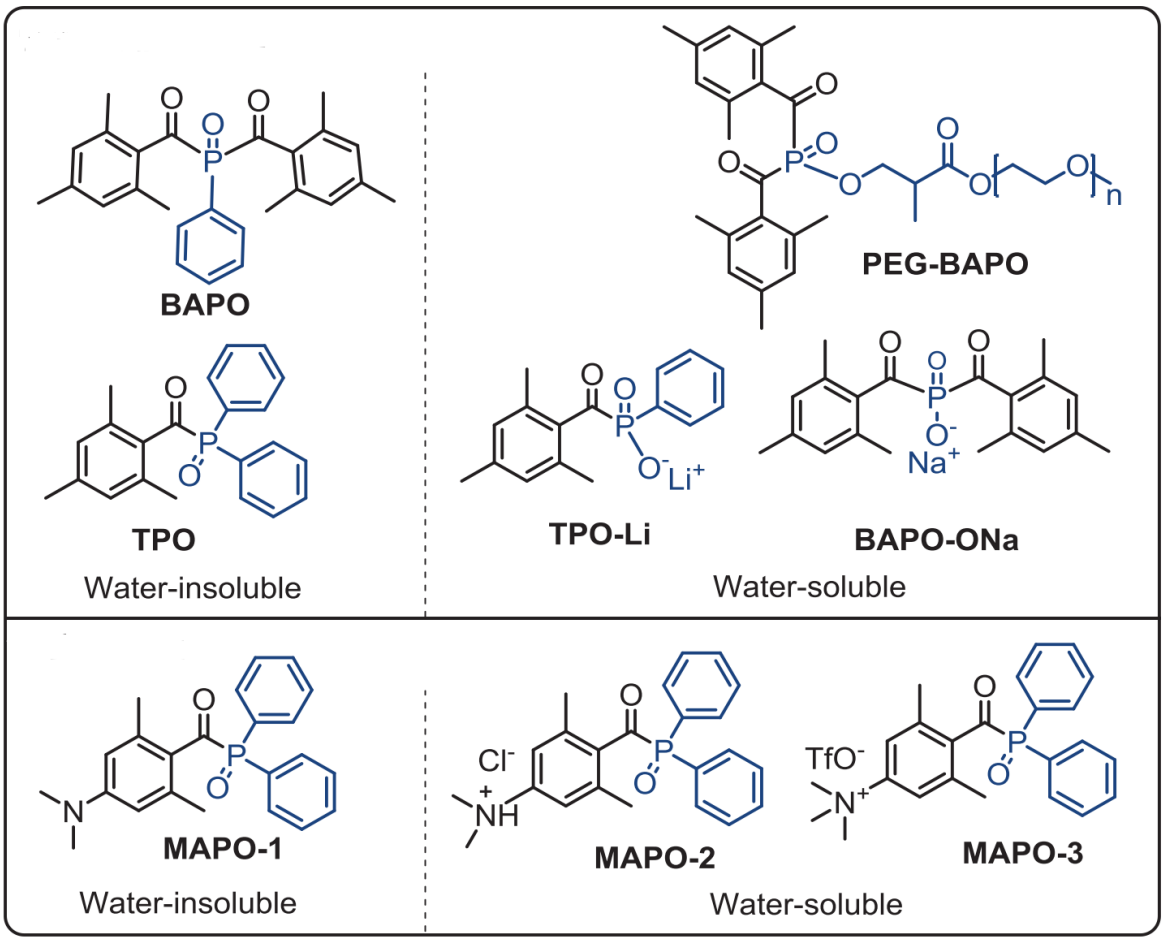

Figure 1.18 Water-soluble photoinitiators obtained by modification[62]

1.1.4 Special photoinitiators for protein polymerization

Besides the modification, there are also many water-soluble photoinitiators, especially dyes.

Figure 1.19 shows the chemicals structures of the flavin series. All the flavin series dyes, riboflavin and its flavin mononucleotide (FMN), flavin adenine dinucleotide (FAD), were both used to fabricate 3D protein structures. According to Kim *et al.*[63] riboflavin is not toxic to cells and was used as a photoinitiator to polymerize dextran-methacrylate hydrogel together with L-arginine as a co-initiator. FMN and FAD have similar chemical structures as riboflavin. FMN was successfully used to polymerize bovine serum albumin (BSA), biotinylated bovine serum albumin (bBSA) and avidin.[64] FAD was also used to polymerize BSA.[65]

Another big group of dyes used for TPP is xanthene dyes, including rose Bengal, eosin Y, erythrosine, rhodamine B and rhodamine 6G, Texas Red (**Figure 1.20**).[66]

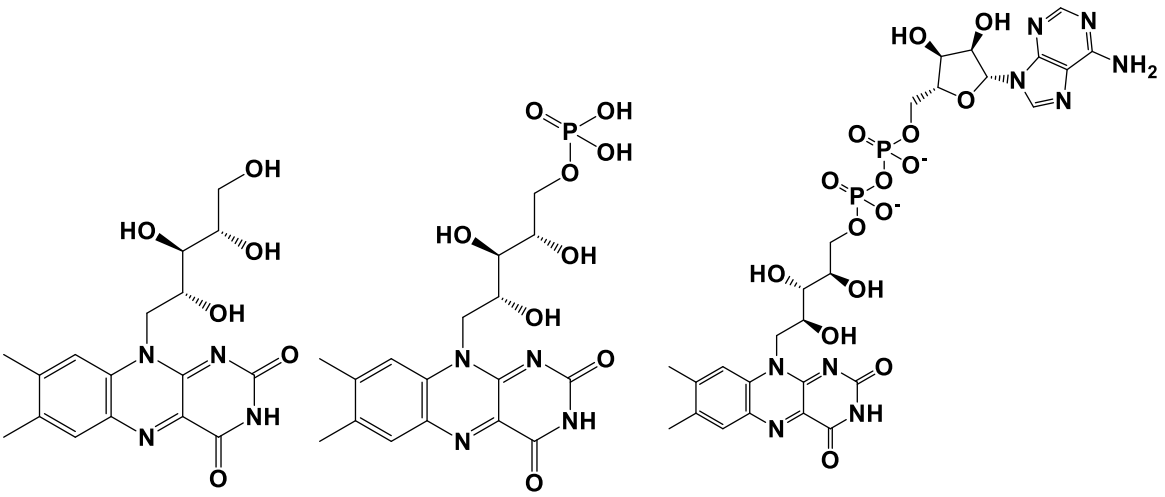

Figure 1.19 Chemical structures of (1) riboflavin (2) flavin mononucleotide (FMN) (3) flavin adenine dinucleotide (FAD).

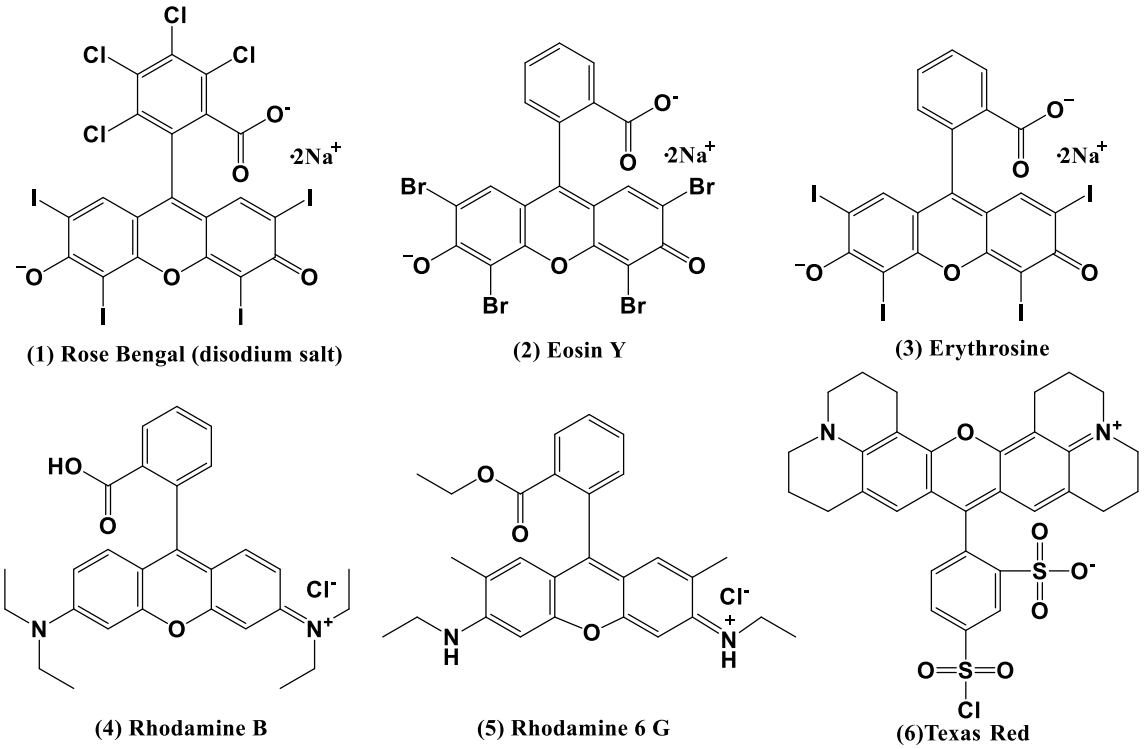

Figure 1.20 Chemical structures of xanthene dyes, (1) rose Bengal. (2) eosin Y, (3) *erythrosine*, (4) rhodamine B, (5) rhodamine 6 G, (6) Texas Red. pH=7

Rose Bengal, eosin Y and erythrosine are both type II photoinitiators, which work together with amines, usually amine residues in proteins as co-initiator.[39] Rose Bengal is widely used to polymerize many proteins, like BSA, avidin, collagen or fibronectin.[67] But rose Bengal does not work very well in acid solution conducting in a change of its photophysical properties, which is a common shortage of xanthene photochemistries (**Figure 1.20**). For example, collagen I is dissolved in acidic solution. Rose Bengal

cannot induce polymerization in acidic solution. Besides, rose Bengal was also tried to polymerize cytoplasmic proteins in living cells.[68] Another interesting trial to be mentioned here, Irgacure 2959 is also used to induce radical polymerization inside living cells for its good biocompatibility[69].

In addition to riboflavin series and xanthene series, there are also some other photoinitiators for protein photopolymerization, like methylene blue (MB)[70], benzophenone dimer (BPD)[71] and sodium 4-[2-(4-morpholino)benzoyl-2-dimethylamino]butylbenzenesulfonate (MBS)[65]. More details will be revealed in the protein parts 1.3.3.

1.1.4.4 Radical quencher

In addition to high effective photoinitiators, radical quenchers (Q) could also decrease the density of radicals (R•) around the focus point, thus getting a smaller size of voxel. Radicals produced by photoinitiators here partly reacted with quenchers, equation (9), forming quenched radicals (RQ•). Quenched radicals will inactivate by release of heat or irradiation, equation (10). Only the rest of radicals can induce polymerization in the process.

$$R\bullet + Q \rightarrow RQ\bullet \quad (9)$$

$$RQ\bullet \rightarrow RQ + \text{heat or } h\nu \quad (10)$$

Park *et al.*[72] tested the quenching effect of 2,6-di-tert-butyl-4-methylphenol (DBMP) as the radical quencher. Three different concentrations of DBMP were tested to improve the lateral resolution of the line patterns. **Figure 1.21** shows the mechanism of the photoreaction with and without radical quencher. With radical quencher, radicals were firstly captured by the radical quencher on the edge of radical existing area, thus reducing the size of voxel. **Figure 1.22** shows the quenching effect is different with varied concentrations of radical quencher, which also is related to the laser power. For 40 mW lower power, the line width was reduced by a very small amount with both 2 wt% and 5 wt% DBMP. For 80 mW lower power, the line width was reduced by about 40 nm with 2 wt% DBMP but about 60 nm with 5 wt% DBMP. For 120 mW lower power, 2 wt% DBMP brought a sharp decrease around 90 nm while 5 wt% DBMP decreased the line width about 110 nm. We can conclude that radical quenchers surely can improve the later resolution, especially with higher laser power.

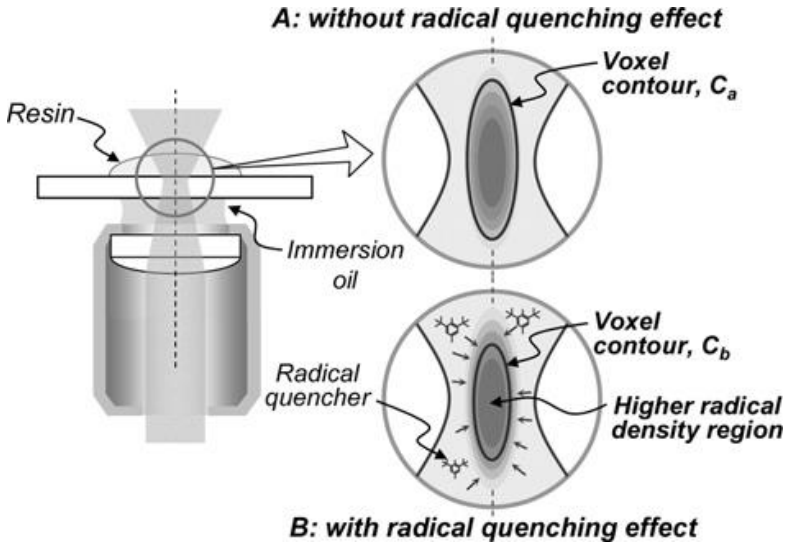

Figure 1.21 Schematic illustration of radical quenching mechanism. In case the radical quencher is mixed into the original resin, the voxel size *Cb* at the bottom right is smaller than the voxel size *Ca*. [72]

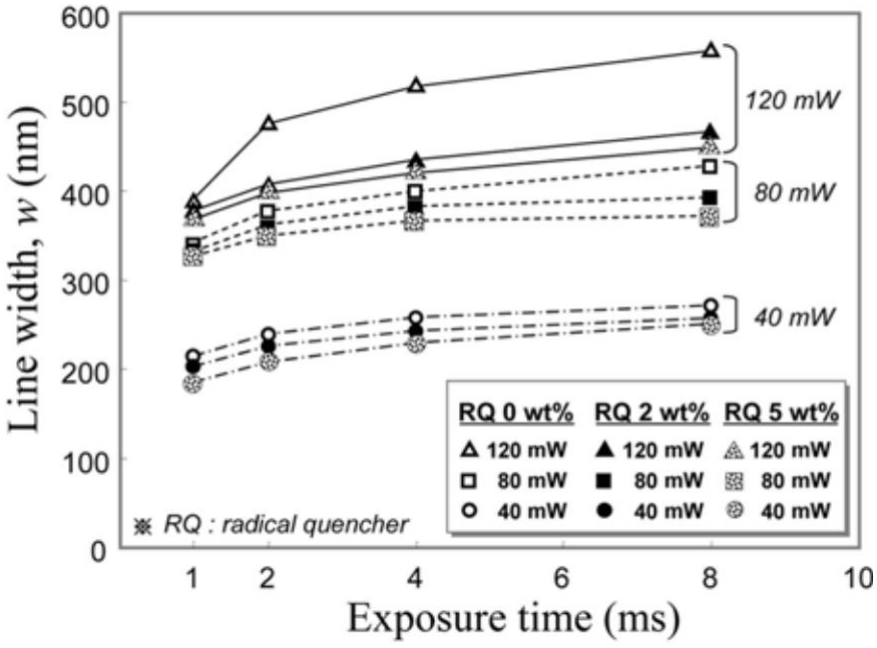

Figure 1.22 The change of line width to three laser gain, 40 mW. 80 mW and 120 mW. The radical quencher concentration varied from 0 wt%, 2 wt% and 5 wt%

The material tested here was SCR500, an urethane acrylate resin from Japan Synthetic Rubber Company. At the same time, they pointed out that the quenching effect would reduce the mechanical strength of polymerized structures due to their short chain lengths. With increased mixing amount of quencher in the resin, the elastic modulus and hardness of the polymerized structure decrease. Specifically, the elastic modulus of the SCR 500 line with radical quenchers of 5 wt% is 2.078 GPa, which constitutes a reduction of roughly 31% relative to that of the original resin line.

1.1.5 Post-process after fabrication by TPP

Polymer structures fabricated by TPP often tend to shrink and to collapse during the fabrication process if it is not stable enough. Sometimes the structures can stay in solution, but they are not able to maintain the shape during drying process. Because delicate structures suffer from their insufficient mechanical stability against capillary forces which mainly arise in the fabrication process during the evaporation of the developer and rinsing liquids.

Purtov *et al.*[73] developed a modified development approach, which enables an additional UV-treatment to post-cross-link created structures before they are dried (**Figure 1.23**). The traditional method to deal with structures like pillars is to wash them with isopropanol (3 times) after 20 minutes of development in propylene glycol monomethyl ether acetate (PGMEA) at room temperature to remove unbound monomeric material, followed by an additional curing step with UV light. They tested their new approach on nanopillar arrays and microscopic pillar structures mimicking the moth-eye and the gecko adhesives, respectively. The results indicated a significant improvement of the mechanical stability of the polymer structures, resulting in fewer defects and reduced shrinkage of the structures.

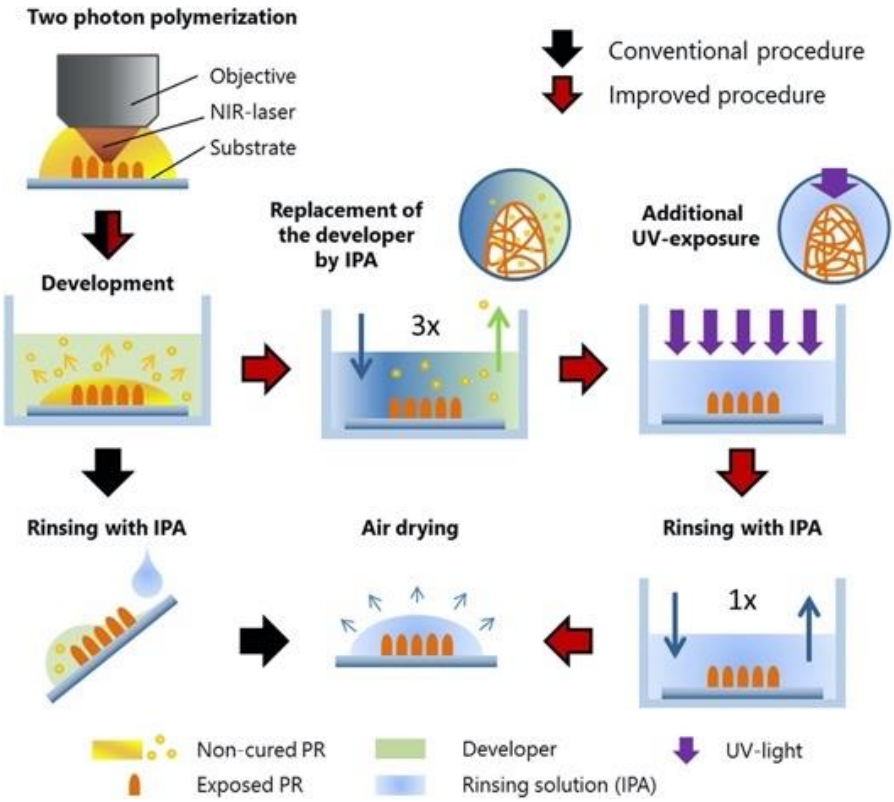

Figure 1.23 Schematic illustration of the conventional and the improved wet development approach.[73]

1.1.6 Conclusion

In this part, we first introduced the mechanism and the equipment set-up of TPP. Secondly, details are put into how to choose the appropriate laser source and adjust the best optical parameters from both theoretical and experimental aspects to improve fabrication accuracy and resolution. For a given system, the main instrument parameters that affect manufacturing resolution are exposure time and laser power. For a given laser power, longer exposure time gives bigger voxel. For a given exposure time, bigger laser power gives bigger voxel. In the actual manufacturing operation, we need to combine the two parameters for debugging. Under the premise of ensuring the stability of the manufacturing structure, the parameter orthogonal test has been carried out to obtain the optimal experimental parameters. What is more, the choice of photoinitiators and the use of radical quenchers can help to get an optimal resolution. After laser fabrication, post-processing helps to enhance the stabilities of 3D microstructures for the next application.

1.2 Materials for TPP

1.2.1 General materials for TPP

Materials for TPP have drawn lots of attention due to its wide applications in the past decades. Many labs and companies have produced commercialized materials in the market and also polymers. There are several kinds, including synthetic polymers like epoxy-based photoresist, (meth)acrylate-based resin, hybrid material, thiol-ene based resin and natural polymers proteins.

For synthetic polymers, some of them have been commercialized and widely used, like SU-8, Ormocil, SZ2080, Ormocer, OrmoComp, NOA 61, IP-resist series, acrylate-based material.

SU-8 is a negative epoxy-based material from Kayaku Advanced materials (https://kayakuam.com/) . The main components are epoxy. **Figure 1.24** shows the chemical structure of SU-8 monomer. SU-8 is very sensitive to ultraviolet, X-ray and high-energy electron beam. Typically, SU-8 is transparent and the Young's modulus is around 3-4 GPa. It has been widely used for microfluidics, optoelectronic, lab-on-chip applications, and to fabricate 3D structures by TPP.[74]

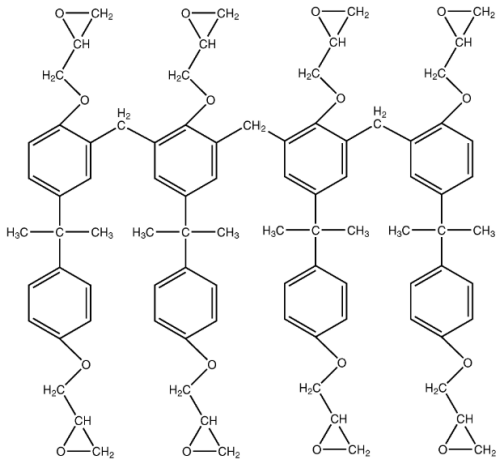

Figure 1.24 Chemical structure of monomer SU-8.[75]

Hybrid Organic-Inorganic Photopolymers (HOIP) is another big group materials in TPP. Commercial Ormocil, SZ2080, Ormocer and OrmoComp all belong to HOIP. All those HOIP were synthesized by sol-gel process. Ormocer is a short form of organically modified ceramic and is developed by Fraunhofer-Institut für Silicatforschung ISC (https://www.ormocere.de/). **Figure 1.25** shows the basic structure of Ormocer.[76] There are four types of parts in the structure. Type I part is the inorganic silica, $Si(OMe)_4$ or $Si(OEt)_4$. Type II is the heteroatoms in inorganic structures containing metal alkoxides like aluminum (Al), Titanium (Ti) and Zirconium (Zr), *etc*. Type III part is organic crosslinking usually consisting of epoxy, alkyl or (meta)arylate. Type IV is the organically functionalized siloxane. The first step of reaction is the formation of inorganic network. Silicon alkoxides, organically modified silicon alkoxides and metal alkoxides could form hyperbranched network by hydrolysis and condensation. In the second step, TPP will be performed. Organic crosslinkers will react with the free (meta)acrylate groups in hydrolyzed silane, forming a solid network.

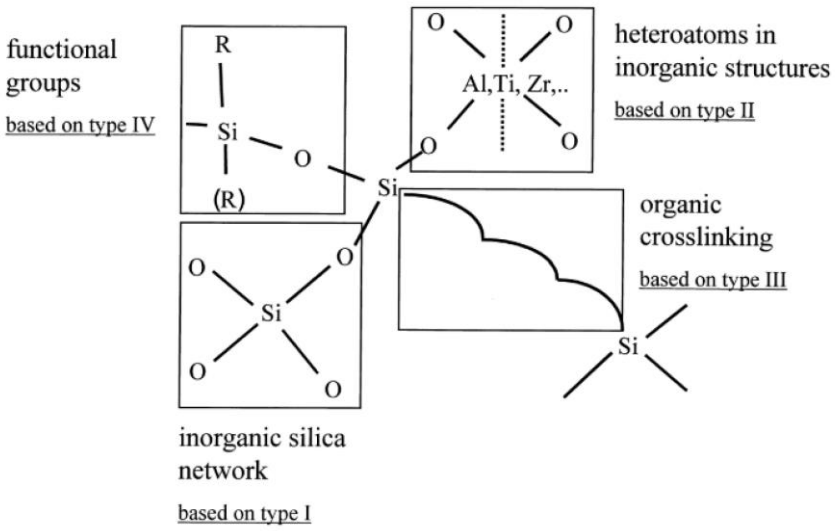

Figure 1.25 Basic structure of Ormocer.[76]

OrmoComp is one kind of Ormocer from Microresist Technology GmbH. The same as Ormocer,

Ormocil is a short form of organically modified silica. SZ2080 is one kind of Ormocil from IESL-FORTH, Greece. SZ2080 holds a similar hybrid organic-in organic network. But the Type II components contain only Zirconium (Zr). The components are shown in **Figure 1.26**.[77] SZ2080 has been widely used in 3D microstructure scaffolds for tissue engineering[77,78] for its excellent mechanical properties and biocompatibility. It has been proved that pyrolysis process after microfabrication could decrease the size of structures fabricated with SZ2080 (Zr-based Ormocil)[79] or similar Ti-based Ormocil[80] by TPP, with a possible resolution beyond 100 nm.

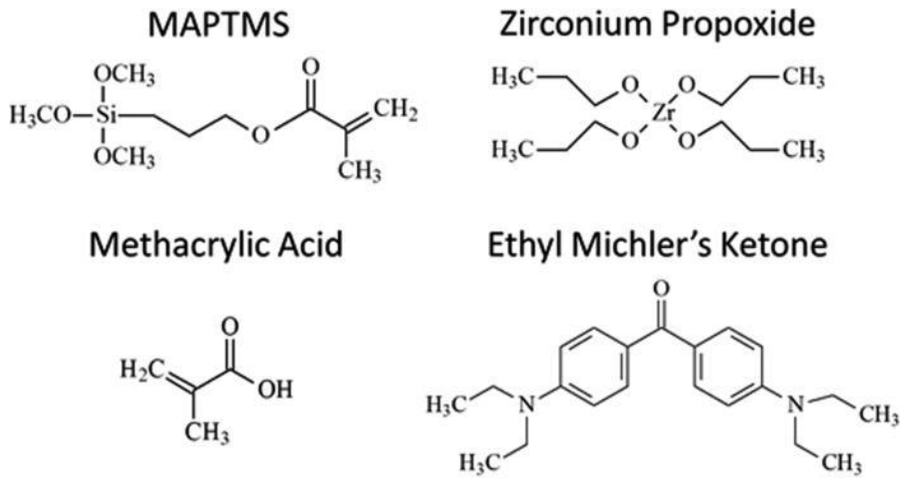

Figure 1.26 Chemical components of SZ2080 (MAPTEMS, zirconium propoxide and methacrylic acid) and photoinitiator.[77]

Norland Optical Adhesive 61 (NOA 61) is a product developed by Norland Products Incorporated (https://www.norlandprod.com/). NOA 61 is a thiol-ene based material and the main components are 30-55% triallyl asocyanuarte and 50-65% mercapto ester (trade secret).[81] In addition to its good clarity, NOA 61 is also low shrinkage and offers a high degree of light flexibility, making it a superior material for optical bonding. It has been used in many fields like optical lens, waveguide, liquid crystal and TPP.

(Meth)Acrylate-based materials attract lots of attention for their excellent fabrication ability. IP-resist series is from Nanoscribe GmbH. One of the representative products is IP-Dip, which consists of 60-80% pentaerythritol triacrylate (PETA). IP-Dip has been used to fabricate complex 3-dimensional (3D) materials. Polyethylene glycol diacrylate (PEGDA), as a representative of arylated-based material, has also been used to fabricate 3D scaffold for cells by TPP.

One of our aims is to fabricate 3D structures by TPP and control the adhesive properties. Klein *et al.*[82] used Ormocomp and then coated it with poly-L-lysine and fibronectin, forming a cell adhesive 3D structure. Later Klein *et al.*[83] fabricated the cell-repellent scaffold with PEGDA 575 and 4.8% pentaerythirol tetraacryalte (PETTA) first, and then a small cube was fabricated with Ormocomp on a

PEGDA scaffold. Thus, special cell adhesive and anti-adhesive surfaces were realized by step-fabrication by TPP with two-component polymer. Later, Richter *et al.*[53] obtained adhesion-controllable 2D and 3D surfaces with different materials. Pure trimethylolpropane ethoxylate triacrylate (TPETA) is a protein-repellent component. TPETA was mixed with 10% phenacyl sulfide and 10% o-methylbenzaldehyde, respectively, forming two different parts of the 3D scaffold by TPP. In this method, spatial material control and selective adsorption of protein were realized, further enabling selective adsorption of different cells.

The spatial control of material realized a spatial control of adhesion and anti-adhesion. But this kind of combination of different materials in 3D is complex, and the mechanical properties at different places are different. Spatial control of adhesion and anti-adhesion with one material substrate will be more useful. This goal can be realized by 3D surface modification. Thiol-ene based material could be an excellent candidate for our need for TPP and surface modification.

1.2.2 Off-stoichiometry thiol-ene (OSTE) resins

1.2.2.1 Click chemistry and thiol-ene (TE) resins

Click chemistry was first developed by Sharpless in 2001 for performing organic reactions.[84] The main purpose was to complete the chemical synthesis of various molecules quickly and reliably through the splicing of small units by inducing carbon-heteroatom bonds (C-X-C) as a new method. With its high efficiency and selectivity, click chemistry has been used in many fields, like molecule design, surface modification, bioconjugation, microchips etc. The most identified types of click chemistry are azide-alkyne cycloaddition, thiol-ene click reactions, Diels-Alder cycloaddition, tereazole cycloaddition, nitrile oxide cycloaddition, oxime/hydrazone formation, etc.[85]

Among the big family of click reactions, thiol-ene click reaction has been a very popular tool of synthesis and modification for its high efficiency and selectivity. Thiol-ene click reaction mainly consists of thiol-ene, as well as thiol-yne click reaction. Depending on how the reaction is initiated, the reaction can be induced by radicals or catalysis. **Figure 1.27** shows the mechanism of thiol-ene click reaction. The thiol-ene click reaction can be thiol addition with pure vinyl or acrylate. Acrylate is a poor electron donor. Upon the introduction of radicals formed either by light or heat, this reaction proceeds *via* the addition of a thiol radical to a vinyl, forming a carbon-centered radical which subsequently abstracts a hydrogen from a thiol, thereby generating the thiolether product and regenerating a thiol radical. The ideal reaction mechanism, consisting of alternating addition and hydrogen abstraction reactions, is achieved by employing electron-rich vinyl functionalities (such as vinyl- and allyl-ethers) which do not undergo homopolymerization.

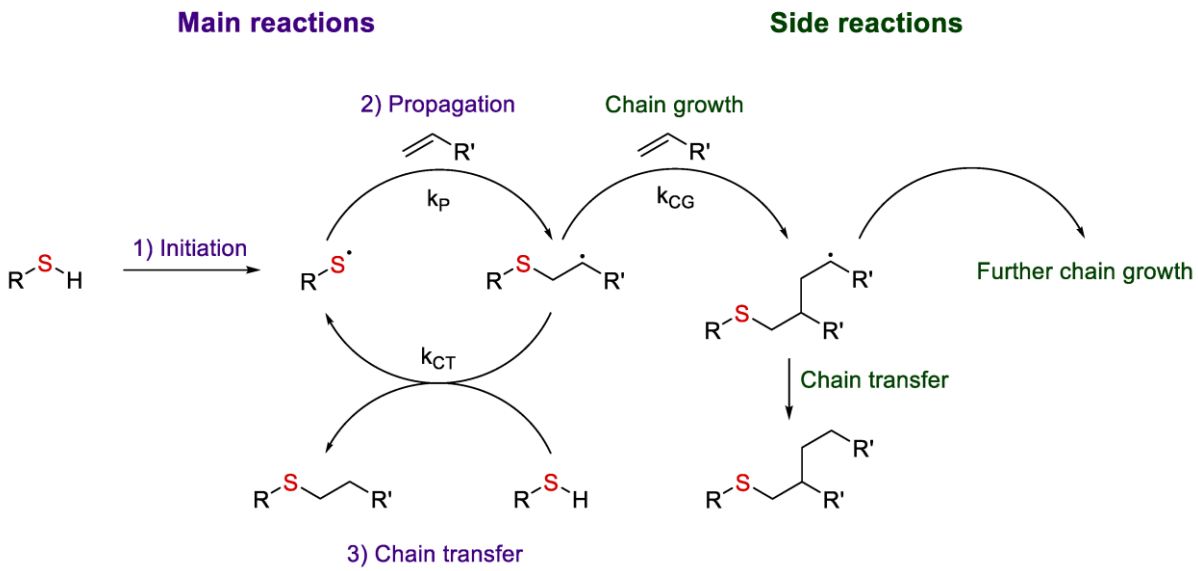

Figure 1.27 Mechanism of thiol-ene click chemistry.[86] During the curing process of OSTE resin, the reaction is mostly the main reaction.

Thiol-ene click addition can be used to build the main frame of materials and also for the surface modification. In the first case, the multi-thiols ended molecules form thiol-carbon ethers with multi-enes, forming the body of the material. When the framework of a material is made by thiol components and alkene components, we define it as thiol-ene (TE) material.

1.2.2.2 Off-stoichiometry thiol-ene (OSTE) resins

According to the ratio of thiol and alkene, the possible thiol-ene reactions were divided into two parts, stoichiometric and off-stoichiometric reactions. When the number of thiols is the same as that of ene, there is no functional groups left if the reaction is homogeneous, or stoichiometric. For the stoichiometric thiol-ene (STE) reaction, all thiols react with alkenes. There is no function group left for further operation. When the ratio of thiol to ene is not 1:1, there will be either thiol group or alkene group left. We define it as off-stoichiometry thiol-ene (OSTE) material. which leaves an opportunity for the subsequent surface modifications. While for the off-stoichiometric reaction, we can control the excess function groups for modification. (**Figure 1.28**). The typical thiols and alkenes are shown in **Figure 1.29** and **Figure 1.30**.

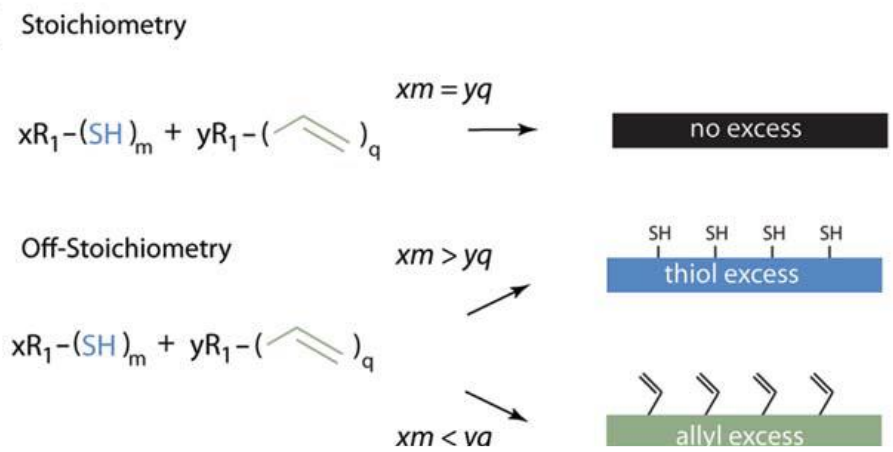

Figure 1.28 Reaction mechanism of UV-initiated radical thiol–ene coupling and (off-)stoichiometry[87]

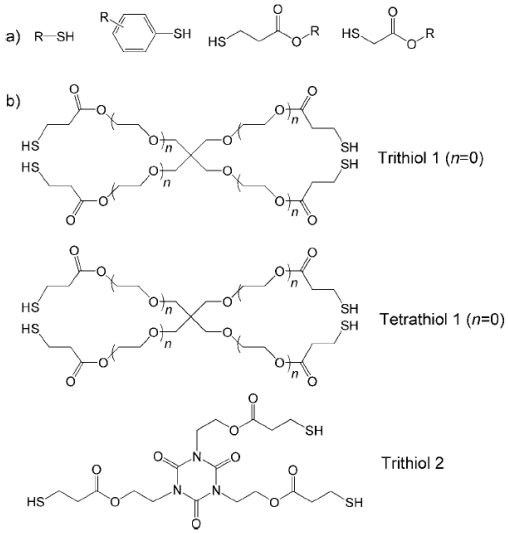

Figure 1.29 a) Common alkyl thiols. (b) Typical multifunctional thiols used in thiol–ene polymerization processes.[88]

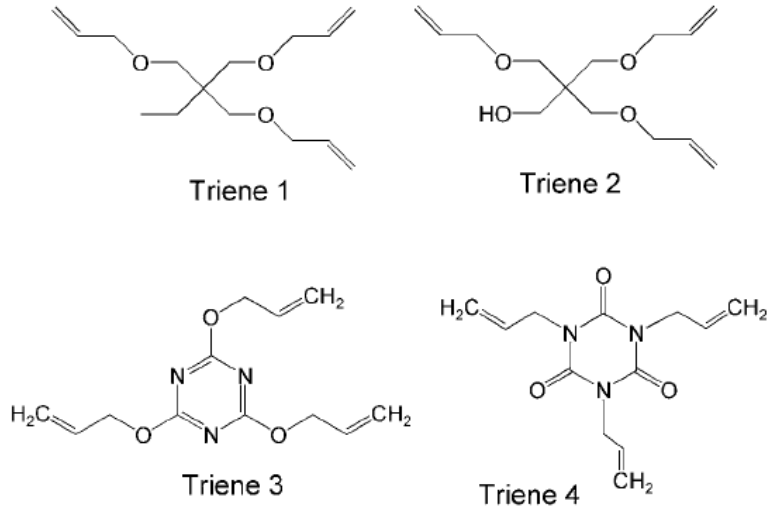

Figure 1.30 Typical multifunctional enes used in thiol–ene polymerization processes.[88]

The off-stoichiometry thiol-ene chemistry was first developed by Carlborg *et al.* at the group of micro- and nanosystems in KTH Royal Institute of Technology, to bridge the gap between research and applications for lab-on-chips[87]. Different from the traditional thiol-ene chemistry, OSTE allowed a powerful control of the excess function group on the surface of cured materials, a precise and permanent surface modification. Besides, more tunable mechanical properties also made it more popular in the lab-on-chip field, including for biofunctionalized sensors[89] and binding to spotted protein and DNA-microarrays[90].

By now the OSTE/STE polymer system has been commercialized and further developed by Mercene Labs. There are four kinds of products now for different uses, Ostemer™ 322 crystal cleaner, Ostemer™ 220 Litho, Ostemer™ 324 Flex and DuoPrime ™ M1814.(https://www.ostemers.com/) Those materials are more specialized for organ-on-chip.

Furthermore, a similar but step-further concept, off-stoichiometry thiol-ene-epoxy (OSTE+), was raised by Saharil *et al.* to broaden the utilization of the OSTE family[91]. This involves a second process of thermo-curing to stiffen and bind to a substrate. The first step is thiol-ene addition. Then the remaining thiol will react with epoxy to produce a chemical stable substrate with high mechanical strength, which is a perfect candidate for microfluidic material. [91]

One of the key points of OSTE resin is the biocompatibility with cells. Errando-Herranz *et al.*[92] tested cell viability of several kinds of components of thiol and alkene (**Figure 1.31**) HEK293A human embryonic kidney cells were seeded on cured OSTE 3T4A, OSTE $4T_1$3A and polystyrene as control for 6 days. Both 50% and 70% thiol excess components were tested for OSTE 3T4A, OSTE $4T_1$3A with 0.1wt% ethyl (2,4,6-trimethylbenzoyl) phenylphosphinate (TPO-L) as photoinitiator. Cell viability on OSTE $4T_1$3A was very low while OSTE 3T4A showed higher cell viability. As a control, HEK293A

cells grew twice faster on polystyrene than on OSTE 3T4A surface. For both OSTE 3T4A and OSTE $4T_1$3A, cell viability was obviously higher on 50% thiol excess surface than that on 70% thiol excess surface. The possible reason was that the unreacted monomer precipitated into the medium. For the third component OSTE $4T_2$3A without photoinitiator, HEP G2 cells were tested on four different thiol excess levels (0, 30, 60 and 90%). After 5 days incubation, cell viabilities on 0%, 30% and 60% thiol excess surface were similar to that on control polystyrene. 90% thiol excess surface showed lower cell viability than the lower thiol excess surface. If uncured monomers, photoinitiator and active thiol on the surface can be possible reasons for the low cell viability.

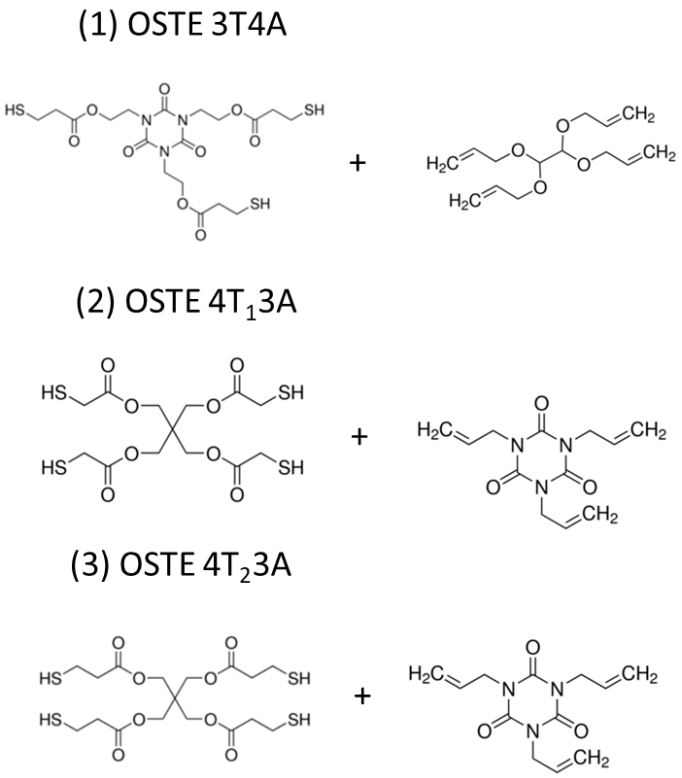

Figure 1.31 Different components found OSTE resin formulations.[92]

For biocompatibility of OSTE resin, Hoffman *et al.*[93] chose poly(ethylene glycol) divinyl ether (Mw = 250 $g.mol^{-1}$) and pentaerythritol tetrakis(3-mercaptopropionate) as alkene and thiol monomers respectively to form 2D surface for cell proliferation assay and cell viability test. Two specimens were prepared. The functional group ratios of thiol to alkene were 1:1 (specimen A) and 2:1(specimen B). XTT (2,3-bis(2-methoxy-4-nitro-5-sulfophenyl)-5-carboxanilide-2H-tetrazolium) is a water-soluble yellow salt which can be transferred into an orange dye by live cells.[94] XTT cell proliferation assay is a widely used cell culture assay to evaluate the proliferation of cells. First, cured specimen A and B were extracted with cell medium to get eluates. XTT cell proliferation assay with human dermal fibroblasts (HDFs) was performed with specimen eluates of specimen A and specimen B. Control was set with polyethylene (PE) tube (negative control) and latex (positive control). For the percentage of cell viability,

specimen A revealed 94.95% coverage whereas the number for specimen B was only 23.92% after 5 days of incubation. Those results showed that monomer or oligomer species extracted from cured high thiol excess specimen (thiol: alkene = 2:1) are cytotoxic.

To further understand the cytotoxicity of OSTE series resin, Ejserholm *et al.*[95] used chemical analysis and cytotoxicity analysis to evaluate the biocompatibility of OSTE+ resin. Tri[2-(3-mercaptopropionyloxy)ethyl] isocyanate was chosen as thiol and trimethylolpropane diallyl ether and 2,4,6-triallyloxy-1,3,5-tria-zine were used as alkenes. D.E.N. 341 Epoxy was component for thiol-epoxy reaction. TOP-L and 1,5-diazabicyclo[4.3.0]non-5-ene (DBN) were used as initiators for the first step thiol-ene reaction and second step thiol-epoxy reaction. Fully cured OSTE+ resin was preincubated in water for seven days as sample one (OSTE+H_2O sample). Both OSTE+H_2O sample and not preincubated OSTE+ sample were extracted in water for 3 days. Extracted eluates were analysis by gas chromatography-mass spectroscopy (GC-MS) and liquid chromatography-mass spectroscopy (LC-MS). For OSTE+H_2O sample, only two initiators were detected by LC-MS. For OSTE+ sample, beside two initiators, two alkenes were also detected by LC-MS, while GC-MS did not reveal any detectable components for all samples. For cytotoxicity, the viability of mouse fibroblast cells was tested with a MTT assy. MTT, 3-(4,5-dimethylthiazol-2-yl)-2,5-diphenyltetrazolium bromide, can be reduced by cells appearing purple. When the eluate was diluted to 50 %, the cell number was reduced by 40% with OSTE+ extract compared to the control. When the eluate was diluted to 25%, the reduction was 15% compared to the control. Whereas OSTE+H_2O sample revealed the same cell viability with the control. These experiments established that with water preincubation, the water-soluble toxic segments could be extracted out.

In summary, there are many reasons that induce cytotoxicity of OSTE or OSTE+ resin. Unreacted monomer or oligomer and remained initiator are all possible toxicity sources to cells. Before being utilized for cells, the resin should be properly preprocessed.

1.2.2.3 Surface modification of thiol or alkene excess surface

The thiol-ene click reaction gives a direction for surface modifications. Special functions can be introduced by grafting the target molecule to/from the original surface. Depending on the functional group excess on the surface, there are two strategies to follow for the surface modification, thiol excess surface and alkene excess surface.

For thiol excess surface, Hoyle *et al.*[96] summarized a multifunctional toolbox of thiol-click reaction that can be used for modification of thiol excess surface. Those reactions can be used to modify all the thiol excess surfaces, not only OSTE resin. Vastesson[97] rearranged the reactions to two types of reactions, catalyzed reactions and radical reactions depending on the mechanisms of the reactions (**Figure 1.32**) Catalyzed reaction can be base-catalyzed and nucleophilic-catalyzed thiol-Michael addition. Radical

reaction can be induced by free radicals to link with alkene or alkyne ended molecules (thiol-ene or thiol-yne addition). Both thiol-Michael addition and thiol-ene/yne addition are thiol-ene click reaction.

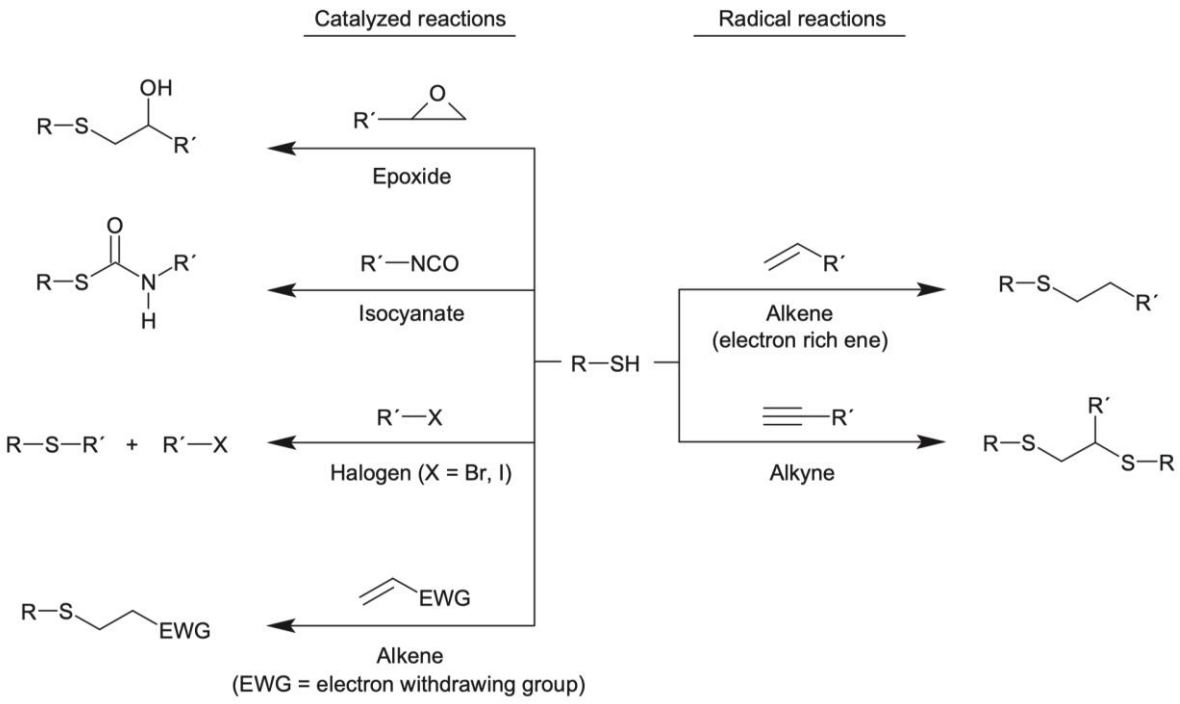

Figure 1.32 Possible thiol-click reactions used for modification of thiol excess surface.[97]

Lafleur *et al.*[98] linked biotin alkyne on a thiol excess surface, which made possible a further link of fluorescently labelled streptavidin. This was a further step to make thiol-ene an ideal candidate in many biochip applications. Similarly, Feidenhans'l *et al.*[99] used the same biotin-streptavidin kit to create microfluidic channels and optical waveguides in one simple step by OSTE. The process is explained in **Figure 1.33**.[100]

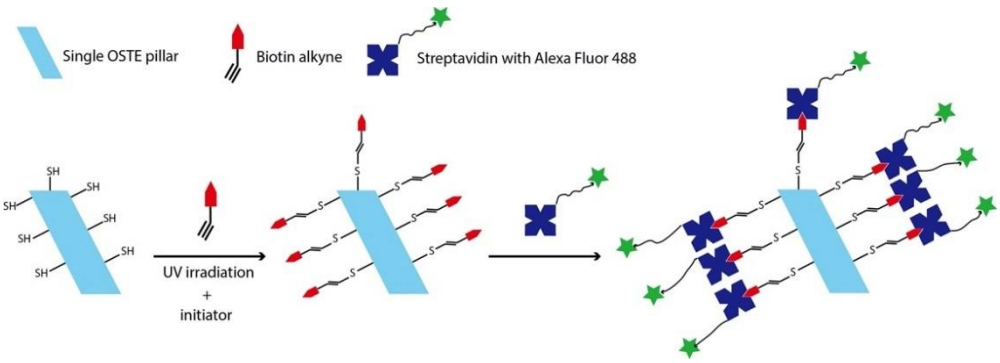

Figure 1.33 Protocol for protein immobilization on OSTE: thiol-yne-biotin.[100]

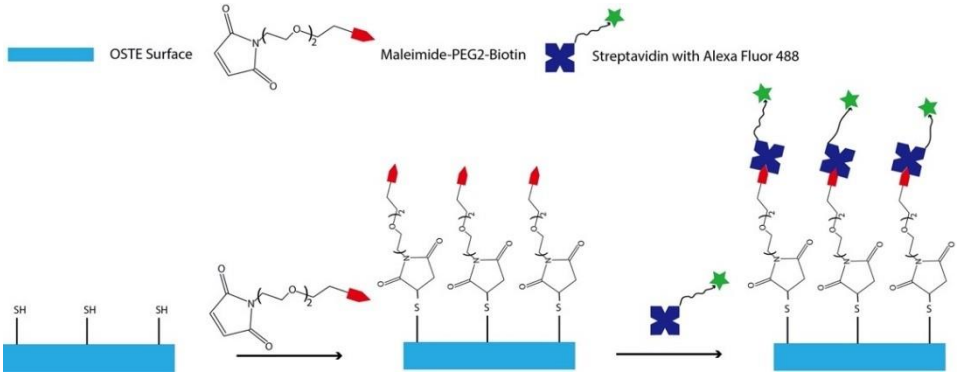

Figure 1.34 Protocol for protein immobilization on OSTE: thiol-maleimide-biotin.[100]

In addition to thiol-yne-biotin strategy, it is also possible to use thiol-maleimide-biotin to link biotin on treated surface. As **Figure 1.34** shows, thiol-maleimide reaction takes place spontaneously after the maleimide component is dropped on the thiol excess surface while thiol-alkyne needs the help of UV process.

By utilizing thiol-ene click strategy, Zhang *et al.*[101] link molecules with different functional groups on thiol-functionalized PDMS surface (**Figure 1.35**): (A) ACR A008-UP (a silicone surfactant with acrylate group), (B) *N*-(5-fluoresceinyl)maleimide, and (C) maleic anhydride, followed in the latter case by ring-opening of the surface anhydride with (D) Me-PEG-OH, (E) chitosan, or (F) rhodamine 123.

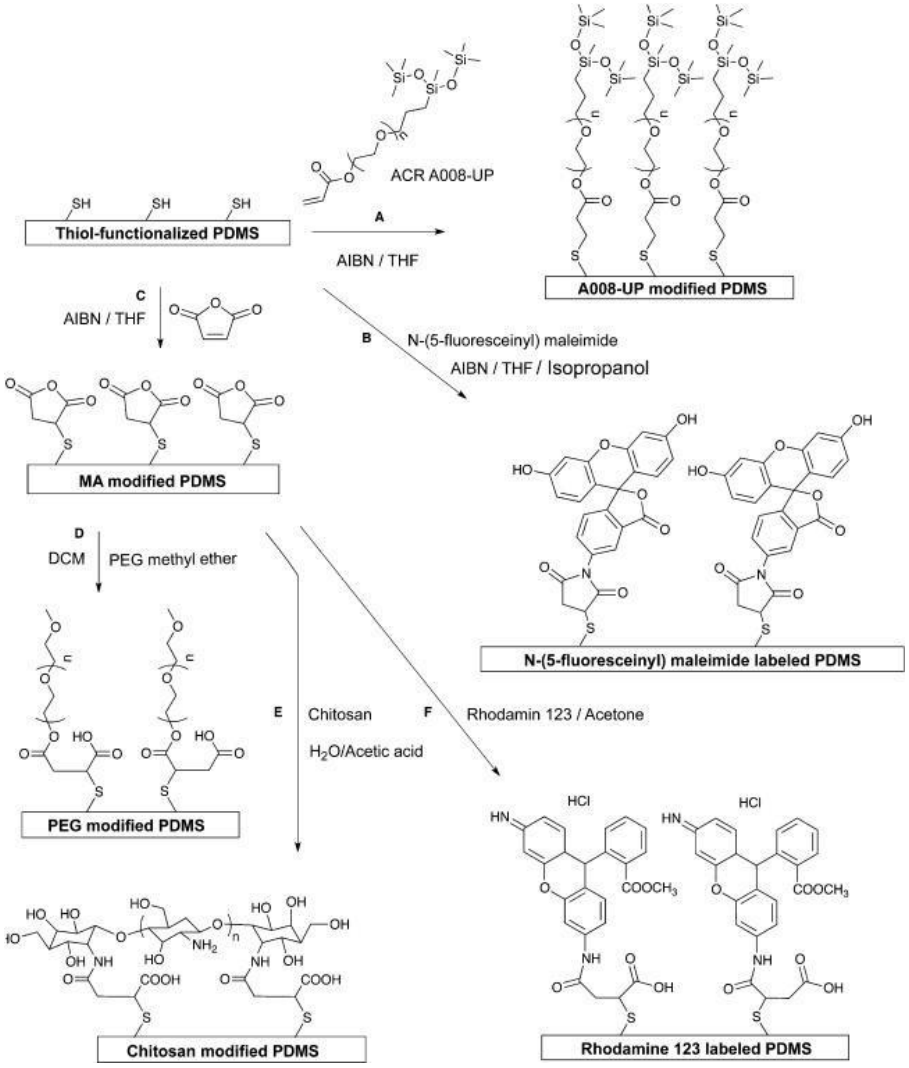

Figure 1.35 Surface modification of thiol-silicones by thiol−ene reactions[101]

For alkene excess surface, thiol-ene click reaction is still an important tool to functionalize the surface. Bourg *et al.*[102] modified alkene excess OSTE surface with aptamer. Pentaerythritol tetrakis(2-mercaptoacetate) and triallyl-1,3,5-triazine-2,4,6(1H,3H,5H) trione were used as thiol and alkene monomer precursors. modified in 3' by C3-SH and in 5' by AlexaFluor®532 immobilization.

In our lab, Oberleitner *et al.*[103] modified the alkene-terminated self-assembled monolayer glass with thiol-ended polyethylene glycol (PEG) to control surface adhesion. Liu *et al.*[104] also reported thiol-ene click reaction can be used as biocompatible method to covalently immobilize thiol-ended PEG, aptamers and Cys-protein on acrylated nanoparticles. By this way, the bio-inactive hydrophobic colloidal nanoparticles were transferred into bioactive hydrophilic ones.

Besides aptamers and Cys-proteins, antibodies are also important biomolecules for bioactive modification. But differently from aptamers and Cys-proteins, there is usually not free thiol in antibodies but disulfide bond. Alonso *et al.*[105] decomposed the immunoglobulin G antibodies (IgG) into half-

antibodies (hIgG). IgG molecules are maintained by disulfide bond. The disulfide bonds can be broken to form hIgGs with free thiols by treatment of tris(2-carboxyethyl)phosphine (TCEP). Then hIgGs were grafted to the vinyl functionalized glass to capture the corresponding proteins. AlexaFluro 647-labelled bovine serum albumin (BSA) was used to check the ability of protein capture of hIgGs modified surface. Similar trail of C-reactive protein (an annular pentameric protein found in blood plasma) demonstrated the potential application of thiol-ene click reaction on clinical analytes.

1.2.2.4 Opportunities in the application of OSTE in TPP

By now, OSTE resins is commonly used in lab-on-chips. But only a small number of studies have used OSTE in the TPP domain. Xiong *et al.*[106] successfully fabricated microstructures with pentaerythritol tetrakis (3-mercaptopropionate) (PETMP), to change their name mentioned in the list di-trimethylolpropane tetraacrylate (Di-TMPTTA) and multiwalled carbon nanotubes.

One of our aims is to develop a material that is suitable for TPP and also can be functionalized by surface modification. As we have discussed above, OSTE resin is a very rich material. A wide variety of thiol and alkene components can be chosen, and varied strategies can be used to functionalize the thiol and alkene excess surface. OSTE is a perfect synthetic polymer system to meet our demand. In this thesis, we will explore the application of OSTE resin in TPP and we will begin to apply it in 3D scaffolds for cell biology together with surface functionalization.

1.2.3 Proteins

Besides synthetic polymers, natural polymers like proteins are also good candidates for materials for 3D scaffolds at the cell scale for their good biocompatibility. Proteins are indispensable to life, and they are abundantly present in extracellular matrix (ECM) and inside cells, bacteria and other living beings. Well-known proteins like fibronectin, elastin, resilin, collagen and keratin come in large quantities from natural sources.[107] Their applications are becoming more and more refined, especially for tissue engineering processes. TPP meets the need in the development of this smaller scale. Proteins from natural sources are one of the obvious choices for TPP.

1.2.3.1 General structure of proteins

To better understand the mechanism of chemical polymerization of proteins, we must firstly Figure out the general structures of proteins. The basic units of proteins are amino acids. There are four parts in an amino acid, the central carbon atom with a hydrogen, the amino group, the carboxyl group and a side chain. The differences between amino acids lie in the side chain. Amino groups and carboxyl groups from different amino acids can react with each other to form peptide bonds. The primary structure of a protein is a sequence of bonded amino acids, named polypeptide or protein.

There are 20 standard canonical amino acids directly coded by the genetic code. **Figure 1.36** shows the chemical structures of the basic 20 amino acids that make up natural proteins in the human body.

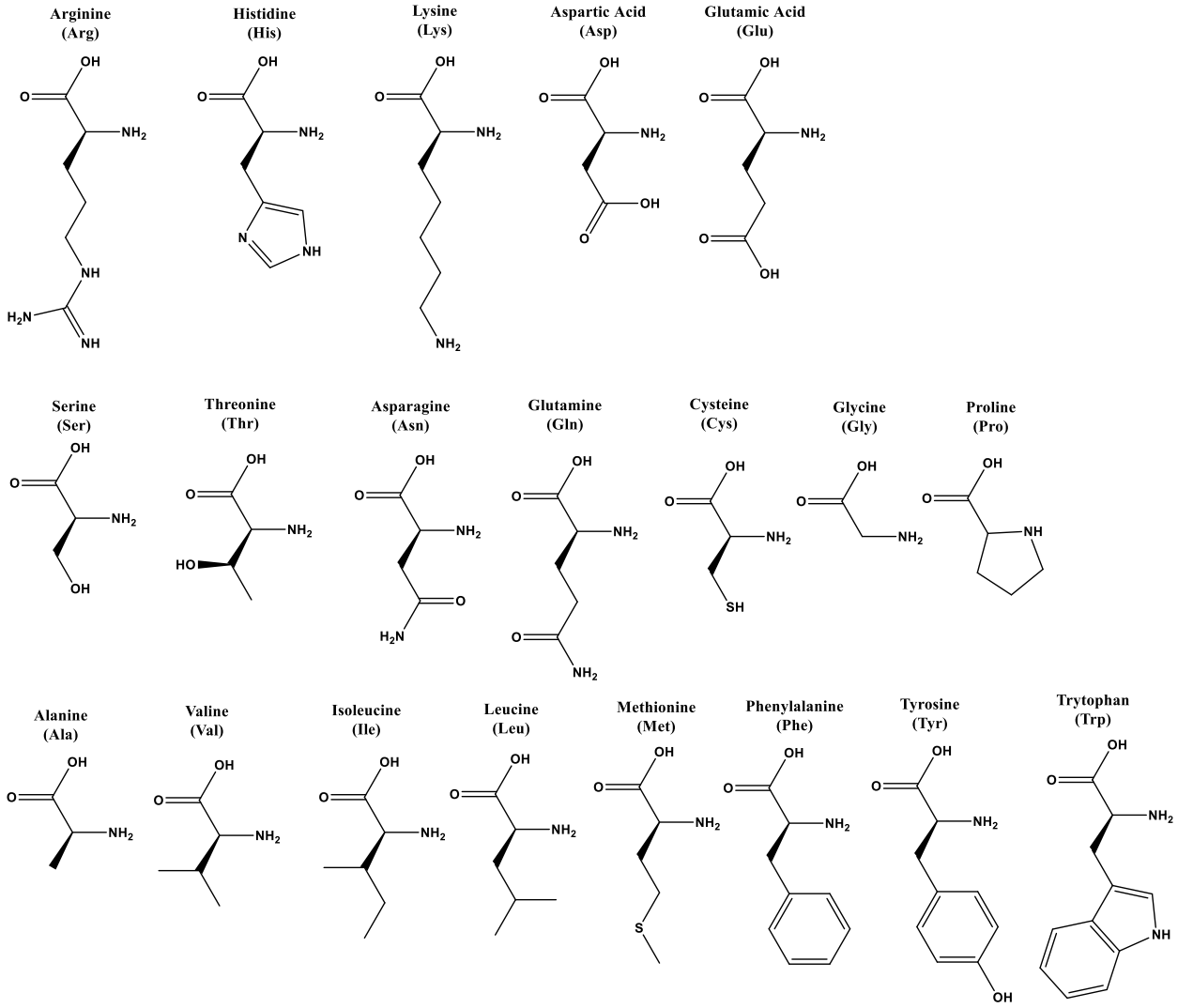

Figure 1.36 Chemical structures of the basic amino acids in proteins.

The secondary structure of proteins is the folding patterns of the polypeptide backbone, with common organizations in alpha helices and beta sheets. Alpha helix is formed by hydrogen bonds between the carbonyl groups (C=O) and the secondary amino groups H(N-H) in one polypeptide chain. The bonded carbonyl and amino groups are separated by three other amino acids. The side chains R of amino acids are outwards of the alpha helix. In beta sheets, a polypeptide chain forms hydrogen bonds with a resulting sheet structure (**Figure 1.36).** The secondary protein structure: alpha helix and beta sheet (**Figure 1.37**). The tertiary structure is the more complex overall 3D conformation of the protein.

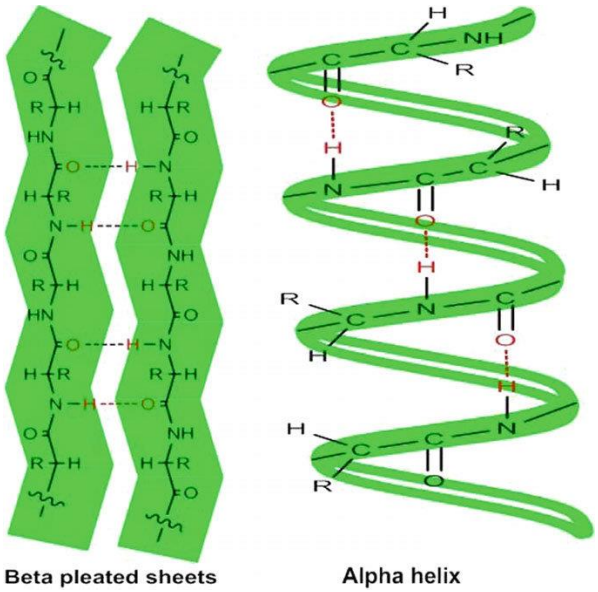

Figure 1.37 The secondary protein structure: alpha helix and beta sheet.[108]

The tertiary structures are maintained by non-covalent bonds like hydrogen bonds, ionic bonds, dipole-dipole interactions, London dispersion and disulfide covalent bonds between sulfur-containing side chains of cysteines. The combination of different multiple polypeptide chains with tertiary structure forms the quaternary structure. The quaternary structure refers to how these protein subunits interact with each other and arrange themselves to form a larger aggregate protein complex. Besides, some other interactions like hydrogen-bonding, disulfide-bridges and salt bridges also helps to form the final shape The final shape of the protein complex is once again stabilized by various interactions, which are essential to maintain their functionality.

Usually, proteins are dissolved in aqueous system due to peptide-water interaction.[109] For chemical applications, pure water is the first choice for the solvent. To better maintain the structure of protein, buffer solutions may mimic the protein environment in cells. During fabrication, other solvents can be chosen to improve the fabrication resolution. Serien *et al.* mixed 50% water and 50% glycerol to meet the refraction index of glass when used in TPP, which would reduce the spherical aberration and light scattering at the surface of glass slide.[110] In addition, some organic solvents like acetone, ethanol and dimethyl sulfoxide (DMSO) are also used together with buffer to improve the fabrication resolution.[110] But it is still not totally understood why DMSO helps improve the resolution, while DMSO can denature the protein. The possible reason is that DMSO retains many chemicals in a solubilized state unlike other organic solvents.[111] DMSO helps rise the homogeneity of the BSA reagent solution.[112]

1.2.3.2 Mechanism of TPP of proteins

The polymerization of proteins can be induced by photo-crosslinking mechanism. Like the general polymerization process, there are chain initiation, chain propagation and chain termination mechanisms.

We have introduced the commonly used photoinitiators for protein polymerization in section 2.4. Proteins can be polymerized with Type I and Type II photoinitiators. But what is the general chemical reaction that happens during polymerization? Serien and Sugioka[67] gave an explanation of the possible mechanisms (**Figure 1.38**).

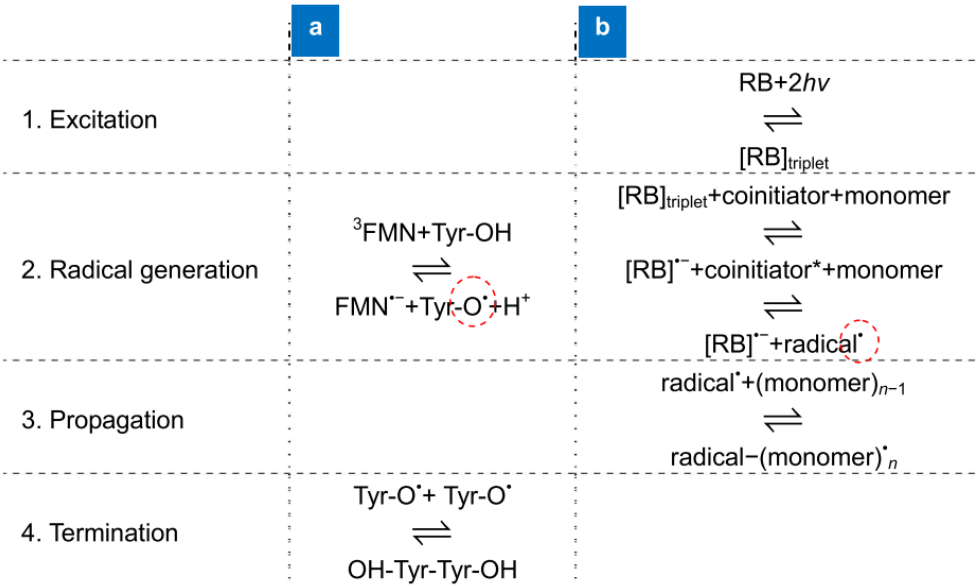

Figure 1.38 Possible mechanisms for protein polymerization[67]

As mentioned in section 2.4, FMN is one of the photoinitiators in riboflavin. FMN could absorb photons and then react with tyrosine, producing Tyr-O· radicals. Two Tyr-O· will combine to form the termination (**Figure 1.38** a). Rose Bengal (RB) can work with triethanolamine undergoing a co-initiation system to induce protein polymerization (**Figure 1.38** b).[113] Sometimes, RB was mixed with proteins directly without additional co-initiator for TPP.

The precise mechanism of polymerization of proteins is not fully understood yet. The principle is that the key determinants for protein polymerization lie on the side chains of amino acids. Aromatic groups, sulfide groups and C-ring with nitrile are all possible polymerization sites. For cysteine and methionine, there are sulfurs in their chemical structures (Figure 5.1). Disulfide bonds in the structure of proteins can be broken and recombined to form new connection between proteins.

1.2.3.3 Proteins for TPP

Serien and Sugioka[67] summarized the commonly used proteins for TPP. Their review included alkaline phosphatase, antibody anti-A (one antibody in blood that can recognize blood type A)[114], avidin, bovine serum albumin (BSA), bBSA, concanavalin A, cytochrome C, enhanced green fluorescent protein, fibrinogen, fibronectin, laminin, lysozyme, regenerated silk fibroin, trypsin or mixtures of several kinds

among them. (**Table 1.3**) Among those proteins, BSA and collagen are the most used. In this part, we will focus on the TPP of BSA and collagen.

Table 1.3 Protein solution conditions. A summary of previous fabrication conditions, focusing on protein and photosensitizer concentrations. Examples of typical solvents and protein databank samples are included. Photoactivator abbreviations: Rose Bengal (RB), methylene blue (MB), flavin mononucleotide (FMN), flavin dinucleotide (FAD), rhodamine B (RhB), rhodamine 6 G (R6G), benzophenone dimer (BPD), sodium 4-[2-(4-morpholino)benzoyl-2-dimethylamino]butylbenzenesulfonate (MBS). Solvent abbreviations are: dimethyl[sulfoxide (DMSO), phosphate-buffered saline (PBS), 4-(2-hydroxyethyl)-1-piperazineethanesulfonic acid (HEPES).

Representative PDB code	Protein (mg/mL)		Photoactivator (mM)		Solvent
1B8J	Alkaline phosphatase (AP)	280–350, 9800, 2100	RB	0.25	Ascorbic acid (1 mM)
	AP-BSA				
1JV5	Antibody anti-A	n.a.	Eosin-Y	0.3	n.a.
1VYO	Avidin	50–400	FMN, FAD, MB, RB	0, 1.2–8.5	Distilled water or buffer (PBS or HEPES), pH ~7.4
			Eosin-Y, MB	14.3, 4.3	DMSO 21% in HEPES buffer
			FAD with RhB	0.250 with 0.407	12.5% HEPES, 19% DMSO, organic solvents
4F5S	Bovine serum albumin (BSA)	50–600, 800–1000[53]	Eosin-Y, Texas-Red, RhB, MBS, R6G, BPD, RB, FMN, FAD, MB	0–100	Distilled water or buffer (PBS or HEPES), pH ~7.3–4
		210–460	Eosin-Y, MB, RB, RhB with FAD	4–14.3, 0.3–0.6 with 0.25	18%–23% DMSO in HEPES buffer (organic solvent)
		0–200	FAD, Benzophenone-biotin	0–2, 3–22	50% DMSO in buffer
		100, 200	MBS	67–100	50%wt glycerol-water
	Biotinylated BSA (b-BSA)	100–300	FMN, FAD	1–5	Buffer (PBS or HEPES, pH ~7.4)
	BSA conjugated with dye (dye-BSA)	200–400	RB, MB	0, 0.25, 5	Acetic or buffer, pH~7.3–4
3HQV	Collagen type-I (Col.I)	15, 30, 45	FMN	0.6, 1.2, 1.8	Acetic acid, aqueous
	Collagen type-I, II, or IV (Col.I, Col.II, Col.IV)	2–3	BPD, RB	0.2, 1	Acetic acid, aqueous
1M3D	Col.IV - BSA	0.15, 25	FAD with RhB	0.125 with 0.3	As purchased (pH=5) mixed DMSO, HEPES buffer, organic solvent
1GKB	ConcanavalinA (ConA)	4.5	RB, Texas-red, RhB	0.5	n.a.
1OCC	Cytochrome c (CytC)	100, 200	FAD	0, 4.5, 10	Supporting electrolyte, pH=7.40.
2Y0G	Enhanced green fluorescent protein (EGFP)	2.35	MBS	10	HEPES-KOH buffer, pH = 7.4

3GHG	Fibrinogen (FNG)	3.9 or as purchased	RB, Texas-red, RhB	0.01–0.1	As purchased
3M7P	Fibronectin (FN)	1–1.29	RB, Texas-red, RhB	2–4	Distilled water
2CMM	Myoglobin (MGN)	40	RB, MB	8.5 or 5	HEPES buffer (pH 7.4)
5IK4	Laminin (LN) mixed with BSA	n.a.	FAD, MB	1–4, 0.25	HEPES buffer (pH 7.4)
2CDS	Lysozyme (Lys)	300–400	MB, FAD	1.2–5	HEPES buffer (pH 7.4)
		320–400	Eosin-Y, FAD, MB	4.3–14.3	DMSO 21%, HEPES buffer
3UA0	Regenerated silk fibroin (RSF)	25	MB	5	Aqueous, pH=7.0
1S0Q	Trypsin (TR)	20	FAD, Eosin-Y	6, 0.3	n.a.

BSA

Albumin is the major protein present in the blood, produced by the liver, and with main functions as a transporter for endogenous and exogenous substances, as well as in the maintenance of oncotic pressure in blood vessels. Bovine Serum Albumin (BSA) is a protein derived from cows. BSA, also known as the fifth component, is a globulin bovine serum containing 583 amino acid residues, with a molecular weight of 66.5 kDa and an isoelectric point of 4.7. As a member of albumins, BSA shares their common properties. About 75~80% of colloid osmotic pressure is maintained by albumin. As transport molecules, albumin can bind and carry lots of small molecules like fatty acids, bilirubin, minerals and hormones and drugs. Besides, albumin also plays important roles in anticoagulation and antioxidant activity.[115] BSA has a wide range of applications in biochemical experiments, such as a blocking agent in Western blotting.[116]

There are 35 cysteine residues in BSA. Among them, 34 cysteine residues form 17 intermolecular disulfide bridges, leaving a single sulfhydryl group.[117] This property broadens its use in polymer science. Disulfide groups and free sulfhydryl groups make BSA a candidate to be photo-polymerized. Disulfide groups can undergo a metathesis process forming a crosslinking network. [118,119]At the same time, free sulfhydryl groups can also take part in the polymerization process.[120]

BSA can be dissolved in pure water or buffers. To effectively polymerize BSA by TPP, we need to find proper photoinitiators and suitable concentration. Losin *et al.*[121] used Rose Bengal and Eosin Y as photoinitiators to polymerize 10 mg/mL BSA in water by TPP at 532 nm.

Turunen *et al.*[122] chose non-toxic flavin mononucleotide (FMN) as the photosensitizer to polymerize high concentration BSA (200 mg/ml) or BSA with biotinylated BSA (bBSA) (100 mg/ml separately). Biotinylated BSA can be labeled by streptavin conjugated to a fluorescent molecule, which gives the fluorescence images of the structure. The successful labeling of structures fabricated with bBSA proved that polymerized bBSA still maintains the ligand-binding ability. The authors tried picosecond Nd:YAG laser (532 nm) and femtosecond Ti:Sapphire laser (800 nm) as sources to compare the polymerized BSA feature size and characteristics. By tuning the fabrication parameters, both laser sources could produce

structures with similar characteristics at sub-micrometer and micrometer scales. Even though, the femtosecond Ti:Sapphire still produced slightly lower aspect ratio than picosecond Nd:YAG laser.

In addition to pure BSA, other proteins can also be mixed with BSA to build 3D polymerized structures. Kaehr and Shear[123] chose BSA, avidin and lysozyme as raw materials. Those three proteins have different isoelectric points, 10.0–10.5, 4.7–4.9, 11.0–11.3 for BSA, avidin and lysozyme respectively. Avidin, BSA and lysozyme have different swelling ratios over a broad range from 2 to 12. The volume of each protein gel reached the minimum volume near the isoelectric point. The authors achieved the preparation of stimuli-responsive structures by adjusting the ratio of proteins at varied pH. When mixing BSA and lysozyme, the size of the protein matrix gel can be tuned in the pH range from 7 to 11.9, during which the size of the gel gradually decreases as the percentage of lysozyme increases.

Besides polymerization of protein mixtures, it is also possible to build hybrid structures with polymer and BSA sequentially. Serien and Takeuchi[124] produced multicomponent microscaffolds by step fabrication with polymers and proteins. First, IP-L 780 photoresist was used to build a basic 3D framework. One drop of BSA solution containing photoinitiators was added to the first structure. A polymerized BSA network was finished on the basic 3D framework.

Collagen

Collagen is a very important protein in animals. It is the main component of extracellular matrix (ECM). There are 24 types of collagens, while the most well-known ones are type I, II, III (fibrillars) and IV (network). The overall conformation of tropocollagen consists in three parallel strands with a left-handed polyproline II-type (PPII) helical coil to form a right-handed helix. Within every single PPII helix, there is a glycine (Gly) residue for every three amino acids tripeptide, Gly-X-Y. X often refers to proline while Y represents hydroxyproline. The overall right-handed helix is maintained by the hydrogen bonds between N-H from glycine and O=C from another proline.[125,126,127] **Figure 1.39** shows the multi-level structure of collagen fibers.

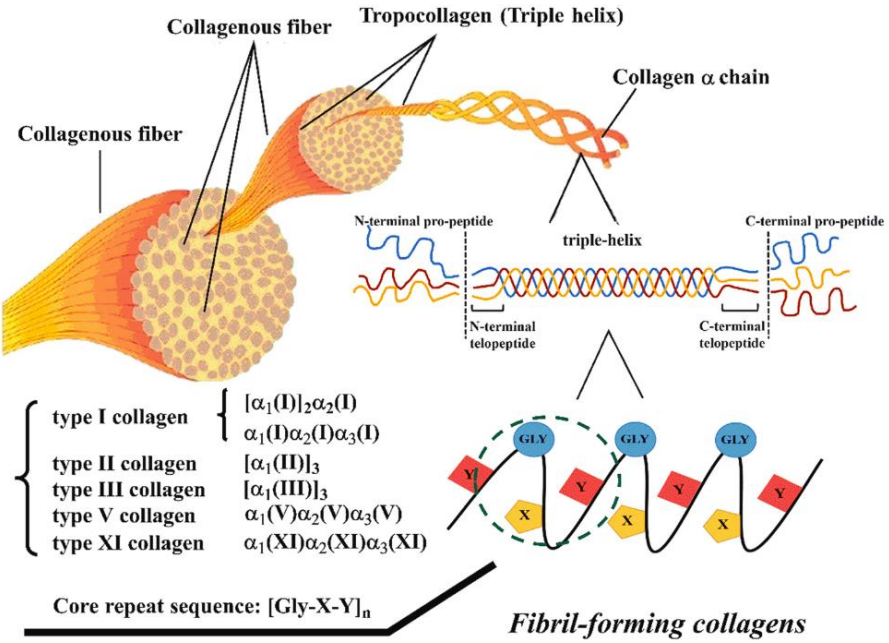

Figure 1.39 The collagen organization for type I, II, III, V and XI collagen.[128]

Type I collagen or collagen I is the most abundant protein in many tissues, like bone, skin, etc. Type I collagen constitutes approximately 95% of total collagen content in the bone and about 80% of the total protein in the bone. [127] In the lab, type I tropocollagens are usually extracted from rat tail tendons.[129] The size of tropocollagen is 300 kDa. Its length is 300 nm with 1.5 nm diameter. The isoelectric point of collagen is ca. 8.2. So, collagen tends to separate into tropocollagen due to repulsive electrostatic interaction when the pH is very low. With the increase in pH, tropocollagen will form fibrils when the positive charge on the surface of tropocollagen is not enough. Based on this principle, a high concentration of collagen solution *in vitro*, 300 mg/mL, is also realized by adjusting the pH of the solution to 3.

In tissue engineering, proteins show enormous potential in the application of tissue scaffold. As the most abundant protein in extracellular matrix, collagen I is a protein that the researchers cannot ignore. Bell *et al.*[130] used TPP technology to polymerize type I collagen. Three concentrations of collagen I were used in the experiment, 5, 15, 30 and 45 mg/ml. The first concentration, 5 mg/ml collagen, is used directly as received in acid-stabilized solution. 15 and 30 mg/ml collagen solution were obtained by dialysis. 45 mg/ml collagen was prepared by directly dissolving collagen in acid solution. Titanium Sapphire 750 nm laser was the laser source and riboflavin 5′ monophosphate (FMN) was chosen as photoinitiator here at a concentration of 1.0 mM for every 25 mg mL−1 of collagen concentration. Different concentrations of type I collagen were tried with varied power and pixel dwell. Collagen 3D

fabrication was only realized with high concentration of collagen at 45 mg/ml. Lower concentrations like 5 mg/ml, 15 mg/ml and 30 mg/ml type I collagen were not sufficient to obtain a 3D structure.

In acid solution, the commonly used photoinitiator Rose Bengal does not work well because of changes in conjugated structure of the molecular structure while Riboflavin series photoinitiators work well. When Rose Bengal is in quinoid form. Rose Bengal water solution is red. When in acid solution, quinoid form transfers into lactonic form (**Figure 1.40**). The original carboxylate forms a lactone, and at the same time a phenolic hydroxyl group is formed.[131] The solution of lactonic form is colorless. Lactonic form of Rose Bengal cannot generate TPP at 532 nm. The key point of TPP of collagen I is to find suitable photoinitiator that works in acid solution.

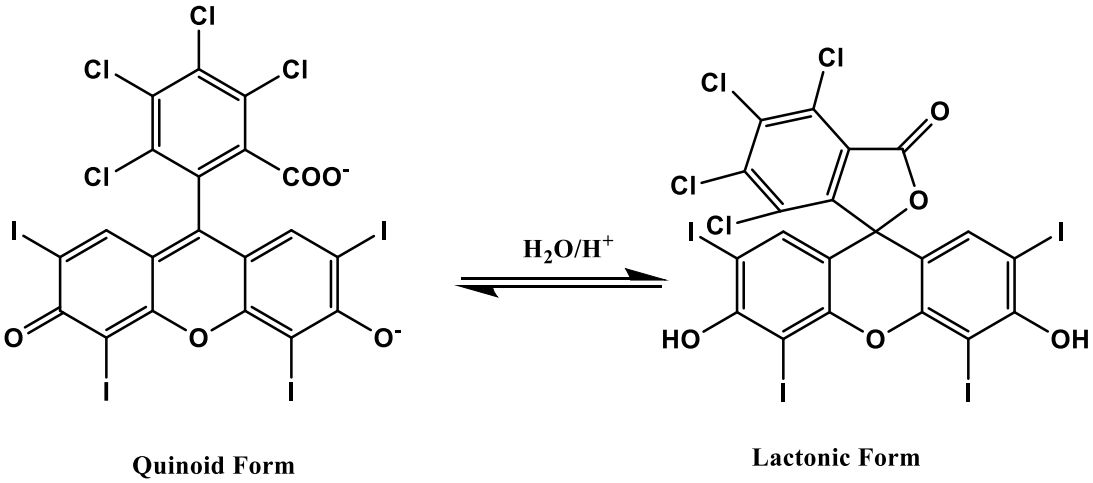

Figure 1.40 The form change of Rose Bengal upon pH change.

1.2.3.4 Opportunities in the application of proteins in TPP

We introduced the basic knowledge of proteins used in TPP in this section. BSA can be used to fabricate structures alone or mixed with other proteins, and it is a potential good protein candidate for its cheap availability. But its application in cell biology is still not well explored. BSA has been used as cell-repellent coating for surface modification. Whether the cell repellent property remains after polymerization needs to be explored. Here we would also like to understand the cell behavior on protein 3D scaffold fabricated by TPP. Moreover, to our knowledge, hybrid structures made by proteins and synthetic polymers are not well reported, and we would like to take advantage of both protein and polymers TPP to fabricate 3D structures with applications in cell biology.

1.3. Poly(ethylene glycol) (PEG) and its applications in anti-adhesion

In section 1.3.2, we chose OSTE as a good candidate to produce TPP structures. Surface modification is a crucial aspect for biomaterial, which can enhance functionality, biocompatibility and performance. Furthermore, local modification can provide the surface different properties in diverse areas. To functionalize the surface of OSTE resins, we cannot ignore the wide range of applications of PEG in surface anti-adhesive treatment. In this section, we will first introduce the basic knowledge of PEG, and then its application in anti-adhesion, revealing the potential of coupling PEG grafting and OSTE resins.

1.3.1 Basic chemical and physical characteristics of poly(ethylene glycol)

Polyethylene glycol, abbreviated as PEG, is a linear or branched polymer that has numerous useful properties, like appreciable flexibility, hydrophilicity, absence of toxicity and bioactivity.[132,133,134] PEG or PEO (polyethylene oxide) is easily dissolved in water, methanol, ethanol, or acetone. Depending on its exact length, its solubility varies in solvent.

In crystal, the PEG unit cell is four-chains monoclinic (**Figure 1.41**). Each chain adopts a distorted structure with seven monomer units forming two helical turns.[135] In water solution, PEG molecule forms a loose coil.

If "g" means gauche (left) conformation of -C-C- bond and "t" stands for the trans conformation of -C-O- bond in the sequence -O-CH_2-CH_2-O-, the helical form consists of "ttg" sequence. However, there are only short-range "ttg" sequences when PEG is in water.[136] Random coil formation is the overall state of short-chain PEG in water.

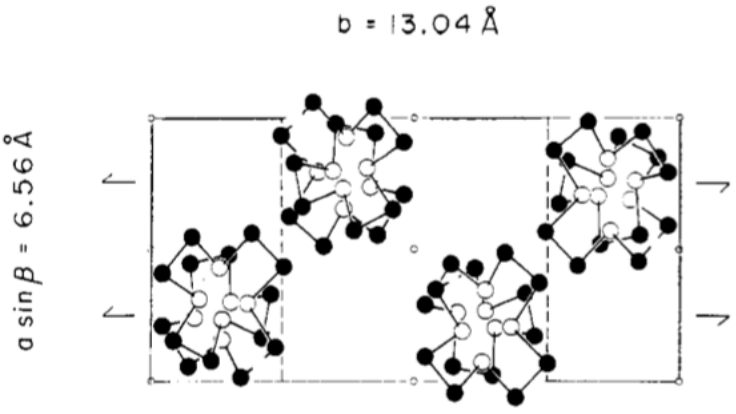

Figure 1.41 Crystal structure of PEG[135]

PEG molecules will form hydrogen bonds with water. From experimental data from Huang *et al.*[137], the maximum hydration number per ethylene glycol (EG) unit was estimated as 1.6, 2.4, and 3.3 for samples with molecular weights 400, 1540, and 70,000 Da, respectively.

1.3.2 Surface immobilization strategies and commonly used PEGs (Polyethylene glycol).

PEGylation was first mentioned as a concept by Abuchowski *et al*.[138] to describe covalent attachment of PEG to bovine liver catalase to explore its immunogenicity and circulating life. Later, PEGylation was used to describe the process of both covalent and non-covalent attachment of PEG.[139,140] PEGylation process is strongly related to its end groups. **Figure 1.42** reveals the commonly used PEGs according to different ending groups. Function groups like NHS, aldehyde maleimide, hydrazide, alkyne, sulfone and thiol bring multiple direct reactions for PEGylation.

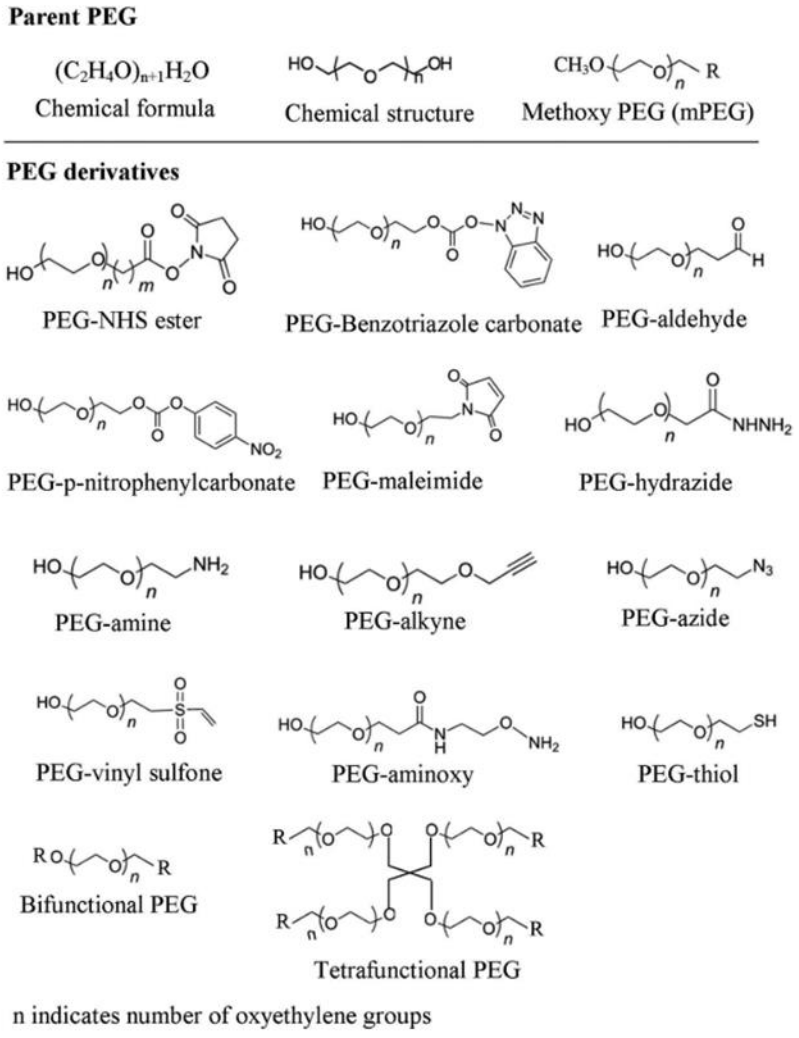

Figure 1.42 Chemical structures of commonly used PEGs and relative derivatives[141]

There are two directions to go with varied PEG and its derivatives for surface treatment: i) adsorption and ii) covalent bonding. Simple adsorption is reversible under certain circumstances while covalent bonding provides more stable surface modification. According to different mechanisms and strategies for covalent bonding can be “grafting to” and “grafting from”. “Grafting to” refers to polymers with

end-functional groups grafted to a solid surface while "grafting from" is polymerization proceeded from the surface.[142]

With the "grafting to" method, many PEGs can be used for PEGylation: PEG-N-Hydroxysuccinimide (PEG-NHS), PEG-NH_2, PEG-isocyanate, PEG (meth)acrylate, PEG-SH, PEG-maleimide, PEG-silane, PEG-epoxide and pure PEG together with coupling compounds, etc.[87,143,144,145,146,147] Our target here that can be linked to OSTE surfaces. For thiol excess surface, PEG (meth)acrylate is more interesting. For alkene excess surface, PEG-SH would be to best to be grafted. **Table 1. 4** shows the typical paired groups for "graft to" strategy.

Table 1. 4 Typical functional groups for PEG grafting

PEG-NHS	-NH_2
PEG-NH_2	-NHS, -maleimide, -epoxide
PEG-isocyanate	-epoxy
PEG (meth)acrylate	-SH
PEG-SH	-(meth)arylate, -maleimide
PEG-maleimide	-NH_2, -SH
PEG-silane	Depending on the functional group of silanes
PEG-epoxide	-NH_2,-isocyanate

When polymers are grafted on the surface, the conformation of polymers also obey rules that vary from different grafting density. R_G, the radius of gyration, is defined as the size of coil conformation of free polymer in solution, while *d* refers to the distance of grafting points. When the grafting density is very low, $R_G < d$, the grafted polymer chains on the surface are independent from each other. The so-called mushroom regime is shown in **Figure 1.43** (a). The free chain keeps the coil conformation in solution but curled up on the surface. When the grafting density is high enough ($R_G > d$, **Figure 1.43** (b)), free polymer chains begin to overlap with each other.[148] Steric repulsion forces mushroom regime to be brush layer. The equilibrium height of the polymer brush layer is dictated by the competition between the stretching of chains away from the surfaces and the entropic elasticity that resists such stretching.

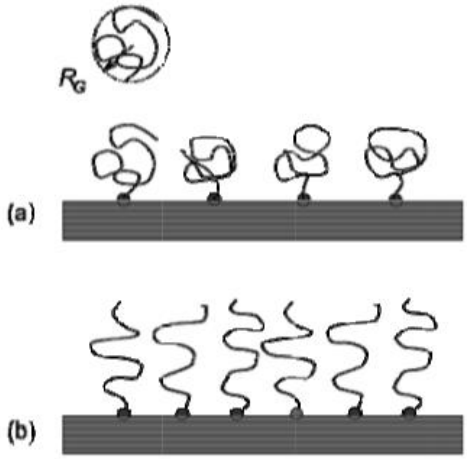

Figure 1.43 Two forms of grafting of polymers to a surface (a) isolated mushrooms (b) stretched brushes.[148]

According to *Alexander-de Gennes* theory,[149,150] the simplest model of a polymer brush defines *L* as the distance between the grafting site and the end of the polymer chain (**Figure 1.44**). Supposing that the distance between the point of grafting determines the blob of the grafted polymer, and the polymer stretches well in a good solvent, the following formula shows the relationship between the height of the brush height (*L*), the number of monomers per chain (*N*) the size of the monomer (a), and the grafting density (σ_g),

$$L \sim N a \sigma_g^{1/3} \quad (11)$$

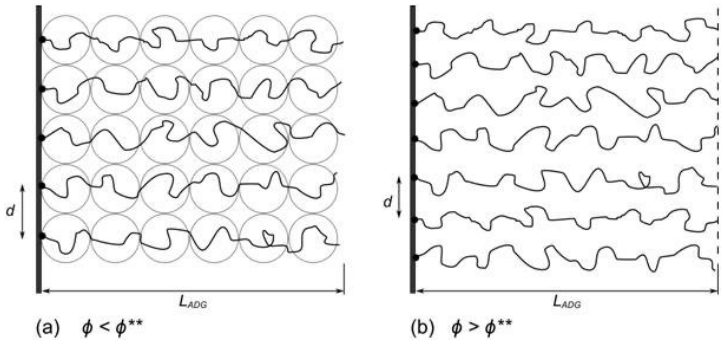

Figure 1.44 Alexander-de Gennes model for polymer brush in a good solvent (a) in concentrated solvent (b).[148] *d* is the distance between two adjacent grafting points. ϕ represents volume fraction or concentration. ϕ^{**} is the cut-off point of concentrated volume fraction.

1.3.3 Surface immobilization of PEG and its application

1.3.3.1 Mechanism for anti-fouling surface modification

Antifouling surfaces commonly refers to surfaces that prevent protein adsorption and cell adhesion. Cell-adhesion mechanisms are generally protein-mediated, and in general cell repellent surfaces also repel proteins. When grafted on material surface, flexible chains of PEG form a hydration layer which separates material substrates from proteins and cells in solution.

The effect of protein resistance comes from both surface hydration (i.e., water barrier) and chain flexibility (i.e. steric repulsion). In detail, the hydrogen bond site -O- in the repeat unite -CH_2CH_2O- is hydrated with a water molecule. A large barrier of water layer blocks the nonspecific protein adsorption. Steric exclusion mainly results from the repulsive force of compression of long polymer chains.

As **Figure 1.45** shows. There are three kinds of mechanisms for surface hydration. First, a long hydrophilic polymer, for example PEG5000, generates a big layer water barrier. Besides PEG, poly-zwitterions can also be used to form a water barrier by even stronger iron bonds with water. For short chains of oligomer ethylene glycol (OEG), self-assembled monolayer seems to be required for protein repellency. Usually, self-assembled layers need the presence of liner alkane units in the structure of grafted molecule.[151].

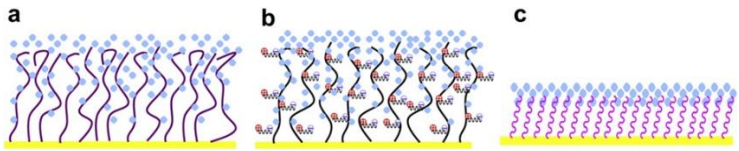

Figure 1.45 Schemes of chain hydration/flexibility. (a) hydrophilic polymers, (b) zwitterionic polymers, and (c) SAMs[152]

1.3.3.2 Applications of surface immobilizations of PEG

Non-covalent attachment is realized by physical adsorption. For example, poly-L-Lysine grafted PEG (PLL-g-PEG) was well-known for its excellent protein-repellent properties by non-specific adsorption. PLL is positively charged, hence PLL-g-PEG can be absorbed on a negatively charged surface. Also, PLL-g-PEG can be linked to bio-conjugation through biotin-streptavidin interaction.[153] Another widely used PEG derivative is dopamine(DA)-PEG. Dopamine (3,4-dihydroxyphenethylamine) can be linked to PEG through amine. Catechol moiety in DA provides strong reversible bonding ability to mimic mussel adhesion in nature. Liu *et al.*[154] used a DA modified four-armed PEG (nanocomposite) hydrogel, which improved cellular infiltration and decreased inflammation in bioimplant experiments in rats.

Different from adhesion, covalent bonding provides a more stable link to the substrate. Carlborg *et al.*[87] grafted PEG 5000-thiol and PEG 5000-allyl by "Click Chemistry" on allyl and thiol excess surface respectively, which brings higher hydrophilicity than the original surface. The length of PEG will also influence the surface property. By using different lengths of PEG methacrylate, Breuckers *et al.*[155] tuned the surface interaction between single cells and PEG modified surface. The results showed that PEG 2000 methacrylate brings a more hydrophilic surface than PEG 360 and PEG 500 methacrylates. For the modified surface with mixed PEG 360, PEG 500 and PEG 2000 methacrylates, cells optically lift experiment showed similar anti-adhesion property thar was brought by PEG 2000 methacrylate.

Instead of the "grafting to" strategy, "grafting from" strategy can be used to form a PEG layer on the original surface. "Grafting from" strategy generates polymer brushes through surface polymerization. Zhang *et al.*[156] grafted well-defined dendronized PEG methacrylate on PDMS substrate by surface-initiated atom transfer radical polymerization (SI-ARTP). Compared to the original polydimethylsiloxane (PDMS) surface, polyPEG-PDMS surface showed excellent bacteria and cell repellences.

In addition to adhesion and surface grafting, entrapment is the third method to immobilize PEG in material. Liu *et al.*[157] added PEG 200 directly into OSTE polymers. With the rise of the percentage of PEG 200, the water contact angle of the cured surface decreased. PEG was embedded in a cured OSTE resin network and PEG loops formed on the surface. After plasma treatment, the contact angle decreased sharply from 40.5° to 4.9° for 15% PEG 200 in thiol:ene = 1.3:1 OSTE resin network.

No matter surface grafting or direct entrapment, there are some important points that cannot be ignored, density and chain length of PEG. Lee *et al.*[158] grafted lipid bilayers with PEG of different size, ranging from M_w= 750 to 2000 and 5000 *Da* and also different densities 1.6~25 mol %. When the distance between two surface points (*d*) of the grafted PEGs on the substrate is bigger than the size of the mushroom (Flory radius R_F), $d > R_F$, PEGs grafted on the surface lie in mushroom state. Human Serum Albumin (HAS) absorption decreased with the increase of grafting density. When grafting densities are high enough, $d < R_F$, then PEGs of all length on the surface lie in brush regime. In this condition, there was no HSA absorbed or bounded directly to the original surface. The effects of different lengths of PEGs lie as follows. First, shorter PEG has a larger mushroom-brush transition grafting density, $d = R_F$. Second, longer PEG chain has a larger R_F and a bigger thickness of brush. So longer PEG chain reaches brush regime at lower concentration than shorter PEG chain and forms a thicker layer of PEG, which prevents HSA adsorption. Perry *et al.*[159] further calculated the concentration of PEG5000 (fluorescein-PEG5000-succinimidyl carboxy methyl ester reacted with free premier amine on the surface) is around 0.083 ± 0.006 PEG/nm^2 to form a brush for anti-adhesion of BSA.

This last conclusion is only based on HSA adsorption experiments on lipid bilayers substrate. Bernhard *et al.*[160] pointed out that different proteins may have different adsorption behaviors. Not only protein

adsorption amount, but also the way of adsorption, were different on same PEG modified surfaces for BSA and fibrinogen. For BSA, PEG modified surface revealed pure repellency property. But fibrinogen showed three states depending on the concentration of PEG, maximum adsorption in the absence of PEG, maximum orientation at intermediate coverage, and total repellency at high PEG concentration.

To further explore cell adhesion and bacterial attachment, Al-Ani *et al.*[161] controlled the PEG grating density by tuning the density of function groups (NH_2) that can be bonded with PEG-aldehyde on the surface. As shown in **Figure 1.46**, different densities of aminopropyl-triethoxysilane (APTES) modified surface were realized by control the concentration of APTES at 1%, 2% and 4% (v/v) in toluene. Then PEG-aldehyde (M_w = 5000) was grafted to NH_2-rich surface at cloud point, forming a high-density polymer brush. Both Mesenchymal Stem Cells (MSCs) and MG63 osteoblast cells revealed the lowest attachment with high density grafting. WHAT is medium of PEG, MSCs density was even higher than that on the surface with low PEG grafted density in PEG grafting density. For bacteria adhesion test, the number of *P. aeruginosa* decreased with the increase of the PEG density.

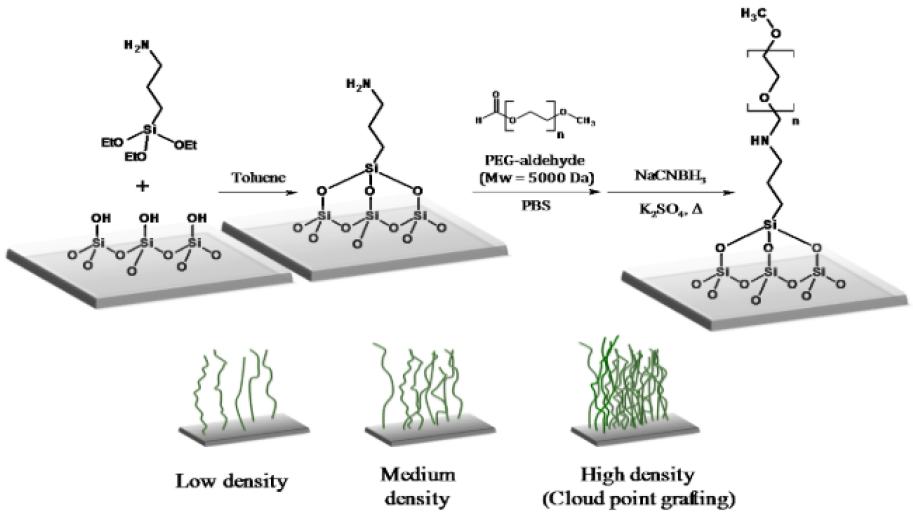

Figure 1.46 PEG-aldehyde grafting onto aminopropyl-triethoxysilane modified silicon wafers. [161]

1.3.4 Conclusion

In this section, we introduced the basic characteristics of PEG and surface modification related to PEG. Conformation and concentration of PEG on modified surface have a big influence on the behavior of protein and cell repellence of the surface. Different PEG derivatives can be used to modify the surface. According to the different mechanisms, surface immobilization can be divided into simple adsorption and direct covalent modification. There are two strategies for covalent modification, “grafting to” and “grafting from”. “Grafting to” generates simple one-layer polymer brush while

"grafting from" produces a relatively denser molecular brush. PEG and its derivatives are good candidates for anti-foul surface modifications. There are lots of potential for its application for biological applications together with well-defined surfaces.

In general, PEG 5000 forms a thicker layer brush with a relatively lower grafted density than PEG 2000 and PEG 750. The general principles of protein adsorption, bacteria and cell adhesion on PEG modified surface are the same. Although the results varied a bit depending on the type of protein/cell, generally high density of grafted PEG 5000 grafted at 0.083 ± 0.006 PEG/nm^2 (brush state on the surface) reduces the attachment of proteins, bacteria and cells.

1.4. Cell behavior on TPP microstructures

It is widely established that cell behaviors are influenced by many factors in the extracellular matrix. The factors are mainly divided into two parts, biophysical and biochemical factors. They include microtopography, roughness, stiffness, mechanical properties, growth factors, cell-cell interaction and cell-substrate binding (surface chemistry). Classically, cell behaviors have often been evaluated on 2D culture conditions. Researchers gradually found that 3D microenvironments generally induced hugely different cell responses compared to 2D surface. Therefore, it is of great interest to find a powerful tool to construct 3D scaffolds at cellular and subcellular scales, to figure out the combined influences of these factors on cell behavior. Two-photon polymerization is a valuable tool to fabricate scaffolds with well-defined microgeometry at these scales. Here, we introduce a few typical examples of the application of two-photon polymerization on cell behaviors, like cell adhesion and cell orientation and alignment.

1.4.1 Stiffness and morphology

Polyethylene glycol diacrylate (PEGDA) is widely used in TPP. Due to its non-adhesive properties for large chain lengths, PEGDA575 can be used to fabricate cell-repellent patterns and 3D structures. Song *et al.*[162] combined cell-repellent patterns and cell adhesive patterns with designed geometry to control cell alignment. 50 wt% PEGDA575 with 3 wt% lithium phenyl-2,4,6- trimethylbenzoylphosphinate (TPO-Li) as photoinitiator in water was used for cell-repellent material while a mixture of 36 wt% PEGDA575 and 9 wt% methacrylated recombinant peptide (RCP)-based photoresist with 3 wt% TPO-Li as photoinitiator was used as cell-adhesive resin.

About stiffness, by changing the laser scanning speed, parallel stiff and soft patterns were achieved with cell adhesive and cell-repellent photoresists. For cell adhesive hydrogel, Young's modulus was 103 kPa with 20 mm/s scan speed and 54 kPa with 60 mm/s scan speed. For cell repellent hydrogel, Young's modulus was 150 kPa with 20 mm/s scan speed and 75 kPa with 60 mm/s scan speed. For human mesenchymal stem cells (hMSCs) test, the aligned F-actin fraction on alternating stiff-soft patterns was 1.2-2 times than that on stiff-only patterns.

About the topography of the substrate, hMSCs showed strong alignment with the parallel lines on stiff patterns after three days of culture. The results showed hMSCs preferred to align on surfaces of high stiffness. For 3D structures, cell behaviors on half sphere dome microstructures both gave comparable results: cells aligned in the direction of stiff/soft patterns, while randomly spreading on the unpatterned surface (**Figure 1.47**).

From the details above, we can find that both stiffness and topography will influence the alignment of the cells.

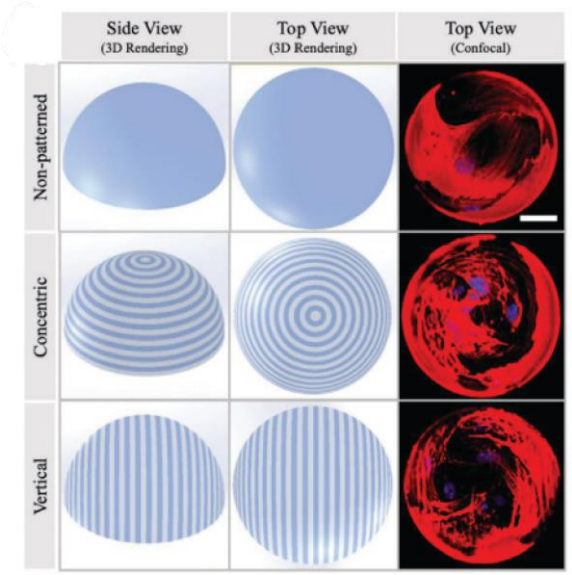

Figure 1.47 Scheme of 3D structure and confocal images of hMSCs alignment. stiff (dark blue) and soft hydrogels (light blue) patterns. (blue, DAPI, red, F-actin, scale bar = 20 μm).

1.4.2 Mechanical properties and 2D force measurements

In recent years, cell force measurement has aroused great interest among researchers because it helps to understand how cells react with the extracellular matrix. Franziska *et al.*[82] developed 3D structures at the cell scale, studied their mechanical properties with atomic force microscopy (AFM), and eventually measured the forces exerted by cells. Ormocomp, a photoresist, was used to fabricate regular octagon framework with pillars and lines. Fibronectin coating helped to increase the settlement of the cells. The mechanical properties of the structures were measured with tipless cantilevers contacting lines between the pillars, with the recorded force-distance curve giving relationship between force and the beam deflection. Cardiomyocytes were seeded on the framework and the rhythmic deformation of the structure by single beating cells were detected, with cellular forces down to 10-20 nN measurable with the setup.

Besides the commercially available products, chemists also devoted themselves to new smart tools for tailoring and visualizing mechanical and viscoelastic properties (hardness, complex elastic modulus, loss factor). Gernhardt *et al.*[163] developed a new material with post-tunable mechanical properties. Anthracene photodimerizes in the presence of UV light, forming dianthracene. By three steps synthesis, anthracene-OEG_6-monoacrylate was successfully synthesized. As shown in **Figure 1.48**, the monoacrylate could react with each other as the mechanism of TPP to fabricate microstructures. Under the illumination of the structure of 415 nm for the post-process, anthracene unites are dimerized, thus the complex modules strengthened from 1.7 to 6.2 GPa. Also, the fluorescence of anthracene was quenched by dimerization, which can be an indicator of mechanical properties. When the fluorescence decreases, the mechanical properties will rise. By adding pentaerythritol triacrylate (PETA) as

crosslinker, the mechanical strength could be improved further. This system promotes the development of materials of TPP with tunable mechanical properties for different demands.

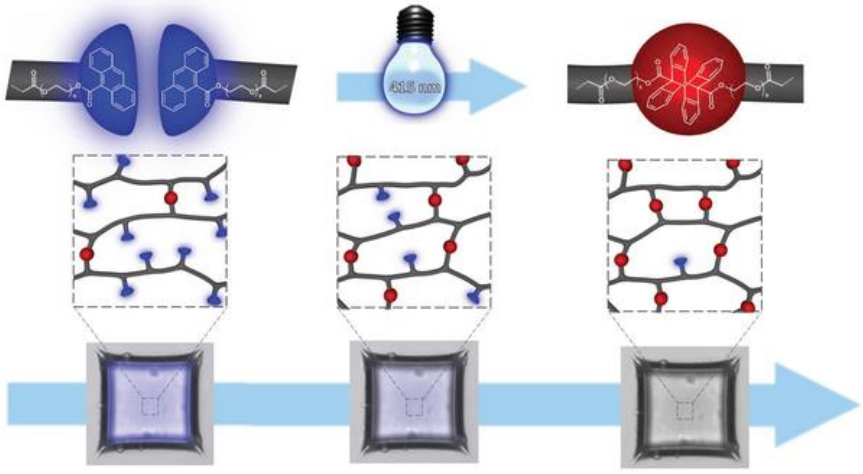

Figure 1.48 Step curing process to tuning the mechanical property of the material.[163]

1.4.3 Microtopography

When talking about topography, an important concept is the difference between 2-dimensional (2D) and 3-dimensional (3D) environments. Historically, 2D flat substrates have been the common choice for cell culture experiments and are still widely used for practical reasons. But the real environment of cell growth is 3D, which is currently the focus of numerous developments, with most cell biology fundamental processes still more understood in 2D while they show striking differences in 3D. The real environment of the cell growth is 3D, which is not fully characterized yet.

Greiner *et al.*[164] tried to figure out the change of cell behavior on the varied substrates from 2D pattern to 3D substrat (**Figure 1.49**). Both the 2D substrates and 3D structures were fabricated with pentaerythriol tetraacrylate (PETTA) for stiff substrate and Ormocomp for soft substrates by TPP and then coated with fibronectin. Diverse types of cells, fibroblast-like or epithelial, were incubated on the surface for three hours. The results of the cell volume measurements showed that cell and nuclear volume of fibroblast-like cells on 3D structures increased than that on 2D flat surface. But both two volumes of epithelial cells mostly kept the same level on 2D and 3D surfaces. The ratio of nucleus to cell volume (N/C) stayed still for fibroblast-like and epithelial cells on 2D and 3D surface. The nucleus and cell volumes depend on the cell types while the N/C does not change.

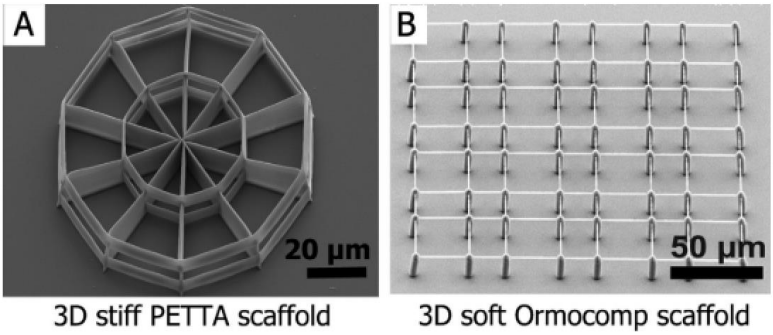

Figure 1.49 3D scaffold fabricated with pentaerythritol tetraacryalte (PETTA) and Ormocomp by TPP

1.4.4 Cell-substrate binding

Tissue engineering is a complex system of combination of physics, chemistry and biology. In addition to biophysical cues, biochemical factors also have a non-negligible influence on cell behaviors. The chemical sites on the substrate's surface determine how cells bind to extracellular matrix. A considerable amount of work was performed on the relationship between cell behavior and the surface chemistry of materials. Here we described some works on the how to control the cell binding by tuning the chemical components both on 2D and 3D conditions.

Klein *et al.*[83] constructed 3D scaffolds with two components, polyethylene glycol diacrylate 575 (PEGDA575) and pentaerythritol tetraacrylate (PETTA). PEGDA 575 mixed with Irgacure 369 (3w/w%) forming protein repellent and hydrophilic photoresist. The elastic modulus of polymerized pure PEGDA 575 is around 140 MPa. To increase the elastic modulus, PETTA was added into PEGDA575. PETTA is both a cross-linker and a protein binding component. When mixed with PEGDA 575, the percentage of PETTA influences the protein both mechanical property and binding ability. Pure PEGDA 575 and PEGDA 575 mixed with 4.8% PETTA were protein and cell repellent. But when the concentration of PETTA increased to 9.1% and even higher, the mixture became protein and cell adhesive. In order to improve the mechanical property and also maintain the cell repellency of the scaffold, PEGDA 575 with 4.8% PETTA was used to fabricate complex 3D structures. At the same time, Ormocomp™ is a protein-binding photoresist. Small cubes were made with Ormocomp on the PEGDA/PETTA structure. Before it was used for cell culture, the scaffold was incubated with fibronectin. Then primary chicken fibroblasts were seeded on the scaffold. After 2 hours incubation, cells were only bound to the fibronectin-coated Ormocomp cube, but not on the PEGDA575/PETTA framework. By this way, the cell shape was well controlled in 3D environment, providing a possible opportunity to study the impact of real 3D distribution of binding sites on cell behaviors.

A tool to explore the influence of the mechanical forces on individual cells was also facilitated by spatial control of cell binding sites. Scheiwe *et al.*[165] used a strategy similar to the one mentioned above. A basic scaffold was made from PEGDA 575/PETTA. Ormocomp cubes were symmetrically distributed on hexagonal scaffold. After incubated with fibronectin, Ormocomp cubes became cell binding sites. Chicken embryonic fibroblasts (CEFs) were seeded on the two-components scaffold. CEFs cells were bound to the six sites, resulting in a hexagonal shape. Successful controlled stretching of the CEFs cells was accomplished using a micromanipulator. CEFs showed different behaviors with static and periodic stretching forces. Paxillin and adhesion kinase levels increased during static stretching while falling during periodic stretching.

Richter *et al.*[166] developed a trail on guiding cell attachment by tuning the surface chemistry for cell binding. Trimethylolpropane ethoxylate triacrylate (TPETA) with a photoinitiator (Irgacure 369, 3% w/w) was used as the basic resin. Phenacyl sulfide methacrylate (PS) and photoenol methacrylate (PE) were mixed separately with the basic resin to make up PS resist and PE resist as basic substrates, which were used form a square matrix. Then the surfaces can be functionalized with different molecules. (**Figure 1.50**)

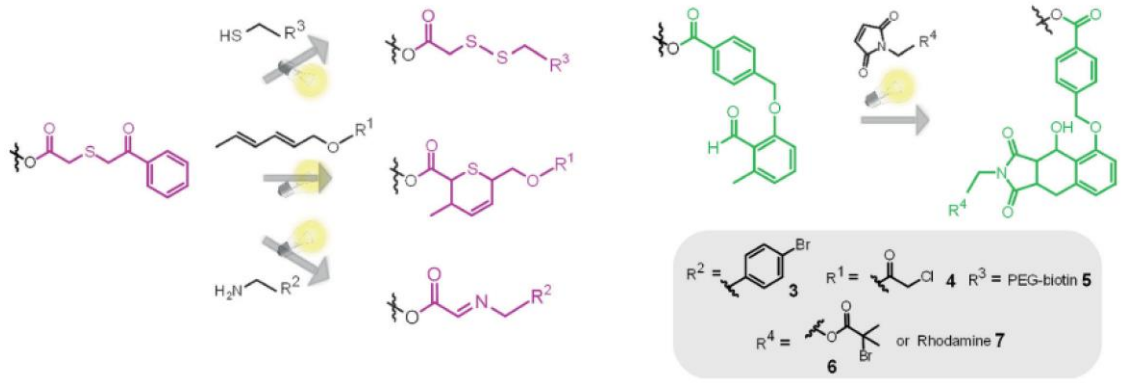

Figure 1.50 Summary of post-modification on phenacyl sulfide (left) or photoenol (right) free surface.

As shown in **Figure 1.51**, A549 lung epithelial cells were seeded on the patterned substrate. Fibronectin (FN, red) can be absorbed on hydrophobic glass but not on PS. When incubated on the substrate, A549 cells (actin, green; nuclei, white) were at 98.4% observed on the FN covered area, but not on the basic resists (PS resist and PE resist). When the basic resins were modified with biotin (Bt), the cell behavior was the same as before modification. The surface resin covered parts were still cell repellent. Around 93.6% cell nuclei were on the glass. Avidin-biotin interaction is widely used as binding tool for the conjugation of biomolecules.[167] Biotinylated vitronectin (Bt-VN, magenta) was grafted on the biotin covered squares by avidin-biotin interaction. The cell repellent surface was transferred into cell-adhesive

surface. The results of A549 cell adhesion experiment showed that the cell coverages on fibronectin covered glass and vitronectin modified basic resins were almost the same. The cell adhesion results on 2D surface points the way for the next steps on 3D scaffold.

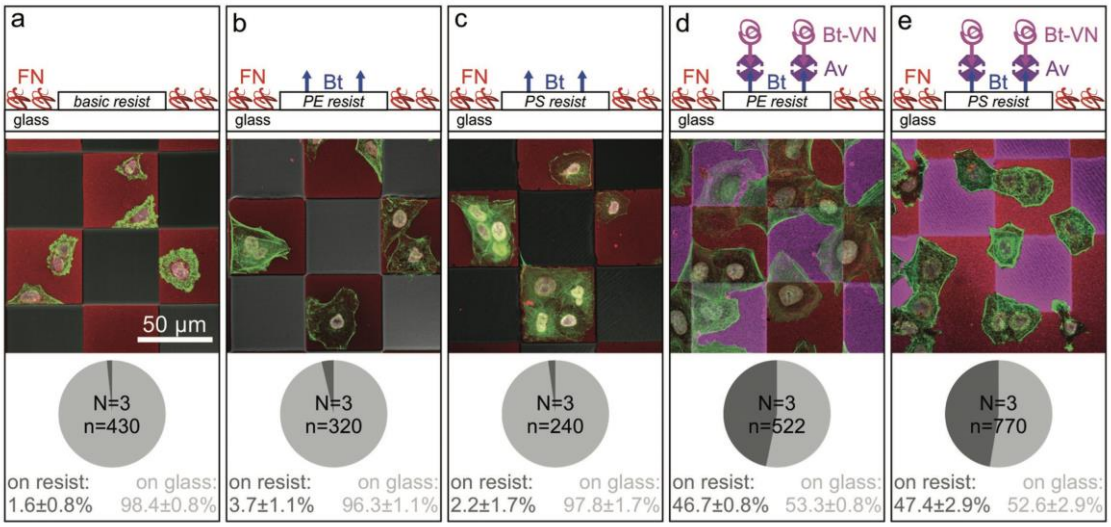

Figure 1.51 Cell binding on the patterned 2D surface. Color code: fibronectin (FN, red), biotin (Bt, blue), biotinylated vitronectin (Bt-VN, magenta), avidin (Av), A549 cells (actin, green; nuclei, white). N: number of independent experiments; n: number of counted cells [166]

As shown in **Figure 1.52**, structures made by varied materials (basic resin, photoenol, organic-inorganic hybrid polymer Ormocomp™) were successfully constructed by stepped digital light processing. Basic resin provided cell-repellent framework. On the top of the scaffold, two parallel photoenol network lines and Ormocomp lines were sequentially fabricated to form squares. Two post-modifications brought distinct functions to the surface. PS was first biotinized and then biotin-vitronectin was grafted *via* avidin. Other parallel Ormocomp lines were functionalized with fibronectin.

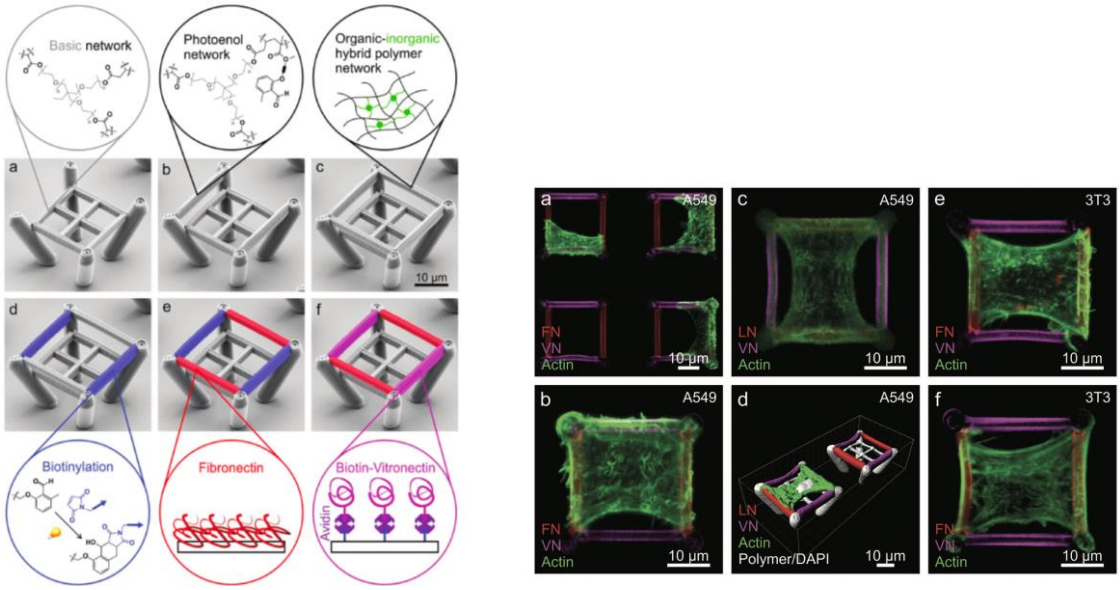

Figure 1.52 Functionalized 3D structures (left) and the cell behavior on the structures (right)[166]

The cell incubation results on the functionalized 3D structures showed the selected adhesion behaviors. The interaction of ECM components with molecules on cells surface mainly involve the four ECM proteins, fibronectin, vitronectin, laminin and type IV collagen.[168] Hence, cell preference for fibronectin and vitronectin has a significant impact on cell behavior on the scaffold surface. Epithelial A549 cells had no preference between fibronectin- or vitronectin-modified surfaces, while fibroblasts 3T3 only bound to fibronectin-covered parallel sides. This work provided us with an example to tune the cell behaviors by well-controlled surface properties.

1.4 Summary

Here we introduced some examples of applications of TPP to basic cell biology from the physical cues to chemical sites. The combination of material engineering and structural design expands the range of the application of TPP. The understanding of basic cell biology, like how cells react to the distribution of stiffness, morphology, microtopography, binding sites and physical forces, can be further explored with well-defined surface chemistry.

1.5 References

(1) Todros, S.; Todesco, M.; Bagno, A. Biomaterials and Their Biomedical Applications: From Replacement to Regeneration. *Processes*. MDPI November 1, 2021. https://doi.org/10.3390/pr9111949.

(2) Hench, L. L.; Thompson, I. Twenty-First Century Challenges for Biomaterials. *Journal of the*

Royal Society Interface. Royal Society August 6, 2010, pp S379–S391. https://doi.org/10.1098/rsif.2010.0151.focus.

(3) Holzapfel, B. M.; Reichert, J. C.; Schantz, J. T.; Gbureck, U.; Rackwitz, L.; Nöth, U.; Jakob, F.; Rudert, M.; Groll, J.; Hutmacher, D. W. How Smart Do Biomaterials Need to Be? A Translational Science and Clinical Point of View. *Advanced Drug Delivery Reviews*. April 2013, pp 581–603. https://doi.org/10.1016/j.addr.2012.07.009.

(4) Huang, G.; Li, F.; Zhao, X.; Ma, Y.; Li, Y.; Lin, M.; Jin, G.; Lu, T. J.; Genin, G. M.; Xu, F. Functional and Biomimetic Materials for Engineering of the Three-Dimensional Cell Microenvironment. *Chem. Rev.* **2017**, *117* (20), 12764–12850. https://doi.org/10.1021/acs.chemrev.7b00094.

(5) Bettinger, C. J. Biodegradable Elastomers for Tissue Engineering and Cell-Biomaterial Interactions. *Macromol. Biosci.* **2011**, *11* (4), 467–482. https://doi.org/10.1002/mabi.201000397.

(6) Flemming, R. G.; Murphy, C. J.; Abrams, G. A.; Goodman, S. L.; Nealey, P. F. Effects of Synthetic Micro- and Nano-Structured Surfaces on Cell Behavior. *Biomaterials* **1999**, *20* (6), 573–588. https://doi.org/10.1016/S0142-9612(98)00209-9.

(7) Wood, A. Contact Guidance on Microfabricated Substrata: The Response of Teleost Fin Mesenchyme Cells to Repeating Topographical Patterns. *J. Cell Sci.* **1988**, *90*, 667–681. https://doi.org/10.1242/jcs.90.4.667.

(8) Koroleva, A.; Deiwick, A.; Nguyen, A.; Schlie-Wolter, S.; Narayan, R.; Timashev, P.; Popov, V.; Bagratashvili, V.; Chichkov, B. Osteogenic Differentiation of Human Mesenchymal Stem Cells in 3-D Zr-Si Organic-Inorganic Scaffolds Produced by Two-Photon Polymerization Technique. *PLoS One* **2015**, *10* (2), 1–18. https://doi.org/10.1371/journal.pone.0118164.

(9) Tay, C. Y.; Yu, H.; Pal, M.; Leong, W. S.; Tan, N. S.; Ng, K. W.; Leong, D. T.; Tan, L. P. Micropatterned Matrix Directs Differentiation of Human Mesenchymal Stem Cells towards Myocardial Lineage. *Exp. Cell Res.* **2010**, *316* (7), 1159–1168. https://doi.org/10.1016/j.yexcr.2010.02.010.

(10) Ann Dalton, B.; Frank Walboomers, X.; Dziegielewski, M.; Evans, M. D. M.; Taylor, S.; Jansen, J. A.; Steele, J. G. Modulation of Epithelial Tissue and Cell Migration by Microgrooves. *J. Biomed. Mater. Res.* **2001**, *56* (2), 195–207. https://doi.org/10.1002/1097-4636(200108)56:2<195::AID-JBM1084>3.0.CO;2-7.

(11) Teixeira, A. I.; Abrams, G. A.; Bertics, P. J.; Murphy, C. J.; Nealey, P. F. Epithelial Contact Guidance on Well-Defined Micro- and Nanostructured Substrates. *J. Cell Sci.* **2003**, *116* (10), 1881–1892. https://doi.org/10.1242/jcs.00383.

(12) Au, A. K.; Huynh, W.; Horowitz, L. F.; Folch, A. 3D-Printed Microfluidics. *Angew. Chemie Int. Ed.* **2016**, *55* (12), 3862–3881. https://doi.org/10.1002/anie.201504382.

(13) Au, A. K.; Bhattacharjee, N.; Horowitz, L. F.; Chang, T. C.; Folch, A. 3D-Printed Microfluidic Automation. *Lab Chip* **2015**, *15* (8), 1934–1941. https://doi.org/10.1039/C5LC00126A.

(14) Ovsianikov, A.; Doraiswamy, A.; Narayan, R.; Chichkov, B. N. Two-Photon Polymerization for Fabrication of Biomedical Devices. *Microfluid. BioMEMS, Med. Microsystems V* **2007**, *6465*, 64650O. https://doi.org/10.1117/12.699979.

(15) Li, B.; Gil, B.; Power, M.; Gao, A.; Treratanakulchai, S.; Anastasova, S.; Yang, G. Z. Carbon-Nanotube-Coated 3D Microspring Force Sensor for Medical Applications. *ACS Appl. Mater. Interfaces* **2019**, *11* (39), 35577–35586. https://doi.org/10.1021/acsami.9b12237.

(16) Palo, M.; Holländer, J.; Suominen, J.; Yliruusi, J.; Sandler, N. 3D Printed Drug Delivery Devices: Perspectives and Technical Challenges. *Expert Rev. Med. Devices* **2017**, *14* (9), 685–696. https://doi.org/10.1080/17434440.2017.1363647.

(17) Luo, Y.; Lin, X.; Huang, P. 3D Bioprinting of Artificial Tissues: Construction of Biomimetic Microstructures. *Macromol. Biosci.* **2018**, *18* (6), 1800034. https://doi.org/10.1002/mabi.201800034.

(18) Koroleva, A.; Gill, A. A.; Ortega, I.; Haycock, J. W.; Schlie, S.; Gittard, S. D.; Chichkov, B. N.; Claeyssens, F. Two-Photon Polymerization-Generated and Micromolding-Replicated 3D Scaffolds for Peripheral Neural Tissue Engineering Applications. *Biofabrication* **2012**, *4* (2), 025005. https://doi.org/10.1088/1758-5082/4/2/025005.

(19) Wang, Y.; Li, X.; Fan, S.; Feng, X.; Cao, K.; Ge, Q.; Gao, L.; Lu, Y. Three-Dimensional Stretchable Microelectronics by Projection Microstereolithography (PμSL). *ACS Appl. Mater. Interfaces* **2021**, *13* (7), 8901–8908. https://doi.org/10.1021/acsami.0c20162.

(20) Chou, S. Y.; Krauss, P. R.; Renstrom, P. J. Nanoimprint Lithography. *J. Vac. Sci. Technol. B Microelectron. Nanom. Struct. Process. Meas. Phenom.* **1996**, *14* (6), 4129–4133. https://doi.org/10.1116/1.588605.

(21) Zlobin, V. A. Development of Electron Beam Lithography for Nanoscale Devices. In *Opto-Ireland 2005: Nanotechnology and Nanophotonics*; Blau, W. J., Kennedy, D., Colreavy, J., Eds.; 2005; Vol. 5824, pp 23–32. https://doi.org/10.1117/12.604662.

(22) Yu, Y.; Hua, S.; Yang, M.; Fu, Z.; Teng, S.; Niu, K.; Zhao, Q.; Yi, C. Fabrication and Characterization of Electrospinning/3D Printing Bone Tissue Engineering Scaffold. *RSC Adv.* **2016**, *6* (112), 110557–110565. https://doi.org/10.1039/C6RA17718B.

(23) Clark, E. A.; Alexander, M. R.; Irvine, D. J.; Roberts, C. J.; Wallace, M. J.; Sharpe, S.; Yoo, J.;

Hague, R. J. M.; Tuck, C. J.; Wildman, R. D. 3D Printing of Tablets Using Inkjet with UV Photoinitiation. *Int. J. Pharm.* **2017**, *529* (1–2), 523–530. https://doi.org/10.1016/j.ijpharm.2017.06.085.

(24) Drobizhev, M.; Makarov, N. S.; Tillo, S. E.; Hughes, T. E.; Rebane, A. Two-Photon Absorption Properties of Fluorescent Proteins. *Nat. Methods* **2011**, *8* (5), 393–399. https://doi.org/10.1038/nmeth.1596.

(25) Fourkas, J. Multiphoton Lithography, Processing and Fabrication of Photonic Structures. In *Laser Growth and Processing of Photonic Devices*; Elsevier, 2012; pp 139–161. https://doi.org/10.1533/9780857096227.2.137.

(26) Göppert-Mayer, M. Über Elementarakte Mit Zwei Quantensprüngen. *Ann. Phys.* **1931**, *401* (3), 273–294. https://doi.org/10.1002/andp.19314010303.

(27) Kaiser, W.; Garrett, C. G. B. Two-Photon Excitation in CaF2: Eu2+. *Phys. Rev. Lett.* **1961**, *7* (6), 229–231. https://doi.org/10.1103/PhysRevLett.7.229.

(28) Rumi, M.; Perry, J. W. Two-Photon Absorption: An Overview of Measurements and Principles. *Adv. Opt. Photonics* **2010**, *2* (4), 451–518. https://doi.org/10.1364/AOP.2.000451.

(29) Xing, J.; Liu, J.; Zhang, T.; Zhang, L.; Zheng, M.; Duan, X. A Water Soluble Initiator Prepared through Host-Guest Chemical Interaction for Microfabrication of 3D Hydrogels via Two-Photon Polymerization. *J. Mater. Chem. B* **2014**, *2* (27), 4318–4323. https://doi.org/10.1039/c4tb00414k.

(30) Zhou, X.; Hou, Y.; Lin, J. A Review on the Processing Accuracy of Two-Photon Polymerization. *AIP Adv.* **2015**, *5* (3), 030701. https://doi.org/10.1063/1.4916886.

(31) Stankevičius, E.; Daugnoraite, E.; Račiukaitis, G. Photopolymerization Differences by Using Nanosecond and Picosecond Laser Pulses. *2018 Conf. Lasers Electro-Optics, CLEO 2018 - Proc.* **2018**, *25* (5), 4819–4830. https://doi.org/10.1364/oe.25.004819.

(32) Gittard, S. D.; Nguyen, A.; Obata, K.; Koroleva, A.; Narayan, R. J.; Chichkov, B. N. Fabrication of Microscale Medical Devices by Two-Photon Polymerization with Multiple Foci via a Spatial Light Modulator. *Biomed. Opt. Express* **2011**, *2* (11), 3167. https://doi.org/10.1364/BOE.2.003167.

(33) Jokanovic, V.; Trisic, D.; Zivkovic, M. Review of Lasers Application in Dentistry. *Stomatol. Glas. Srb.* **2020**, *67* (1), 36–49. https://doi.org/10.2298/sgs2001036j.

(34) Kawata, S.; Sun, H.-B.; Tanaka, T.; Takada, K. Finer Features for Functional Microdevices. *Nature* **2001**, *412* (6848), 697–698. https://doi.org/10.1038/35089130.

(35) Sun, H. B.; Takada, K.; Kim, M. S.; Lee, K. S.; Kawata, S. Scaling Laws of Voxels in Two-Photon Photopolymerization Nanofabrication. *Appl. Phys. Lett.* **2003**, *83* (6), 1104–1106.

https://doi.org/10.1063/1.1599968.

(36) Sun, H. B.; Tanaka, T.; Kawata, S. Three-Dimensional Focal Spots Related to Two-Photon Excitation. *Appl. Phys. Lett.* **2002**, *80* (20), 3673–3675. https://doi.org/10.1063/1.1478128.

(37) Sun, H. B.; Maeda, M.; Takada, K.; Chon, J. W. M.; Gu, M.; Kawata, S. Experimental Investigation of Single Voxels for Laser Nanofabrication via Two-Photon Photopolymerization. *Appl. Phys. Lett.* **2003**, *83* (5), 819–821. https://doi.org/10.1063/1.1598293.

(38) Li, S.; Liu, X.; Zhang, S.; Zhou, Y.; Wan, X.; Li, N.; Li, J.; Zhang, L. D–π–A–π–D Initiators Based on Benzophenone Conjugate Extension for Two-Photon Polymerization Additive Manufacturing. *Photonics* **2022**, *9* (3), 183. https://doi.org/10.3390/photonics9030183.

(39) Tomal, W.; Ortyl, J. Water-Soluble Photoinitiators in Biomedical Applications. *Polymers (Basel).* **2020**, *12* (5), 1–30. https://doi.org/10.3390/POLYM12051073.

(40) Gruber, H. F. Photoinitiators for Free Radical Polymerization. *Prog. Polym. Sci.* **1992**, *17* (6), 953–1044. https://doi.org/10.1016/0079-6700(92)90006-K.

(41) Fouassier, J. P.; Lalevée, J. Multicomponent Photoinitiating Systems. In *Photoinitiators for Polymer Synthesis*; Wiley-VCH Verlag GmbH & Co. KGaA: Weinheim, Germany, 2012; pp 269–282. https://doi.org/10.1002/9783527648245.ch10.

(42) Schafer, K. J.; Hales, J. M.; Balu, M.; Belfield, K. D.; Van Stryland, E. W.; Hagan, D. J. Two-Photon Absorption Cross-Sections of Common Photoinitiators. *J. Photochem. Photobiol. A Chem.* **2004**, *162* (2–3), 497–502. https://doi.org/10.1016/S1010-6030(03)00394-0.

(43) Negres, R. A.; Hales, J. M.; Kobyakov, A.; Hagan, D. J.; Van Stryland, E. W. Two-Photon Spectroscopy and Analysis with a White-Light Continuum Probe. *Opt. Lett.* **2002**, *27* (4), 270–272. https://doi.org/10.1364/ol.27.000270.

(44) Ajami, A.; Husinsky, W.; Liska, R.; Pucher, N. Two-Photon Absorption Cross Section Measurements of Various Two-Photon Initiators for Ultrashort Laser Radiation Applying the Z-Scan Technique. *J. Opt. Soc. Am. B* **2010**, *27* (11), 2290. https://doi.org/10.1364/josab.27.002290.

(45) Torgersen, J. Efficient Photoinitiators for Two-Photon Polymerization. In *Photocured Materials*; The Royal Society of Chemistry, 2014; Vol. 2015-Janua, pp 75–86. https://doi.org/10.1039/9781782620075-00075.

(46) Dudek, M.; Tarnowicz-Staniak, N.; Deiana, M.; Pokładek, Z.; Samoć, M.; Matczyszyn, K. Two-Photon Absorption and Two-Photon-Induced Isomerization of Azobenzene Compounds. *RSC Advances*. Royal Society of Chemistry November 1, 2020, pp 40489–40507. https://doi.org/10.1039/d0ra07693g.

(47) Albota, M.; Beljonne, D.; Brédas, J.-L.; Ehrlich, J. E.; Fu, J.-Y.; Heikal, A. A.; Hess, S. E.; Kogej,

T.; Levin, M. D.; Marder, S. R.; McCord-Maughon, D.; Perry, J. W.; Röckel, H.; Rumi, M.; Subramaniam, G.; Webb, W. W.; Wu, X.-L.; Xu, C. Design of Organic Molecules with Large Two-Photon Absorption Cross Sections. *Science (80-.).* **1998**, *281* (5383), 1653–1656. https://doi.org/10.1126/science.281.5383.1653.

(48) Whitby, R.; Ben-Tal, Y.; MacMillan, R.; Janssens, S.; Raymond, S.; Clarke, D.; Jin, J.; Kay, A.; Simpson, M. C. Photoinitiators for Two-Photon Polymerisation: Effect of Branching and Viscosity on Polymerisation Thresholds. *RSC Adv.* **2017**, *7* (22), 13232–13239. https://doi.org/10.1039/c6ra27176f.

(49) Pawlicki, M.; Collins, H. A.; Denning, R. G.; Anderson, H. L. Two-Photon Absorption and the Design of Two-Photon Dyes. *Angew. Chemie - Int. Ed.* **2009**, *48* (18), 3244–3266. https://doi.org/10.1002/anie.200805257.

(50) Li, Z.; Siklos, M.; Pucher, N.; Cicha, K.; Ajami, A.; Husinsky, W.; Rosspeintner, A.; Vauthey, E.; Gescheidt, G.; Stampfl, J.; Liska, R. Synthesis and Structure-Activity Relationship of Several Aromatic Ketone-Based Two-Photon Initiators. *J. Polym. Sci. Part A Polym. Chem.* **2011**, *49* (17), 3688–3699. https://doi.org/10.1002/pola.24806.

(51) Rumi, M.; Ehrlich, J. E.; Heikal, A. A.; Perry, J. W.; Barlow, S.; Hu, Z.; McCord-Maughon, D.; Parker, T. C.; Röckel, H.; Thayumanavan, S.; Marder, S. R.; Beljonne, D.; Brédas, J. L. Structure - Property Relationships for Two-Photon Absorbing Chromophores: Bis-Donor Diphenylpolyene and Bis(Styryl)Benzene Derivatives. *J. Am. Chem. Soc.* **2000**, *122* (39), 9500–9510. https://doi.org/10.1021/ja994497s.

(52) https://cleanenergywiki.org/index.php?title=Two_Photon_Absorption#Measuring_the_Two-Photon_Absorption_Cross_Section.

(53) Richter, B.; Hahn, V.; Bertels, S.; Claus, T. K.; Wegener, M.; Delaittre, G.; Barner-Kowollik, C.; Bastmeyer, M. Guiding Cell Attachment in 3D Microscaffolds Selectively Functionalized with Two Distinct Adhesion Proteins. *Adv. Mater.* **2017**, *29* (5). https://doi.org/10.1002/adma.201604342.

(54) Hafner, J.; Grijalva, D.; Ludwig-Husemann, A.; Bertels, S.; Bensinger, L.; Raic, A.; Gebauer, J.; Oelschlaeger, C.; Bastmeyer, M.; Bieback, K.; Lee-Thedieck, C.; Willenbacher, N. Monitoring Matrix Remodeling in the Cellular Microenvironment Using Microrheology for Complex Cellular Systems. *Acta Biomater.* **2020**, *111*, 254–266. https://doi.org/10.1016/j.actbio.2020.04.053.

(55) Jhaveri, S. J.; McMullen, J. D.; Sijbesma, R.; Tan, L. S.; Zipfel, W.; Ober, C. K. Direct Three-Dimensional Microfabrication of Hydrogels via Two-Photon Lithography in Aqueous Solution. *Chem. Mater.* **2009**, *21* (10), 2003–2006. https://doi.org/10.1021/cm803174e.

(56) Williams, C. G.; Malik, A. N.; Kim, T. K.; Manson, P. N.; Elisseeff, J. H. Variable Cytocompatibility of Six Cell Lines with Photoinitiators Used for Polymerizing Hydrogels and Cell Encapsulation. *Biomaterials* **2005**, *26* (11), 1211–1218. https://doi.org/10.1016/j.biomaterials.2004.04.024.

(57) Eren, T. N.; Kariksiz, N.; Demirci, G.; Tuncel, D.; Okte, N.; Yagci Acar, H.; Avci, D. Irgacure 2959-Functionalized Poly(Ethyleneimine)s as Improved Photoinitiators: Enhanced Water Solubility, Migration Stability and Visible-Light Operation. *Polym. Chem.* **2021**, *12* (18), 2772–2785. https://doi.org/10.1039/d1py00298h.

(58) Sun, F.; Li, Y.; Zhang, N.; Nie, J. Initiating Gradient Photopolymerization and Migration of a Novel Polymerizable Polysiloxane α-Hydroxy Alkylphenones Photoinitiator. *Polymer (Guildf).* **2014**, *55* (16), 3656–3665. https://doi.org/10.1016/j.polymer.2014.06.040.

(59) Wang, J.; Stanic, S.; Altun, A. A.; Schwentenwein, M.; Dietliker, K.; Jin, L.; Stampfl, J.; Baudis, S.; Liska, R.; Grützmacher, H. A Highly Efficient Waterborne Photoinitiator for Visible-Light-Induced Three-Dimensional Printing of Hydrogels. *Chem. Commun.* **2018**, *54* (8), 920–923. https://doi.org/10.1039/c7cc09313f.

(60) Wang, J.; Siqueira, G.; Müller, G.; Rentsch, D.; Huch, A.; Tingaut, P.; Levalois-Grützmacher, J.; Grützmacher, H. Synthesis of New Bis(Acyl)Phosphane Oxide Photoinitiators for the Surface Functionalization of Cellulose Nanocrystals. *Chem. Commun.* **2016**, *52* (13), 2823–2826. https://doi.org/10.1039/C5CC09760F.

(61) Benedikt, S.; Wang, J.; Markovic, M.; Moszner, N.; Dietliker, K.; Ovsianikov, A.; Grützmacher, H.; Liska, R. Highly Efficient Water-Soluble Visible Light Photoinitiators. *J. Polym. Sci. Part A Polym. Chem.* **2016**, *54* (4), 473–479. https://doi.org/10.1002/pola.27903.

(62) Le, C. M. Q.; Petitory, T.; Wu, X.; Spangenberg, A.; Ortyl, J.; Galek, M.; Infante, L.; Thérien-Aubin, H.; Chemtob, A. Water-Soluble Photoinitiators from Dimethylamino-Substituted Monoacylphosphine Oxide for Hydrogel and Latex Preparation. *Macromol. Chem. Phys.* **2021**, *222* (19), 1–10. https://doi.org/10.1002/macp.202100217.

(63) Kim, S. H.; Chu, C. C. Visible Light Induced Dextran-Methacrylate Hydrogel Formation Using (-)-Riboflavin Vitamin B2 as a Photoinitiator and L-Arginine as a Co-Initiator. *Fibers Polym.* **2009**, *10* (1), 14–20. https://doi.org/10.1007/s12221-009-0014-z.

(64) Turunen, S.; Käpylä, E.; Terzaki, K.; Viitanen, J.; Fotakis, C.; Kellomäki, M.; Farsari, M. Pico- and Femtosecond Laser-Induced Crosslinking of Protein Microstructures: Evaluation of Processability and Bioactivity. *Biofabrication* **2011**, *3* (4), 045002. https://doi.org/10.1088/1758-5082/3/4/045002.

(65) Serien, D.; Sugioka, K. Three-Dimensional Printing of Pure Proteinaceous Microstructures by

Femtosecond Laser Multiphoton Cross-Linking. *ACS Biomater. Sci. Eng.* **2020**, *6* (2), 1279–1287. https://doi.org/10.1021/acsbiomaterials.9b01619.

(66) Campagnola, P. J.; Delguidice, D. M.; Epling, G. A.; Hoffacker, K. D.; Howell, A. R.; Pitts, J. D.; Goodman, S. L. 3-Dimensional Submicron Polymerization of Acrylamide By Multiphoton Excitation of Xanthene Dyes. *Macromolecules* **2000**, *33* (5), 1511–1513. https://doi.org/10.1021/ma991042e.

(67) Serien, D.; Sugioka, K. Fabrication of Three-Dimensional Proteinaceous Micro- and Nano-Structures by Femtosecond Laser Cross-Linking. *Opto-Electronic Adv.* **2018**, *1* (4), 1–18. https://doi.org/10.29026/oea.2018.180008.

(68) Basu, S.; Rodionov, V.; Terasaki, M.; Campagnola, P. J. Multiphoton-Excited Microfabrication in Live Cells via Rose Bengal Cross-Linking of Cytoplasmic Proteins. *Opt. Lett.* **2005**, *30* (2), 159–161. https://doi.org/10.1364/ol.30.000159.

(69) Geng, J.; Li, W.; Zhang, Y.; Thottappillil, N.; Clavadetscher, J.; Lilienkampf, A.; Bradley, M. Radical Polymerization inside Living Cells. *Nat. Chem.* **2019**, *11* (6), 578–586. https://doi.org/10.1038/s41557-019-0240-y.

(70) Sun, Y. L.; Dong, W. F.; Yang, R. Z.; Meng, X.; Zhang, L.; Chen, Q. D.; Sun, H. B. Dynamically Tunable Protein Microlenses. *Angew. Chemie - Int. Ed.* **2012**, *51* (7), 1558–1562. https://doi.org/10.1002/anie.201105925.

(71) Basu, S.; Cunningham, L. P.; Pins, G. D.; Bush, K. A.; Taboada, R.; Howell, A. R.; Wang, J.; Campagnola, P. J. Multiphoton Excited Fabrication of Collagen Matrixes Cross-Linked by a Modified Benzophenone Dimer: Bioactivity and Enzymatic Degradation. *Biomacromolecules* **2005**, *6* (3), 1465–1474. https://doi.org/10.1021/bm049258y.

(72) Park, S. H.; Lim, T. W.; Yang, D.-Y.; Kim, R. H.; Lee, K.-S. Improvement of Spatial Resolution in Nano-Stereolithography Using Radical Quencher. *Macromol. Res.* **2006**, *14* (5), 559–564. https://doi.org/10.1007/BF03218724.

(73) Purtov, J.; Verch, A.; Rogin, P.; Hensel, R. Improved Development Procedure to Enhance the Stability of Microstructures Created by Two-Photon Polymerization. *Microelectron. Eng.* **2018**, *194* (March), 45–50. https://doi.org/10.1016/j.mee.2018.03.009.

(74) Arscott, S. SU-8 as a Material for Lab-on-a-Chip-Based Mass Spectrometry. *Lab Chip* **2014**, *14* (19), 3668–3689. https://doi.org/10.1039/c4lc00617h.

(75) Liu, C.; Liu, Y.; Sokuler, M.; Fell, D.; Keller, S.; Boisen, A.; Butt, H. J.; Auernhammer, G. K.; Bonaccurso, E. Diffusion of Water into SU-8 Microcantilevers. *Phys. Chem. Chem. Phys.* **2010**, *12* (35), 10577–10583. https://doi.org/10.1039/c002478c.

(76) Haas, K. H.; Wolter, H. Synthesis, Properties and Applications of Inorganic-Organic Copolymers (ORMOCER®s). *Curr. Opin. Solid State Mater. Sci.* **1999**, *4* (6), 571–580. https://doi.org/10.1016/S1359-0286(00)00009-7.

(77) Skoog, S. A.; Nguyen, A. K.; Kumar, G.; Zheng, J.; Goering, P. L.; Koroleva, A.; Chichkov, B. N.; Narayan, R. J. Two-Photon Polymerization of 3-D Zirconium Oxide Hybrid Scaffolds for Long-Term Stem Cell Growth. *Biointerphases* **2014**, *9* (2), 029014. https://doi.org/10.1116/1.4873688.

(78) Mačiulaitis, J.; Deveikyte, M.; Rekštyte, S.; Bratchikov, M.; Darinskas, A.; Šimbelyte, A.; Daunoras, G.; Laurinavičiene, A.; Laurinavičius, A.; Gudas, R.; Malinauskas, M.; Mačiulaitis, R. Preclinical Study of SZ2080 Material 3D Microstructured Scaffolds for Cartilage Tissue Engineering Made by Femtosecond Direct Laser Writing Lithography. *Biofabrication* **2015**, *7* (1). https://doi.org/10.1088/1758-5090/7/1/015015.

(79) Seniutinas, G.; Weber, A.; Padeste, C.; Sakellari, I.; Farsari, M.; David, C. Beyond 100 nm Resolution in 3D Laser Lithography — Post Processing Solutions. *Microelectron. Eng.* **2018**, *191*, 25–31. https://doi.org/10.1016/j.mee.2018.01.018.

(80) Desponds, A.; Banyasz, A.; Montagnac, G.; Andraud, C.; Baldeck, P.; Parola, S. Microfabrication by Two-Photon Lithography, and Characterization, of SiO2/TiO2 Based Hybrid and Ceramic Microstructures. *J. Sol-Gel Sci. Technol.* **2020**, *95* (3), 733–745. https://doi.org/10.1007/s10971-020-05355-3.

(81) *Norland Products Incorporated Safety Data Sheet and SDS Information NOA 61*; 2022. https://www.norlandprod.com/adhesives/NOA 61.html.

(82) Klein, F.; Striebel, T.; Fischer, J.; Jiang, Z.; Franz, C. M.; Von Freymann, G.; Wegener, M.; Bastmeyer, M. Elastic Fully Three-Dimensional Microstructure Scaffolds for Cell Force Measurements. *Adv. Mater.* **2010**, *22* (8), 868–871. https://doi.org/10.1002/adma.200902515.

(83) Klein, F.; Richter, B.; Striebel, T.; Franz, C. M.; Freymann, G. Von; Wegener, M.; Bastmeyer, M. Two-Component Polymer Scaffolds for Controlled Three-Dimensional Cell Culture. *Adv. Mater.* **2011**, *23* (11), 1341–1345. https://doi.org/10.1002/adma.201004060.

(84) Kolb, H. C.; Finn, M. G.; Sharpless, K. B. Click Chemistry: Diverse Chemical Function from a Few Good Reactions. *Angew. Chemie - Int. Ed.* **2001**, *40* (11), 2004–2021. https://doi.org/10.1002/1521-3773(20010601)40:11<2004::AID-ANIE2004>3.0.CO;2-5.

(85) Xi, W.; Scott, T. F.; Kloxin, C. J.; Bowman, C. N. Click Chemistry in Materials Science. *Adv. Funct. Mater.* **2014**, *24* (18), 2572–2590. https://doi.org/10.1002/adfm.201302847.

(86) Krizhanovskiy, I.; Temnikov, M.; Kononevich, Y.; Anisimov, A.; Drozdov, F.; Muzafarov, A.

The Use of the Thiol-Ene Addition Click Reaction in the Chemistry of Organosilicon Compounds: An Alternative or a Supplement to the Classical Hydrosilylation? *Polymers (Basel).* **2022**, *14* (15). https://doi.org/10.3390/polym14153079.

(87) Carlborg, C. F.; Haraldsson, T.; Öberg, K.; Malkoch, M.; Van Der Wijngaart, W. Beyond PDMS: Off-Stoichiometry Thiol-Ene (OSTE) Based Soft Lithography for Rapid Prototyping of Microfluidic Devices. *Lab Chip* **2011**, *11* (18), 3136–3147. https://doi.org/10.1039/c1lc20388f.

(88) Hoyle, C. E.; Bowman, C. N. Thiol-Ene Click Chemistry. *Angew. Chemie - Int. Ed.* **2010**, *49* (9), 1540–1573. https://doi.org/10.1002/anie.200903924.

(89) Sandström, N.; Shafagh, R. Z.; Vastesson, A.; Carlborg, C. F.; Van Der Wijngaart, W.; Haraldsson, T. Reaction Injection Molding and Direct Covalent Bonding of OSTE+ Polymer Microfluidic Devices. *J. Micromechanics Microengineering* **2015**, *25* (7), 075002. https://doi.org/10.1088/0960-1317/25/7/075002.

(90) INTEGRATION WITH MICROARRAYS 25 ˚ C. **2011**, No. microTAS, 311–313.

(91) Saharil, F.; Gylfason, K. B.; Liu, Y.; Haraldsson, T.; Bettotti, P.; Kumar, N.; Van Der Wijngaart, W. Dry Transfer Bonding of Porous Silicon Membranes to OSTE(+) Polymer Microfluidic Devices. *Proc. IEEE Int. Conf. Micro Electro Mech. Syst.* **2012**, No. February, 232–234. https://doi.org/10.1109/MEMSYS.2012.6170133.

(92) Errando-Herranz, C.; Vastesson, A.; Zelenina, M.; Pardon, G.; Bergström, G.; Van Der Wijngaart, W.; Haraldson, T.; Brismar, H.; Gylfason, K. B. Biocompatibility of OSTE Polymers Studied by Cell Growth Experiments. *17th Int. Conf. Miniaturized Syst. Chem. Life Sci. MicroTAS 2013* **2013**, *1*, 143–145.

(93) Hoffmann, A.; Leonards, H.; Tobies, N.; Pongratz, L.; Kreuels, K.; Kreimendahl, F.; Apel, C.; Wehner, M.; Nottrodt, N. New Stereolithographic Resin Providing Functional Surfaces for Biocompatible Three-Dimensional Printing. *J. Tissue Eng.* **2017**, *8*, 204173141774448. https://doi.org/10.1177/2041731417744485.

(94) Paull, K. D.; Shoemaker, R. H.; Boyd, M. R.; Parsons, J. L.; Risbood, P. A.; Barbera, W. A.; Sharma, M. N.; Baker, D. C.; Hand, E.; Scudiero, D. A.; Monks, A.; Alley, M. C.; Grote, M. The Synthesis of XTT: A New Tetrazolium Reagent That Is Bioreducible to a Water-soluble Formazan. *Journal of Heterocyclic Chemistry*. 1988, pp 911–914. https://doi.org/10.1002/jhet.5570250340.

(95) Ejserholm, F.; Stegmayr, J.; Bauer, P.; Johansson, F.; Wallman, L.; Bengtsson, M.; Oredsson, S. Biocompatibility of a Polymer Based on Off-Stoichiometry Thiol-Enes + Epoxy (OSTE+) for Neural Implants. *Biomater. Res.* **2015**, *19* (1), 1–10. https://doi.org/10.1186/s40824-015-0041-3.

(96) Hoyle, C. E.; Lowe, A. B.; Bowman, C. N. Thiol-Click Chemistry: A Multifaceted Toolbox for Small Molecule and Polymer Synthesis. *Chem. Soc. Rev.* **2010**, *39* (4), 1355–1387. https://doi.org/10.1039/b901979k.

(97) Vastesson, A. Thiol–Ene and Thiol-Ene-Epoxy Based Polymers for Biomedical Microdevices, KTH Royal Institite of technology, 2017.

(98) Lafleur, J. P.; Kwapiszewski, R.; Jensen, T. G.; Kutter, J. P. Rapid Photochemical Surface Patterning of Proteins in Thiol-Ene Based Microfluidic Devices. *Analyst* **2013**, *138* (3), 845–849. https://doi.org/10.1039/c2an36424g.

(99) Feidenhans'l, N. A.; Lafleur, J. P.; Jensen, T. G.; Kutter, J. P. Surface Functionalized Thiol-Ene Waveguides for Fluorescence Biosensing in Microfluidic Devices. *Electrophoresis* **2014**, *35* (2–3), 282–288. https://doi.org/10.1002/elps.201300271.

(100) Guo, W. Synthetic Paper for Point-of-Care Diagnostics Capillary Control, Surface Modifications, and Their Applications., KTH Royal Institute of Technology, 2020.

(101) Zhang, J.; Chen, Y.; Brook, M. A. Facile Functionalization of PDMS Elastomer Surfaces Using Thiol-Ene Click Chemistry. *Langmuir* **2013**, *29* (40), 12432–12442. https://doi.org/10.1021/la403425d.

(102) Bourg, S.; D'Orlyé, F.; Griveau, S.; Bedioui, F.; da Silva, J. A. F.; Varenne, A. Multiple Zones Modification of Open Off-Stoichiometry Thiol-Ene Microchannel by Aptamers: A Methodological Study & a Proof of Concept. *Chemosensors* **2020**, *8* (24). https://doi.org/10.3390/CHEMOSENSORS8020024.

(103) Oberleitner, B.; Dellinger, A.; Déforet, M.; Galtayries, A. 2013-CC+.Pdf. **2013**.

(104) Liu, Y.; Hou, W.; Sun, H.; Cui, C.; Zhang, L.; Jiang, Y.; Wu, Y.; Wang, Y.; Li, J.; Sumerlin, B. S.; Liu, Q.; Tan, W. Thiol-Ene Click Chemistry: A Biocompatible Way for Orthogonal Bioconjugation of Colloidal Nanoparticles. *Chem. Sci.* **2017**, *8* (9), 6182–6187. https://doi.org/10.1039/c7sc01447c.

(105) Alonso, R.; Jiménez-Meneses, P.; García-Rupérez, J.; Bañuls, M. J.; Maquieira, Á. Thiol-Ene Click Chemistry towards Easy Microarraying of Half-Antibodies. *Chemical Communications*. 2018, pp 6144–6147. https://doi.org/10.1039/c8cc01369a.

(106) Xiong, W.; Liu, Y.; Jiang, L. J.; Zhou, Y. S.; Li, D. W.; Jiang, L.; Silvain, J. F.; Lu, Y. F. Laser-Directed Assembly of Aligned Carbon Nanotubes in Three Dimensions for Multifunctional Device Fabrication. *Adv. Mater.* **2016**, *28* (10), 2002–2009. https://doi.org/10.1002/adma.201505516.

(107) Abascal, N. C.; Regan, L. The Past, Present and Future of Protein-Based Materials. *Open Biol.*

2018, *8* (10), 180113. https://doi.org/10.1098/rsob.180113.

(108) Saha, S.; Arshad, M.; Zubair, M.; Ullah, A. *Keratin as a Biopolymer*; Springer International Publishing, 2019. https://doi.org/10.1007/978-3-030-02901-2_6.

(109) Prabhu, N.; Sharp, K. Protein-Solvent Interactions. *Chem. Rev.* **2006**, *106* (5), 1616–1623. https://doi.org/10.1021/cr040437f.

(110) Serien, D.; Takeuchi, S. Fabrication of Submicron Proteinaceous Structures by Direct Laser Writing. *Appl. Phys. Lett.* **2015**, *107* (1), 10–15. https://doi.org/10.1063/1.4926659.

(111) EBASHI, S.; KOGA, R. The Use of Dimethyl Sulfoxide(DMSO) for Protein Fractionation. *Proc. Japan Acad. Ser. B* **1988**, *64* (10), 323–326. https://doi.org/10.2183/pjab.64.323.

(112) Spivey, E. C.; Ritschdorff, E. T.; Connell, J. L.; McLennon, C. A.; Schmidt, C. E.; Shear, J. B. Multiphoton Lithography of Unconstrained Three-Dimensional Protein Microstructures. *Adv. Funct. Mater.* **2013**, *23* (3), 333–339. https://doi.org/10.1002/adfm.201201465.

(113) Pitts, J. D.; Campagnola, P. J.; Epling, G. A.; Goodman, S. L. Submicron Multiphoton Free-Form Fabrication of Proteins and Polymers: Studies of Reaction Efficiencies and Applications in Sustained Release. *Macromolecules* **2000**, *33* (5), 1514–1523. https://doi.org/10.1021/ma9910437.

(114) Branch, D. R. Anti-A and Anti-B: What Are They and Where Do They Come From? *Transfusion* **2015**, *55* (July), S74–S79. https://doi.org/10.1111/trf.13087.

(115) Chen, C. B.; Hammo, B.; Barry, J.; Radhakrishnan, K. Overview of Albumin Physiology and Its Role in Pediatric Diseases. *Curr. Gastroenterol. Rep.* **2021**, *23* (8), 11. https://doi.org/10.1007/s11894-021-00813-6.

(116) Mahmood, T.; Yang, P. C. Western Blot: Technique, Theory, and Trouble Shooting. *N. Am. J. Med. Sci.* **2012**, *4* (9), 429–434. https://doi.org/10.4103/1947-2714.100998.

(117) Jeyachandran, Y. L.; Mielczarski, E.; Rai, B.; Mielczarski, J. A. Quantitative and Qualitative Evaluation of Adsorption/Desorption of Bovine Serum Albumin on Hydrophilic and Hydrophobic Surfaces. *Langmuir* **2009**, *25* (19), 11614–11620. https://doi.org/10.1021/la901453a.

(118) Lunzer, M.; Maryasin, B.; Zandrini, T.; Baudis, S.; Ovsianikov, A.; Liska, R. A Disulfide-Based Linker for Thiol-Norbornene Conjugation: Formation and Cleavage of Hydrogels by the Use of Light. *Polym. Chem.* **2022**, *13* (9), 1158–1168. https://doi.org/10.1039/d1py00914a.

(119) Nandi, R.; Agam, Y.; Amdursky, N. A Protein-Based Free-Standing Proton-Conducting Transparent Elastomer for Large-Scale Sensing Applications. *Adv. Mater.* **2021**, *33* (32), 1–10. https://doi.org/10.1002/adma.202101208.

(120) Chemtob, A.; Feillée, N.; Vaulot, C.; Ley, C.; Le Nouen, D. Self-Photopolymerization of Poly(Disulfide) Oligomers. *ACS Omega* **2019**, *4* (3), 5722–5730. https://doi.org/10.1021/acsomega.9b00021.

(121) Iosin, M.; Stephan, O.; Astilean, S.; Dupperay, A.; Baldeck, P. L. Microstructuration of Protein Matrices by Laser-Induced Photochemistry. *J. Optoelectron. Adv. Mater.* **2007**, *9* (3), 716–720.

(122) Turunen, S.; Käpylä, E.; Terzaki, K.; Viitanen, J.; Fotakis, C.; Kellomäki, M.; Farsari, M. Pico- and Femtosecond Laser-Induced Crosslinking of Protein Microstructures: Evaluation of Processability and Bioactivity. *Biofabrication* **2011**, *3* (4), 045002. https://doi.org/10.1088/1758-5082/3/4/045002.

(123) Kaehr, B.; Shear, J. B. Multiphoton Fabrication of Chemically Responsive Protein Hydrogels for Microactuation. *Proc. Natl. Acad. Sci. U. S. A.* **2008**, *105* (26), 8850–8854. https://doi.org/10.1073/pnas.0709571105.

(124) Serien, D.; Takeuchi, S. Multi-Component Microscaffold with 3D Spatially Defined Proteinaceous Environment. *ACS Biomater. Sci. Eng.* **2017**, *3* (3), 487–494. https://doi.org/10.1021/acsbiomaterials.6b00695.

(125) Shoulders, M. D.; Raines, R. T. Collagen Structure and Stability. *Annu. Rev. Biochem.* **2009**, *78*, 929–958. https://doi.org/10.1146/annurev.biochem.77.032207.120833.

(126) Coradin, T.; Wang, K.; Law, T.; Trichet, L. Type I Collagen-Fibrin Mixed Hydrogels: Preparation, Properties and Biomedical Applications. *Gels* **2020**, *6* (4), 1–22. https://doi.org/10.3390/gels6040036.

(127) Henriksen, K.; Karsdal, M. A. Type I Collagen. In *Biochemistry of Collagens, Laminins and Elastin: Structure, Function and Biomarkers*; Elsevier Inc., 2016; pp 1–11. https://doi.org/10.1016/B978-0-12-809847-9.00001-5.

(128) Song, X.; Li, Z.; Li, Y.; Hou, H. Typical Structure, Biocompatibility, and Cell Proliferation Bioactivity of Collagen from Tilapia and Pacific Cod. *Colloids Surfaces B Biointerfaces* **2022**, *210* (5), 112238. https://doi.org/10.1016/j.colsurfb.2021.112238.

(129) Rittié, L. Type I Collagen Purification from Rat Tail Tendons. *Methods Mol. Biol.* **2017**, *1627*, 287–308. https://doi.org/10.1007/978-1-4939-7113-8_19.

(130) Bell, A.; Kofron, M.; Nistor, V. Multiphoton Crosslinking for Biocompatible 3D Printing of Type I Collagen. *Biofabrication* **2015**, *7* (3), 035007. https://doi.org/10.1088/1758-5090/7/3/035007.

(131) Lamberts, J. J. M.; Neckers, D. C. Rose Bengal and Non-Polar Derivatives: The Birth of Dye Sensitizers for Photooxidation+. *Zeitschrift fur Naturforsch. - Sect. B J. Chem. Sci.* **1984**, *39* (4),

474–484. https://doi.org/10.1515/znb-1984-0412.

(132) Jeong, B.; Kibbey, M. R.; Birnbaum, J. C.; Won, Y. Y.; Gutowska, A. Thermogelling Biodegradable Polymers with Hydrophilic Backbones: PEG-g-PLGA. *Macromolecules* **2000**, *33* (22), 8317–8322. https://doi.org/10.1021/ma000638v.

(133) Miller, J. S.; Shen, C. J.; Legant, W. R.; Baranski, J. D.; Blakely, B. L.; Chen, C. S. Bioactive Hydrogels Made from Step-Growth Derived PEG-Peptide Macromers. *Biomaterials* **2010**, *31* (13), 3736–3743. https://doi.org/10.1016/j.biomaterials.2010.01.058.

(134) Veronese, F. M.; Pasut, G. PEGylation, Successful Approach to Drug Delivery. *Drug Discov. Today* **2005**, *10* (21), 1451–1458. https://doi.org/10.1016/S1359-6446(05)03575-0.

(135) Takahashi, Y.; Tadokoro, H. Structural Studies of Polyethers, (-(CH 2)m-O-) n . X. Crystal Structure of Poly(Ethylene Oxide). *Macromolecules* **1973**, *6* (5), 672–675. https://doi.org/10.1021/ma60035a005.

(136) Alessi, M. L.; Norman, A. I.; Knowlton, S. E.; Ho, D. L.; Greer, S. C. Helical and Coil Conformations of Poly(Ethylene Glycol) in Isobutyric Acid and Water. *Macromolecules* **2005**, *38* (22), 9333–9340. https://doi.org/10.1021/ma051339e.

(137) Huang, L.; Nishinari, K. Interaction between Poly(Ethylene Glycol) and Water as Studied by Differential Scanning Calorimetry. *Journal of Polymer Science, Part B: Polymer Physics*. 2001, pp 496–506. https://doi.org/10.1002/1099-0488(20010301)39:5<496::AID-POLB1023>3.0.CO;2-H.

(138) Abuchowski, A.; McCoy, J. R.; Palczuk, N. C.; van Es, T.; Davis, F. F. Effect of Covalent Attachment of Polyethylene Glycol on Immunogenicity and Circulating Life of Bovine Liver Catalase. *J. Biol. Chem.* **1977**, *252* (11), 3582–3586. https://doi.org/10.1016/s0021-9258(17)40292-4.

(139) Milton Harris, J.; Martin, N. E.; Modi, M. Pegylation: A Novel Process for Modifying Pharmacokinetics. *Clin. Pharmacokinet.* **2001**, *40* (7), 539–551. https://doi.org/10.2165/00003088-200140070-00005.

(140) Estephan, Z. G.; Schlenoff, P. S.; Schlenoff, J. B. Zwitteration as an Alternative to PEGylation. *Langmuir* **2011**, *27* (11), 6794–6800. https://doi.org/10.1021/la200227b.

(141) D'souza, A. A.; Shegokar, R. Polyethylene Glycol (PEG): A Versatile Polymer for Pharmaceutical Applications. *Expert Opin. Drug Deliv.* **2016**, *13* (9), 1257–1275. https://doi.org/10.1080/17425247.2016.1182485.

(142) Minko, S. Characterization of Polymer Surfaces by Wetting and Electrokinetic Measurements - Contact Angle, Interfacial Tension, Zeta Potential. *Grafting Solid Surfaces "Grafting to"*

"Grafting from" Methods **2008**, 103–138. https://doi.org/10.1007/978-3-540-73865-7_6.

(143) Hynninen, V.; Vuori, L.; Hannula, M.; Tapio, K.; Lahtonen, K.; Isoniemi, T.; Lehtonen, E.; Hirsimäki, M.; Toppari, J. J.; Valden, M.; Hytönen, V. P. Improved Antifouling Properties and Selective Biofunctionalization of Stainless Steel by Employing Heterobifunctional Silane-Polyethylene Glycol Overlayers and Avidin-Biotin Technology. *Sci. Rep.* **2016**, *6* (April), 1–12. https://doi.org/10.1038/srep29324.

(144) Harbers, G. M.; Emoto, K.; Greef, C.; Metzger, S. W.; Woodward, H. N.; Mascali, J. J.; Grainger, D. W.; Lochhead, M. J. Functionalized Poly(Ethylene Glycol)-Based Bioassay Surface Chemistry That Facilitates Bio-Immobilization and Inhibits Nonspecific Protein, Bacterial, and Mammalian Cell Adhesion. *Chem. Mater.* **2007**, *19* (18), 4405–4414. https://doi.org/10.1021/cm070509u.

(145) Tai, N. L.; Adhikari, R.; Shanks, R.; Adhikari, B. Starch-Polyurethane Films Synthesized Using Polyethylene Glycol-Isocyanate (PEG-Iso): Effects of Molecular Weight, Crystallinity, and Composition of PEG-Iso on Physiochemical Characteristics and Hydrophobicity of the Films. *Food Package. Shelf Life* **2017**, *14* (April), 116–127. https://doi.org/10.1016/j.fpsl.2017.10.003.

(146) Rhodes, A.; Sandhu, S. S.; Onis, S. J. Surface Modification of Biomaterials by Covalent Binding of Poly(Ethylene Glycol) (PEG). *Surf. Modif. Biomater. Methods Anal. Appl.* **2011**, 39–55. https://doi.org/10.1533/9780857090768.1.39.

(147) Xiao, X. F.; Jiang, X. Q.; Zhou, L. J. Surface Modification of Poly Ethylene Glycol to Resist Nonspecific Adsorption of Proteins. *Fenxi Huaxue/ Chinese J. Anal. Chem.* **2013**, *41* (3), 445–453. https://doi.org/10.1016/S1872-2040(13)60638-6.

(148) Weir, M. P.; Parnell, A. J. Water Soluble Responsive Polymer Brushes. *Polymers (Basel).* **2011**, *3* (4), 2107–2132. https://doi.org/10.3390/polym3042107.

(149) Alexander, S. Polymer Adsorption on Small Spheres. A Scaling Approach. *J. Phys.* **1977**, *38* (8), 977–981. https://doi.org/10.1051/jphys:01977003808097700.

(150) de Gennes, P. G. Conformations of Polymers Attached to an Interface. *Macromolecules* **1980**, *13* (5), 1069–1075. https://doi.org/10.1021/ma60077a009.

(151) Oberleitner, B.; Dellinger, A.; Castanet, A. S.; Galtayries, A.; Semetey, V. A Facile and Versatile Approach to Design Self-Assembled Monolayers on Glass Using Thiol–Ene Chemistry. *Chem. Commun.* **2013**, *49* (16), 1615–1617. https://doi.org/10.1039/c2cc38425f.

(152) Chen, S.; Li, L.; Zhao, C.; Zheng, J. Surface Hydration: Principles and Applications toward Low-Fouling/Nonfouling Biomaterials. *Polymer (Guildf).* **2010**, *51* (23), 5283–5293. https://doi.org/10.1016/j.polymer.2010.08.022.

(153) Marie, R.; Beech, J. P.; Vörös, J.; Tegenfeldt, J. O.; Höök, F. Use of PLL-g-PEG in Micro-Fluidic Devices for Localizing Selective and Specific Protein Binding. *Langmuir* **2006**, *22* (24), 10103–10108. https://doi.org/10.1021/la060198m.

(154) Liu, Y.; Meng, H.; Konst, S.; Sarmiento, R.; Rajachar, R.; Lee, B. P. Injectable Dopamine-Modified Poly(Ethylene Glycol) Nanocomposite Hydrogel with Enhanced Adhesive Property and Bioactivity. *ACS Appl. Mater. Interfaces* **2014**, *6* (19), 16982–16992. https://doi.org/10.1021/am504566v.

(155) Breukers, J.; Horta, S.; Struyfs, C.; Spasic, D.; Feys, H. B.; Geukens, N.; Thevissen, K.; Cammue, B. P. A.; Vanhoorelbeke, K.; Lammertyn, J. Tuning the Surface Interactions between Single Cells and an OSTE+ Microwell Array for Enhanced Single Cell Manipulation. *ACS Appl. Mater. Interfaces* **2021**, *13* (2), 2316–2326. https://doi.org/10.1021/acsami.0c19657.

(156) Zhang, Z.; Wang, J.; Tu, Q.; Nie, N.; Sha, J.; Liu, W.; Liu, R.; Zhang, Y.; Wang, J. Surface Modification of PDMS by Surface-Initiated Atom Transfer Radical Polymerization of Water-Soluble Dendronized PEG Methacrylate. *Colloids Surfaces B Biointerfaces* **2011**, *88* (1), 85–92. https://doi.org/10.1016/j.colsurfb.2011.06.019.

(157) Liu, W.; Li, Y.; Ding, X. Cell Adhesion Pattern Created by OSTE Polymers. *Biofabrication* **2017**, *9* (2), 025006. https://doi.org/10.1088/1758-5090/aa669c.

(158) Lee, H.; Larson, R. G. Adsorption of Plasma Proteins onto PEGylated Lipid Bilayers: The Effect of PEG Size and Grafting Density. *Biomacromolecules* **2016**, *17* (5), 1757–1765. https://doi.org/10.1021/acs.biomac.6b00146.

(159) Perry, J. L.; Reuter, K. G.; Kai, M. P.; Herlihy, K. P.; Jones, S. W.; Luft, J. C.; Napier, M.; Bear, J. E.; DeSimone, J. M. PEGylated PRINT Nanoparticles: The Impact of PEG Density on Protein Binding, Macrophage Association, Biodistribution, and Pharmacokinetics. *Nano Lett.* **2012**, *12* (10), 5304–5310. https://doi.org/10.1021/nl302638g.

(160) Bernhard, C.; Roeters, S. J.; Franz, J.; Weidner, T.; Bonn, M.; Gonella, G. Repelling and Ordering: The Influence of Poly(Ethylene Glycol) on Protein Adsorption. *Phys. Chem. Chem. Phys.* **2017**, *19* (41), 28182–28188. https://doi.org/10.1039/c7cp05445a.

(161) Al-Ani, A.; Pingle, H.; Reynolds, N. P.; Wang, P. Y.; Kingshott, P. Tuning the Density of Poly(Ethylene Glycol) Chains to Control Mammalian Cell and Bacterial Attachment. *Polymers (Basel).* **2017**, *9* (8), 343. https://doi.org/10.3390/polym9080343.

(162) Song, J.; Michas, C.; Chen, C. S.; White, A. E.; Grinstaff, M. W. Controlled Cell Alignment Using Two-Photon Direct Laser Writing-Patterned Hydrogels in 2D and 3D. *Macromol. Biosci.* **2021**, *21* (5), 1–5. https://doi.org/10.1002/mabi.202100051.

(163) Gernhardt, M.; Blasco, E.; Hippler, M.; Blinco, J.; Bastmeyer, M.; Wegener, M.; Frisch, H.; Barner-Kowollik, C. Tailoring the Mechanical Properties of 3D Microstructures Using Visible Light Post-Manufacturing. *Adv. Mater.* **2019**, *31* (30), 1–6. https://doi.org/10.1002/adma.201901269.

(164) Greiner, A. M.; Klein, F.; Gudzenko, T.; Richter, B.; Striebel, T.; Wundari, B. G.; Autenrieth, T. J.; Wegener, M.; Franz, C. M.; Bastmeyer, M. Cell Type-Specific Adaptation of Cellular and Nuclear Volume in Micro-Engineered 3D Environments. *Biomaterials* **2015**, *69*, 121–132. https://doi.org/10.1016/j.biomaterials.2015.08.016.

(165) Scheiwe, A. C.; Frank, S. C.; Autenrieth, T. J.; Bastmeyer, M.; Wegener, M. Subcellular Stretch-Induced Cytoskeletal Response of Single Fibroblasts within 3D Designer Scaffolds. *Biomaterials* **2015**, *44*, 186–194. https://doi.org/10.1016/j.biomaterials.2014.12.018.

(166) Richter, B.; Hahn, V.; Bertels, S.; Claus, T. K.; Wegener, M.; Delaittre, G.; Barner-Kowollik, C.; Bastmeyer, M. Guiding Cell Attachment in 3D Microscaffolds Selectively Functionalized with Two Distinct Adhesion Proteins. *Adv. Mater.* **2017**, *29* (5), 1–6. https://doi.org/10.1002/adma.201604342.

(167) Lyu, Y.; Martínez, Á.; D'incà, F.; Mancin, F.; Scrimin, P. The Biotin–Avidin Interaction in Biotinylated Gold Nanoparticles and the Modulation of Their Aggregation. *Nanomaterials* **2021**, *11* (6), 1559. https://doi.org/10.3390/nano11061559.

(168) Kozik, A.; Karkowska-Kuleta, J.; Zajac, D.; Bochenska, O.; Kedracka-Krok, S.; Jankowska, U.; Rapala-Kozik, M. Fibronectin-, Vitronectin- and Laminin-Binding Proteins at the Cell Walls of Candida Parapsilosis and Candida Tropicalis Pathogenic Yeasts. *BMC Microbiol.* **2015**, *15* (1), 197. https://doi.org/10.1186/s12866-015-0531-4.

Chapter II. Off-stoichiometry thiol-ene resin

2.1 Introduction

With the development of two-photon polymerization, many commercial materials have been successfully used, like polyethylene glycol (di)acrylate, SU8, OrmoComp and NOA 61. With those materials, varied structures like micro-lens, needles matrix, cubes, complex three-dimension (3D) structures have been realized to meet the demands in optical, medical devices or tissue engineering, etc. Besides, another material, thiol-ene resin, was developed for two-photon polymerization due to its possibilities to create chemically modified microstructures with high-resolution.[1] Thiol-ene resin usually consists of a thiol-component, an alkene-component and a photoinitiator. **Figure 2.1** shows the common alkenes and thiols. According to the structures, they are divided into soft and rigid molecules. From **(A)** to **(D)**, they are three armed structures with rigid six-membered ring. Three arms increase the cross-linking density and rigid six-membered ring enhances the rigidity of the networks. From (E) to (H), they are softer than rigid molecules, but multi-arms will also improve the rigidity for the cured materials. From (I) to (K), they are soft thiols with similar structures like **(E)** to **(H)**. And **(L)** is a rigid thiol with a six-membered ring. With light or catalysis induced thiol-ene click reaction, the two components will polymerize forming a highly cross-linked material. Commonly used thiols and alkenes are **(J)** three-armed thiol trimethylolpropane tris(3-mercaptopropionate), **(K)** four-armed thiol pentaerythritol tetrakis(3-mercatoprpionate) and **(B)** three-armed 1,3,5-Triallyl-1,3,5-triazine-2,4,6(1H,3H,5H)-trione, **(H)** polyethylene glycol diacrylate.

(A)

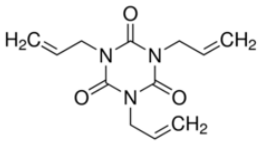

1,3,5-Triallyl-1,3,5-triazine-2,4,6(1H,3H,5H)-trione
Melting point: 20.5 °C

(B)

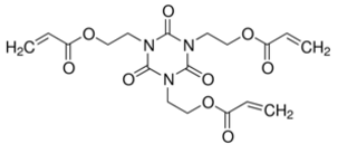

Tris[2-(acryloyloxy)ethyl] isocyanurate
Melting point: 52-53 °C

(C)

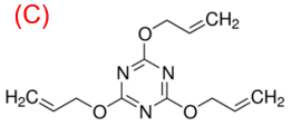

2,4,6-Triallyloxy-1,3,5-triazine
Melting point: 26-28 °C

(D)

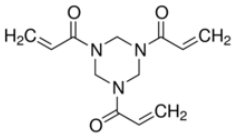

1,3,5-Triacryloylhexahydro-1,3,5-triazine
Melting point: 156 °C

(E)

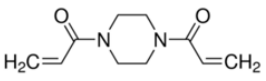

1,4-Bis(acryloyl)piperazine
Melting point: 91.5-91.3 °C

(F)

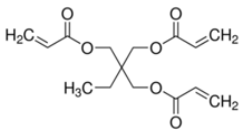

Trimethylolpropane triacrylate
Melting point: -66 °C

(G)

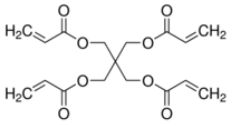

Pentaerythritol tetraacrylate
Melting point: 18 °C

(H)

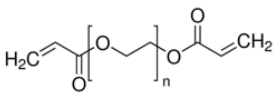

Poly(ethylene glycol) diacrylate
PEGDA 250 PEGDA 575
Liquid rt.

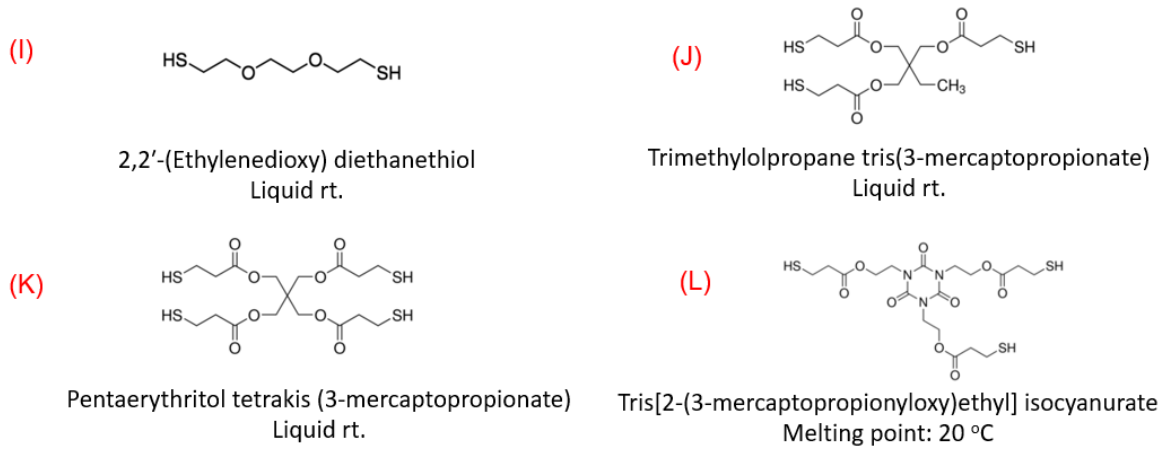

Figure 2.1 Common alkenes and thiols. From (A) to (D), rigid structures alkenes. From (E) to (H), soft structures alkenes. From (I) to (K), soft structures thiols. (L), rigid structure thiol.

Based on thiol-ene resin chemistry, off-stoichiometry thiol-ene (OSTE) resin was initially used in lab-on-chips.[2] With good biocompatibility, tunable mechanical properties and controllable surface chemistry, OSTE was successfully used as biomaterial besides PDMS and SU8 photoresist. When we want to choose the components for thiol-ene resin used in two-photon polymerization, there are a wide range of candidates for both thiols and alkenes from **Figure 2.1**. By tuning the ratio of thiol-ene, we can obtain surface with excess thiol or alkene groups. OSTE resin relies on thiol-ene click chemistry. **Figure 2.2 (A)** shows the mechanism of thiol-ene click chemistry. The photoinitiator produces radicals under UV illumination. Radicals react with thiol group which induces propagation with alkenes. When the total number of thiol groups equals that of alkene groups, there is no functional group left after full reaction. This composition is stoichiometric. Otherwise, there will be thiol or alkene groups left after polymerization with off-stoichiometric composition (**Figure 2.2 (B)**). Off-stoichiometry ratio brings the opportunity for post-modification. Both thiol and alkene excess surfaces can be modified with target functional groups with special properties. With different ratios of thiol and alkene groups, the rigidity of the final material also varies.

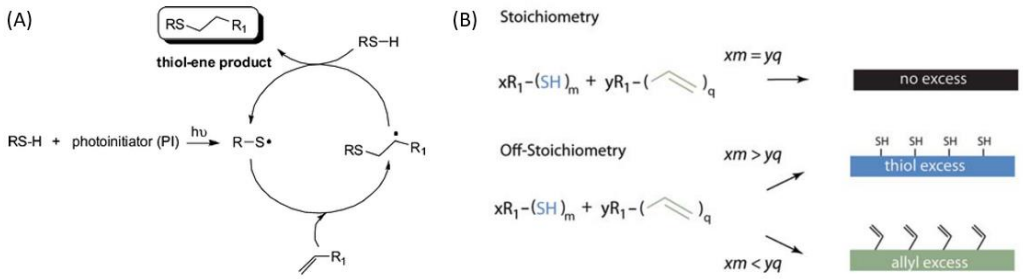

Figure 2.2 (A)Mechanism of thiol-ene click reaction and (B) OSTE resin.[3,4]

Usually, a photoinitiator is needed in light-induced thiol-ene click reaction. Commercial photoinitiators like Irgacure 365, Irgacure 651, Irgacure 2959, ITX, TOP-L are usually used to form light-induced thiol-ene resist systems. With different ratios of thiol and alkene components, we can obtain materials with varied surface properties and mechanical properties. Besides, cell toxicity is an important factor to consider when using photoinitiators in biological applications. To avoid cytotoxicity problems caused by photoinitiators, photoinitiator-free materials have recently been constructed for two-photon polymerization.[5] Functional groups like S-H, S-S, C=C, C=O, aromatic compound have strong absorption in UV or visible region. The photoinitiator-free material avoids the toxicity problem of photoinitiators. However, whether the material without photoinitiator can be polymerized by TPP remains to be well studied. Therefore, whether to add photoinitiator and how to choose photoinitiator are also important issues. For applications related to biology, like medical devices and tissue engineering, higher standards are needed. Biocompatibility is the basis demand for biomaterials. Former exploration by Errando-Herranz *et al.*[6] showed that the biocompatibility of OSTE resins depends on the ratio of thiol-ene. Monomer leaching can be possible reasons for low cell viability. Hoffman *et al.*[7] also showed that monomer or oligomer species extracted from cured high thiol excess specimen can also be responsible for cytotoxicity. For development of new materials for OSTE resin, biocompatibility is a basement. With basic biocompatibility, cells can adhere to the surface of OSTE resin. Controllable bioactivities, like bio-adhesive and bio-repellent functions, are important tools for biological applications. Surface modification is a potential way to extend the raw materials to more bioactive ones after two-photon polymerization. Thiol-ene click reaction is a powerful tool to do surface modification.

In this chapter, we are developing an OSTE resin that can be used in one- and two-photon polymerization for biological applications. First, we will tune the resin formulation by OPP and TPP. By controlling the ratio of thiol and alkene groups, we will obtain thiol or alkene excess surfaces. Second, polyethylene glycol (PEG) derivatives will be grafted to the surface by one- or two-photon grafting to modulate the property by light-induced surface modification. By surface analysis

techniques, like attenuated total reflectance-Fourier transform infrared (ATR-FTIR), water contact angle, X-ray photoelectron spectrometry (XPS), surface properties will be characterized after surface modification in 2D surfaces. The surface will also be validated with bacteria and cells. After tuning the conditions for surface modification on 2D surfaces, the best parameters will be transferred to 3D surface modifications.

2.2 One-photon polymerization of OSTE resin

2.2.1 Raw material and formation of OSTE resin

As mentioned above, the main components of OSTE resin are a thiol fraction and an alkene fraction. We need materials with easy tunable mechanical properties. The combination of soft and rigid molecules is an ideal formulation. From **Figure 2.1** four-armed thiol (K) pentaerythritol tetrakis(3-mercatopropionate) was chosen for its soft structure and three-armed alkene (A) 1,3,5-Triallyl-1,3,5-triazine-2,4,6(1H,3H,5H)-trione for its rigidity. To analytically characterize the surface properties of the cured resin, we need an analytical characterization technique to monitor the reaction. Attenuated total reflectance-Fourier transform infrared (ATR-FTIR) is versatile tool for qualitative and quantitative analysis. First, we can obtain information about single molecules. Second, we can track the reaction kinetics of bulk material. Also, ATR-FTIR offers molecular composition on the surface of the material.

As is shown in **Figure 2.3**, the contributions of ATR-FTIR of trialkene are as follows : 3085 cm^{-1} C-H stretching linked to the carbon-carbon double bond, 2987 cm^{-1} and 2954 cm^{-1} C-H of CH_2 stretching, 1678 cm^{-1} C=O stretching of carbonyl, 1645 cm^{-1} C=C stretching, 1446 cm^{-1} CH_2 bending, 1410 cm^{-1} bending of the backbone of the ring, 1317 cm^{-1} C-N stretching, 991 cm^{-1} and 928 cm^{-1} =C-H bending, 763 cm^{-1} monosubstituted C-H bending.

Figure 2.4 shows the contributions of ATR-FTIR of tetrathiol: 2945 cm^{-1} C-H asymmetric stretching, 2904 cm^{-1} C-H symmetric stretching, 2569 cm^{-1} S-H stretching, 1730 cm^{-1} C=O stretching, 1471 C-H scissoring, 1356 cm^{-1} C-H bending, 1232 cm^{-1} and 1144 cm^{-1} C-O stretching.

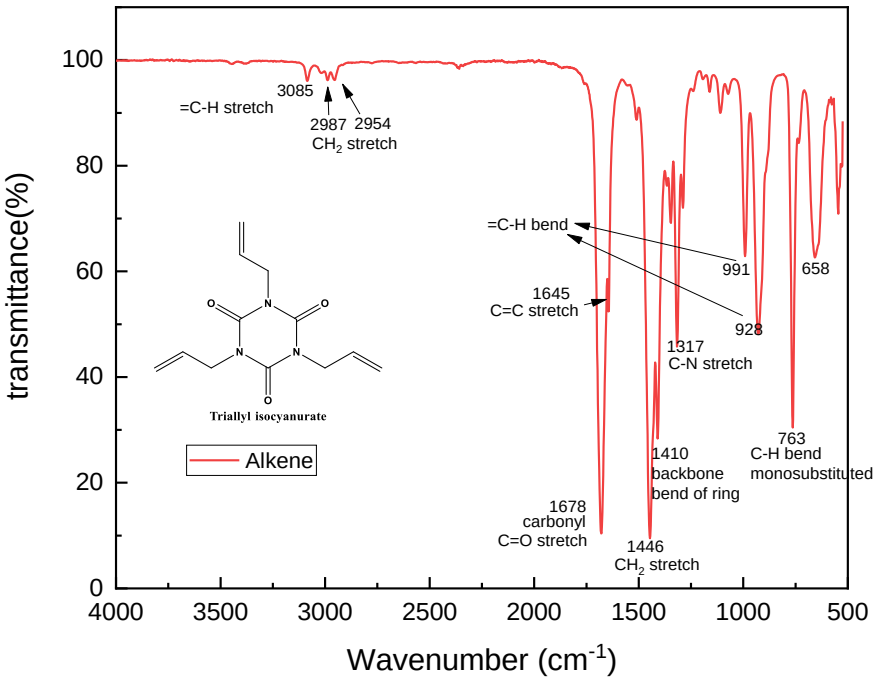

Figure 2.3 ATR-FTIR of tris(prop-2-en-1-yloxy)-1,3,5-triazine (trialkene) (trialkene)

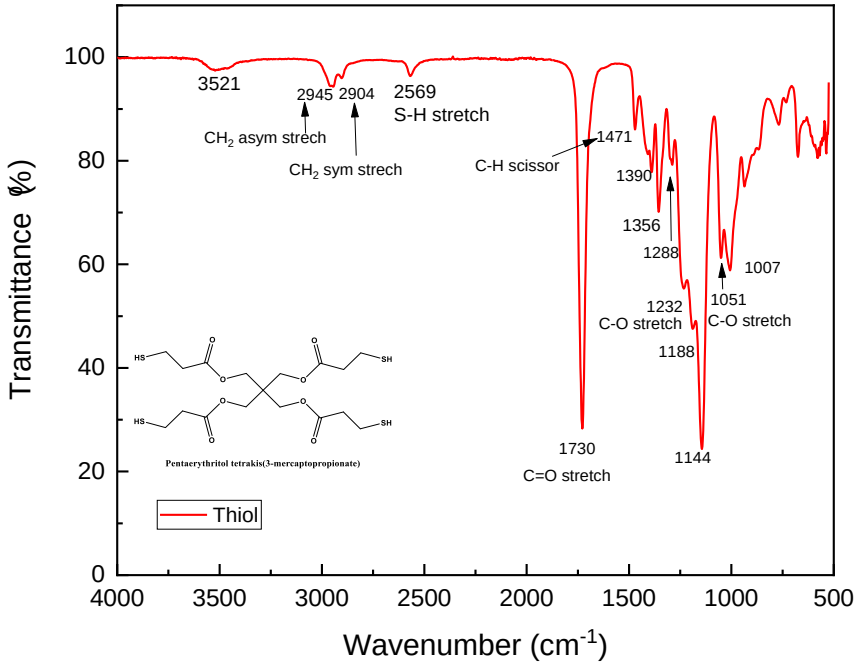

Figure 2.4 ATR-FTIR of thiol pentaerythritol tetrakis(3-mercatopropionate) (tetrathiol)

As mentioned above, we were not sure whether photoinitiator will be needed or not for our OSTE resin. In the past, we chose Irgacure 651 as photoinitiator together with PEGDA 250 and PEGDA 575 for UV polymerization and microfabrication.[8] We chose Irgacure 651 as photoinitiator to test the reactivity of thiol-ene resin and compared the behavior of our resin with or without PI.

2.2.2 Equal stoichiometry thiol-ene resin (thiol:ene = 1:1) and its reactivity

To better understand the formulation of the OSTE resin, we should figure out the reactivity of the equal stoichiometry thiol-ene resin. There are 4 thiol groups in one tetrathiol molecule and 3 alkene groups in one trialkene molecule. Supposing there are *x* mole tetrathiol and *y* mole trialkene in the thiol-ene resin (*x* tetrathiol-*y* trialkene), the ratio of thiol:ene = 4*x* : 3*y*. Equal stoichiometry thiol-ene resin means that thiol:ene = 4*x* : 3*y* =1:1. In theory, there is no functional group left on the surface after full polymerization. First, we tried to monitor the ratio of thiol:ene by one-photon polymerization of 2D surfaces. Then the possibility of TPP of equal stoichiometry thiol-ene resin was tested.

To make sure the resin is fully polymerized, the curing kinetics of polymerization of thiol-ene resin in one-photon polymerization should be figured out. By ATR-FTIR, we can know the signal change of functional groups before and after curing. Here we used 7.2 mW/cm^{-2} 254 nm UV resource to perform curing. There were two formulations, one without photoinitiator and another with 2 w/w% Irgacure 651 as photoinitiator. Curing kinetics of both formulations were tracked by ATR-FTIR.

2.2.2.1 Curing kinetics of equal stoichiometry thiol-ene resin (thiol:ene = 1:1) without photoinitiator

Figure 2.5 shows the curing kinetics of 1:1 thiol-ene resin without photoinitiator. From 10 min to 30 min curing, FTIR spectrum still had variation at the asymmetric stretching and symmetric stretching of the hydrogen-carbon bond from alkyl group at 2929 cm^{-1} and 2960 cm^{-1}, which means 10 min curing was not long enough to finish the curing process. Thiol:ene = 1:1 resin without photoinitiator was not efficient enough for one-photon curing in 10 minutes.

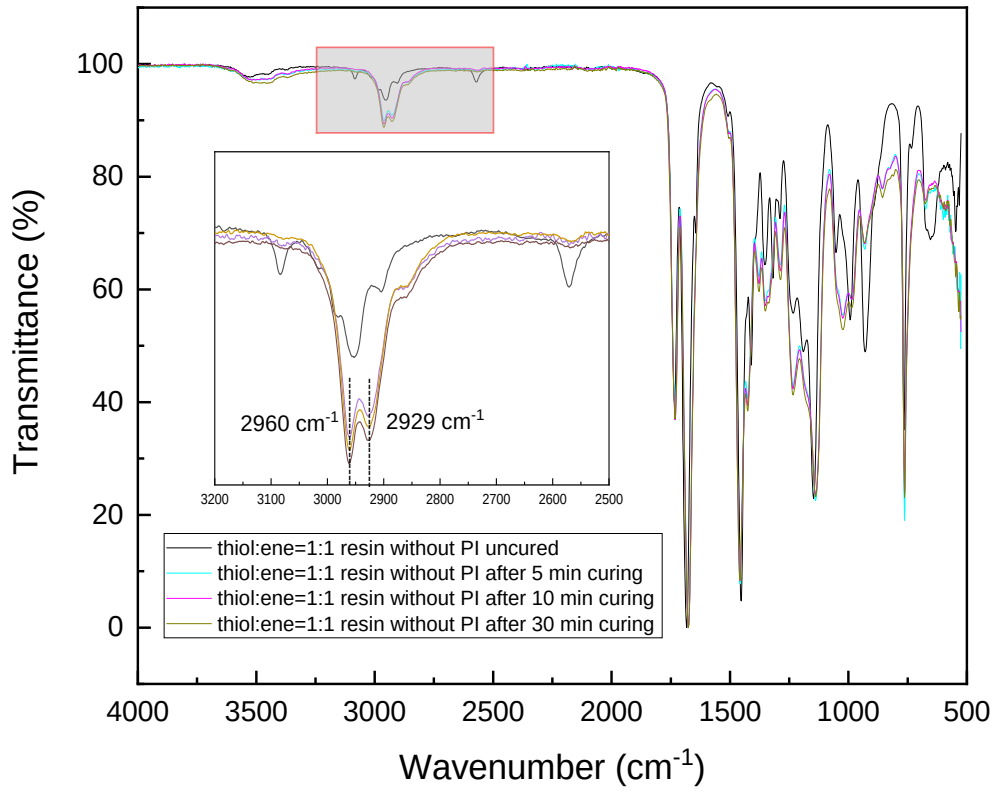

Figure 2.5 Curing kinetics of thiol:ene= 1:1 resin without photoinitiator under illumination with 7.2 mW/cm^{-2}, 254 nm UV.

We already know that the remaining photoinitiator is toxic to cells. Photoinitiator-free resin has been developed to prevent the possible cytotoxicity from residual photoinitiator. The aim is to develop material for both for one- and two-photon polymerization. So, we also tested the reactivity of photoinitiator free thiol:ene = 1:1 resin for microfabrication by TPP. Here, we designed a small 3D structure for the test (**Figure 2.6**). The small 3D structure was a regular open hexagon structure. The height of one pillar is 5 µm. The diameter of the circumcircle of top hexagon is 8 µm.

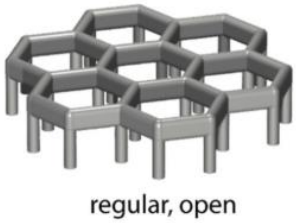

Figure 2.6 Small 3D structure used for the test of thiol:ene = 1:1 resin without photoinitiator. Regular open hexagonal structure *D8K1H7-open*.

After microfabrication, the small structures were washed with acetone. But the structures were not stable and could not be maintained. Considering the long curing time by one-photon polymerization and the low stability of the structure by two-photon polymerization, equal stoichiometric thiol-ene resin without photoinitiator was not the best formulation.

2.2.2.2 Curing kinetics of equal stoichiometry thiol-ene resin (thiol:ene = 1:1) with photoinitiator

Besides photoinitiator free thiol:ene = 1:1 resin. We also tested the formulation with 2 wt% Irgacure 651 as the photoinitiator. To figure out the curing kinetics of polymerization of the thiol-ene resin, we tracked the FTIR signal over at 5, 10 and 15 min (**Figure 2.7**). The FTIR spectrum did not show any evolution after 10 minutes of curing at 2929 cm^{-1} and 2960 cm^{-1}. Compared with the situation without photoinitiator, thiol-ene resin with 2 wt% Irgacure 651 is more efficient in one-photon polymerization. Here, we kept the curing time as 10 min for the later curing process for resin preparation in one photon polymerization. All the curing was performed with 7.2 mW/cm^{-2}, 254 nm UV.

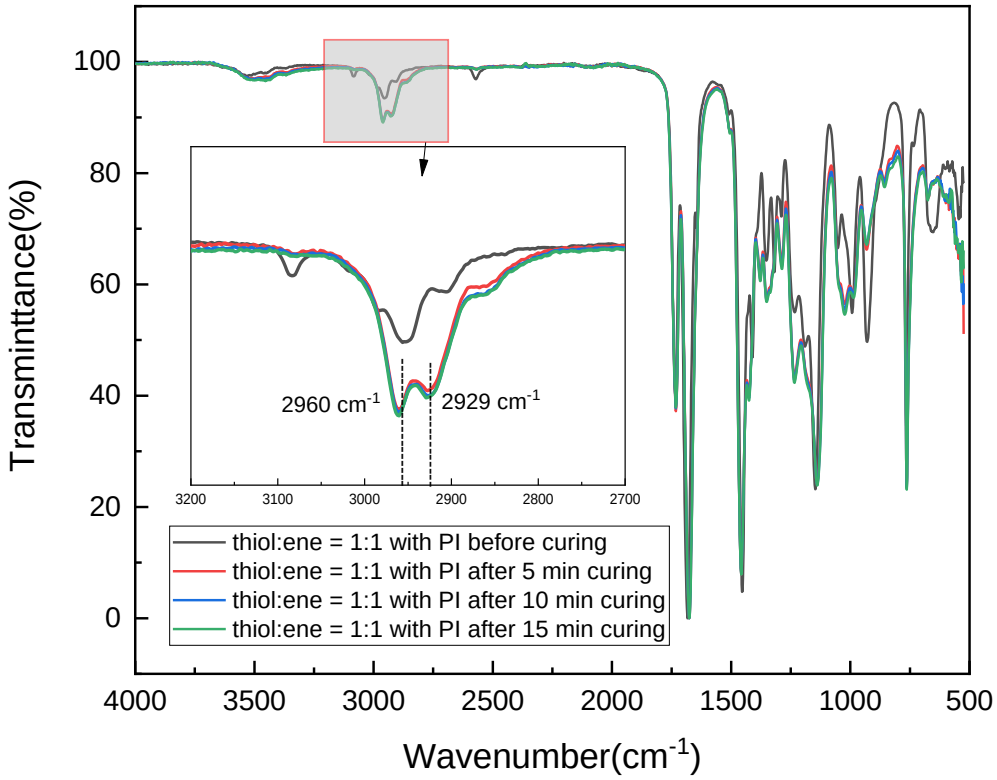

Figure 2.7 Curing kinetics of thiol:ene =1:1 resin with 2 wt% Irgacure 651 as the photoinitiator (PI) under illumination with 7.2 mW/cm^{-2}, 254 nm UV.

To better understand the reaction during the curing. We extract the ATR-FTIR figures of thiol:ene = 1:1 resin with 2 wt% Irgacure 651 as photoinitiator before curing and after 10 minutes curing under illumination with 7.2 mW/cm^{-2}, 254 nm UV. Typical peaks of trialkene are 1645 cm^{-1} from the stretching of carbon-carbon double bond and 3065 cm^{-1} from the stretching of carbon-hydrogen bond linked to carbon-carbon double bond (**Figure 2.3**). The typical peak of tetrathiol comes from the stretching of sulfhydryl bond at 2569 cm^{-1} (**Figure 2.4**). Before curing (thiol:ene = 1:1 resin, 2 wt% Irgacure 651 as photoinitiator), the three distinct peaks mentioned remain evident, allowing us to assess the level of curing in the thiol-ene resin by analyzing the changes in these characteristic peaks (**Figure 2.8**, black line).

After 10 min curing with 7.2 mW/cm^{-2} 254 nm UV light, the peak at 3085 cm^{-1} of C-H and 2570 cm^{-1} of S-H both disappeared, which means alkene and thiol functional groups totally reacted with each. (**Figure 2.8**, red line). The peak at 1645 cm^{-1} disappeared also with the consumption of alkene. The intensity of the absorption peak of carbonyl groups from trialkene at 1678 cm^{-1} and tetrathiol at 1730 cm^{-1} remained unchanged but shifted to lower wavenumber. The peak at 928 cm^{-1} and 991 cm^{-1} (=C-

H bending sharply) decreased after the polymerization, which further evidence the depletion of carbon-carbon double bonds. In theory, the reaction between thiol and alkene groups of thiol:ene = 1:1 resin should be complete. It is the case that **Figure 2.8** shows.

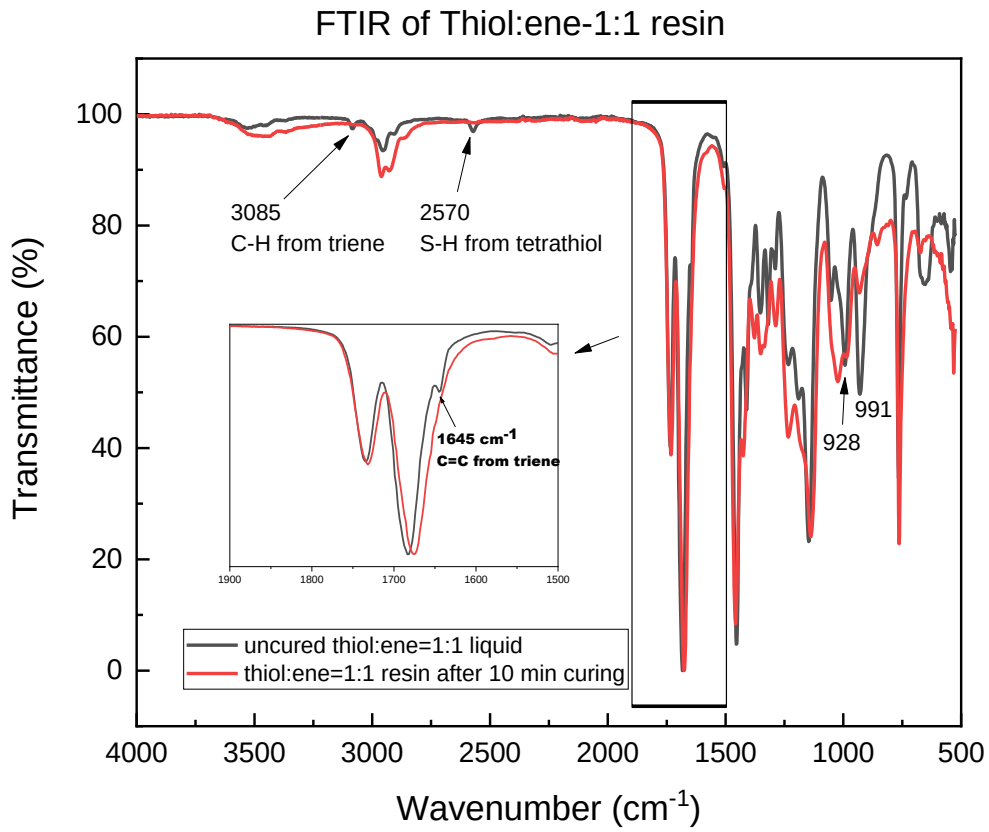

Figure 2.8 ATR-FTIR of thiol:ene = 1:1 resin with 2 wt% Irgacure 651 as the photoinitiator before and after 10 min curing under illumination with 7.2 mW/cm^{-2}, 254 nm UV.

2.2.3 Off-ratio stoichiometry thiol-ene resin

When the ratio of thiol and alkene functional groups (*4x:3y*) is not 1:1 (*x* tetrathiol-*y* trialkene, *4x≠3y*), there will be unreacted thiol or alkene functional groups left after polymerization. When *4x>3y*, there will be a thiol excess surface after polymerization, otherwise there will be an alkene excess surface.

To explore the ratio boundary of the two components of the resin, we set the following test criteria. In formulations of all ratios, 2w/w% Irgacure 651 was added as photoinitiator. All the samples were mixed overnight. Four drops resin was spread on glass slides then cured in 7.2 mW/cm^{-2} 254 nm UV curing chamber for 10 min. If the spread resin can be peeled off from the glass slides, we confirmed

the formulation suitable for one-photon polymerization. Then we tested the ATR-FTIR of the cured resin. After testing, we confirmed the range thiol:ene of the formulation for one-photon polymerization is from 5:1 to 1:5.

2.2.3.1 ATR-FTIR of OSTE resin with different ratios

We tracked ATR-FTIR of thiol-ene resins with confirmed integer ratios ranging from 5:1 to 1:5 before and after curing for 10 minutes with 7.2 mW/cm^{-2} 254 nm UV. For all the formular, 2 wt% Irgacure 651 was added as photoinitiator. **Figure 2.9** shows the ATR-FTIR of the resin before curing. With the increase of alkene component, the absorption at 1645 cm^{-1} increases gradually with the increase of alkene proportion. After polymerization, alkene excess OSTE resin still show strong signal at 3085 cm^{-1}, which comes from the =C-H while thiol excess OSTE resin show a peak at 2570 cm^{-1} which comes from S-H (**Figure 2.10**).

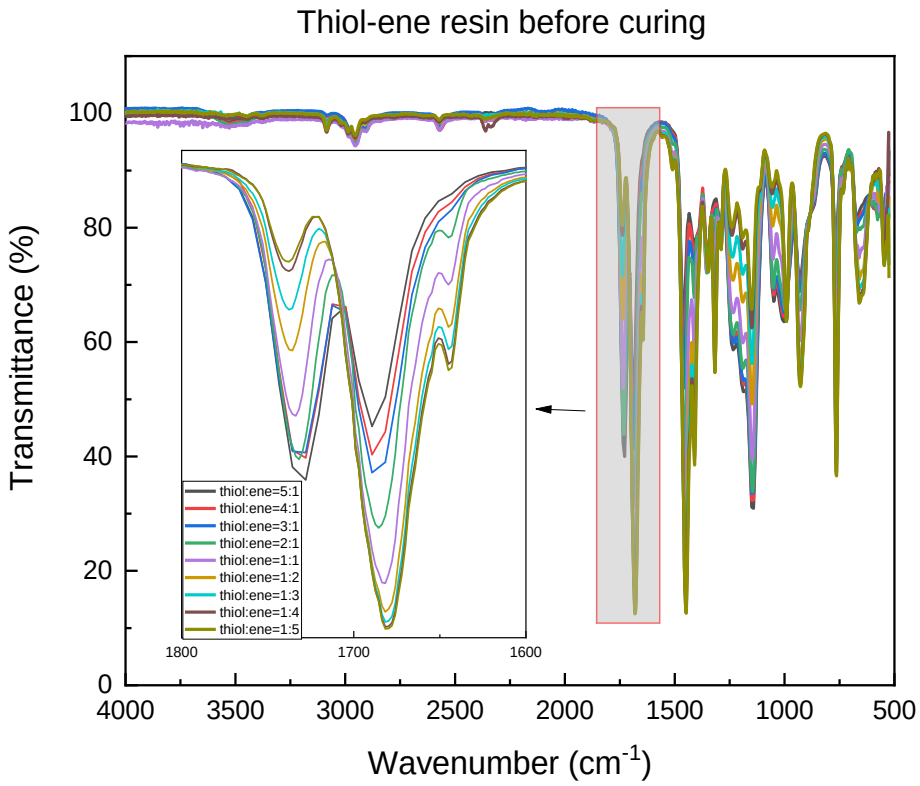

Figure 2.9 FTIR of all integer ratios thiol-ene resin before curing, all formulations contain 2 wt% Irgacure 651 as photoinitiator.

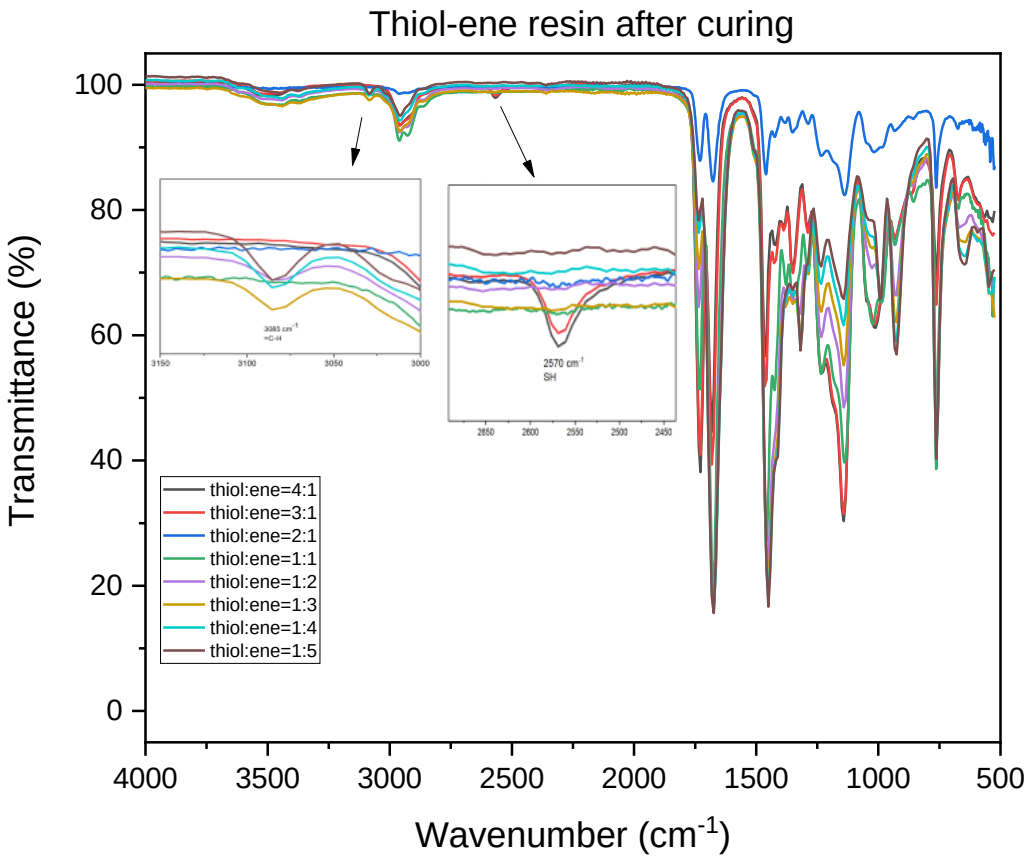

Figure 2.10 FTIR of all integer ratios thiol-ene resin after curing under illumination with 7.2 mW/cm-2, 254 nm UV. All formulations contain 2 wt% Irgacure 651 as photoinitiator.

We have successfully applied NOA 61, a commercial material (optical glue, https://www.norlandproducts.com), in two-photon polymerization in our previous research in the lab.[8, 9] NOA 61 exhibits good biocompatibility and mechanical stability. To better understand the property of NOA61, Bechoux *et al.*[10] used Surface Assisted Laser Desorption Ionization (SALDI) mass spectrometry techniques to analyze the component of NOA61. The results showed the possible components of NOA 61 are the same tetrathiol and trialkene we chose. We compared the ATR-FTIR of NOA 61 with different ratios OSTE. From the **Figure 2.11**, we can figure out that the absorption at 1645 cm^{-1} (alkene group) of NOA 61 is almost the same as thiol:ene = 1:1.2 OSTE resin . It means the thiol:ene ratio of NOA 61 is most closed to 1:1.2. As a reference, we will compare NOA 61 with thiol:ene = 1:1.2 OSTE resin in different tests, like water contact angle, bacteria, and cell test.

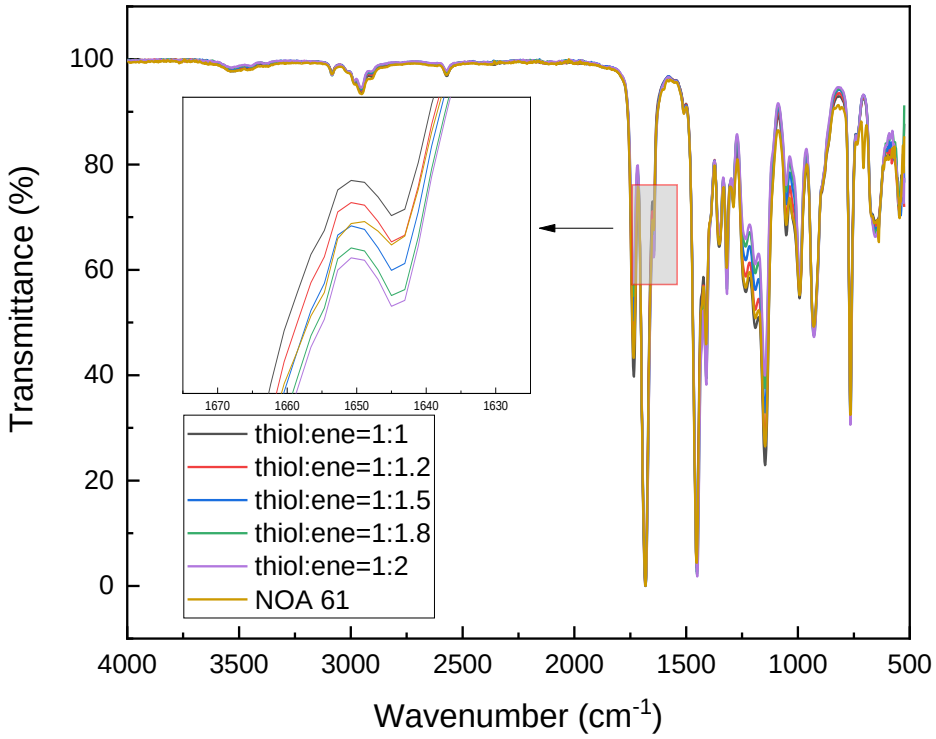

Figure 2.11 FTIR of NOA 61 and different thiol-ene resins with ratios from 1:1 to 1:2 under illumination with 7.2 mW/cm-2, 254 nm UV. All formulations contain 2 wt% Irgacure 651 as photoinitiator.

2.2.3.2 Cell viability

One key requirement for material application is its low toxicity in a biological environment. Cell toxicity is a crucial factor that influences cell growth. Any trace amount of unpolymerized small molecules could be toxic to cells. Biocompatibility toxicity can be tested by many methods like the MTT assay[11,12] MTT is a yellow tetrazolium dye to assess cell metabolic activity and give access to cell viability, proliferation and toxicity. Ejserholm *et al.*[13] used LC-MS (liquid chromatography-mass spectroscopy) and GC-MS (gas chromatography-mass spectroscopy) to analyze the water extraction of thiol-ene based material for neural implants. Together with MTT assays, the extracted two alkenes were proved to be responsible for cell toxicity. After 7 days of extraction in water, several components were tested in water. The results of cell growth showed that OSTE+ (OSTE + Epoxy) material was nontoxic to cells after long-time pre-incubation in water. Errando-Herranz *et al.*[6] viewed the cell viability on photoinitiator-free OSTE resin with different ratios of thiol to alkene components on resin formulation. Results showed that high excess of thiol on the surface decreases cell viability. Zeng *et al.*[14] tested seven commercial photoinitiators with different cells. Cytotoxicity and

cytocompatibility of the same photoinitiator varied for different cells. . Here we quantified the viability of classical, widely-used renal Madin-Darby canine kidney (MDCK) epithelial cells, estimated here from cell growth test, on the different formulations of OSTE resin. Since the extraction could be an effective way to prevent the cytotoxicity, we also explored the role of washing process on cell viability. The test range ratio of thiol:ene in the formulation is from 2:1 to 1:2. As Errando-Herranz *et al.*[6] did in their test, no photoinitiator was added in our test to prevent the toxicity of the photoinitiator. All the resins were spread on the bottom of 35 mm petri dishes and cured under illumination of 7.2 mW/cm^{-2} 254 nm UV for 10 minutes.

MDCK cells were seeded on different surfaces, 2.5 ml at 0.2 million/ml for each sample. Cell density was 0.05 million/cm$^{2.}$ Without washing process, the surfaces were just sterilized with ethanol and PBS+P/S (penicillin/streptomycin). The cells were confluent on no excess (1:1) surface and all the alkene excess surfaces. Here no photoinitiator was added to prevent cytotoxicity from photoinitiator. The results showed the formulations of the alkene excess surface are not toxic to MDCK cells, while all the thiol excess surface shows extremely low cell viability (**Table 2.1**). The possible cytotoxicity may be attributed to the unpolymerized tetrathiol.

Table 2.1 Cell viability on the surfaces of photoinitiator-free OSTE resin after curing without washing step for one trail

	Thiol excess surface					Alkene excess surface			
Thiol: Ene	2:1	1.8:1	1.5:1	1.2:1	1:1	1:1.2	1:1.5	1:1.8	1:2
Coverage	2%	3%	6%	13%	100%	100%	100%	100%	100%

To verify our hypothesis that cytotoxicity originates from free small molecule tetrathiol, we further designed a washing experiment to the cured thiol excess surface. The goal was to extract out the unpolymerized molecule then validate it again with cell viability test. First, we must choose a proper solvent for extraction. Here we selected several solvents acetone, methanol, ethanol and water, to test the extraction capacity. We chose thiol:ene = 1:1 thiol-ene resin without photoinitiator as the test model. Resin was spread on glass slides and then cured under 7.2 mW/cm^{-2} 254 nm UV for 10 minutes. The cured resins on glass slides were weighted. Then the resins and slides were put into solvent both for 12 hours overnight. After drying, they were weighted again to calculate the extracted fraction Δ weight. **Table 2.2** shows the results that acetone was the best solvent for extraction. 15.55 mg components were extracted out. Methanol, ethanol and water could not extract the unpolymerized

fraction. Here we conclude that acetone is a good solvent for uncured components and a nice solvent for OSTE extraction. We will use quick acetone flow to wash the unreacted components after two-photon polymerization.

Table 2.2 Weight change of resin after incubation for 12 hours in different solvents. All the samples were weighed after drying.

Weight/mg	Acetone	Methanol	Ethanol	Water	Control
Slide weight/mg	113.46	112.98	112.88	113.37	113.07
Weight before washing/mg (slide + cured OSTE resin)	202.21	302.86	186.77	207.66	202.08
Weight after washing/mg (slide + cured OSTE resin)	104.30 (Resin detached)	302.93	186.88	208.48	202.11
Δ weight of the resin/mg	-15.55	+0.07	+0.11	+0.82	+0.03

From the solvent selection experiment above, we chose acetone to wash the thiol excess OSTE resin. The surfaces were washed with an acetone bath for short or long times before cell seeding. Cell viability increased a bit after a fleeting time (1 minute) wash with acetone but was still very low for thiol:ene = , 2:1, 1.8:1, and 1.5:1 surface. After a long time of washing (10 minutes 3times), cell viability on all ratios almost reached 100%. These experiments confirmed our former hypothesis that the cytotoxicity observed came from unpolymerized tetrathiol. After a long time of washing, the unpolymerized monomers were extracted by acetone.

Table 2.3 Cell viability on thiol excess surface after acetone washing for one trail

	Short time 1 min wash in acetone bath				Long time wash 10 min x 3 times in acetone bath			
Thiol: Ene	2:1	1.8:1	1.5:1	1.2:1	2:1	1.8:1	1.5:1	1.2:1
Coverage	3%	5%	4%	100%	91%	100%	100%	93%

In this section, we confirmed that thiol excess surface may be toxic due to the unpolymerized small thiol molecule. By long time washing with acetone, the unreacted thiol can be extracted out. But the ratio of thiol:ene will be different from that before washing. While alkene excess surface is not toxic to cells. So, in the coming section, we will focus on alkene excess surface. To better understand the properties of alkene excess surface, we will test water contact angle, bacteria and cell adhesion will be evaluated in the coming parts.

2.2.3.3 Water contact angle

Water contact angle provides important information about the wettability and surface energy of the material. The value will assess the hydrophilicity or hydrophobicity nature of the surface. There are two kinds of methods to measure the water contact angle, static and dynamic contact angle (**Figure 2.12**). Static contact angle (α) refers to the angle between the liquid droplet ad the surface when the drop stays at equilibrium. Dynamic contact angle measurements give access both to advancing and receding contact angles. Advancing contact angle (β) refers to the angle when the liquid droplet gradually increases during the wetting process while receding contact angle (γ) refers to the angle when the liquid droplet gradually decreases during the dewetting process. Dynamic contact angles can be influenced by many factors like roughness and surface chemistry.

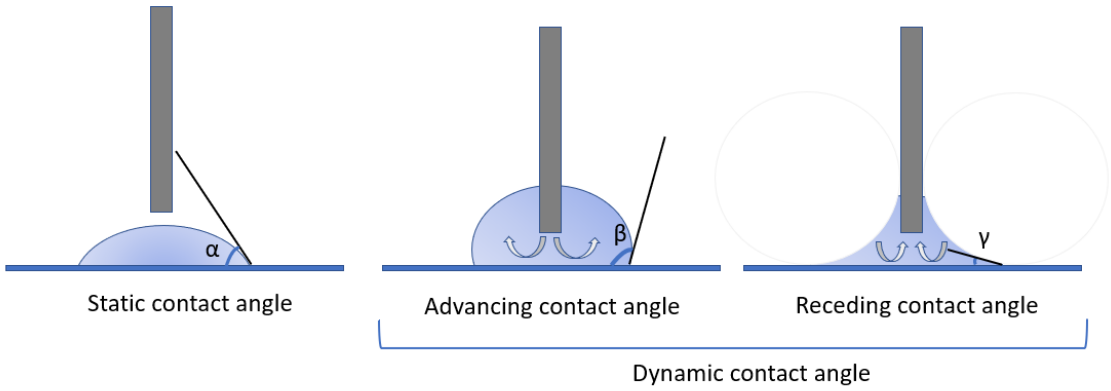

Figure 2.12 Static and dynamic contact angles

Table 2.4 shows static and dynamic contact angles of thiol-ene resin with different integer ratios from 1:1 to 1:5. With the increase of alkene component, the static contact angle increases. Alkyl group is a typical function group with hydrophobic effect.[15] Alkene group is relatively less hydrophobic than alkyl group but still a water-repellent function group.[16] Alkene groups are insoluble in water. The polarity of alkenes is lower than that of many other substances. The presence of alkene components on the surface reduces the polarity of the surface, making it less attractive to polar liquids, like water, to wet it. An increased contact angle can also be attributed to the reduced interaction between liquid and surface. Besides, the presence of an alkene component on the surface reduces the

surface energy, making it less favorable for the liquid droplet to spread. Thus, the droplet tends to become more spherical, increasing the contact angle. The same tendency goes to advancing and receding contact angle. In total, OSTE surface with higher ratio of alkene group is more hydrophobic. The static, advancing and receding contact angles increase with the increase of alkene ratio from 1:1 to 1:5.

Table 2.4 Water contact angle of thiol-ene resin with different ratios. Every sample was tested 3 times and standard deviation was calculated.

Ratio of thiol:ene	1:1	1:2	1:3	1:4	1:5
Static contact angle	53±1	60 ± 2	61 ± 3	68±1	70±1
Advancing contact angle	57±1	63 ± 1	68±1	69±1	*See Note*
Receding contact angle	17±1	27 ± 1	28±2	34±1	*See Note*

Note: The advancing and receding contact angle of thiol:ene=1:5 varied very unevenly. And the variance was very large, more than 10 degrees. The values were not comparable with the dynamic contact angle values of other surfaces. Therefore, the specific values were not given here.

2.2.3.4 Bacteria adhesion on the surface of alkene excess OSTE resin

Our aim is to develop OSTE resins that can be applied as biomaterials for cell culture and tissue engineering. Therefore, a comprehensive understanding of bacteria and cell bioadhesion properties of OSTE resin helps us to harness it for cells. According to our knowledge, bacteria adhesion on OSTE resin has not been evaluated yet. In this part, bacteria and cell adhesion experiments were performed to explore their behavior on OSTE surface with different ratios.

Gram negative Green Fluorescent Protein-expressing *Escherichia coli* (GFP *E. coli*) MG1655 has been widely used and is a well-known model organism with well-characterized plasmid. GFP *E. coli* is easy to cultivate, and the expression of green fluorescent protein makes counting very convenient. Hence, we chose GFP *E. coli* to do adhesion experiments on the surface of our OSTE resin. The adhesion experiments were performed three times for each sample.

For each ratio OSTE resin, 2 wt% Irgacure 651 was added as photoinitiator. Several drops of resin were spread on the bottom of 35mm Petri dish then cured with 7.2 mW/cm^{-2} 254 nm UV for 10 minutes. Then the OSTE coated Petri dishes were washed with methanol and dried naturally overnight at room temperature. 2 ml 1 x 10^8 cfu/ml was seeded on each surface then incubated for 1h

at 37 ºC with 0.5% CO_2. Then the floating bacteria were removed by washings. For each sample, 10 images were taken with Leica fluorescence microscope to get an average number of bacteria The objective of here is 20× water lens. The size of the field of view per images is 0.149 cm^{-2}.

Figure 2.16 shows the adhesive bacteria number on different ratio of thiol-ene resin. The numbers of bacteria were roughly at the same level with a little trend to increase with the higher 'ene' ratio. From the contact angles of six ratios of thiol-ene resin revealed in **Table 2.4**, we can know that with the increase of free "ene" composition on the surface, the hydrophobicity of the surface also increases. *E. coli* tended to congregate more on highly hydrophobic surfaces, which is the same as Arias *et al.*[17] revealed in their test. One point that needs to be emphasized is that not only hydrophobicity but also other material physicochemical properties like surface chemistry, surface energy and mechanical properties will influence the bacteria adhesion.[18,19]

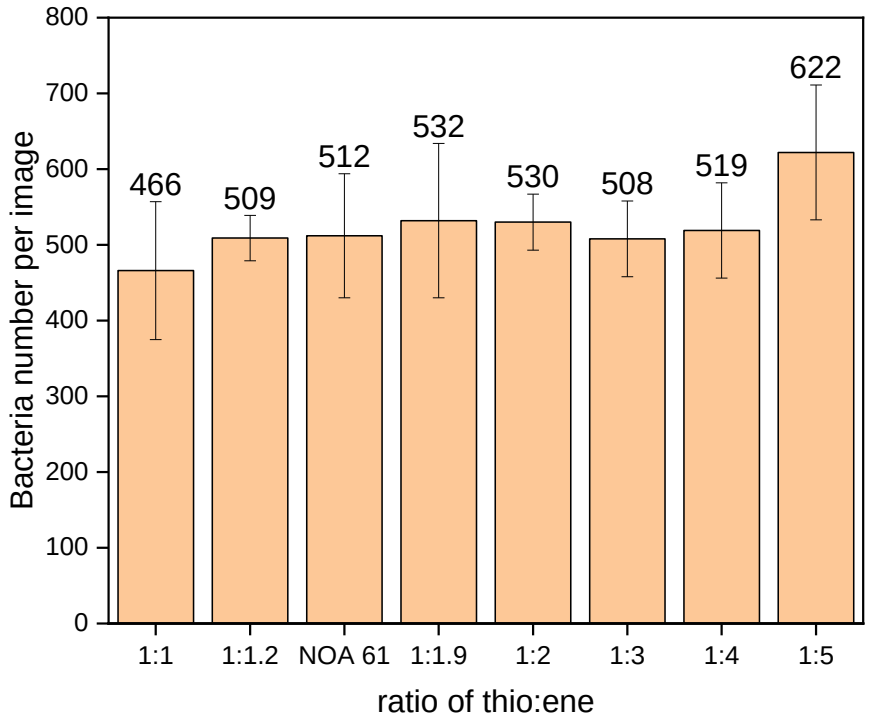

Figure 2.13 Adhesive bacteria number per image (0.0015 cm^{-2}) on different ratio of thiol:ene resin. The error bar is the standard deviation. n=10.

2.2.4 Mechanical properties of OSTE resins

The mechanical properties of OSTE resins are a crucial aspect that cannot be overlooked to gain a deeper understanding of their behavior. The Young's modulus (E) is a typical indicator of material properties. It describes the tensile and compressive elasticity of the material. The Young's modulus of OSTE resin depends on the structures of thiol and alkene components and also on their proportions. With the same thiol and alkene, Carlborg *et al.*[4] showed the E modulus of a thiol-ene 1.9:1 resin is 250 MPa at 25 °C, with a glass transition temperature (Tg) at 35 °C. With more choices of different molecules and ratios, Haraldsson *et al.*[2] showed that in general, E modulus of OSTE is in the range of 10 MPa < E < 2000 MPa. Handorf *et al.*[20] shows the general range of Young's modulus of organs. The Young's modulus of bone is between 15 MPa < E < 20 MPa (**Figure 2.14**). By tuning the components of OSTE, we can mimic stiffnesses appropriate to provide support for cells.

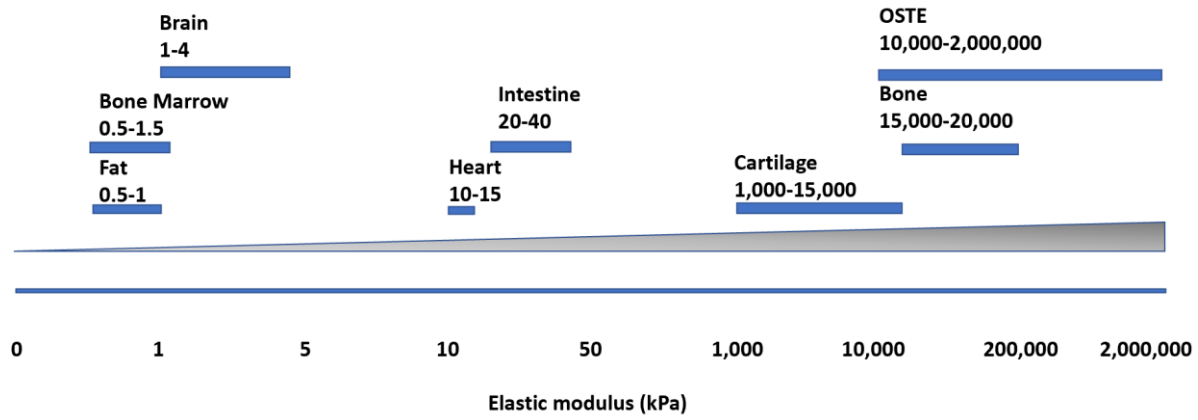

Figure 2.14 The Young's modulus of general organs and OSTE resin

To explore the full range of the formulation, we tried to polymerize the OSTE from thiol excess formulation to alkene excess formulation by one-photon polymerization and two-photon polymerization. The one-photon polymerization was carried out by 7.2 mW/cm^{-2} 254 nm UV for 10 min. The resin was spread on 35 mm Petri dishes. If the resin formed a film after curing and could be removed completely, we assessed that the formulation of the resin was usable. Two-photon polymerization was carried out by microlight microfabrication system. If there was stable structure after fabrication and washing, we kept the ratio of thiol-ene resin as a material for two-photon polymerization. As is shown in **Figure 2.15**, the full range of OSTE resin investigated was from 5:1 to 1:5.

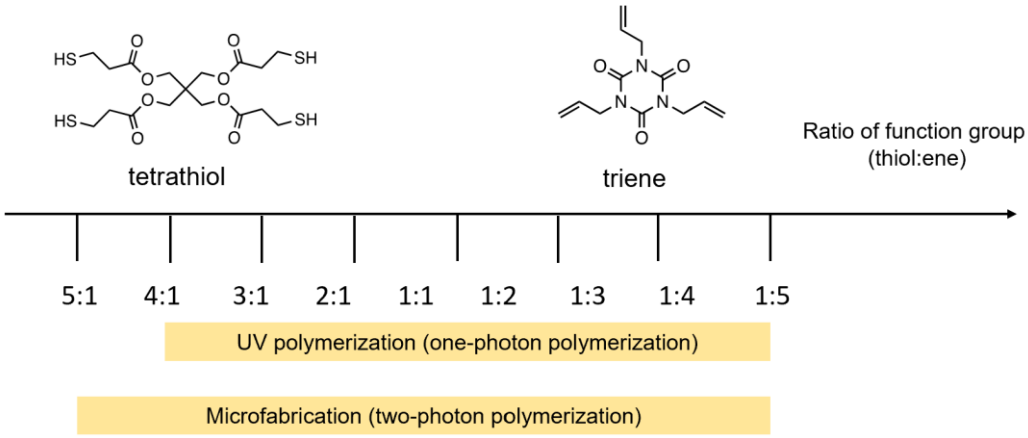

Figure 2.15 The range of available OSTE resin for one- and two-photon polymerization.

2.3 Two-photon polymerization of OSTE resin

2.3.1 Two-photon polymerization system

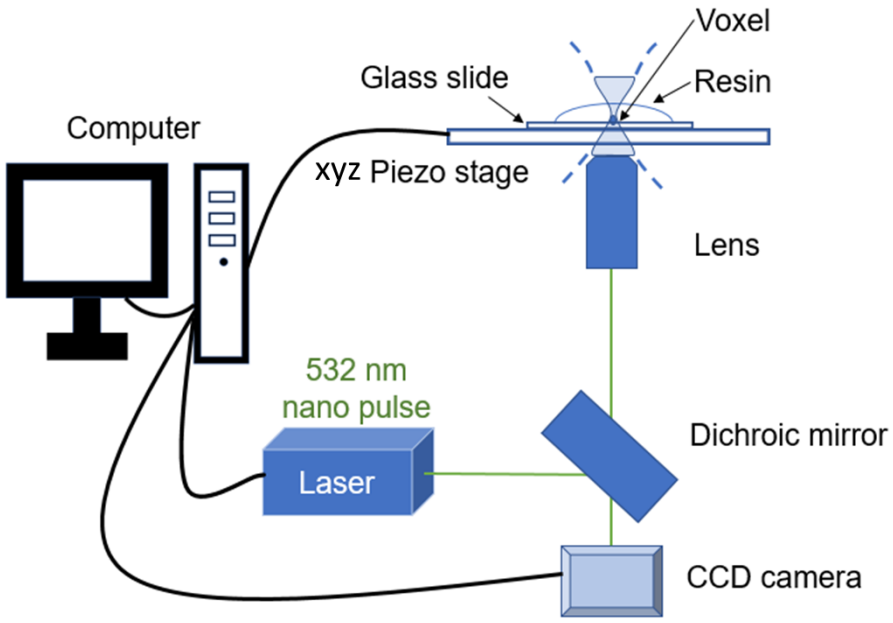

Figure 2.16 The two-photon polymerization system.

A self-improved two-photon polymerization system is shown in **Figure 2.16**.[9,21] The laser source is a 532 nm green laser from QSwitch Teem Photonics laser (Grenoble, France), 10 kHz, 5 ns pulses. The microscope is an IX70 module from Olympus with a 60× water objective (NA 1.2) LPlanApo

or a 100× oil objective (NA 1.4). A xyz-piezo stage and a 3D stage are from Physik Instrumente, Karlsruhe, Germany. A Guppy CCD camera is used during fabrication to monitor the structure. Lithos software is used to control laser focus position, laser gain, exposure time and sequence fabrication.

In our set-up, there are three fabrication optical parameters that we can change, the lens, the laser gain, and the exposure time. For the lens, a 60× (NA 1.2) water lens and a 100× (NA 1.4) oil lens are used. Laser gain is the parameter entered into the laser controller. We tested the output laser intensity with the detector. **Table 2.5** shows the correspondence between the laser gain parameters and the actual output of the laser power. Laser gain is a dimensionless parameter while the unit of the laser power is mW. The range of laser gain is between 0 to 1. Exposure time is the period for every single step with a unit of μs.

Table 2.5 Correspondence between the laser gain and the output of the laser

Laser gain	0.1	0.2	0.3	0.4	0.5	0.6	0.7
Output (mW)	0.18	0.51	0.95	1.52	2.32	3.53	6.80

To validate our formulation of the resin, we designed several 3D structures[9] to test the influence of different photoinitiators. **Figure 2.17** (a) is a regular closed hexagonal structure that we name from its geometrical parameters *D*8*K*1*H*5-closed. *D* is the diameter in μm of the circumcircle of the elementary hexagon and *D*8 means the diameter is 8 μm. *K* represents the number of layers of hexagons that circle the central structure and *K*1 means there is only one layer. *H* is the height of hexagon structure and *H*5 means the height is 5 μm. **Figure 2.17** (b) is a regular open hexagonal structure characterized as *D*8*K*1*H*5-open.The structure is open, our denomination to mean that only the top part is connected. The top hexagonal structure is supported by pillars. **Figure 2.17** (c) is an elongated open structure *l7L14H7-open*. As the explanation by **Figure 2.17** (d), *L* is the length of the

elongated direction based on *D* while *l* is the distance between two vertices in the direction perpendicular to the stretching direction.

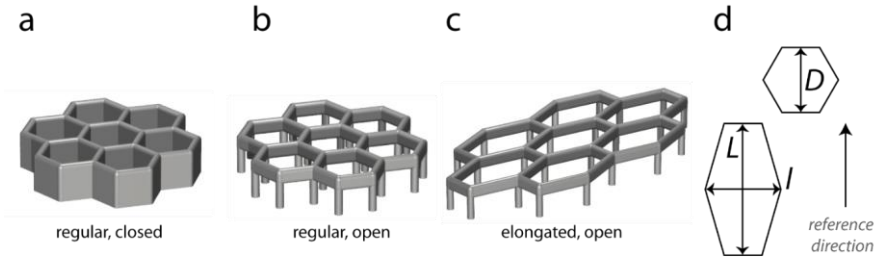

Figure 2.17 Structures designed for two-photon polymerization[9] (a) regular closed hexagonal structure *D*8*K*1*H*5-closed. (b) regular open hexagonal structure *D*8*K*1*H*5-open. (c) elongated open hexagonal structure *l*7L14*H*7-open. (d) elongated direction and parameters.

The aim here is to find a photoinitiator that can be used both in one-photon and two-photon polymerization. Our aim is to find the best photoinitiator which has a big two-photon absorption near 266 nm (half of 532 nm). We have introduced the commonly used photoinitiators used in two-photon polymerization in Chapter I. Table 1.2 shows the one-photon and two-photon absorption of commonly of the photoinitiators. The maximum two-photon absorption wavelength $\lambda^{(2)}_{max}$ of Irgacure 651 is 265 nm. Its two-photon absorption across section δ_{meas} is 28 GM (test by Z-scan method). Irgacure 651 is a good candidate for our needs. $\lambda^{(2)}_{max}$ of Irgacure 369 is 318 nm while δ_{meas} is 27 GM (test by WLC method).[22] We can also try Irgacure 369 as a comparison. Another photoinitiator Irgacure 2959 has maximum one-photon λ_{max} at 275 nm. To our knowledge, there is no data of $\lambda^{(2)}_{max}$ of Irgacure 2959 in the literature. But in Table 1.2, the $\lambda^{(2)}_{max}$ of a photoinitiator is always near its $\lambda_{max.}$ We assume that $\lambda^{(2)}_{max}$ of Irgacure 2959 is also near 275 nm, which is closed to 266 nm. Besides, Irgacure 2959 is popular for its low cell toxicity. Irgacure 2959 is also a possible candidate for the photoinitiator. At last, we chose Irgacure 369, Irgacure 651 and Irgacure 2959 are three possible candidates for our goal.

For the exploration of the possibility of two-photon polymerization with three different photoinitiators Irgacure 369, Irgacure 651 and Irgacure 2959, we chose *D*8*K*1*H*5-open (**Figure 2.17** b) as the structure to do test. Thiol:ene = 1:1 resin was used with0.2 w/w % and 0.5 w/w % photoinitiator.

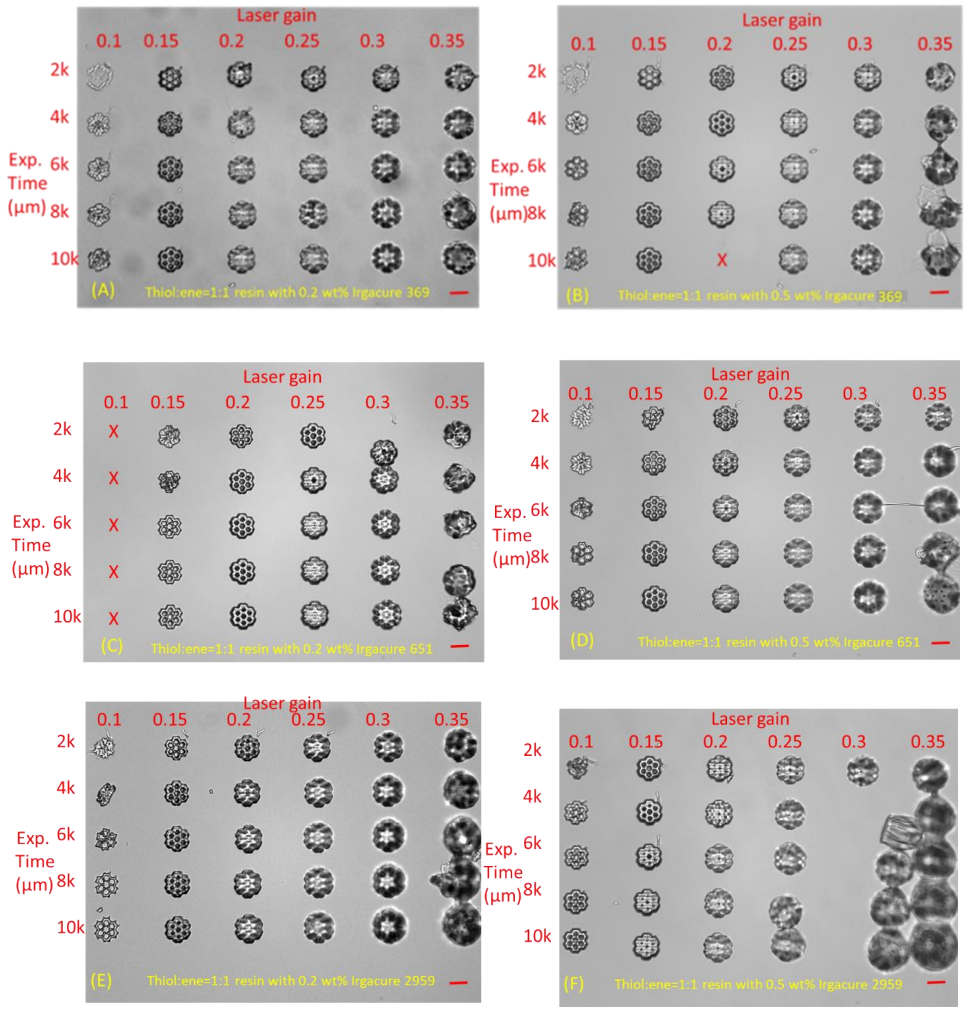

Figure 2.18 Images of matrix of parameters test of two-photon polymerization for small hexagon structure *D8K1H7*-open with thiol:ene =1:1 resin. (A) and (B), parameters test with Irgacure 369. (C) and (D), parameters test with Irgacure 651. (E) and (F), parameters test with Irgacure 2959. Vertical axis, exposure time (µs), k=1000. Horizontal axis, laser gain. Scale bar, 20 µm.

The structures were fabricated on unsilanized glass slides. After fabrication, the unpolymerized part was washed by quick acetone flow. Images were taken by optical microscopy with a water 63x lens. In chapter I, we introduced the theory of two-photon polymerization. Laser power and exposure time are two important parameters that influence resolution and stability. Our goal is to determine the appropriate parameters to obtain stable structures with high resolution. According to the two-photon polymerization theory, lower laser powers with shorter exposure times give smaller voxel and better resolution. **Figure 2.18** shows the results of parameters test with a small open hexagon structure *D8K1H5-open.*

For thiol:ene = 1:1 resin with 0.2 wt% Irgacure 365, the best stable structures came with laser gain (LG) 0.15 for all exposure time (ET). When LG > 0.15, all structures were over-polymerized, When

LG < 0.15, all structures collapsed. With 0.2 wt% Irgacure 365, only two more structures with stables structures were obtained with LG0.2/ET2000 and LG0.2/ET4000.

For thiol:ene = 1:1 resin with 0.2 wt% Irgacure 651, there were no structures with LG0.1. Stable structures with nice resolution came with LG0.15/ET(6k-10k), LG0.2/ET(2k-10k) and LG0.25/ET2k. With a higher concentration of 0.5 wt% Irgacure 651, stable structures came with lower laser gain LG0.15/ET(4000-10000) LG0.2/ET2000.

For thiol:ene = 1:1 resin with 0.2 wt% Irgacure 2959, stable structures with nice resolution came with LG0.1/ET(8000-10000), LG0.2/ET2000. With a higher concentration of 0.5 wt% Irgacure 651, stable structures came with LG0.1/ET(6000-10000), LG0.2/ET2000. With LG higher than 0.2, all the structures polymerized both for 0.2 wt% and 0.5 wt% Irgacure 2959.

Irgacure 2959 showed easier over-polymerization at 0.5wt% and 0.2wt%, which means Irgacure 2959 has a bigger two-photon absorption than Irgacure 369 and Irgacure 651. In terms of resolution and structural stability, 0.5wt% Irgacure 651 and 0.2wt% Irgacure 2959 seemed the best choices of photoinitiators. Considering only the two concentrations (0.2 wt% and 0.5 wt%) we tested, Irgacure 651 brought the highest number of stable structures at lower laser gain. We chose 0.5 wt% Irgacure as the concentration for the later test. Another point that should be pointed out is that more concentration can be tested with all three photoinitiators. With a lower concentration of photoinitiator, the laser power at which we start to get stable structures will be higher and *vice versa*.

In the following experiment, we focused on 0.5 wt% Irgacure 651 as the photoinitiator for the formulation of thiol-ene resin for two-photon polymerization. Besides the thiol:ene ratio 1:1, we tried different ratio from 2:1 to 1:2 with elongated open hexagonal structure *l*7L14*H*7-open (**Figure 2.17** c)

After determining the best parameters on small hexagon structures, we transferred them to big elongated open hexagon structures. **Figure 2.20** (A) shows the elongated structures *l7L14H7-open* with different ratios of thiol-ene resin 2:1, 1.5:1, 1.2:1, 1:1, 1:1.2, 1:1.5, 1:2. 0.5 wt% Irgacure 651 was added for all the formulations as photoinitiator. Here we could find that only the structure fabricated with 1:1.5 thiol-ene was stable on the untreated glass slide after washing with quick acetone flow. The stability of the structure is not only related to the mechanical property but also to the bonds with the glass slide. We tried to compare the stability of the structures on untreated glass slides with that of the structures on silanized glass slides. Before silanization, the glass slides should be cleaned with Piranha solution. Piranha solution is a strong cleaning agent for organic dust. Three parts concentrated sulfuric acid and one part 30 wt% hydrogen peroxide solution are typical mixtures of piranha solution. The 30 mm glass coverslips were cleaned with piranha solution to remove the organic dust on the surface. 3-(trimethoxysilyl)propyl methacrylate was used as the silanizing agent.

Figure 2.19 shows the mechanism of the silanization on the glass. After silanization, the glass was functionalized with methacrylate on the surface.

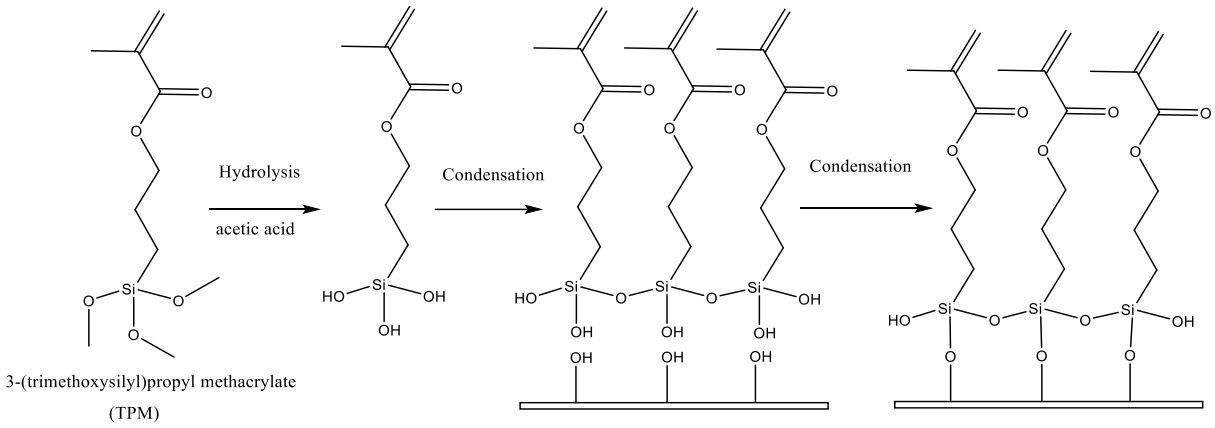

Figure 2.19 Mechanism of silanization on glass.

When we fabricate structures with thiol-ene resin on silanized slides, thiol groups in the resin will react with the methacrylate on the glass by thiol-ene click chemistry. In this way, the structures are tightly bonded on the glass. The structures will be more stable on the substrate. As **Figure 2.20** (B) shows, all the structures were stable after washing with quick acetone flow. There were no edge depressions as the structures on untreated glass slides.

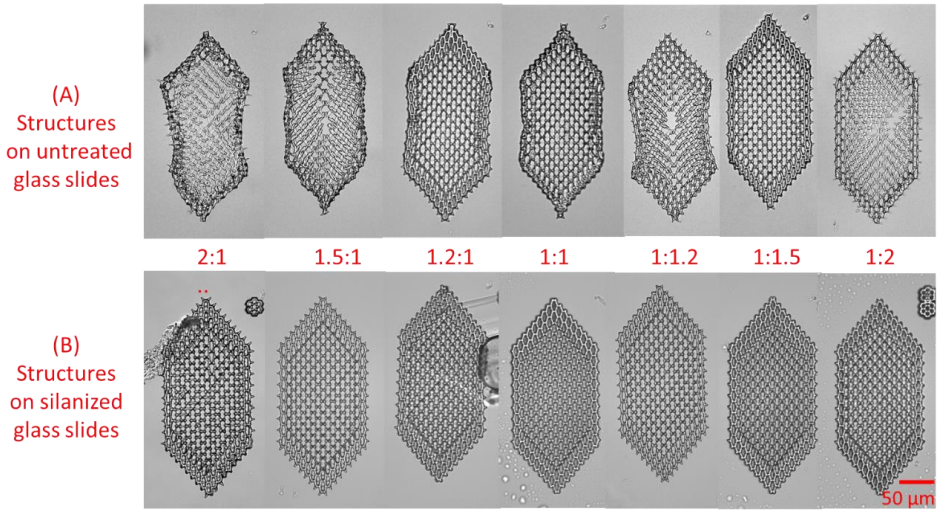

Figure 2.20 Elongated open hexagon structures *l7L14H7-open* with different ratios of thiol-ene resin with 0.5 wt% Irgacure 651 after acetone wash. Fabrication parameters laser gain/exposure time: 0.15/2000 µs.

By now, we can confirm the formula for OSTE resin for two-photon polymerization. 0.5 wt% Irgacure 651 is added as the photoinitiator. Silanized glass slides will help improve the stability of the structures. In the coming experiments, 3D structures will be fabricated on silanized glass slides.

2.3.2 MDCK cells adhesion on two-photon polymerized carpets.

We designed a 280 μm x 280 μm carpet with a line-by-line method. After fabrication by two-photon polymerization, the carpet was washed with quick acetone flow for MDCK adhesion test. MDCK cells were seeded on carpet for two hours followed by twice washing with phosphate-buffered saline (PBS). The floating cells were removed. Then the cells were fixed with 4% paraformaldehyde (PFA) and then strained with phalloidin and Hoechst. From **Figure 2.21** we can find that MDCK cells were randomly located on the carpet. All the cells were well spread on the surface. Here we transfer our MDCK adhesion results from bulk material.

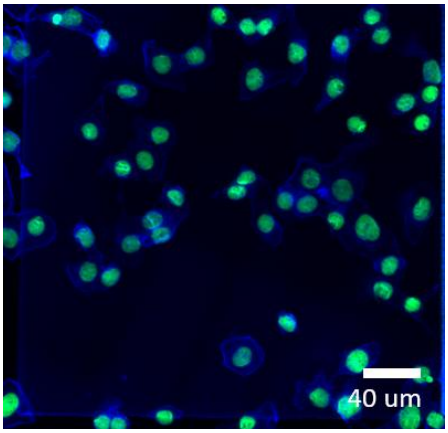

Figure 2.21 MDCK cells on a two-photon polymerized carpet. The image was taken with spinning disk confocal microscope. Labeling, Green, nuclei. Blue, F-actin.

2.4 Parameters of Modification of 2D alkene excess surface by UV (one-photon) grafting

Bioadhesion of bacteria, protein and cells on biomaterials is a critical factor for lots of side effects like infection, inflammation or allergic reaction. It is a crucial topic to design anti-adhesive material to mitigate or even prevent those side effects. Researchers have developed many strategies to prevent cell adhesion, like improving surface free energy, steric repulsion, topography, hydration or electrostatic interaction (**Figure 2.22**).[23]

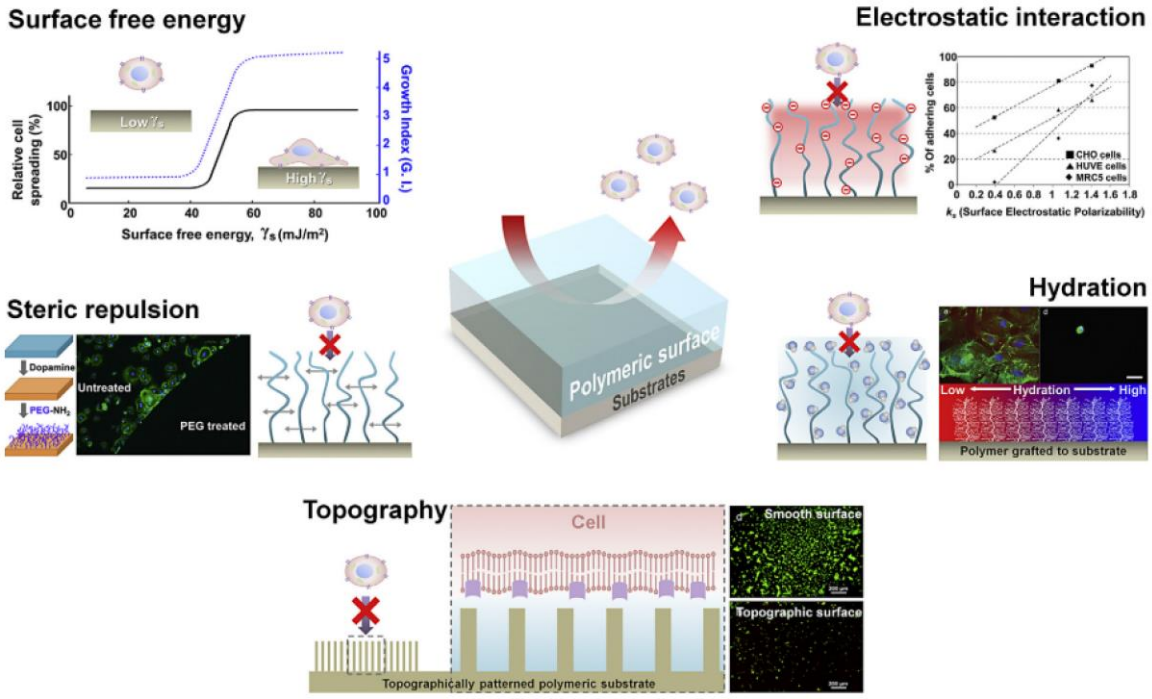

Figure 2.22 Strategies to provide cell anti-adhesive surface: cell sheet engineering, multicellular spheroids, cell encapsulation, and blood contacting devices.[23]

Polyethylene glycol (PEG) has been widely used, such as biomedicine, biomaterials, and drug delivery system. The modification of a surface with PEG can impart several beneficial characteristics, biocompatibility, and most important anti-adhesive property. PEG modification is widely used to control non-specific adhesion.[24] As shown in **Figure 2.22,** PEG can offer a layer of brush on the surface of the material, providing steric repulsion to prevent bacteria and cell adhesion. At the same time, PEG combined with water forms a hydrated layer. In addition, as will be discussed in chapter III, besides surface chemistry, tunning topography of the surface is also a way to control the adhesion behavior.[25]

PEG modification can be achieved through various techniques, including physical adsorption, covalent bonding, or self-assembly methods. The most stable modification method for arming the material surface is covalent boding. From our former experiment, OSTE resin has been proved to be bacteria and cell adhesive material. With covalent PEG on the surface, we predict that an anti-adhesive surface will be constructed on the surface of OSTE resin. It typically requires functionalization of the surface with reactive groups, such as amino (NH_2), carboxyl (COOH), or thiol (SH) groups. OSTE resin with alkene excess can be modified with both “grafting from” and “grafting to” methods. “Grafting from” means surface-initiated polymerization with involves initiation, chain growth and termination. “Grafting from” needs a complex control progress. While the “grafting to” strategy on alkene excess surface can be achieved by thiol-ene click reaction on the

precise control. PEG layer on the surface provides a steric layer and hydrated water layer, thus rejecting cells.

From the evaluation before, we already know that alkene excess surfaces are cell-adhesive surfaces, no matter cured by UV or TPP. One of aims of this thesis is to construct cell-repellent surfaces on the basis of OSTE resin both on 2D and 3D surfaces. PEG would be nice choice for us. **Figure 2.23** shows the "grafting to" strategy that we used in our surface modification.

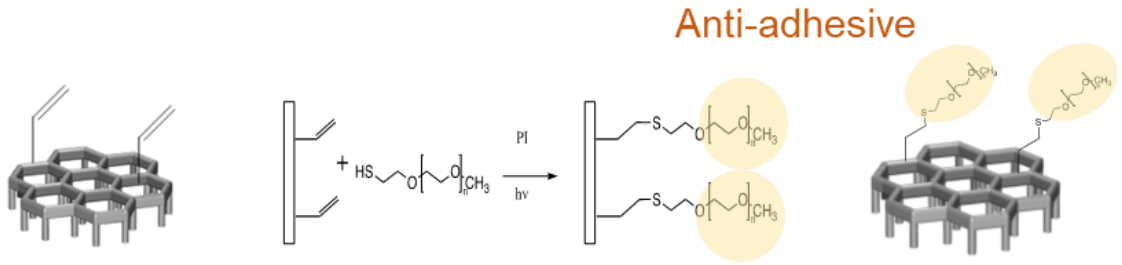

Figure 2.23 "Grafing to" strategy of surface modification on alkene excess surface of OSTE resin with Me-PEG-SH by thiol-ene click chemistry.

PEG grafting relies on a photo-induced thiol-ene click reaction. We have generally shown the mechanism of thiol-ene click in chapter I. Here specifically, we briefly describe the process of surface grafting on alkene excess surface. UV-induced radicals from photoinitiator will react with Me-PEG-SH producing new radical Me-PEG-S·. Then Me-PEG-S· will react with the alkyl group on the surface, forming the grafting on the surface. Grafted PEG layer on the surface will produce an anti-adhesive layer on the surface. In the following part, we explored the parameters for Me-PEG-SH grafting to obtain the best anti-adhesive property.

There are several keys factors that influence the success and efficiency of thiol-ene click reaction on the surface. First, the reactivity of both thiol and alkene groups. Thiol-PEG molecules in solution may have multiple conformations, and not all the conformations are favorable for the click reaction. The conformations of PEG chain in solution are influenced by various factors, like the chain length, chain architecture and the solvent. Here we chose several linear thiol-PEG derivatives as the candidates to be grafted to the surface. The alkene groups density on the surface will also influence the final grafting density on the surface. Besides, the concentration of photoinitiator and UV grafting time will influence the grafting.

Table 2.6 shows the information of Me-PEG-SH derivatives used in this study. There are four kinds of Me-PEG-SH. *O*-(2-Mercaptoethyl)-*O'*-methyl-hexa(ethylene glycol) (from *Sigma*) exhibiting 7 ethylene glycol units (Me-PEG308-SH) is liquid in room temperature. Me-PEG750-SH, Me-

PEG2000-SH, Me-PEG5000-SH (from *RAPP Polymer*) are solid at room temperature. The only difference between those four PEG-SH derivatives is the length of their chains. The Flory radius (R_F) was calculated by $R_F = \alpha N^{3/5}$ where N is the number of subunits in PEG.[26] We have introduced that the conformation of PEG in crystalized form is in a *tgg* helical form in chapter I. Oesterhelt[27] *et al.* showed that PEG chains keeps in a *tgg* helical conformation in water, the unit length of PEO α is 0.28 nm. The contour length of Me-PEG-SH chain is its length at maximum physically possible extension.

Table 2.6 Average unit and molecule weight of different PEGs

Linear Formula	Number of PEO unit (-CH_2-CH_2-O-)	Mw of PEG (Dalton)	Contour length (nm)	Flory radius (nm)
Me-PEG308-SH	7	308	2.0	0.9
Me-PEG750-SH	17	750	4.8	1.5
Me-PEG2000-SH	45	2000	12.6	2.8
Me-PEG5000-SH	114	5000	31.9	4.8

In this part, we explored the grafting parameters for OSTE 2D surface by thiol-ene click chemistry. During the process, ATR-FTIR and water contact angles, as well as X-ray photoelectron spectroscopy, will be measured to characterize the modification. Bacteria and cell adhesion assays will be used to monitor the anti-adhesive properties of the modified OSTE surface.

2.4.1 Bacteria adhesion experiment on Me-PEG5000-SH modified surface.

In the literature, PEG5000 modified surfaces have been widely shown to be anti-adhesive properties.[28,29] Here we started with Me-PEG5000-SH grafting on thiol:ene = 1:1.9 surface. The parameters that could influence the grafting can be UV grafting time, concentration of Me-PEG5000-SH and photoinitiator. In the sub-section, we designed one set of experiments to validate the best grafting parameters.

First, we tested the influence of different grafting times. The procedure was as follows Me-PEG5000-SH was dissolved in methanol at 10 mg/ml, 5 w/w% Irgacure 651 as photoinitiator. The grafting was performed under 7.2 mW/cm^{-2} 254 nm UV illumination for 10, 30 and 60 minutes respectively. All the modified surface was evaluated by bacteria adhesive experiment following the protocol described

in 2.2.3. **Figure 2.24** showed the results of bacteria adhesive experiment. After 10 minutes grafting, the bacteria number on the modified surface reached a plateau. 10 minutes illumination was enough to reach the optimal anti-adhesive properties with Me-PEG5000-SH. We set 10 minutes UV grafting for the later experiment.

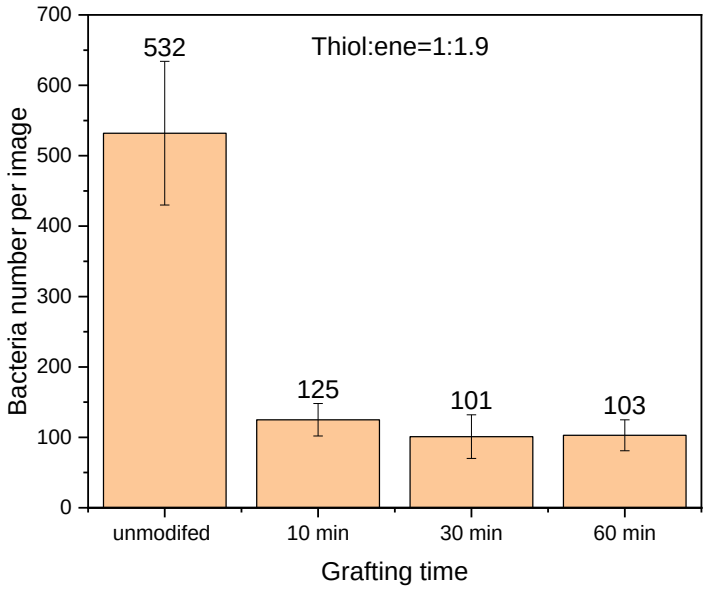

Figure 2.24 Average bacterial number per image (0.0015 cm^{-2}) of *E. coli* MG1655 on Me-PEG5000-SH modified thiol:ene=1:1.9 resin surface with different grafting times. The same weight centration photoinitiator, 5 w/w% Irgacure 651 was added as photoinitiator. The error bar is the standard deviation. One set of experiments, mean value of 10 images for each sample.

In the following experiment, we kept 5 w/w% Irgacure 651 relevant to the weight of Me-PEG5000-SH as photoinitiator and 10 minutes UV grafting time but tested the varied concentrations of Me-PEG5000-SH, 10/40/80 mg/ml, to graft the same surface thiol:ene =1:1.9 OSTE resin. As shown in **Figure 2.25**, the bacteria adhesion results showed that 40 mg/ml is the best compromise for an optimal grafting density. When the concentration was 10 mg/ml, the Me-PEG5000-SH was not high enough to obtain anti-adhesive properties. When concentration increased to 80 mg/ml, the number of bacteria adhering on the modified surface remained similar as the surface modified with 40 mg/ml Me-PEG5000-SH. To use less Me-PEG5000-SH to acquire nice anti-adhesive property, we concluded that 40 mg/ml Me-PEG5000-SH is a nice concentration for surface modification.

Here the concentration of photoinitiator was set as same weight concentration, 5 w/w% to the weight of Me-PEG5000-SH. We also set the concentration of photoinitiator as same mass concentration to

graft the surface of thiol:ene = 1:1.9 OSTE resin. 4 mg/ml Irgacure 651. **Figure 2.26** shows that for 10/40/ 80 mg/ml Me-PEG5000-SH modified surfaces, the bacteria numbers were at the same level as shown in **Figure 2.25**. Note, the control in **Figure 2.24**, **Figure 2.25** and **Figure 2.26** was the same result of one experiment. Those three figures were from a big set of experiment.

By now, we concluded that 40 mg/ml Me-PEG5000-SH with 5 w/w% Irgacure 651 as photoinitiator, 10 minutes UV grafting time as the parameters for the later experiment. We also tracked the ATR-FTIR before and after grafting with those concluded parameters. But we did not see clear differences that came from the grafted Me-PEG5000-OH. The possible reason was that the grafted Me-PEG5000-OH density was not high enough to be detected by ATR-FTIR.

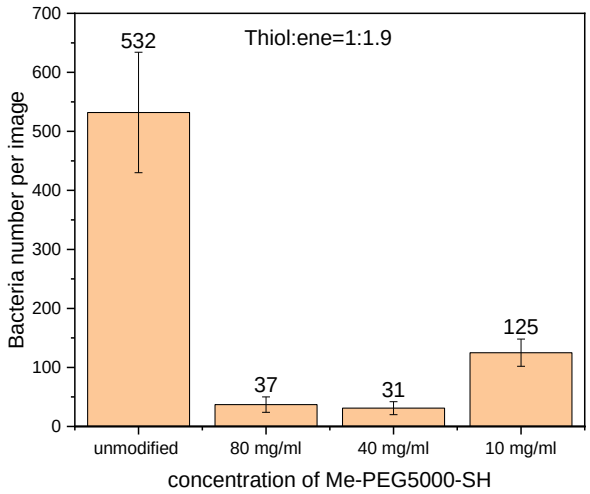

Figure 2.25 Average numbers per image (0.0015 cm^{-2}) of *E. coli* MG1655 in one image on OSTE surface modified with different concentrations of Me-PEG5000-SH. The same weight centration photoinitiator, 5 w/w% Irgacure 651 was added as photoinitiator. Grafting time was 10 minutes. The error bar is the standard deviation.One set of experiments, mean value of 10 images for each sample.

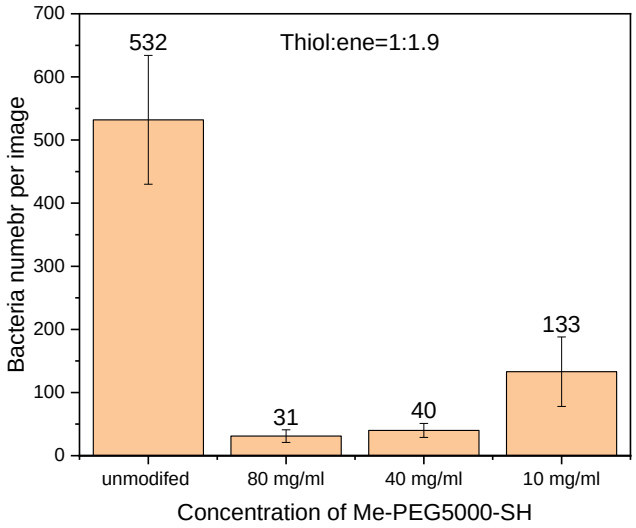

Figure 2.26 Average numbers per image (0.0015 cm^{-2}) of *E. coli* MG1655 in one image on OSTE surface modified with different concentrations of Me-PEG5000-SH with the same molar concentration photoinitiator, 4 mg/ml Irgacure 651 as photoinitiator**.** Grafting time was 10 minutes. The error bar is the standard deviation. One set of experiments, mean value of 10 images for each sample.

2.4.2 The effect of thiol-ene ratio of OSTE (1:1 to 1:5)

The grafting density on the surface influences the adhesion of bacteria and cells on the surface. The grafting density is linked to not only the parameters we concluded above (PEG concentration, photoinitiator and grafting time) but also the density of the alkene groups on the surface. Here, we tried to graft Me-PEG5000-SH on the surface of OSTE resin with different ratios of thiol:ene. We unified the parameters for modification as follows, 40 mg/ml Me-PEG5000-SH with 5 w/w% Irgacure 651 as photoinitiator in methanol, 254 nm UV illumination for 10 min. Then all the surfaces were washed with methanal bath 3 times, 5 minutes each time on an orbital shaker. After dying in air, we performed the same GFP *E. coli* MG1655 adhesive experiment as before. **Figure 2.27** shows the bacteria numbers on the different ratios of OSTE resin.

Before grafting, the average numbers of *E. coli* per image (0.0015 cm^{-2}) were all very high and there was a trend for the number of bacteria to increase with alkene fraction. After grafting with Me-PEG5000-SH, the average bacteria numbers decreased with the increase of alkene proportions accounting for a higher grafting density of Me-PEG5000-SH with increasing alkene density.

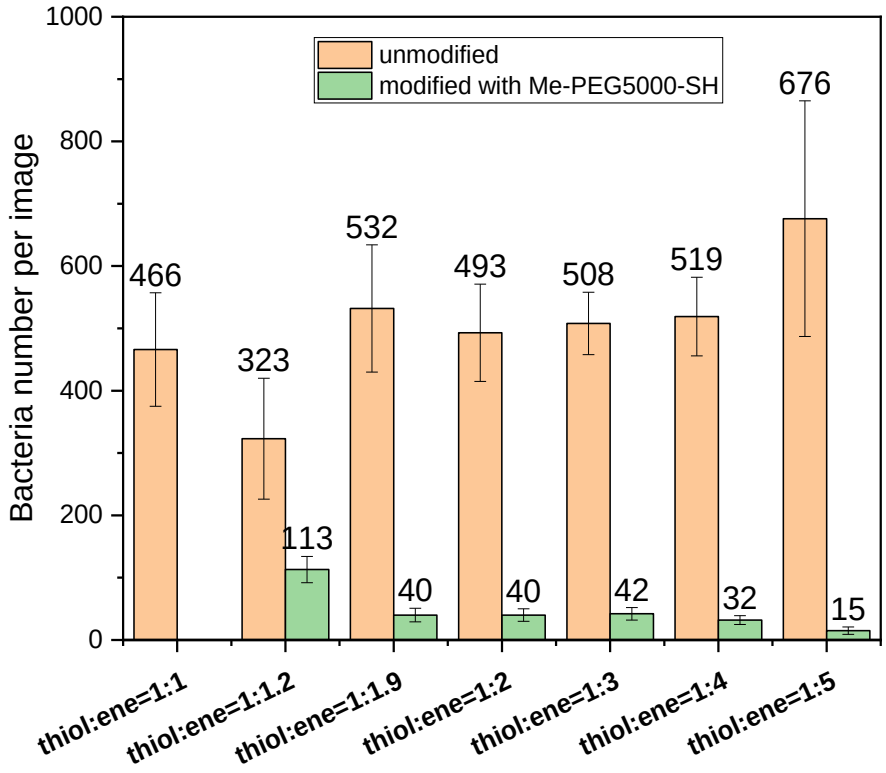

Figure 2.27 Average numbers per image (0.0015 cm^{-2}) of *E. coli* MG1655 on modified and unmodified OSTE surfaces with different ratio of thiol:ene. 40 mg/ml ($8x10^{-3}$ mmol/ml) Me-PEG5000-SH with 5 w/w% Irgacure 651 as photoinitiator in methanol. Grafting time was 10 minutes. The error bar is the standard deviation. One set of experiments, mean value of 10 images for each sample.

2.4.3 The effect of length of Me-PEG-SH

In the section above, we only grafted Me-PEG5000-SH on the surfaces of alkene excess OSTE resin. In **Table 2.6,** we revealed Me-PEG-SH with different lengths. To explore the effect of length of Me-PEG-SH, we designed a comparison between the long chain Me-PEG5000-SH and the short chain Me-PEG308-SH.

The concentration of Me-PEG5000-SH in methanol used for modification 40 mg/ml equals to $8x10^{-3}$ mmol/ml. We tried the same molar concentration of Me-PEG308-SH in methanol to modify the thiol:ene= 1:5 OSTE resin. The results showed that bacteria on Me-PEG308-SH modified surface was only reduced to about 1/3 of unmodified (**Figure 2.28** and **Figure 2.29**). Compared to Me-PEG5000-SH modified surface, the bacteria number on Me-PEG308-SH modified surface was around 12 times more than that on Me-PEG5000-SH modified surface. With the same molar concentration in methanol for grafting, longer Me-PEG5000-SH covers more area of the surface than

Me-PEG308-SH. If we want to obtain the same level anti-adhesion to *E. coli*, the grafting density of Me-PEG308-SH should be higher than that of Me-PEG5000-SH since Me-PEG308-SH has a shorter chain. In the following section, we paid attention to higher grafting density of Me-PEG308-SH.

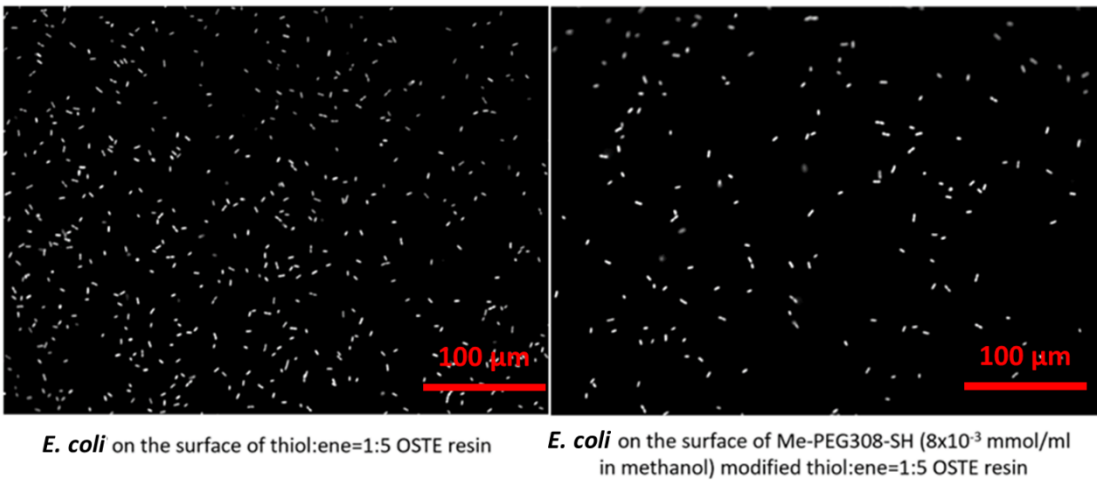

Figure 2.28 *E. coli* MG1655 on the surface of unmodified and Me-PEG308-SH modified thiol:ene = 1:5 OSTE resin. White dot, *E. coli* MG1655. Scale bar, 100 µm.

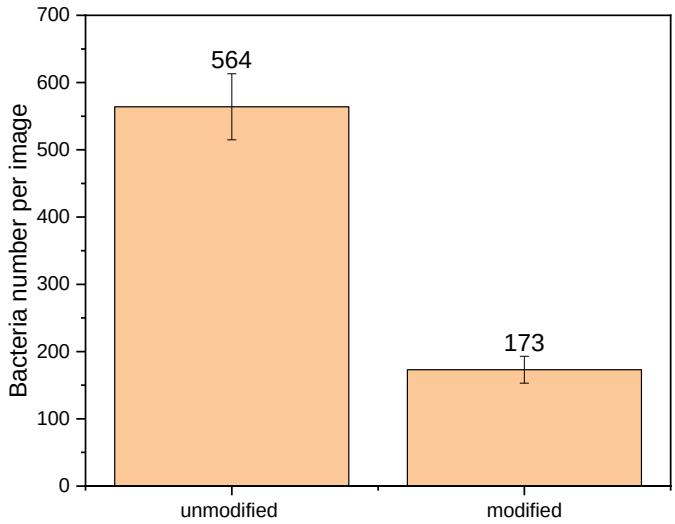

Figure 2.29 Average number per image (0.0015 cm^{-2}) of *E. coli* MG1655 on the surface of unmodified and Me-PEG308-SH modified thiol:ene =1:5 OSTE resin. $8x10^{-3}$ mmol/ml Me-PEG308-SH was used with 5 w/w% Irgacure 651 as photoinitiator in methanol. The grafting time was 10 minutes. All the parameters were the same as that used for Me-PEG5000-SH grafting. The error bar is the standard deviation. One set of experiments, mean value of 10 images for each sample.

2.4.4 Effect of the concentration of Me-PEG308-SH

The number of average units of -CH_2-CH_2-O- of Me-PEG5000-SH is 45 while that of Me-PEG308-SH is only 7. According to the Pierre-Gille de Gennes theory, the conformation of PEG grafted on a surface can be in three conditions. **Figure 2.30** shows the possible conformations of grafted PEG chains on a substrate depending on its density. ***D*** is the distance between two neighboring grafting points. L is the length of PEG chain. We have summarized the $\mathbf{R_F}$ of Me-PEG-SH in **Table 2.6.** The Flory radius $\mathbf{R_F}$ of Me-PEG5000-SH is 4.8 nm while that of Me-PEG308-SH is 0.9 nm. No matter the conformation of Me-PEG-SH is mushroom or Brush. The density to cover all the surface is higher for shorter Me-PEG308-SH.

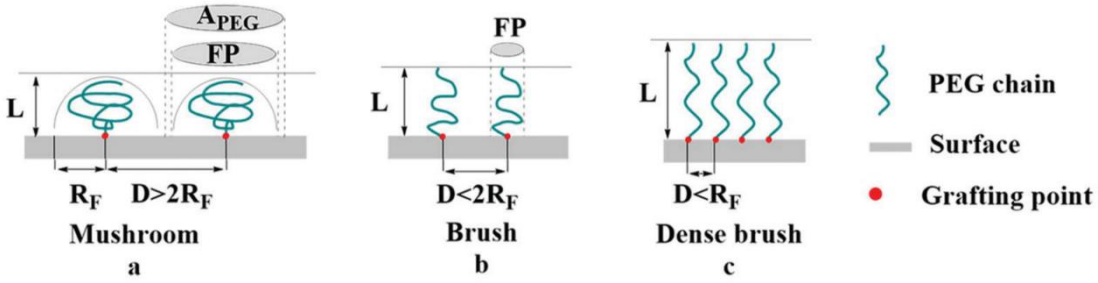

Figure 2.30 Different conformations of grafted PEG chains on substrate[30]

If the conformation of Me-PEG308-SH was in brush or dense brush, there will be no space for E. coli settlement. For the set of experiments above in sub-section 2.4.3, we can find that lots of *E. coli* on Me-PEG308-SH modified thiol:ene = 1:5 OSTE resin (**Figure 2.28**). So, the conformation of Me-PEG308-SH mush be in mushroom condition. For high density grafting, Kingshott *et al.*[31] concluded that "cloud point (CP)" grafting is the best grafting condition for high density. Cloud point refers to the temperature blow which the solution will undergo phase separation or phase transition. Pingle *et al.*[32] successfully obtained a PEG-aldehyde modified surface to prevent *Pseudomonas aeruginosa via* CP grafting. Al-Ani *et al.*[33] grafted PEG5000-aldehyde onto amino-rich surface at 60 °C by reductive amination CP grafting. Our grafting strategy here was photo-induced thiol-ene click reaction. Heating is not a possible choice for our setting. Methanol is a good solvent to dissolve all the four kinds of Me-PEG-SH (PEG Mw = 308, 750, 2000, 5000). If we chose another solvent with lower solubility of PEG, we may have a condition like CP grafting. The meaning of CP grafting is to get a very high concentration of PEG in the solution and also reduced chain repulsion during the grafting reaction and hence greater chain packing density at the interface.[31] In our lab, we have successfully constructed a high density of Me-PEG308-SH molecular layers on the material surface by click chemistry on silicon wafer and glass slides.[34] A high grafting density was realized by

dissolve Me-PEG308-SH in glycerol. Glycerol is very viscous. It is very easy to get a high density of Me-PEG308-SH dissolved in glycerol with a tiny amount chemical. In the following experiment, we tried to replace methanol with glycerol as a solvent to graft Me-PEG-SH on to OSTE resin at high density.

Me-PEG5000-SH and Me-PEG2000-SH are powders at room temperature. We tried to dissolve Me-PEG5000-SH and Me-PEG2000-SH in glycerol at 40 mg/ml. The samples were mixed with vortex rotating mixer overnight. They were still not dissolved. Me-PEG750-SH is a highly sticky liquid and almost in solid state. But after 2 hours of heating at 40 ^{o}C, Me-PEG750-SH turned to liquid. We tried to mix Me-PEG750-SH and glycerol and heated it to 40 ^{o}C. The mixture was also liquid. Me-PEG308-SH is liquid in room temperature. We tried to mix Me-PEG308-SH and glycerol 1:1 (v/v) with vortex mixer overnight. The mixture was in liquid state.

Here we tried Me-PEG308-SH with glycerol. The grafting method[34] was as follows. Me-PEG308-SH was dissolved in glycerol (1.5 mmol/ml). Irgacure 651 was added at 20 mM as photoinitiator. Quartz glass was covered onto the drop on the surface. Grafting was performed under 7.2 mW/cm^{-2} 254 nm UV illumination for 10 min. Similarly, we tried grafting Me-PEG308-SH on the alkene excess surface of OSTE. The grafting was performed on thiol:ene =1:2, 1:3, 1:4, 1:5 resin. To distinguish from the protocol of modification with Me-PEG308-SH/methanol/Irgacure 651 in section 2.4.3, we name this protocol as Me-PEG308-SH/glycerol/Irgacure 651 system in the following analysis. We tracked the ATR-FTIR before and after grafting.

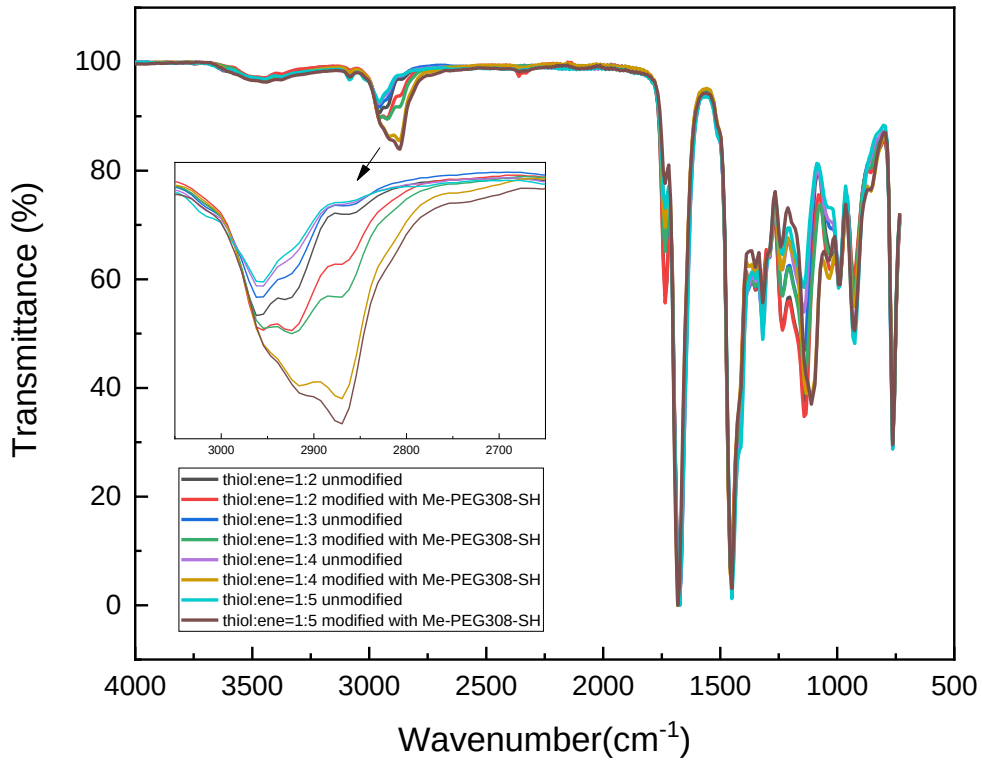

Figure 2.31 ATR-FTIR of unmodified and Me-PEG308-SH modified alkene excess thiol:ene resin from 1:2 to 1:5. The surface modification was performed with Me-PEG308-SH/glycerol/Irgacure 651 system. Grafting was performed illumination with 7.2 mW/cm-2 254 nm UV for 10 minutes.

Figure 2.31 shows the ATR-FTIR signal change of Me-PEG308-SH modified alkene excess OSTE resin. After modification with Me-PEG308-SH, the signal at 2869 cm^{-1} increases. This enhancement of the absorption signal 2869 cm^{-1} comes from the stretch of the repeated -CH_2-CH_2-O- skeleton in Me-PEG308-SH. In a longitudinal comparison, signal at 2869 cm^{-1} of Me-PEG308-SH modified surface becomes stronger while increasing the proportion of alkene groups on the surface.

To further confirm the grafting of Me-PEG308-SH, we used X-ray Photoelectron Spectrometer (XPS) to figure out the grafting. We tested XPS of fours samples in

Table 2.7.

Table 2.7 Samples for XPS analysis. Surface modification was performed with Me-PEG308-SH/glycerol/Irgacure 651 system. Grafting was performed illumination with 7.2 mW/cm-2 254 nm UV for 10 minutes.

	Thiol:ene = 1:2		Thiol:ene = 1:5	
Samples	Sample 1	Sample 2	Sample 3	Sample 4
Modification	unmodified	Me-PEG308-SH	unmodified	Me-PEG308-SH

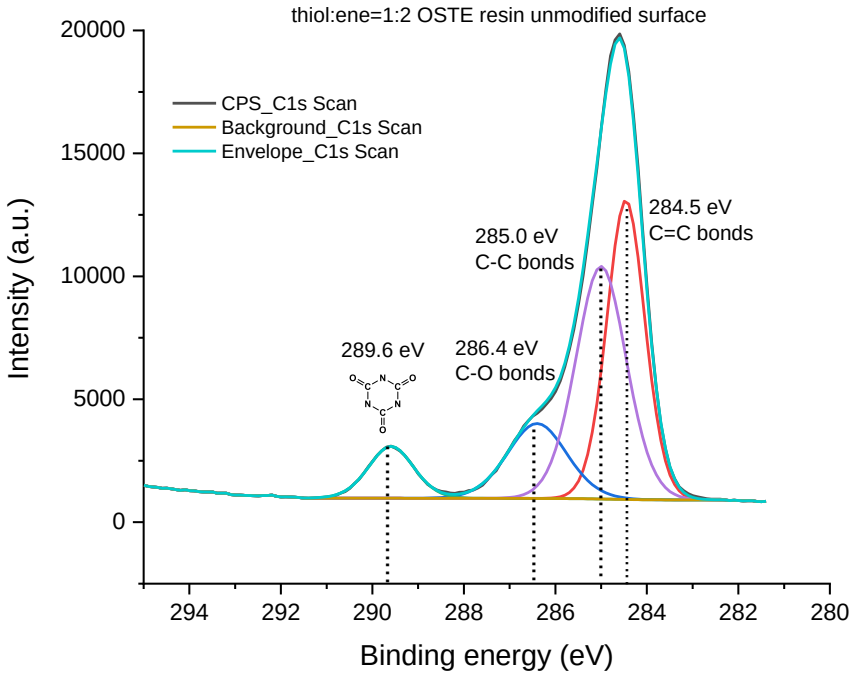

Figure 2.32 XPS spectrum of unmodified thiol:ene = 1:2 OSTE resin surface (Sample 1).

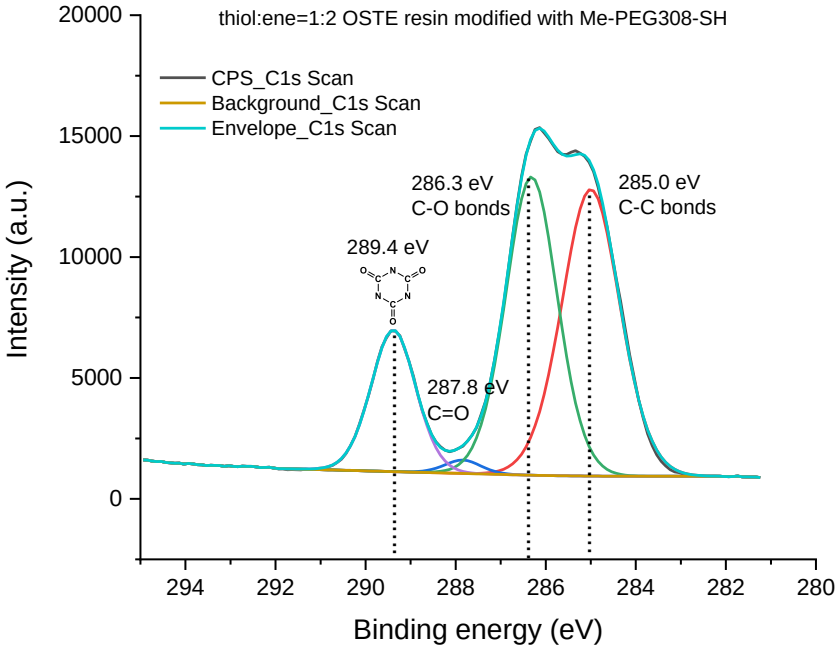

Figure 2.33 XPS spectrum of thiol:ene = 1:2 OSTE resin surface modified with Me-PEG308-SH/glycerol/Irgacure 651 system (Sample 2).

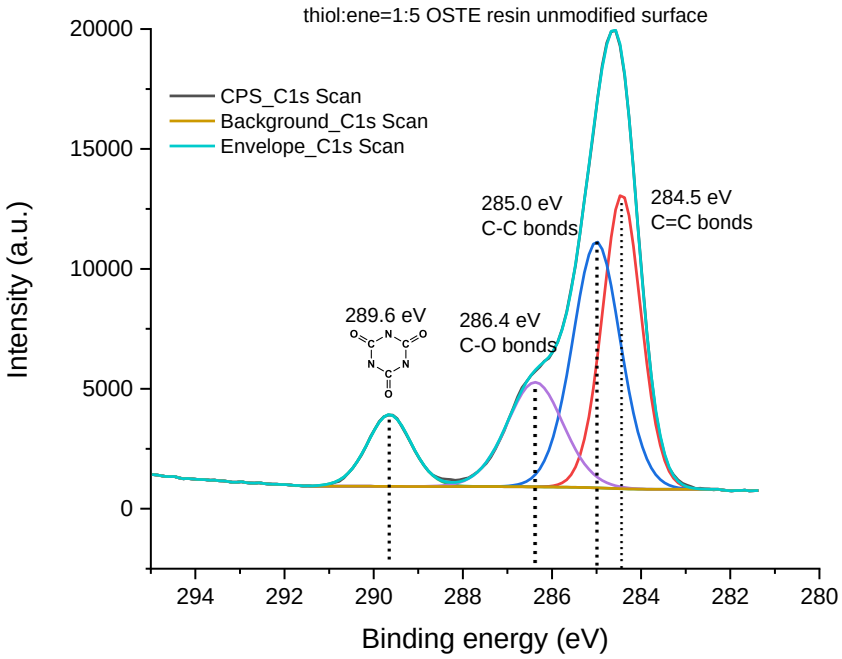

Figure 2.34 XPS spectrum of unmodified thiol:ene = 1:5 OSTE resin surface (Sample 3).

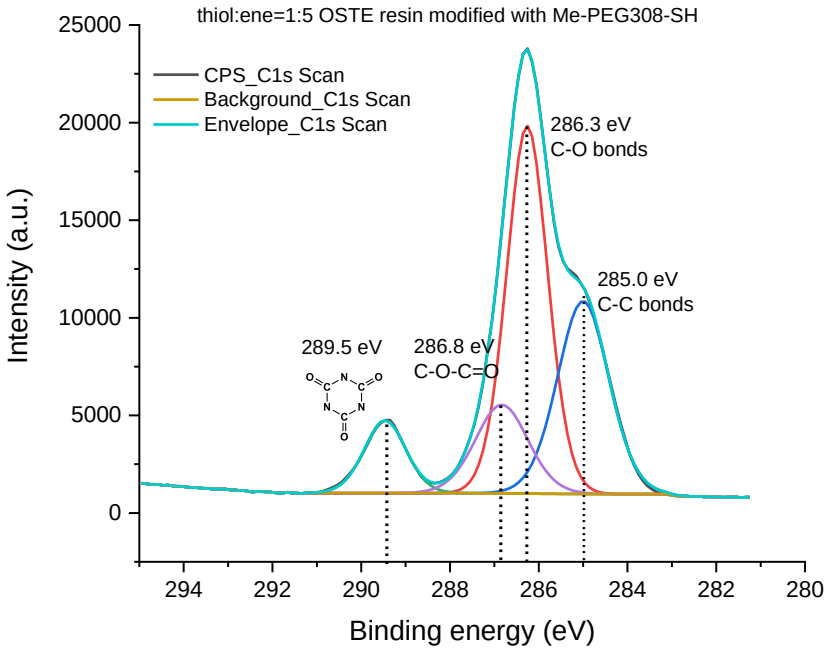

Figure 2.35 XPS spectrum of thiol:ene = 1:5 OSTE resin surface modified with Me-PEG308-SH/glycerol/Irgacure 651 system (Sample 4).

Figure 2.32 and **Figure 2.34** show the carbon C1s XPS spectrum of unmodified thiol:ene = 1:2 and 1:5 OSTE surface. We can find the peak at 284.5 eV (C=C) was higher than the peak at 285.0 eV (C-C). After grafting with Me-PEG308-SH/glycerol/Irgacure 651, the peak at 284.5 eV (C=C) disappeared (**Figure 2.33** and **Figure 2.35**). The peak at 285.0 eV (C-C) increased due to the grafted Me-PEG308-SH. The carbon C1s XPS signal changes agree with the ATR-FTIR spectrum in **Figure 2.31.** After our confirmation of the grafting efficiency with FTIR and XPS analysis, we tested all the Me-PEG308-SH/glycerol/Irgacure 651 modified surfaces with E. coli adhesion experiment as above. **Figure 2.36** shows the numbers of E. coli on Me-PEG308-SH/glycerol/Irgacure 651 modified OSTE resin. All the four ratios of OSTE resin showed excellent bacteria-repellent property after modification. Compared to Me-PEG5000-SH/methanol/Irgacure 651 modified OSTE resin, Me-PEG308-SH/glycerol/Irgacure 651 modified surface showed relatively better bacteria repellent properties, especially with lower ratio thiol:ene = 1:2 OSTE resin.

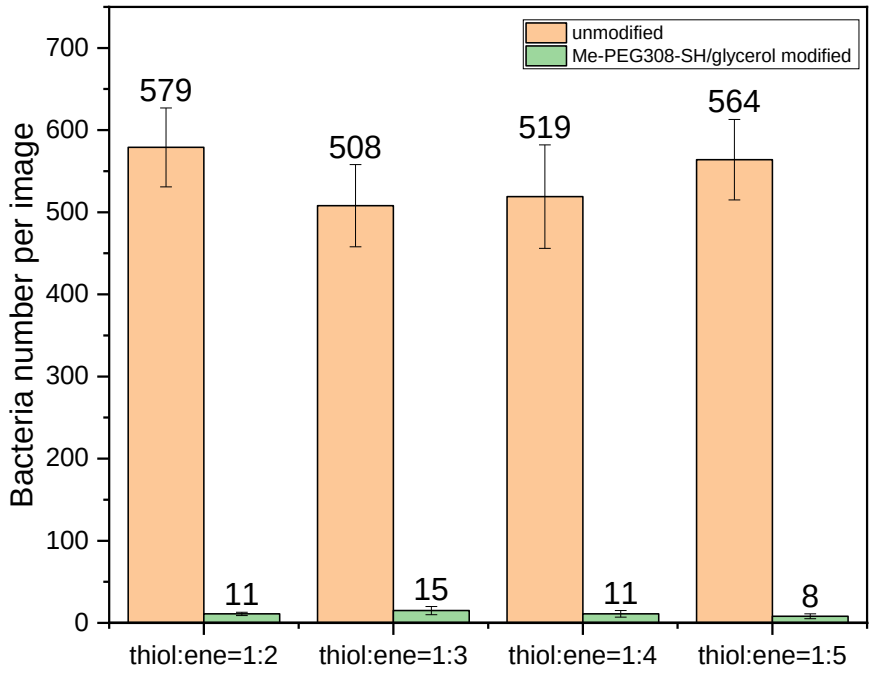

Figure 2.36 Average bacterial number per image (0.0015 cm^{-2}) of *E. coli* MG1655 on unmodified and Me-PEG308-SH/glycerol/Irgacure 651 modified OSTE resin. The error bar is the standard deviation. Mean value of 10 images for each sample in single experiment. Similar results were got for three times repeated.

2.5 MDCK cells behavior on Me-PEG308-SH modified surfaces.

We have validated that Me-PEG308-SH could be the best molecule for one-photon grafting to bring anti-adhesion of bacteria. Here we tested the cell repellency of the modified alkene excess surface.

2.5.1 One-photon polymerized surface followed by one-photon grafting

Considering the bacteria repellency results of Me-PEG5000-SH modified surface, when the ratio of alkene was higher than 1:2, a significant reduction in the number of bacteria adsorbed on the surface of the material was observed. The same results were obtained for Me-PEG308-SH modified alkene excess OSTE surface. Here we tested Me-PEG308-SH modified alkene excess OSTE surface for MDCK cell adhesion. Me-PEG308-SH was dissolved in glycerol at 1.5 mmol/ml. Irgacure 651 was added at 20 mM as photoinitiator. 20 µl mixture was dropped on OSTE resin surface. A quartz slide was covered on the drop for grafting. The samples were exposed to 254 nm (7.2 mW/cm^{-2}) UV light

for 10 minutes. After grafting the surfaces were washed with methanol 4 times (5 minutes per time) and dried in air overnight.

Figure 2.37 shows the MDCK cells on the unmodified and Me-PEG308-SH modified surfaces. **Figure 2.38** shows that when the ratio was 1:2, the numbers of MDCK cells on the Me-PEG308-SH modified surface reduced to half of that on unmodified 1:2 OSTE resin. When the ratios were 1:3, 1:4 or 1:5, there were no MDCK cells on the Me-PEG308-SH modified surface. The possible reason for the different results in cell repellency comes from the density of alkenyl groups on the surface. The Flory radius $\boldsymbol{R_F}$ of Me-PEG308-SH is 0.9 nm. When the ratio was 1:2, the distance between the grafting sites $\boldsymbol{D}$ was bigger than 1.8 nm ($\boldsymbol{2R_F}$), the conformation of grafted Me-PEG308-SH in the substrate was mushroom. Only part of the surface was covered by grafted Me-PEG308-SH, but there were still uncovered spaces between two adjacent molecules for MDCK cells to attach. When the ratios were 1:3, 1:4 and 1:5, the densities of the grafting sites (free alkene groups) were higher and the grafted Me-PEG308-SH were denser than that on 1:2 OSTE surface. The conformation of the grafted molecule was brush. The whole surface would then be covered by Me-PEG308-SH, forming a hydration layer that prevents the cells from contacting the OSTE surface. From the XPS analysis, we can calculate the increase at 250 eV (C-C) on thiol:ene = 1:2 OSTE resin surface was 4.02 % after grafting while the value was 11.59% for thiol:ene = 1:5 OSTE resin surface, which means the grafting density of Me-PEG308-SH on thiol:ene = 1:5 OSTE resin surface was three times of the grafting density on thiol:ene = 1:2 OSTE resin surface.

Besides, there was a tendency for cell numbers to decrease with the increase of alkene component from thiol:ene = 1:2 to thiol:ene = 1:5. A possible reason is that as the alkene component increases, the mechanical strength of the cured substrate decreases and becomes softer and softer.[35] Besides, with the increase of alkene component, the hydrophobicity also increases. Mammalian cells are more inclined to adhere to hydrophilic surfaces.[36] This is another possible reason that there were more MDCK cells on surface with lower alkene component.

Hence, this result establishes a method to prepare a large area of cell repellent OSTE surface.

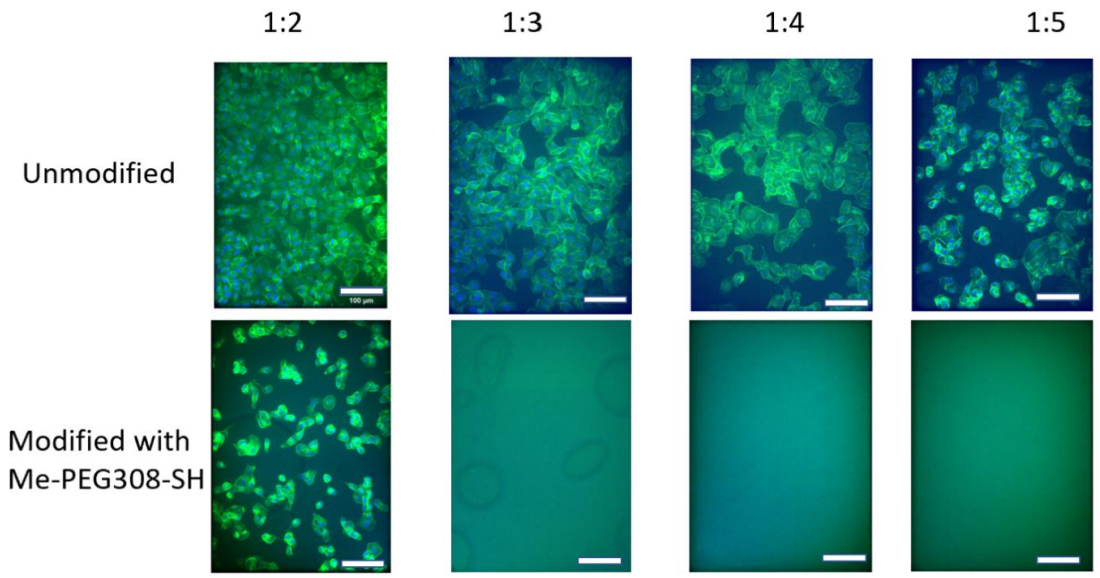

Figure 2.37 Confocal images of MDCK cells on unmodified and Me-PEG308-SH/glycerol/Irgacure 651 modified OSTE surface with different integer ratios of thiol:ene. Blue, nuclei. Green, F-actin. Scale bar 100 μm.

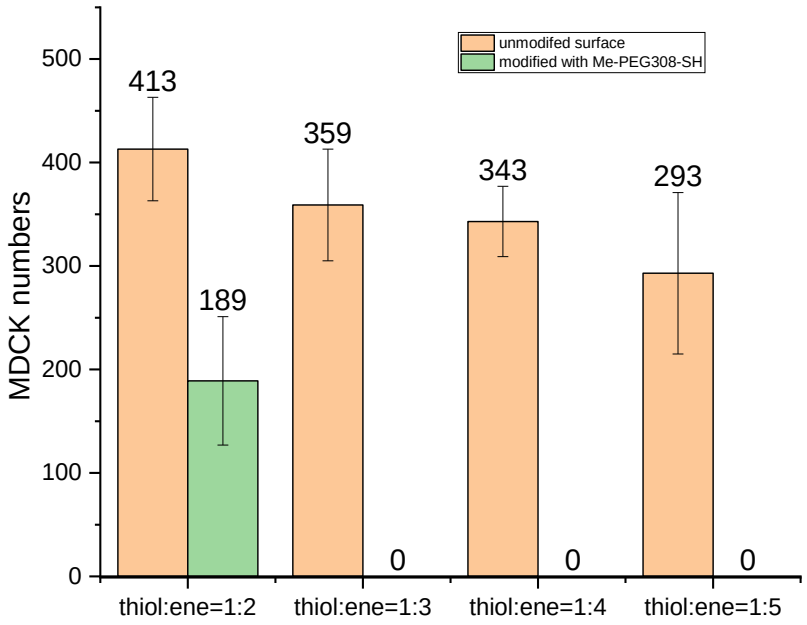

Figure 2.38 Average numbers per image (0.0023 cm^{-2}) of MDCK cells per image on unmodified and Me-PEG308-SH/glycerol/Irgacure 651 modified OSTE surface with different ratio of thiol:ene. The error bar is the standard deviation**.** Mean value of 10 images for each sample in single experiment. Similar results were got for three times repeated.

2.5.2 Two-photon polymerized surface followed by two-photon grafting

To transfer the results from one-photon polymerization and one-photon grafting to two-photon polymerization and two-photon grafting, we designed a carpet to test MDCK cells repellency.

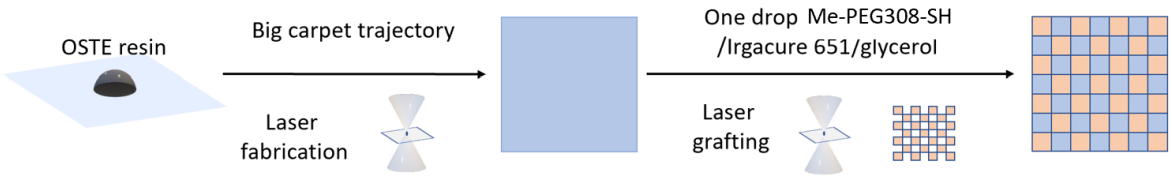

Figure 2.39 Process of carpet fabrication by two-photon polymerization and two-photon grafting

As is shown in **Figure 2.39**, one drop of OSTE resin was deposited on a silanized slide. Then a big carpet (280 μm x 280 μm) was first fabricated (blue). The unpolymerized OSTE resin was washed away by quick flow acetone. Then another drop of mixture of Me-PEG308-SH, glycerol and Irgacure 651 was put on the big carpet. Another trajectory composed of small squares arrays (40 μm x 40 μm) was fabricated on the big carpet. Array of small squares aligned to edges of large squares. After fabrication, the remaining glycerol was removed by quick flow acetone wash. Thus, we got a large square carpet with alternating small unmodified squares (blue) and Me-PEG308-SH modified small squares(orange).

MDCK cells were seeded on the sterilized carpet. 2 hours after seeding, MDCK cells were fixed and stained as described above. **Figure 2.40** (A) shows that MDCK cells were located randomly on the big carpet produced by two-photon polymerization, which is the same as their behavior on one-photon polymerized surfaces On **Figure 2.40** (B), MDCK cells were only located on unmodified small squares on 2D surface. The shape of MDCK cells was restricted to a square. A highly effective anti-adhesive pattern was realized here. In the literature, Silbernagel *et al.*[37] designed hexagon and rectangle 3D-scaffolds by two-photon polymerization to explore their influence on the morphology of cardiomyocytes derived from induced pluripotent stem cells (iPSC-CMs). The cells were shaped inside the 3D scaffolds (**Figure 2.41**). Sibernagel and colleagues shaped the morphology of cells inside 3D scaffolds. We achieved similar control of cell morphology in the 2D plane with spatially selective modifications by two-photon grafting.

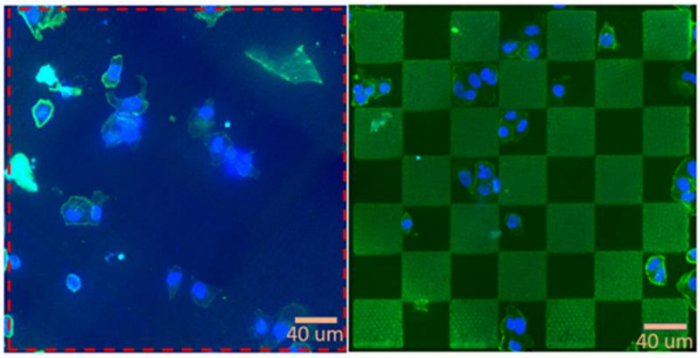

Figure 2.40 MDCK cells on unmodified (A) and Me-PEG308-SH modified (B) thiol:ene = 1:5 resin by two-photon polymerization and two-photon grafting. The red dashed line on (A) is the edge of the carpet. Blue: nuclei. Green: F-actin. Scale bar 40 µm.

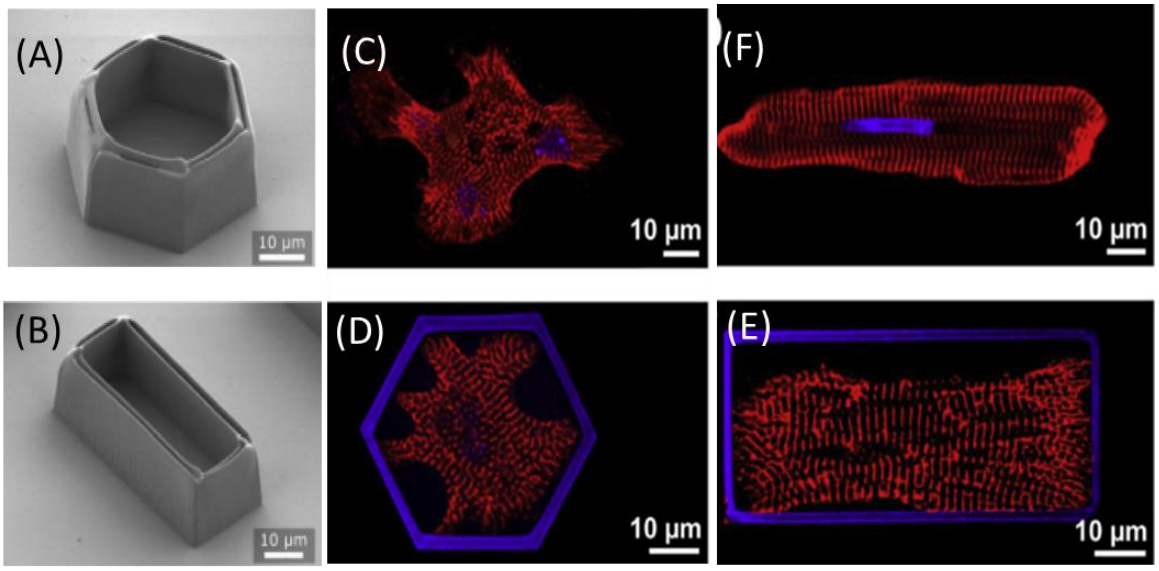

Figure 2.41 Cell morphology controlled by 3D scaffold by Silbernagel *et al*.[37] (A) and (B), 3D scaffolds. (C) α-actinin (red) and nuclei (blue) of non-pattered iPSC-CMs (C) and isolated adult cardiomyocyte (F). (D) and (E) iPSC-CMs grown in 3D scaffold (A) and (B). Red, α-actinin. Blue, autofluorescence if the scaffold. Scale bar 10 µm.

As seen in 2.5.1, we have successfully constructed the surface by one-photon polymerization followed by one-photon grafting, which enables us to form a big area of cell-repellent surface. One photon polymerization is a very fast process.

In 2.5.2, we have seen that two-photon polymerization provides us with precise control at the sub-micron scale, but the fabrication speed is slower than with one-photon polymerization. The same goes for two-photon grafting. Two-photon grafting is also time-consuming. But its high penetration depth provides capability for 3D grafting. Besides, its high resolution makes it possible to do very

local modifications in both 2D and 3D without a mask. If we only need to modify the microstructure without distinction, the combination of two-photon polymerization with one-photon grafting could be a nice choice. In the following part, we will explore the possibility of combination of two-photon polymerization and one-photon grafting and its influence on cell behavior.

2.5.3 Two-photon polymerized surface followed by one-photon grafting

Figure 2.40 shows the process of two big carpets with two-photon polymerization and one-photon grafting. Here we fabricated a big carpet (280 μm x 280 μm) by two-photon polymerization. After washing with quick acetone flow, we put one drop of mixture of Me-PEG308-SH, glycerol and Irgacure 651 on the carpet, and under illumination (254 nm UV, 7.2 mW/cm^{-2}) for 10 minutes, the carpet was grafted with Me-PEG308-SH. Then the sample was put back to microfabrication stage to fabricate another big carpet next to the modified one.

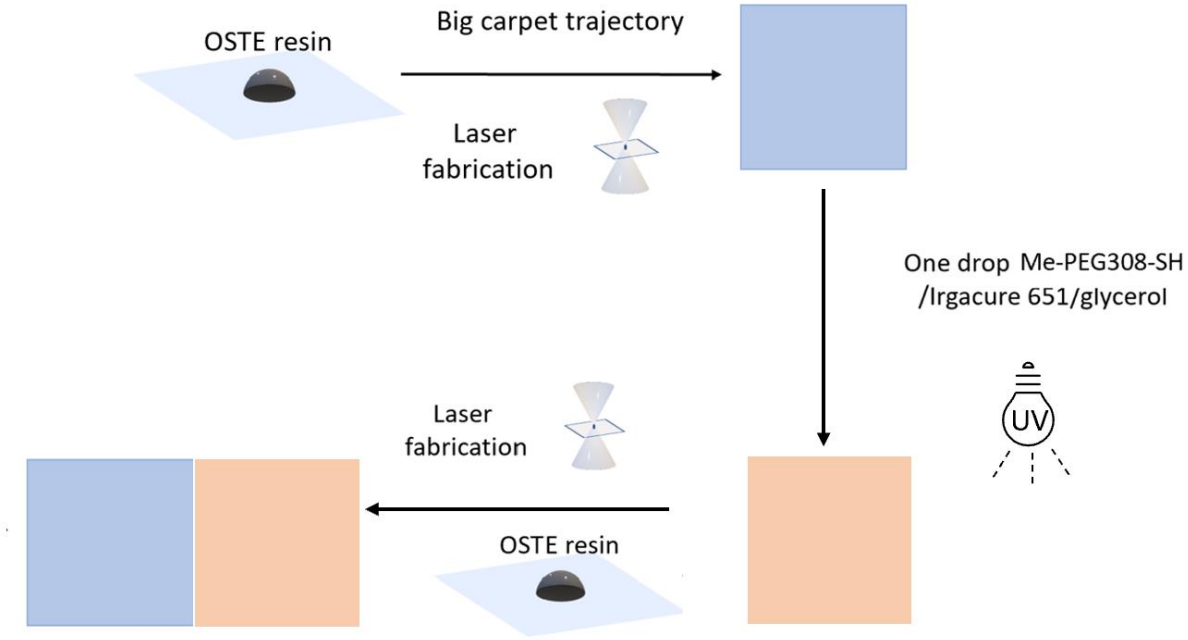

Figure 2. 42 Fabrication procedure of two big carpets with the combination of two-photon polymerization and one photon grafting. Bule, unmodified big carpet. Orange, Me-PEG308-SH modified big carpet.

The same as we did in 2.5.3, MDCK cells were seeded on big carpets as described before. After two hours incubation, MDCK cells only colonized unmodified carpet fabricated by two-photon polymerization without modification, while there was no cell on the one modified by one-photon polymerization (**Figure 2.43**).

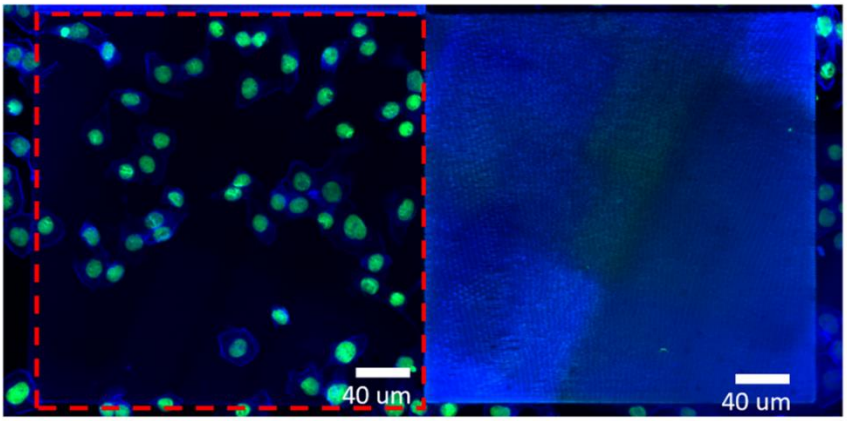

Figure 2.43 MDCK cells on unmodified (left, inside red dashed square) and Me-PEG308-SH modified (right, blue) thiol:ene = 1:5 resin by two-photon polymerization and one-photon grafting Blue: nuclei. Green: F-actin. Scale bar 40 µm.

From the results before, we achieved one-photon grafting and two-photon grafting on 2D carpet fabricated by one-photon and two-photon polymerization. One-photon polymerization and one-photon grafting provide high-throughput polymerization and big-area grafting. Two-photon polymerization and two-photon grafting make it possible to construct precise microstructures and path-controlled surface modification at the cellular scale. Combination of one-photon and two-photon techniques, we leverage the strengths of both techniques to achieve a more optimal solution. Two-photon polymerization followed by one-photon grafting helped us successfully fully grafting on big scale rapidly. By designing the pattern of stepwise polymerization and using alternately two-photon polymerization and one-photon grafting, we achieved also controllable adsorption-resistant surfaces at the cellular scale.

2.6 Summary and perspectives

In this chapter, we developed the formulation of OSTE resin for one- and two-photon polymerization. To achieve anti-adhesive function, different kinds of Me-PEG-SH with different PEG chain lengths ware grafted onto the surface by one-photon grafting. The longer Me-PEG5000-SH modified surfaces have good resistance to *E. coli* but not MDCK cells adsorption. Modifications with shorter Me-PEG308-SH brought excellent anti-adhesion for both *E. coli* and MDCK cells. Combination of one- and two-photon polymerization and grafting, cellular scaled anti-adhesive patterns were successfully constructed on 2D surface.

One of the big advantages of two-photon grafting is the ability to perform local modification. 2D modification is a pre-step for 3D modification. Based on the anti-adhesion results on 2D surface at cellular scale, we can foresee that results on 2D could be transferred to 3D surface by adapting the design of the laser trajectory.

2.7 References

(1) O'Halloran, S.; Pandit, A.; Heise, A.; Kellett, A. Two-Photon Polymerization: Fundamentals, Materials, and Chemical Modification Strategies. *Adv. Sci.* **2023**, *10* (7), 1–18. https://doi.org/10.1002/advs.202204072.

(2) Haraldsson, T.; Carlborg, C. F.; van der Wijngaart, W. OSTE: A Novel Polymer System Developed for Lab-on-Chip. *Microfluid. BioMEMS, Med. Microsystems XII* **2014**, *8976*, 897608. https://doi.org/10.1117/12.2041918.

(3) Lowe, A. B. Thiol-Ene "Click" Reactions and Recent Applications in Polymer and Materials Synthesis. *Polym. Chem.* **2010**, *1* (1), 17–36. https://doi.org/10.1039/b9py00216b.

(4) Carlborg, C. F.; Haraldsson, T.; Öberg, K.; Malkoch, M.; Van Der Wijngaart, W. Beyond PDMS: Off-Stoichiometry Thiol-Ene (OSTE) Based Soft Lithography for Rapid Prototyping of Microfluidic Devices. *Lab Chip* **2011**, *11* (18), 3136–3147. https://doi.org/10.1039/c1lc20388f.

(5) Nakayama, A.; Kumamoto, Y.; Minoshima, M.; Kikuchi, K.; Taguchi, A.; Fujita, K. Photoinitiator-Free Two-Photon Polymerization of Biocompatible Materials for 3D Micro/Nanofabrication. *Adv. Opt. Mater.* **2022**, *10* (18), 2200474. https://doi.org/10.1002/adom.202200474.

(6) Errando-Herranz, C.; Vastesson, A.; Zelenina, M.; Pardon, G.; Bergström, G.; Van Der Wijngaart, W.; Haraldson, T.; Brismar, H.; Gylfason, K. B. Biocompatibility of OSTE Polymers Studied by Cell Growth Experiments. *17th Int. Conf. Miniaturized Syst. Chem. Life Sci. MicroTAS 2013* **2013**, *1*, 143–145.

(7) Paull, K. D.; Shoemaker, R. H.; Boyd, M. R.; Parsons, J. L.; Risbood, P. A.; Barbera, W. A.; Sharma, M. N.; Baker, D. C.; Hand, E.; Scudiero, D. A.; Monks, A.; Alley, M. C.; Grote, M. The Synthesis of XTT: A New Tetrazolium Reagent That Is Bioreducible to a Water-soluble Formazan. *Journal of Heterocyclic Chemistry*. 1988, pp 911–914. https://doi.org/10.1002/jhet.5570250340.

(8) Coscoy, S.; Baiz, S.; Octon, J.; Rhoné, B.; Perquis, L.; Tseng, Q.; Amblard, F.; Semetey, V. Microtopographies Control the Development of Basal Protrusions in Epithelial Sheets.

Biointerphases **2018**, *13* (4), 041003. https://doi.org/10.1116/1.5024601.

(9) Ucla, P.; Ju, X.; Demircioglu, M.; Baiz, S.; Muller, L.; Germain, S.; Monnot, C.; Semetey, V.; Coscoy, S. Dynamics of Endothelial Engagement and Filopodia Formation in Complex 3D Microscaffolds. *Int. J. Mol. Sci.* **2022**, *23* (5), 2415. https://doi.org/10.3390/ijms23052415.

(10) Bechoux, V.; Fouquet, T.; Verge, P.; Bomfim, J. A. S. Utilisation d'un Adhésif à Polymérisation UV Pour Combler Les Surfaces Lacunaires d'objets d'art En Verre Ou à Revêtements Vitreux TT - Using a UV Curing Adhesive to Fill Surface Gaps on Glass Art Objects or Glassy Coatings. *CeROArt Conserv. Expo. Restaur. d'objets d'art* **2015**, No. 10.

(11) van Meerloo, J.; Kaspers, G. J. L.; Cloos, J. Cell Sensitivity Assays: The MTT Assay. In *Cancer Cell Culture*; 2011; Vol. 731, pp 237–245. https://doi.org/10.1007/978-1-61779-080-5_20.

(12) Kumar, P.; Nagarajan, A.; Uchil, P. D. Analysis of Cell Viability by the MTT Assay. *Cold Spring Harb. Protoc.* **2018**, *2018* (6), 469–471. https://doi.org/10.1101/pdb.prot095505.

(13) Ejserholm, F.; Stegmayr, J.; Bauer, P.; Johansson, F.; Wallman, L.; Bengtsson, M.; Oredsson, S. Biocompatibility of a Polymer Based on Off-Stoichiometry Thiol-Enes + Epoxy (OSTE+) for Neural Implants. *Biomater. Res.* **2015**, *19* (1), 1–10. https://doi.org/10.1186/s40824-015-0041-3.

(14) Zeng, B.; Cai, Z.; Lalevée, J.; Yang, Q.; Lai, H.; Xiao, P.; Liu, J.; Xing, F. Cytotoxic and Cytocompatible Comparison among Seven Photoinitiators-Triggered Polymers in Different Tissue Cells. *Toxicol. Vitr.* **2021**, *72*, 105103. https://doi.org/10.1016/j.tiv.2021.105103.

(15) Murshid, N.; Wang, X. Hydrophobic Effect of Alkyl Groups Stabilizing Self-Assembled Colloids in Water. *J. Phys. Chem. B* **2017**, *121* (25), 6280–6285. https://doi.org/10.1021/acs.jpcb.7b04353.

(16) Kyte, J. The Basis of the Hydrophobic Effect. *Biophys. Chem.* **2002**, *100* (1–3), 193–203. https://doi.org/10.1016/S0301-4622(02)00281-8.

(17) Arias, S. L.; Devorkin, J.; Civantos, A.; Allain, J. P. Escherichia Coli Adhesion and Biofilm Formation on Polydimethylsiloxane Are Independent of Substrate Stiffness. *Langmuir* **2021**, *37* (1), 16–25. https://doi.org/10.1021/acs.langmuir.0c00130.

(18) Tuson, H. H.; Weibel, D. B. Bacteria-Surface Interactions. *Soft Matter* **2013**, *9* (17), 4368–4380. https://doi.org/10.1039/c3sm27705d.

(19) Katsikogianni, M. G.; Missirlis, Y. F. Interactions of Bacteria with Specific Biomaterial Surface Chemistries under Flow Conditions. *Acta Biomater.* **2010**, *6* (3), 1107–1118. https://doi.org/10.1016/j.actbio.2009.08.006.

(20) Handorf, A. M.; Zhou, Y.; Halanski, M. A.; Li, W. J. Tissue Stiffness Dictates Development, Homeostasis, and Disease Progression. *Organogenesis* **2015**, *11* (1), 1–15. https://doi.org/10.1080/15476278.2015.1019687.

(21) Coscoy, S.; Baiz, S.; Octon, J.; Rhoné, B.; Perquis, L.; Tseng, Q.; Amblard, F.; Semetey, V. Microtopographies Control the Development of Basal Protrusions in Epithelial Sheets. *Biointerphases* **2018**, *13* (4), 041003. https://doi.org/10.1116/1.5024601.

(22) Schafer, K. J.; Hales, J. M.; Balu, M.; Belfield, K. D.; Van Stryland, E. W.; Hagan, D. J. Two-Photon Absorption Cross-Sections of Common Photoinitiators. *J. Photochem. Photobiol. A Chem.* **2004**, *162* (2–3), 497–502. https://doi.org/10.1016/S1010-6030(03)00394-0.

(23) Lih, E.; Oh, S. H.; Joung, Y. K.; Lee, J. H.; Han, D. K. Polymers for Cell/Tissue Anti-Adhesion. *Prog. Polym. Sci.* **2015**, *44*, 28–61. https://doi.org/10.1016/j.progpolymsci.2014.10.004.

(24) Harbers, G. M.; Emoto, K.; Greef, C.; Metzger, S. W.; Woodward, H. N.; Mascali, J. J.; Grainger, D. W.; Lochhead, M. J. Functionalized Poly(Ethylene Glycol)-Based Bioassay Surface Chemistry That Facilitates Bio-Immobilization and Inhibits Nonspecific Protein, Bacterial, and Mammalian Cell Adhesion. *Chem. Mater.* **2007**, *19* (18), 4405–4414. https://doi.org/10.1021/cm070509u.

(25) Won, S.; Phillips, K. S.; Gu, H.; Kazemzadeh-narbat, M. Biomaterials How Microbes Read the Map : Effects of Implant Topography on Bacterial Adhesion and Biofilm Formation. *Biomaterials* **2021**, *268* (December 2020), 120595. https://doi.org/10.1016/j.biomaterials.2020.120595.

(26) Ma, Z.; Lebard, D. N.; Loverde, S. M.; Sharp, K. A.; Klein, M. L.; Discher, D. E.; Finkel, T. H. TCR Triggering by PMHC Ligands Tethered on Surfaces via Poly (Ethylene Glycol) Depends on Polymer Length. **2014**, *9* (11), 1–10. https://doi.org/10.1371/journal.pone.0112292.

(27) Oesterhelt, F.; Rief, M.; Gaub, H. E. Single Molecule Force Spectroscopy by AFM Indicates Helical Structure of Poly(Ethylene-Glycol) in Water. *New J. Phys.* **1999**, *1*, 6. https://doi.org/10.1088/1367-2630/1/1/006.

(28) Lee, H.; Larson, R. G. Adsorption of Plasma Proteins onto PEGylated Lipid Bilayers: The Effect of PEG Size and Grafting Density. *Biomacromolecules* **2016**, *17* (5), 1757–1765. https://doi.org/10.1021/acs.biomac.6b00146.

(29) D'souza, A. A.; Shegokar, R. Polyethylene Glycol (PEG): A Versatile Polymer for Pharmaceutical Applications. *Expert Opin. Drug Deliv.* **2016**, *13* (9), 1257–1275. https://doi.org/10.1080/17425247.2016.1182485.

(30) Shi, L.; Zhang, J.; Zhao, M.; Tang, S.; Cheng, X.; Zhang, W.; Li, W.; Liu, X.; Peng, H.; Wang, Q. Effects of Polyethylene Glycol on the Surface of Nanoparticles for Targeted Drug Delivery. *Nanoscale* **2021**, *13* (24), 10748–10764. https://doi.org/10.1039/d1nr02065j.

(31) Kingshott, P.; Thissen, H.; Griesser, H. J. Effects of Cloud-Point Grafting, Chain Length, and Density of PEG Layers on Competitive Adsorption of Ocular Proteins. *Biomaterials* **2002**, *23* (9), 2043–2056. https://doi.org/10.1016/S0142-9612(01)00334-9.

(32) Pingle, H.; Wang, P.-Y.; Thissen, H.; McArthur, S.; Kingshott, P. Colloidal Crystal Based Plasma Polymer Patterning to Control Pseudomonas Aeruginosa Attachment to Surfaces . *Biointerphases* **2015**, *10* (4), 04A309. https://doi.org/10.1116/1.4936071.

(33) Al-Ani, A.; Pingle, H.; Reynolds, N. P.; Wang, P. Y.; Kingshott, P. Tuning the Density of Poly(Ethylene Glycol) Chains to Control Mammalian Cell and Bacterial Attachment. *Polymers (Basel).* **2017**, *9* (8), 343. https://doi.org/10.3390/polym9080343.

(34) Oberleitner, B.; Dellinger, A.; Castanet, A. S.; Galtayries, A.; Semetey, V. A Facile and Versatile Approach to Design Self-Assembled Monolayers on Glass Using Thiol–Ene Chemistry. *Chem. Commun.* **2013**, *49* (16), 1615–1617. https://doi.org/10.1039/c2cc38425f.

(35) Discher, D. E.; Janmey, P.; Wang, Y. Tissue Cells Feel and Respond to the Stiffness of Their Substrate. *Science (80-.).* **2005**, *310* (5751), 1139–1143. https://doi.org/10.1126/science.1116995.

(36) Ferrari, M.; Cirisano, F.; Morán, M. C. Mammalian Cell Behavior on Hydrophobic Substrates: Influence of Surface Properties. *Colloids and Interfaces* **2019**, *3* (2), 48. https://doi.org/10.3390/colloids3020048.

(37) Silbernagel, N.; Körner, A.; Balitzki, J.; Jaggy, M.; Bertels, S.; Richter, B.; Hippler, M.; Hellwig, A.; Hecker, M.; Bastmeyer, M.; Ullrich, N. D. Shaping the Heart: Structural and Functional Maturation of IPSC-Cardiomyocytes in 3D-Micro-Scaffolds. *Biomaterials* **2020**, *227*, 119551. https://doi.org/10.1016/j.biomaterials.2019.119551.

Chapter III. Three-dimensional (3D) structure of OSTE resin for cell biology

3.1 Introduction

Cell culture on two-dimensional (2D) surfaces has been used for more than 100 years in biology research.[1] But there is a strong limitation of spatial architecture with this traditional cultural method.[2] *In vivo*, cells are located in a real 3D microenvironment, which provides biophysical support, biochemical clues as well and spatial clues for multicellular tissue organization. Important biophysical characteristics are stiffness and microtopography, and biochemical clues can be small molecular signals or chemical functions of the surface of the substrate. All those factors will influence functions such as cell migration, adhesion, proliferation, and gene expression.[3] It is central to better mimic the real 3D microenvironment to account for cell-cell interactions, metabolic profiling, and characteristics of tumors or other diseases, with important application fields in stem cell research and drug discovery.

The engineering of 3D substrates benefits from the high flexibility of the biomaterials that can be used. 3D scaffolds can be fabricated using a wide range of biomaterials, including natural polymers (e.g., collagen, fibrin), synthetic polymers (e.g., poly(lactic-co-glycolic acid), PLGA), ceramics, and hydrogels. This versatility allows researchers to choose materials with specific properties, degradation rates, and bioactive functionalities, depending on the desired application.

Commonly, 3D cell scaffolds are mostly built with single materials. The types of materials are homogeneous in spatial distribution, which holds the advantage of providing cells with homogeneous support, with cells having no spatial preference for materials in the structure. For example, in the culture dishes used to culture cells in the laboratory, there is no spatial selectivity from the substrate in the adsorption, proliferation, and differentiation of cells on the dishes. However, in a real cell environment, the distribution of material types may be discontinuous. Multiple materials may be present at the same time. In the extracellular matrix, these differences may be a non-uniform distribution of different kinds of collagen. When we mimic the extracellular matrix (ECM) to provide a growth environment for cells, we can choose different materials to make various parts of the cell scaffold.[4,5] It is also possible to use the same material to fabricate the entire scaffold and then modify the cell scaffold locally with chemical modifications. The former can produce different mechanical strengths and different chemical surfaces in space while the latter will only change the chemical surface. The use of these two approaches will facilitate the exploration of basic cell biology.

In addition to fundamental cell biology, 3D scaffolds for cell culture play a significant role in tissue engineering and implantable medicine. One of the priorities of tissue engineering and implantable materials is to avoid non-specific adsorption. In biology concepts, non-specific adsorption can refer to the nonspecific binding of proteins, antibodies, or other biomolecules to surfaces, such as cell membranes, laboratory equipment, or artificial materials.

We have successfully controlled bacteria and cell adhesion in Chapter II. By tuning the formula of the OSTE resin, surfaces with different densities of alkene excess functional groups were obtained in 2D surfaces. By grafting Me-PEG-SH of different lengths, we had an anti-adhesive 2D surface that repelled cells. The control of cell adhesion behavior in three dimensions can be more complex. Both the size and spatial distribution of anti-adhesion sites affect the adhesion behavior of cells.

In this chapter, first, we will evoke the influence of the microtopographies of 3D OSTE resins on cell behavior, through past studies of the group, and we will focus on a work that I finished together with my colleague Pierre UCLA on 3D microtopographies eliciting endothelial protrusions, filopodia, characteristic for the onset of angiogenesis. This first part will rely on the use of a commercial OSTE resin, NOA61, characterized chemically in Chapter II. Second, we will transfer the best repellent conditions from 2D surfaces to 3D structures/scaffolds with our homemade OSTE resins described in Chapter II. A modified 3D surface will be carried out to explore the cell behavior on a spatially distributed anti-adhesion surface.

3.2 The role of topography on cell behavior

3.2.1 Epithelial cells on closed hexagonal structures

As we have discussed before in Chapter II, NOA 61 is also one kind of commercial OSTE resin, and the ratio of thiol:ene is approximately 1:1.2. From the former work of the laboratory[6], we know that the topography of the structure that cells colonized would influence the formation of membrane protrusions. Madin-Darby canine kidney (MDCK) cells were seeded on regular closed hexagonal structures (lattice) made of NOA 61. The lattice size D varied from 1.5 to 19 μm (**Figure 3.1** (A)). Cells generated basal protrusions in hexagonal lattices. When the sizes were different, the formations of protrusions also varied. The relationship between the formation of protrusions and the geography and size of the structures were analyzed. The behaviors of epithelial cells are summarized in **Figure 3.1** (C). When the size of the hexagon was smaller than 3 μm, there was no basal protrusion formed. When the sizes were between 3 to 5 μm, only half of the lattices were filled to the bottom by newly induced protrusions. When the sizes

were located between 5 to 11 µm, all the bottoms of the lattices were filled with protrusions, with partial penetration of the nuclei that remained however largely on the top. When the sizes of the lattices were above 11 µm, cells fell totally inside the lattices, while still forming a monolayer on top of the structure. In summary, the epithelial cells formed in all conditions a continuous epithelial layer on the surface of the hexagon and produced numerous, extensive, and deep basal protrusions when the size of the lattice varied from 5 to 11 µm. Strikingly, these basal protrusions increase the three-dimensional basal surface area of the cell in contact with the substrate by 3-fold. Such architectures could be useful in bioimplants when the aim is to increase the surface area, hence possibly the adhesion, between the cells and the implant surface.

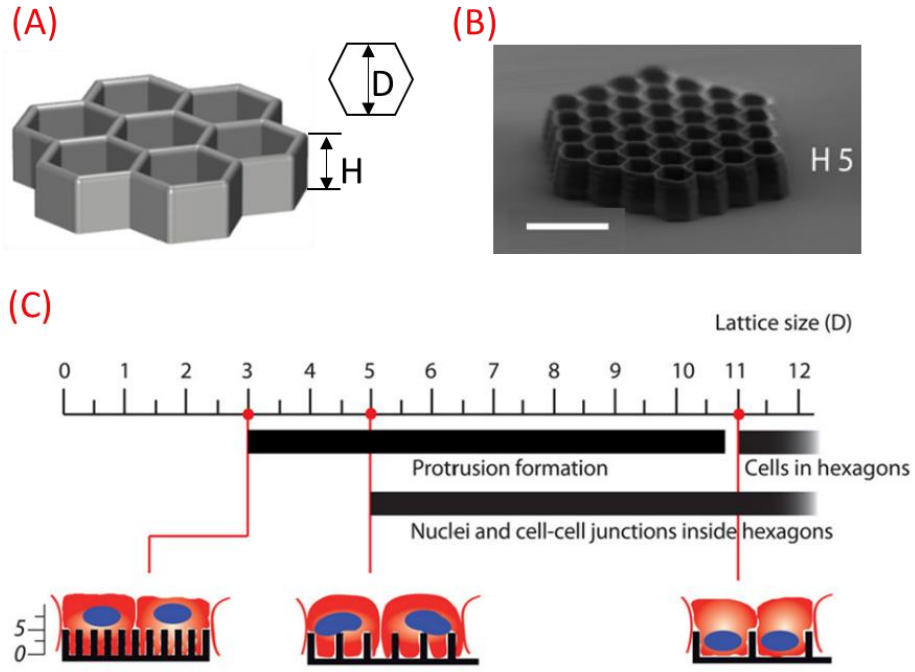

Figure 3.1 (A) Schematic of microstructures (B) SEM image of typical closed hexagon structure, D = 3.5 and H = 5 µm, scale bar 10 µm (left). (C) Recapitulative scheme of protrusion formation, and nuclei and junction engagement as a function of lattice size D for height H=5 µm (right).[6]

3.2.2 Endothelial cells on closed and open hexagonal structures

In the external environment of the cell, there are a large number of factors that affect cellular activity, including but not limited to microtopography, chemical factors, mechanical strength, and bioelectrical signals.[7] Understanding the role of these factors individually, as well as in combination, on cellular activity becomes very important. Human Umbilical Vein Endothelial cells (HUVEC) are cells derived

from the umbilical vein endothelium. HUVEC cells can be used as experimental models to study physiological and pathological processes related to endothelium, e.g., angiogenesis[8]. Angiogenesis means the formation of new blood vessels from pre-existing ones. It is important to refine the understanding of endothelial-extracellular matrix (ECM) interaction during angiogenesis. It is well known that the overall ECM stiffness as well as the local 3D fiber geometry (e.g., fiber size or 3D arrangement) will have a significant impact on cell fate in general.

As of today, TPP allows the largest precision in the creation of 3D microstructures, enabling the creation of complex scaffolds that guide migration, differentiation, and invasion. We used these flexible structures to better understand the behavior of endothelial (blood vessel) cells in fibrillar environments characteristic of the extracellular matrix lining blood vessels.

It is noteworthy that endothelial cells behave differently when cultured on microstructures like microgrooves or micropillars that modulate their phenotypes and their migration patterns. Here, specific membrane protrusions, actin-rich filopodia, could be induced when endothelial HUVECs were cultured on 3D microstructures.

We have seen in the last part that protrusions could be induced by controlling the size of the closed hexagonal structures with epithelial cells. Endothelial cells may behave differently from epithelial cells, and indeed on hexagonal honeycombs seen previously (**Figure 3.1** and **Figure 3.2 (**a)), they covered the structure with a monolayer organization, but without forming basal protrusions (**Figure 3.4** (a)). To explore the influence of microtopographies on the behavior of endothelial cells, we designed more complex structures of hexagons on pillars (called “open” hexagons) for HUVEC cells in **Figure 3.2**. We know that when the size of the hexagonal structure is just a bit smaller than the size of cells, epithelial MDCK cells would form a monolayer on the top and also the formation of protrusions under the layer to even down to the bottom. The average size of HUVEC cells is around 17 µm. We chose 8 µm as the diameter of the inscribed circle of regular closed and open structures **Figure 3.2** (a) and (b).

In literature, endothelial cells were shown to colonize grooved substrates faster than flat substrates, [9] and such grooved substrates generally result in alignment and biased migration in the direction of the grooves or asymmetric features. With that in mind, we considered elongating the open hexagonal structures mentioned above. The elongated structures are defined as follows. As shown in **Figure 3.2** (d), the length in the elongated direction is *L* while the length in the vertical stretching direction is *l.* For elongated structures, we fabricated the elongated open *l7L14* structure *(l7L14-open).* An open elongated hexagonal structure *l7L14-open* means that *L* and *l* are 14 and 7 µm respectively. The height of the structures was adapted to 7 µm. For open structures (**Figure 3.2** (b) and (c)), the height includes the thickness of the

top crown and the pillars. The height of the pillars only was around 2~4 µm. **Figure 3.2** (e) (f) and (g) show the SEM images of the *D8-closed* structure and elongated l*7L14-open* structures.

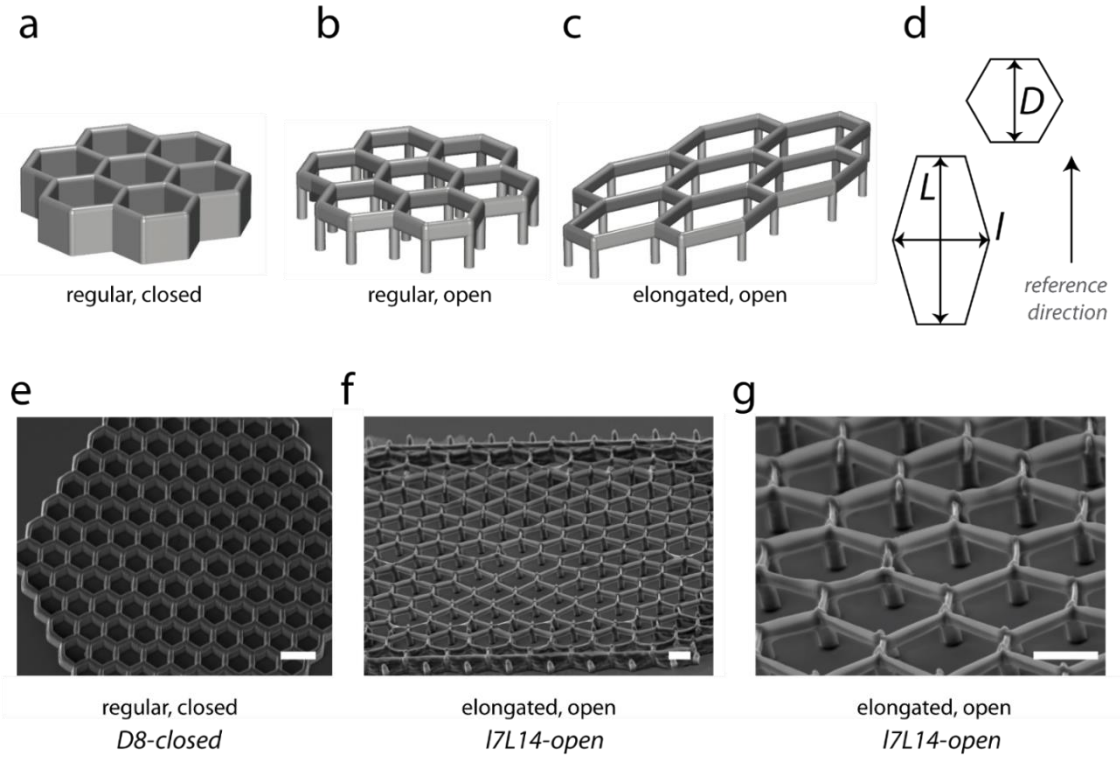

Figure 3.2 Microfabrication of microstructures. Microstructures were realized with NOA61 (Norland Optical Adhesive) by two-photon polymerization. (a) Hexagonal lattices previously described are referred to here as "closed" microstructures. (b, c) "Open" microstructures (hexagons on pillars), with a total height H of 7 µm (including the typical pillar height of 2–4 µm), and variable horizontal dimensions. Regular (b) and elongated (c) hexagons were used. (d) Scheme of dimensions measured for regular (D) and elongated (l, L) hexagons. (e–g) SEM imaging of D8-closed (e) and *l7L14-open* (f, g) structures. (e) Top view, (f, g) side views, bars 10 µm.[10]

The material here to fabricate the structure was NOA 61. HUVEC cell culture was performed with the following process by my colleague Pierre UCLA. HUVEC cells were cultured with endothelial cell growth medium 2 (Promocell) with a standard vascular endothelial growth factor (VEGF) concentration at 0.5 ng/ml unless otherwise specified. They were seeded on the structures at a density of 20,000–30,000 cells/cm^2 and fixed after ~1 day of cell coverage on structures.

3.2.2.1 Elongation control of cells in monolayer

We observed the arrangement of HUVEC cells on normal and elongated open structures by two-photon confocal microscopy. The results showed that there were confluent monolayer cells on both regular structures *D10-open* (**Figure 3.3** b) and elongated *l7L14-open* structures (**Figure 3.3** a). Elongation or not had no influence on cell colonization with the type of cell seeding used here (above the structure). But considering the orientation of cells, clear differences appeared from regular structures to elongated ones.

One of our questions here was to know whether the elongation of the hexagonal structure will induce the elongation of HUVEC cells. To better understand the orientation of the cells, we set the elongation direction as the initial direction (the black arrow in **Figure 3.3**) and then calculated the angle of the cells corresponding to the initial direction. **Figure 3.3** c and d show the angles of HUVEC cells on *l7L14-closed and l7L14-open* structures. The nuclei were on the top of the structures. According to the quantification, the mean angles were 30 ± 21°, n = 127, and 29 ± 24°, n = 70. For regular open structures, we tried several sizes of hexagonal structures *D4.5, D6.6, D8.8, D10,* or *D13.5-open* structures. The mean angles are 44 ± 26° for 1051 cells, which are close to 45° indicating a random orientation.

Elongation only occurs on elongated structures, no matter if it is closed or open. Comparing the mean angles of cells on elongated and normal structures, we can conclude that horizontal elongation of the hexagonal structures could control the elongation of cells, which agrees with the literature that shows the cell shape and nuclei elongated in the same direction.[11].

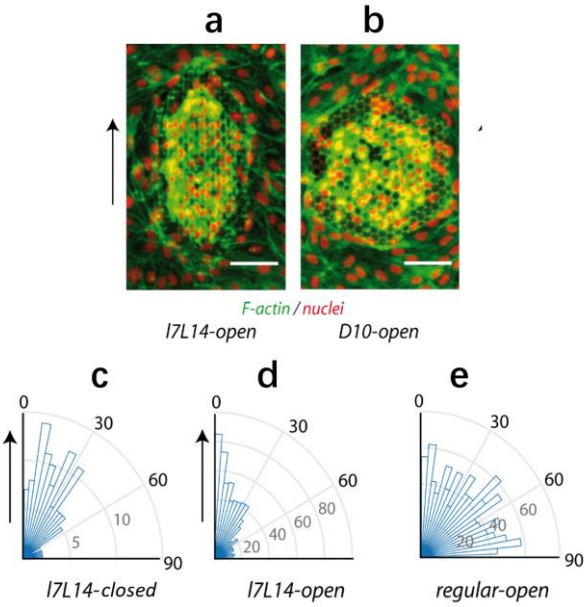

Figure 3.3 Cellular organization in the top monolayer. (a, b) Global HUVECs coverage of (**a**) *l7L14-open* and (**b**) *D10-open* microstructures. red: nuclei, green: F-actin, bar 50 µm. (**c-e**) Histograms of nuclei orientations in the top layer above the microstructures. (**c**) *l7L14-closed* (127 nuclei in 7 structures) (**d**) *l7L14-open* (700 nuclei in 15 structures) (**e**) *D4.5*, *D6.6*, *D8.8*, *D10*, and *D13.5-open* microstructures (1051 nuclei in 23 structures). The vertical arrow in (**a**) represents the reference axis for the elongated structure. For regular structures, the reference axis was chosen perpendicular to one side of the hexagon.[10]

3.2.2.2 Vertical pillars-controlled engagement from monolayer

In addition to the elongation of cells, we also found engagement of the cell in the vertical direction was different. Focusing on *l7L14* structures only, we compared the *l7L14-closed and l7L14-open* structures. For *l7L14-closed* structures, cells only engaged on the top of the structures. There was no significant engagement at the bottom of the structure (**Figure 3.4** a and **Figure 3.5** a). In contrast, the engagement of the *l7L14-open* structures was deep to the bottom (**Figure 3.4** b, c, and **Figure 3.5** b). Quantification here was performed by Pierre UCLA.

Engagement of nuclei to the bottom only occurred on *l7L14-open*, not on *l7L14-closed* structures. From the previous work in our lab[6], we know that the sizes of the hexagon will influence the vertical engagement of the cells. Here we have similar trails with *D-open* structures. Vertical engagement to the bottom was observed at a high frequency for *D13.5-open*, *D10-open, D8.8-open, and D6.6-open* structures, but very rarely for *D4.5-open* structures (**Figure 3.5** c). Here we can have a similar conclusion as that concluded from regular closed structures with epithelial cells[12].

For the engagement, we can see that the edge of the cell membrane deformed, creating filament-like structures. Deformation of the plasma membrane is essential for cell migration, trafficking, and division. It is the cytoskeleton of the cellular actin that shapes plasma membrane protrusions and invaginations, initiating movement. Cell's direction of movement depends largely on two types of protrusions: lamellipodia and filopodia. Filopodia and lamellipodia are specialized cellular structures found in eukaryotic cells, particularly in animal cells, that play essential roles in various cellular processes such as cell motility, adhesion, and communication. These dynamic structures are enriched with actin filaments, which are key components of the cell cytoskeleton and are essential for maintaining cell shape and movement.

From **Figure 3.4** a and b, we can find that deep filopodia existed in an open hexagonal structure. However, a weak concentration of vascular endothelial growth factor (VEGF) at 0.5 ng/ml was present in the basal endothelial media, a concentration not sufficient to trigger 3D angiogenesis. However, to check the possible dependence on VEGF, we seeded HUVEC cells on *l7L14-open* microstructures with different concentrations of this growth factor. After long incubation, we found that all the concentrations of VEGF induced the formation of filopodia. From the literature, we know that a relatively low concentration of VEGF will not be able to induce filopodia in 2D cultures.[13] Here, filopodia were generated in structures even without VEGF (**Figure 3.4** e). We could conclude that the formation of the filopodia is independent of VEGF, which means only the microgeometry of our *l7L14-open* microstructures can trigger the formation of filopodia. At last, we observed that the induced filopodia had a preferential orientation at the bottom of elongated structures, in line with the importance of the geometry of the substrate for filopodia generation and maintenance.

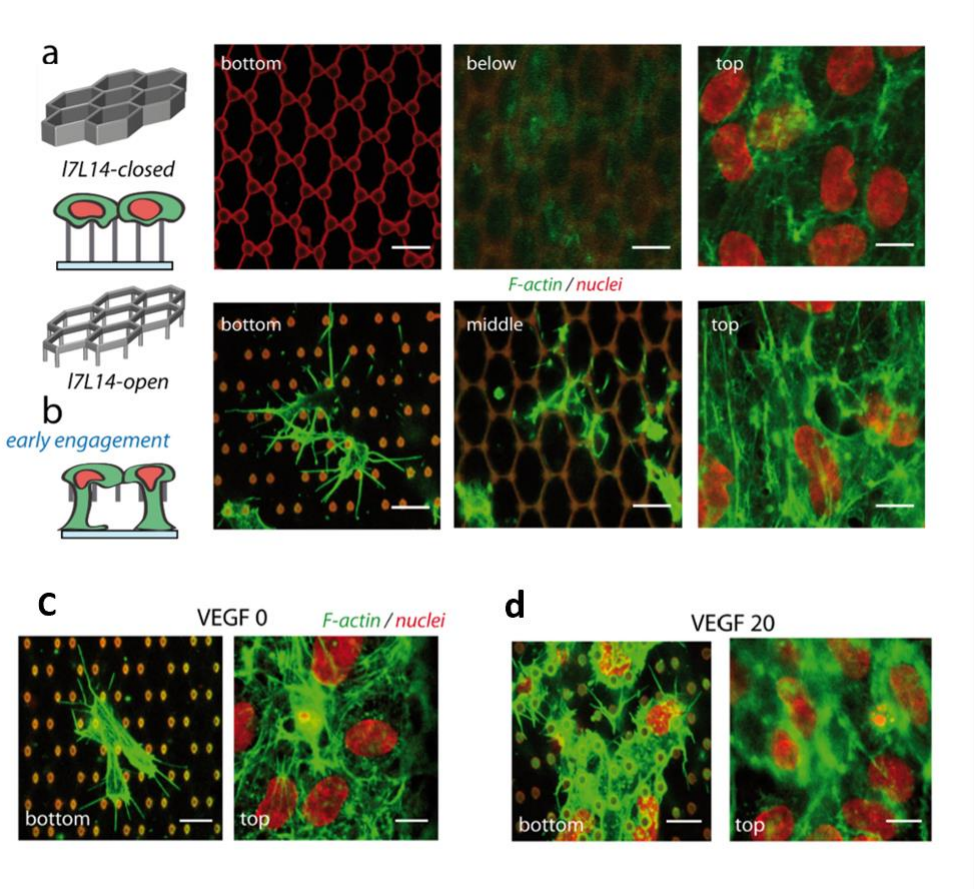

Figure 3.4 HUVECs organization on closed and open microstructures. (a) and (b) Left, schemes of hexagonal lattices, and side or 3D views of typical HUVECs organization after colonization. Right, confocal planes, denoised images. Cells were cultivated in standard conditions (VEGF 0.5 ng/mL) unless otherwise specified. *(a)* Closed microstructures. Confocal planes on HUVECs on *l7L14*-closed microstructure. Left, bottom plane (contact with the bottom substrate); middle, 1.2 µm below the top of the structure; top, above the structure. *(b)* Open *l7L14*-open structures, with vertical engagement and formation of filopodia in the bottom plane: from left to right, bottom plane; middle plane; top, above the structure. (c) and (d) Dependence on VEGF. HUVECs were cultivated on *l7L14*-open microstructures with different VEGF concentrations. Cell organization was studied

from fixed samples. *(c)* Culture without VEGF: ECGM media (Promocell), which contains no VEGF supplement *(d)* 20 ng/mL VEGF. scale bar 10 µm. Red: nuclei and microstructure autofluorescence, green: F-actin.[10]

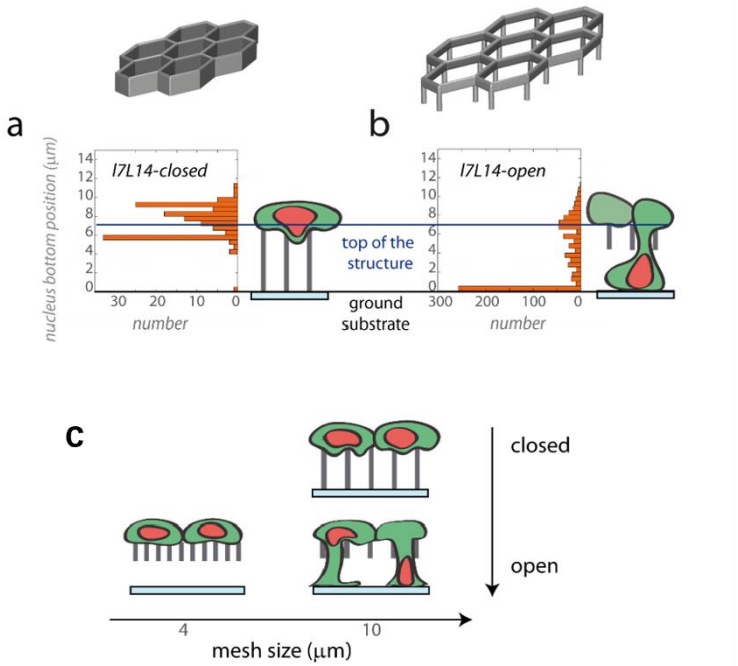

Figure 3.5 Dependence of geometry and pore size for nuclei engagement. HUVECs were cultivated on elongated (a) *l7L14*-closed microstructures (127 nuclei in 7 structures) and (b) *l7L14*-open structures (700 nuclei in 15 structures), or on regular open structures with different horizontal dimensions *D* (quantifications performed by Pierre UCLA) (c) Recapitulative scheme showing nuclei engagement in the function of the pore size and on the closed or open nature of the microstructure[10]

Cell migration must proceed by producing protrusions to sense the outside microenvironment.[14] With distinct types of cell migration, various kinds of protrusions are also produced. Cell migration includes integrin-free migration (amoeboid migration), and integrin-based migration (mesenchymal migration) with mesenchymal protrusions including filopodia and dactylopodia.[15] The mesenchymal mode is characterized by slow migration speed and extracellular matrix (ECM) degradation, while cells in amoeboid mode move fast and do not degrade the ECM.[16] In our experiments, we found that HUVEC cells produced filopodia and dactylopodia characteristic of the mesenchymal mode, as well as membrane blebs characteristic of the amoeboid mode on *l7L14-open* microstructures, with spontaneous

interconversions between these different modes as depicted in **Figure 3.6**. The mechanisms governing these interconversions were studied with specific inhibitors of actomyosin contractility and focal adhesion kinase[17],

Figure 3.6 summarizes the role of microstructures on endothelial cell behavior. With TPP of OSTE-based NOA61 resin, we fabricated closed and open regular and elongated structures. Elongated structures could induce the elongation of the cells on the top monolayer. When the structures were open, both for regular and elongated ones, vertical engagement on the structures was triggered. Microstructures could induce the formation of filopodia, even in the absence of VEGF that triggers it *in vivo* in the first step of angiogenesis.

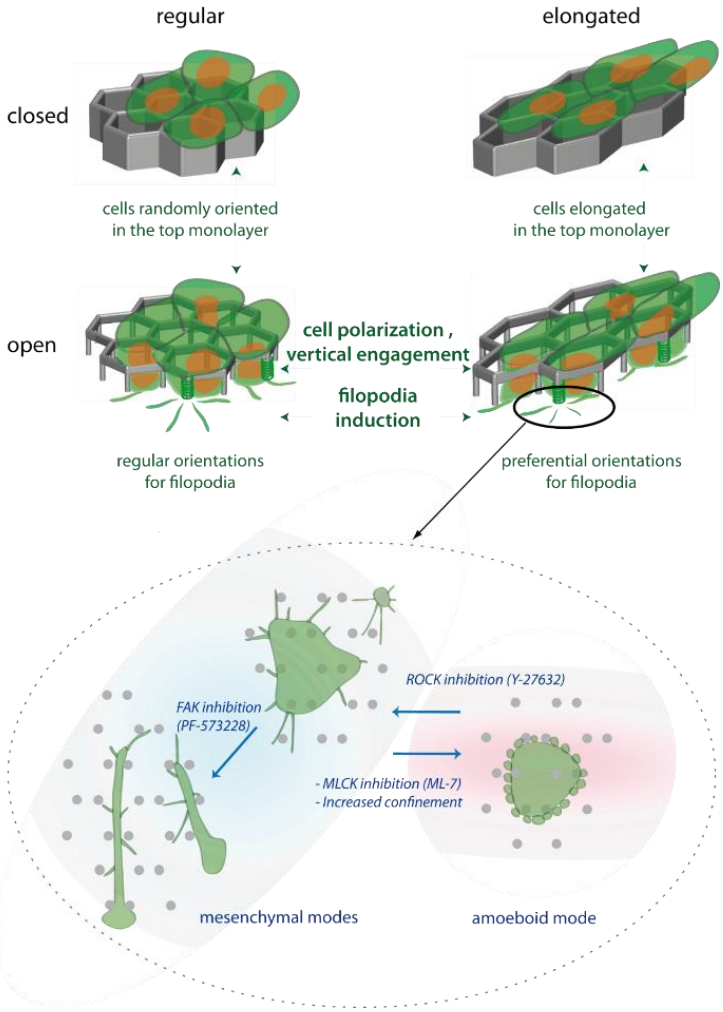

Figure 3.6 Recapitulative scheme of the global cell behavior in the microstructures (Top) Organization of endothelial HUVECs in the function of the elongation of hexagons and of the open or closed nature of the

microstructure. These two characteristics modulate the orientation of the top monolayer, the vertical engagement and the induction of filopodia, and the orientation of the filopodia. (Bottom) Zoom of the different protrusive modes present in the bottom plane (pillars) of open elongated structures, and transitions between them: from left to right, dactylopodia and filopodia in the mesenchymal mode, and membrane blebs in the amoeboid mode.[10]

As mentioned above, geometry is only one aspect that influences the behavior of cells in 3D environment. Surface chemistry also plays a key role in cell activity, especially in cell adhesion/binding situations. In Chapter II, we realized the control of anti-adhesion on OSTE surface on a 2D surface. In the following part, we will try to control the surface chemistry of elongated hexagonal structures to explore the effect of both surface chemistry and geometry.

3.3 The role of surface chemistry on cell behavior

3.3.1 Fully modified OSTE 3D structures

From anti-adhesion experiments on 2D surfaces in Chapter II, we already know that Me-PEG308-SH and Me-PEG750-SH modified surfaces can bring anti-adhesive properties for *E. coli* and MDCK cells for high ratio OSTE alkene excess surface. Here we transfer this strategy to 3D surfaces. We chose the structure ***c*** from **Figure 3.2** for the cell adhesion experiment. We used thiol:ene = 1:5 OSTE resin with 0.5 w/w % Irgacure 651 to fabricate structure *l7L14-open* with a height of 7μm. After fabrication, the structure was rinsed with floating acetone to remove the unpolymerized part. For full modification, one drop of Me-PEG308-SH/Glycerol/Irgacure 651 was put onto the structure and illuminated under 254 nm UV light (7.2 mW per cm^2) for 10 minutes. After grafting, the structure was washed with methanol 3 times, 5 minutes each time. Then we seeded MDCK cells for 2 hours to see the colony situation on the unmodified and modified structures. **Figure 3.6** shows the MDCK adhesion results. The unmodified structure was fully colonized by MDCK cells while there were no cells on the Me-PEG308-SH modified structure and all the cells were around. Here, we successfully transferred the cell repellency functionalization of 2D surfaces to complex 3D structures by one-photon (UV) grafting.

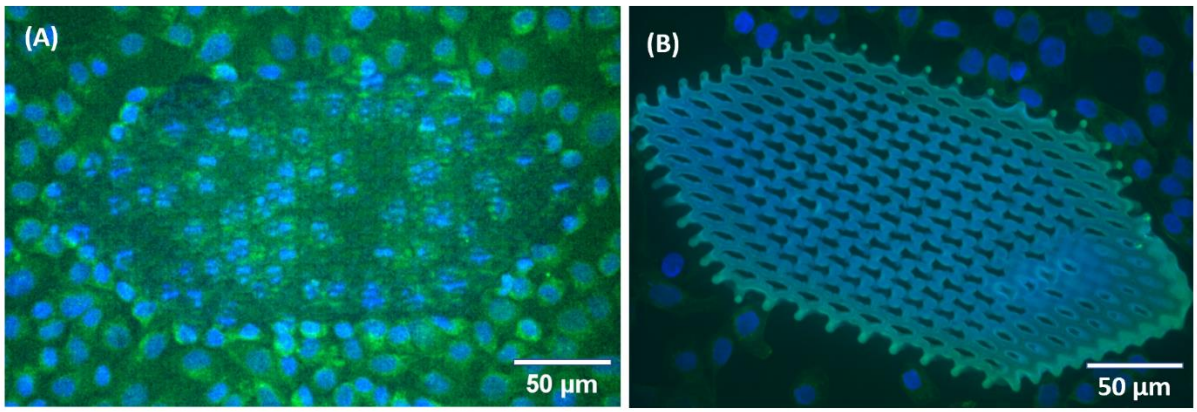

Figure 3.6 Confocal spinning microscope images of MDCK cells on unmodified and modified 3D structures. (A) unmodified structure *l7L14*-open with thiol:ene = 1:5 OSTE resin, *h* = 7µm (B) Me-PEG308-SH modified structure *l7L14*-open with thiol:ene = 1:5 OSTE resin, *h* = 7µm. Blue: nuclei. Green: F-actin. Scale bar 50 µm.

3.3.2 Locally modified OSTE 3D structures

In the experiment above, the modification was carried out by one-photon grafting. One-photon grafting with UV is fast for large-scale modifications. However, the whole area of the structure was totally modified. If only a part of the structure needed to be modified, one-photon grafting could be used with a photo mask, but a photo mask would shadow all the parts in the *Z* direction, which means a 3D area. So, both the top crown and pillars below would be shadowed. In contrast, two-photon modification is expected to provide local control of the modifications even in the *Z* direction. In theory, it is possible to modify the top crown or pillars due to the voxel property of the laser. (**Figure 3.7**).

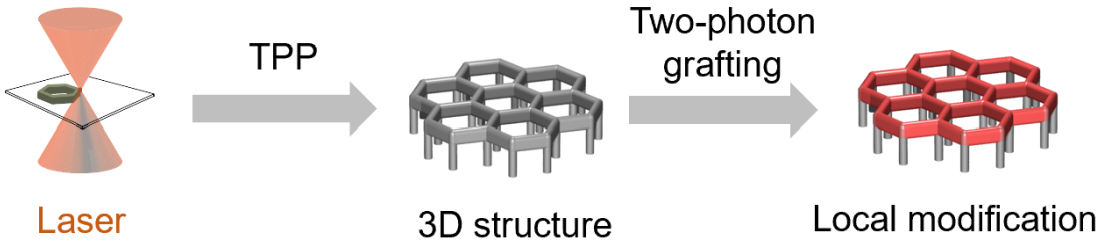

Figure 3.7 scheme of local modification by two-photon grafting. Red crown, local modified part.

However, to obtain suspended hexagons with top crowns and pillars of different adhesive properties, alternative strategies could theoretically be used that do not involve surface modifications, like building first the pillars in an adhesive resin and second the crown in an anti-adhesive resin. Some other spatial adhesion patterns could not be achieved with sequential fabrication steps in different resins; for instance, suspended fibers with different adhesive properties along their length, because such fibers can only be built in one step so that we cannot change material during the fabrication. That is why we considered designing structures with suspended fibers and already performed the first step of fabrication with our OSTE resin. The structures' length, width, and height were 20 µm, 10 µm, and 12 µm, respectively. We initially fabricated fibers with thiol:ene = 1:3, 1:4, and 1:5 alkene excess OSTE resin. 0.5 wt% Irgacure 651 was added as photoinitiator. **Figure 3.8** shows the initial trails of fibers we fabricated by TPP. The local modification of the hexagonal structure and fibers is unfinished. However, it is expected that local modification of the fiber can be realized by two-photon grafting, providing an innovative tool for cell biology.

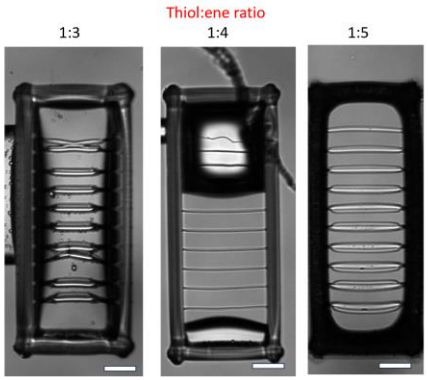

Figure 3.8 Initial trails of fibers fabricated with thiol:ene = 1:3, 1:4, and 1:5 OSTE resin. Scale bar 3 µm.

3.4 Summary and perspectives

In this chapter, we explored the possibility of using OSTE resin to generate scaffolds as a tool for basic cell biology. Open structures fabricated with commercial OSTE resin (NOA 61) induced the engagement from the endothelial monolayer, with the generation of numerous filopodia associated with a phenotype evocative of tip cells. This process was independent of vascular endothelial growth factor (VEGF), suggesting that endothelial filopodia, not observed classically in 2D cultures, could be triggered by microtopography alone. Next, to combine microtopography and controlled surface chemistry, we used our self-developed OSTE resin. When the ratio of the OSTE resin was 1:5, we obtained a cell-repellent

surface by grafting Me-PEG308-SH. By one-photon grafting, the fully modified structure was totally cell-repellent. Future steps will be to perform local surface modifications by two-photon polymerization, which will provide precise 3D spatial positioning of the anti-adhesive areas, including in the Z direction. This will provide a new tool for the control of local adhesion.

3.5 References

(1) Ferreira, L. P.; Gaspar, V. M.; Mano, J. F. Design of Spherically Structured 3D in Vitro Tumor Models -Advances and Prospects. *Acta Biomater.* **2018**, *75*, 11–34. https://doi.org/10.1016/j.actbio.2018.05.034.

(2) Costa, E. C.; Moreira, A. F.; de Melo-Diogo, D.; Gaspar, V. M.; Carvalho, M. P.; Correia, I. J. 3D Tumor Spheroids: An Overview on the Tools and Techniques Used for Their Analysis. *Biotechnol. Adv.* **2016**, *34* (8), 1427–1441. https://doi.org/10.1016/j.biotechadv.2016.11.002.

(3) Dhaliwal, A. Three Dimensional Cell Culture : A Review. *Mater. Methods* **2012**, *2*, 162. https://doi.org/10.13070/mm.en.2.162.

(4) Klein, F.; Richter, B.; Striebel, T.; Franz, C. M.; Freymann, G. Von; Wegener, M.; Bastmeyer, M. Two-Component Polymer Scaffolds for Controlled Three-Dimensional Cell Culture. *Adv. Mater.* **2011**, *23* (11), 1341–1345. https://doi.org/10.1002/adma.201004060.

(5) Richter, B.; Hahn, V.; Bertels, S.; Claus, T. K.; Wegener, M.; Delaittre, G.; Barner-Kowollik, C.; Bastmeyer, M. Guiding Cell Attachment in 3D Microscaffolds Selectively Functionalized with Two Distinct Adhesion Proteins. *Adv. Mater.* **2017**, *29* (5). https://doi.org/10.1002/adma.201604342.

(6) Coscoy, S.; Baiz, S.; Octon, J.; Rhoné, B.; Perquis, L.; Tseng, Q.; Amblard, F.; Semetey, V. Microtopographies Control the Development of Basal Protrusions in Epithelial Sheets. *Biointerphases* **2018**, *13* (4), 041003. https://doi.org/10.1116/1.5024601.

(7) Huang, G.; Li, F.; Zhao, X.; Ma, Y.; Li, Y.; Lin, M.; Jin, G.; Lu, T. J.; Genin, G. M.; Xu, F. Functional and Biomimetic Materials for Engineering of the Three-Dimensional Cell Microenvironment. *Chem. Rev.* **2017**, *117* (20), 12764–12850. https://doi.org/10.1021/acs.chemrev.7b00094.

(8) Park, H. J.; Zhang, Y.; Georgescu, S. P.; Johnson, K. L.; Kong, D.; Galper, J. B. Human Umbilical

Vein Endothelial Cells and Human Dermal Microvascular Endothelial Cells Offer New Insights into the Relationship between Lipid Metabolism and Angiogenesis. *Stem Cell Rev.* **2006**, *2* (2), 93–102. https://doi.org/10.1385/SCR:2:2:93.

(9) Sprague, E. A.; Tio, F.; Ahmed, S. H.; Granada, J. F.; Bailey, S. R. Impact of Parallel Micro-Engineered Stent Grooves on Endothelial Cell Migration, Proliferation, and Function: An in Vivo Correlation Study of the Healing Response in the Coronary Swine Model. *Circ. Cardiovasc. Interv.* **2012**, *5* (4), 499–507. https://doi.org/10.1161/CIRCINTERVENTIONS.111.967901.

(10) Ucla, P.; Ju, X.; Demircioglu, M.; Baiz, S.; Muller, L.; Germain, S.; Monnot, C.; Semetey, V.; Coscoy, S. Dynamics of Endothelial Engagement and Filopodia Formation in Complex 3D Microscaffolds. *Int. J. Mol. Sci.* **2022**, *23* (5), 2415. https://doi.org/10.3390/ijms23052415.

(11) Bray, M. A. P.; Adams, W. J.; Geisse, N. A.; Feinberg, A. W.; Sheehy, S. P.; Parker, K. K. Nuclear Morphology and Deformation in Engineered Cardiac Myocytes and Tissues. *Biomaterials* **2010**, *31* (19), 5143–5150. https://doi.org/10.1016/j.biomaterials.2010.03.028.

(12) Coscoy, S.; Baiz, S.; Octon, J.; Rhoné, B.; Perquis, L.; Tseng, Q.; Amblard, F.; Semetey, V. Microtopographies Control the Development of Basal Protrusions in Epithelial Sheets. *Biointerphases* **2018**, *13* (4), 041003. https://doi.org/10.1116/1.5024601.

(13) Nakatsu, M. N.; Sainson, R. C. A.; Pérez-Del-Pulgar, S.; Aoto, J. N.; Aitkenhead, M.; Taylor, K. L.; Carpenter, P. M.; Hughes, C. C. W. VEGF121 and VEGF165 Regulate Blood Vessel Diameter Through Vascular Endothelial Growth Factor Receptor 2 in an in Vitro Angiogenesis Model. *Lab. Investig.* **2003**, *83* (12), 1873–1885. https://doi.org/10.1097/01.LAB.0000107160.81875.33.

(14) Olson, H. M.; Nechiporuk, A. V. Lamellipodia-like Protrusions and Focal Adhesions Contribute to Collective Cell Migration in Zebrafish. *Dev. Biol.* **2021**, *469*, 125–134. https://doi.org/10.1016/j.ydbio.2020.10.007.

(15) Canales Coutiño, B.; Mayor, R. Mechanosensitive Ion Channels in Cell Migration. *Cells Dev.* **2021**, *166*, 203683. https://doi.org/10.1016/j.cdev.2021.203683.

(16) Talkenberger, K.; Ada Cavalcanti-Adam, E.; Voss-Böhme, A.; Deutsch, A. Amoeboid-Mesenchymal Migration Plasticity Promotes Invasion Only in Complex Heterogeneous Microenvironments. *Sci. Rep.* **2017**, *7* (1), 1–12. https://doi.org/10.1038/s41598-017-09300-3.

(17) Ghosh, I.; Singh, R. K.; Mishra, M.; Kapoor, S.; Jana, S. S. Switching between Blebbing and

Lamellipodia Depends on the Degree of Non-Muscle Myosin II Activity. *J. Cell Sci.* **2021**, *134* (1), 1–12. https://doi.org/10.1242/jcs.248732.

Chapter IV. Two-photon Polymerization of Proteins

4.1 Introduction

In addition to synthetic organic polymers, natural protein materials are also particularly important materials for two-photon polymerization. Protein is a naturally occurring biomolecule in living organisms and has natural biocompatibility.

The Extracellular Matrix (ECM) is a complex structure surrounding the cell that consists of a group of molecules such as proteins, polysaccharides, growth factors and other biomolecules. The ECM plays a variety of important roles in tissues and organs. Using proteins as the raw material for 2PP, the prepared cell scaffolds can better mimic the extracellular matrix (ECM) in tissues, providing an environment conducive to cell attachment, proliferation, and differentiation. This biocompatibility enhances the scaffold's ability to support cellular activity and tissue regeneration. Protein scaffolds have similar structures to natural ECM. Proteins, such as collagen, elastin, or fibronectin, are major components of the extracellular matrix and play a key role in cell behavior and tissue development. By using proteins as raw material for the preparation of cellular scaffolds from 2PP, the structure and composition of the natural ECM can be recreated. This structural similarity helps guide cell behavior, including attachment, migration, and differentiation, and promotes tissue regeneration and normal tissue function.

4.2 Formulation of protein pre-polymerization solution

The formulation of the pre-polymerization solution consists of protein, photoinitiator and solvent. Bovine Serum Albumin (BSA) is commonly used as one of the components of cell culture media.[1] Due to its good solubility and stability, BSA is often used as a protein standard. In the laboratory, BSA is used to quantify protein concentrations, to calibrate chromatography and electrophoresis systems, and to assess protein purity and enzymatic activity.

BSA is commonly used in immunological experiments as a diluent, blocking agent or detergent for antigens or antibodies. It can reduce non-specific binding and background signal and improve the specificity and sensitivity of the experiment. Among all the proteins for two-photon polymerization, BSA is cheap and easily obtained from bovine serum. BSA and biotinylated BSA have been used to build varied 3D structures. BSA, as a common protein, has a variety of experimental and applied functions. Hence, we chose BSA as the module protein for two-photon polymerization. BSA is easily dissolved in water.

There were many attempts to have a convenient BSA solution for TPP. Different solvents, such as water, water/DMSO and water/glycerol have been used.[2] It is still unclear why DMSO improves

feature sizes. A possible reason for this is that proteins are more homogeneously distributed in the DMSO-water system. But the addition of DMSO risks damaging the protein. Glycerol also improves the viscosity of the solution, but pure water is easier to operate so we chose pure water as the solvent of the system.

Concerning the choice of the photoinitiator, as introduced briefly in Chapter I, there are several candidates, water-soluble xanthene dyes, riboflavin (Vitamin B) series, both organic and water-soluble Irgacure 2959, phosphine oxide series and benzophenone derivative salts. In this part, we chose five possible photoinitiators to test the polymerization of BSA. Rose Bengal, Flavin mononucleotide (FMN), Irgacure 2959, self-synthesized benzophenone and TPO-Li salt. Bacteria multiply very easily in BSA water solutions, so we added antibiotics to inhibit the growth of bacteria in all solutions. Kanamycin is an aminoglycoside antibiotic. Aminoglycosides work by binding to the bacterial 30S ribosomal subunit, causing misreading of t-RNA, leaving the bacterium unable to synthesize proteins vital to its growth.3 We chose a concentration of kanamycin of 0.5 mg/ml in water for all samples. Generally, BSA, photoinitiator and kanamycin were dissolved in distilled water, mixed with a rotating mixer for 2 hours. After mixing, the solution was centrifuged at 15000 rpm for 5 minutes. Only the upper layer solution was retained for two-photon polymerization.

4.2.1 Choice of photoinitiator

The first aim here is to polymerize BSA to get a stable 3D structure (the same open elongated hexagonal structure for cell culture). In the literature, we have known that BSA can be polymerized with lots of photoinitiators. Here we typical photoinitiators to try to polymerize BSA. As we have described in Chapter I, there are several kinds of choices. Organic dyes are the common choice for protein polymerization. Among the dyes, Rose Bengal (xanthene series) and flavin mononucleotide (flavin series) are nice ones. Iosin *et al.*[4] obtained a simple BSA grid with 10 mg/ml BSA, 10 mg/ml Rose Bengal, using a 532 nm laser. But there is no more complex 3D structure shown. Lin *et al.*[5] polymerized 20 mg/ml BSA with 2 mg/ml Rose Bengal using a 730 nm laser. In our equipment set-up, the wavelength of the laser is 532 nm. We would like to try Rose Bengal as the photoinitiator. FMN is also a non-toxic photoinitiator for protein polymerization, Turunen *et al.*[6] showed that FMN has a big multiple-photon absorption at 532 nm. FMN was chosen as the second candidate for our experiment. Besides dyes, traditional available photoinitiators are also possible choices. But most of them are water-insoluble, except Irgacure 2929. The solubility in water of Irgacure 2959 is around 1 mg/ml. Irgacure 2959 was also chosen in our test. In chapter one, we have introduced the method to modify water-insoluble molecules into water-soluble molecules. Ionization or conversion of molecules into salt form is a remarkably effective way to increase the solubility of photoinitiators in water. Here we tried to synthesize a water-soluble benzophenone derivative by this method. At the

same time, a commercially available ionized molecule TPO-Li was chosen for fit spectrum at 532 nm.

4.2.1.1 Rose Bengal

We have introduced the water-soluble xanthene dyes in Chapter 1. Rose Bengal belongs to the group of xanthene dyes. It is well known that xanthene dyes work as photoinitiators together with amine as the co-initiator. A charge transfer intermediate between the excited dye and the amine plays a significant role in the deactivation of excited states of xanthene dyes by amines.[7] **Figure 4.1** shows the mechanism of Rose Bengal as a type II photoinitiator. Amine is needed as a co-initiator to produce radicals. When mixed with proteins, amine could be the free amine group in protein and no more extra amin is needed.

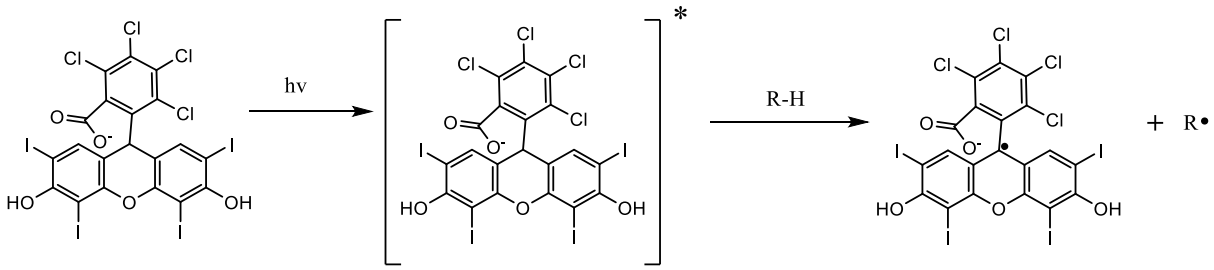

Figure 4.1 Mechanism of Rose Bengal as a photoinitiator

To better describe the parameter test results, we define two expression forms. First, we define BSA10/ RB0.5 as the formula of the solution consisting of 10 mg/ml BSA and 0.5 mg/ml Rose Bengal solution. Second, we define the fabrication parameters. LG0.2/ET2000, meaning the laser gain is 0.2 and the exposure time of the laser is 2000 µs.

In the literature, a wide range of concentrations of BSA (0-1000 mg/ml) was used to perform TPP.[1] But few stable 3D structures fabricated with relatively lower concentrations of BSA (for example, <50 mg/ml) were shown. To find the best formulation for TPP, we tested three concentrations of BSA, 10/25/50 mg/ml, with RB as photoinitiator to fabricate hexagonal open structure we designed in Chapters II and III, *D8K1H5-open* (**Figure 4.2** a). *D* is the diameter of the inscribed circle of the top hexagon, 5 µm. *H* is the height, 5 µm. With our equipment set-up, 532 nm ns pulse and 60x water lens, we tested the varied fabrication parameters to find the best laser gain and exposure time. After fabrication, the structures were washed with pure water and stored in pure water. Then observed with a Leica optical microscope with a water lens. Structures.

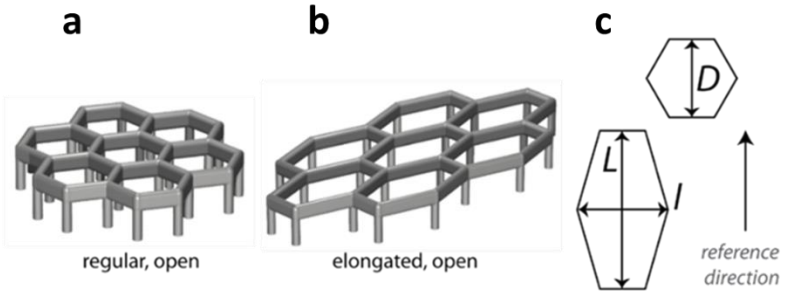

Figure 4.2 Structures designed for BSA polymerization. (a) open hexagonal structure *D8K1H5-open* (b) elongated open hexagonal structure *l7L14H7-open* (c) elongation direction and parameters

Figure **4.3** shows the parameter test of BSA/Rose Bengal solution. For BSA10/RB0.5, over-polymerization occurred from extremely low laser gain 0.2. For BSA25/RB0.5, laser gain/exposure parameters LG0.2/ET2000, LG0.2/ET4000 and LG0.2/ET6000 were not able to generate stable structure. When exposure time increased to 8000 μs, we started to obtain a partial structure. Stable structures with nice resolution appeared when laser gain was 0.4. For BSA50/RB0.5 BSA solution, there was no polymerization when laser gain was LG0.2/ET= (all values). When Rose Bengal concentration was set at 0.5 mg/ml, the best manufacturing parameters moved towards long exposure time and high laser gain with increasing BSA concentration from 10 mg/ml to 50 mg/ml. The tested laser gain range was 0.2, 0.4, 0.6, 0.8. The relationship between laser gain and the actual laser output intensity has been shown in Chapter II.

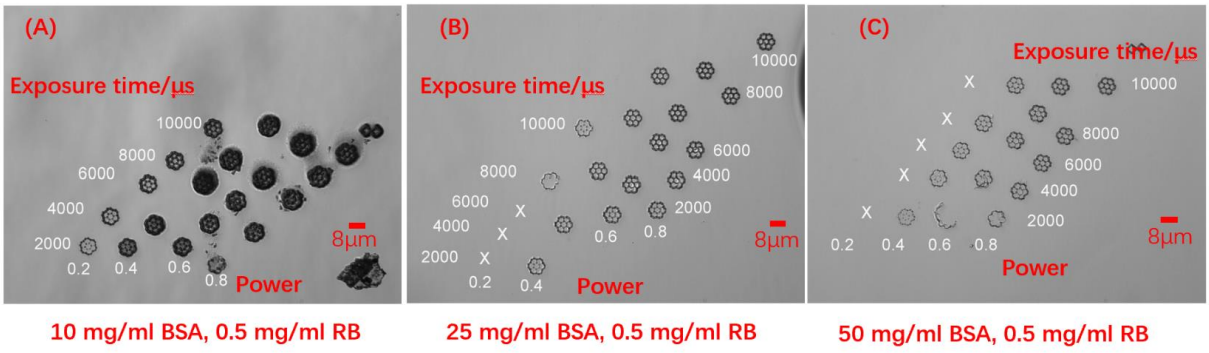

Figure 4.3 Images of fabrication parameter test of BSA/RB water solution with *D8K1H5-open* structures. Structures were washed with pure water and observed in water. (A) BSA10/RB0.5. (B) BSA25/RB0.5. (C) BSA50/RB0.5. Scale bar, 8 μm.

To figure out the shift of the best fabrication parameter, we tested the UV absorption of pure BSA water solution without Rose Bengal. **Figure 4.4** shows the UV-visible spectra of different BSA concentration water solutions. We can find that the absorption intensity of the gradient solution at 266 nm increases while increasing BSA concentration, which explains why there was a shift of stable 3D hexagon structures from low laser gain to high laser gain for two-photon polymerization. When the concentration of BSA was 10 mg/ml, the absorption of BSA is relatively low. With the same laser gain, more light will induce radicals to polymerize BSA. The BSA solution started to be over-polymerize at 0.4 laser gain. With 25 mg/ml, BSA solution gave stable structures when laser gain ranging from 0.2 to 0.6 even part of the energy was absorbed by BSA. When the concentration of BSA was 50 mg/ml, there was no structure when laser gain was 0.2. BSA itself absorbed more energy, thus the energy that can be absorbed by photoinitiator Rose Bengal was less.

The absorbance of BSA increased as the concentration of BSA increased. Therefore, under a certain concentration of photoinitiator, higher laser intensity and longer exposure time are required to provide high energy to the photoinitiator to generate free radical polymerisation. So, there was a shift of the best fabrication parameters to longer exposure time and higher laser gain.

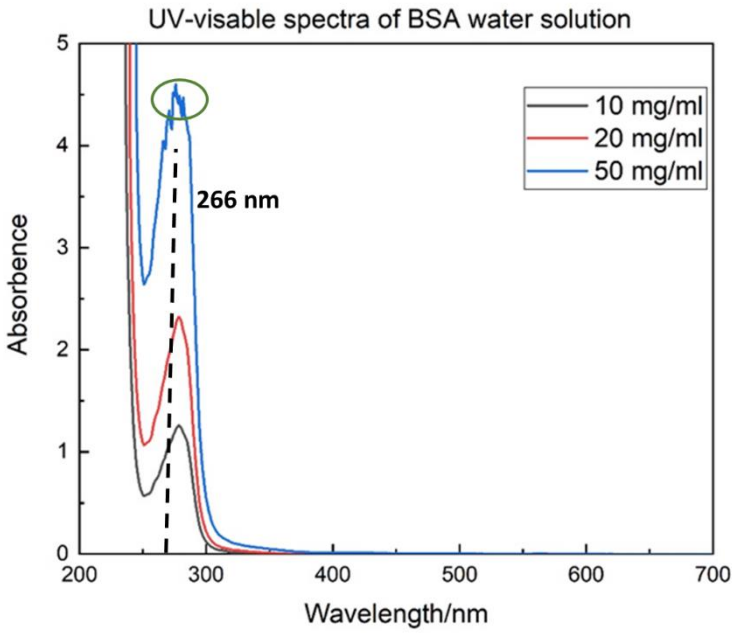

Figure 4.4 UV-visible spectra of BSA water solution. For 50 mg/ml BSA, this concentration was so high that it reached saturation and was outside the normal test range of the instrument (green circle). Dashed line at 266 nm.

In this part, we acquired the best structure with nice resolution at 25 mg/ml BSA together with Rose Bengal. In the following test, we set 25 mg/ml as the standard concentration of BSA for the test of photoinitiators.

4.2.1.2 Flavin mononucleotide (FMN)

Flavin mononucleotide (FMN) is one of the riboflavin series of photoinitiators. **Figure 4.5** shows the chemical structure of FMN and UV-visible spectrum. FMN has four absorption peaks in the UV-visible range 223, 267, 373 and 444 nm. Like Rose Bengal, FMN is a type II photoinitiator.[8] The mechanism of flavin series photoinitiator follows the same path (**Figure 4.6**).[9]

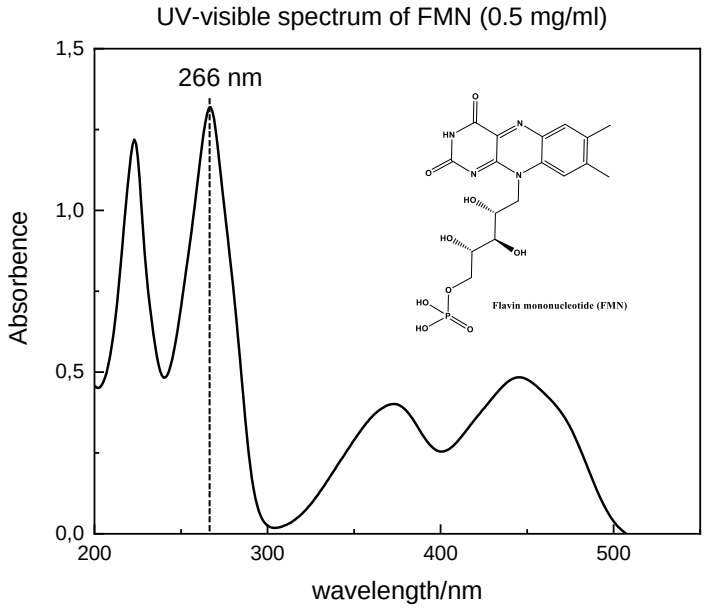

Figure 4.5 Chemical structure of FMN and its UV-visible spectrum (0.5 mg/ml)

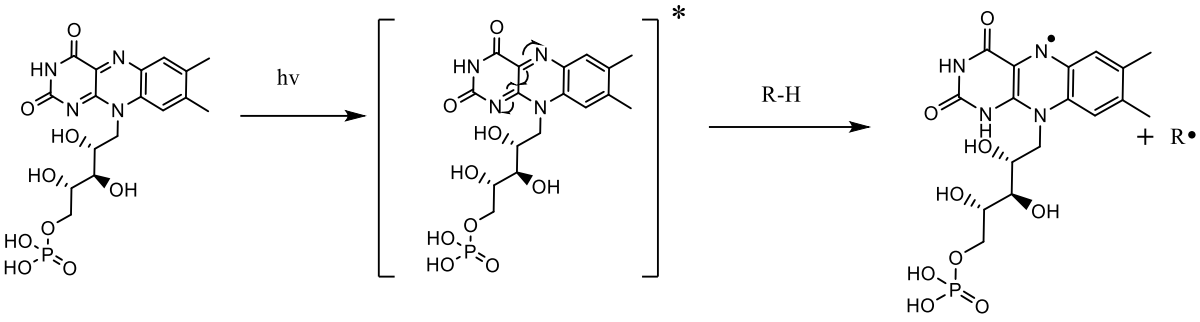

Figure 4.6 Mechanism of FMN as a photoinitiator. When FMN is used for protein polymerization, the co-initiator R-H can be the free amine group in the protein itself.

We tested two formulations of BSA/FMN solution. The same hexagonal structure *D8K1H5-open* was tested as BSA/RB solution. **Figure 4.7** shows the results for small open hexagon structures *D8K1H5*. Those images were taken by charged-couple device (CCD) camera of our TPP equipment set-up just after fabrication. They were not washed by water. BSA 25 mg/ml with FMN 0.5 mg/ml (BSA25/FMN0.5) did not allow to generate stable structure with nice resolution. When the laser gain increased or the exposure time extended, we still obtained a stable structure. When the concentration of BSA increased to 50 mg/ml, we could not get a nice structure with nice resolution either.

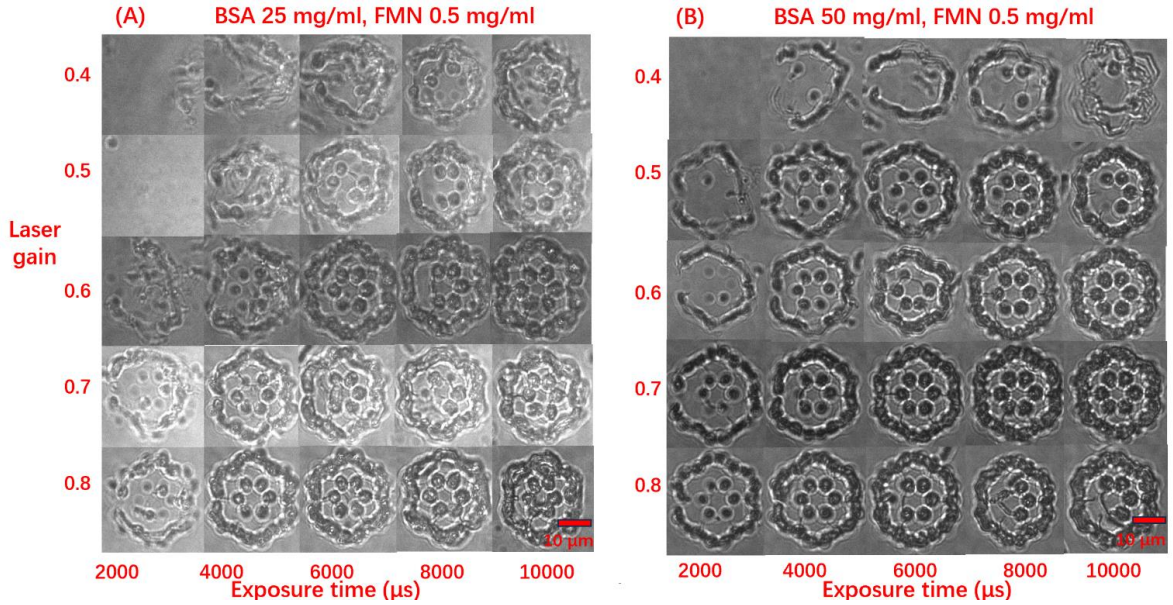

Figure 4.7 Images of *D8K1H5-open* acquired with different parameters. Images were taken just after fabrication by charged-couple device (CCD) camera of our TPP equipment set-up. Those structures were still in the BSA/FMN solution without washing. Concentrations of BSA/FMN (A)BSA25/FMN0.5. (B)BSA50/FMN0.5 Scale bar 10 µm.

To have images with better resolution, we washed the structures with pure water and then take images we acquired pictures of polymerized BSA/FMN structures with fluorescence microscope. The excitation of the laser of the microscope was 470 nm. Images were taken with green fluorescent protein (GFP) filter. **Figure 4.8** shows the fluorescence images in the GFP channel. We started to obtain a relatively stable structure with a nice resolution at LG0.6/ET8000. Compared to BSA25/RB0.5, structures fabricated with BSA25/FMN0.5 were relatively unruly. By now, BSA/RB appears to be a better formula than BSA/FMN.

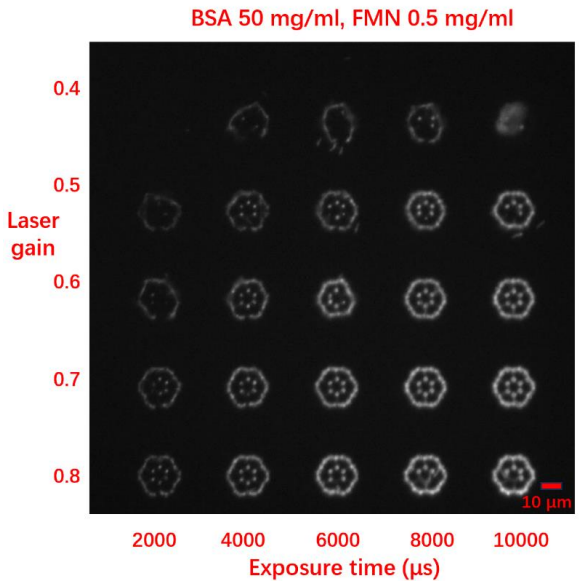

Figure 4.8 Fluorescence images of fabrication parameter test of BSA solution with FMN. Images were taken with fluorescence microscope with water lens. All structures were washed with pure water, Concentrations of formulation, BSA50/FMN0.5. Scale bar 10 µm.

4.2.1.3 Irgacure 2959

Most of the photoinitiators used in resins are dissolved in organic solvents. Only a few, like Irgacure 2929, also known as 2-Hydroxy-4′-(2-hydroxyethoxy)-2-methylpropiophenone (**Figure 4.9**), have limited water solubility, around 1 mg/ml. This photoinitiator is sensitive to UV-A and visible light in the range of 300-450 nm and it is one of the commonly used photoinitiator for two-photon polymerization. Irgacure 2959 functions via Norrish type I reaction, during which process an excited carbonyl compound is cleaved into an acyl-alkyl radical pair (from an acyclic carbonyl compound) or an acyl-alkyl diradical (from a cyclic carbonyl compound). [10] It is also well known for its low toxicity for bio-applications.

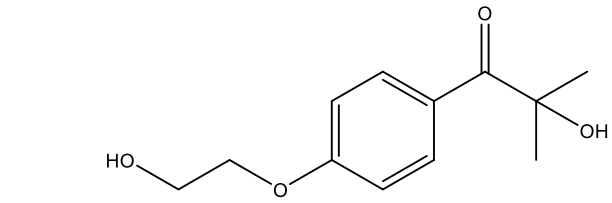

2-Hydroxy-4'-(2-hydroxyethoxy)-2-methylpropiophenone (Irgacure 2959)

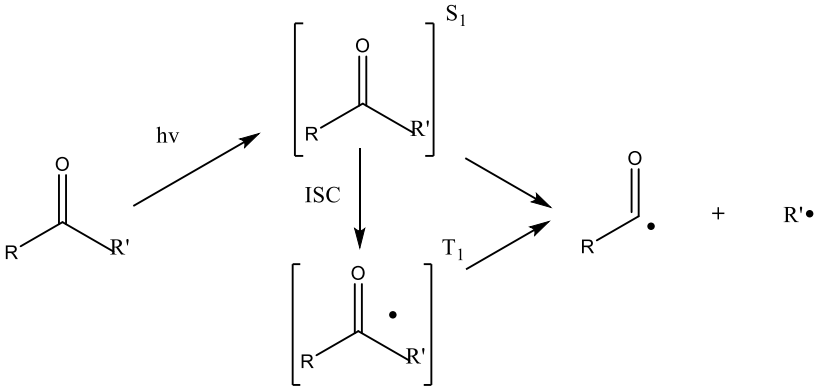

Norrish type I reaction

Figure 4.9 Chemical structure of Irgacure 2959 and the mechanism of Norris type I reaction. ISC, inter-system crossing.[10]

Here we tested the feasibility of Irgacure 2959 as a two-photon polymerization photoinitiator to initiate protein polymerization. The components are BSA 25 mg/ml and Irgacure 2959 0.5 mg/ml (BSA25/Irga2959 0.5) in distilled water. The structure used for the parameter test was still the small open hexagon structure *D8K1H5-open*. The tested exposure time ranges from 2000 μs to 10000 μs. After fabrication, we took pictures with a CCD camera. **Figure 4.10** shows the results of the parameter test. When the laser gain was 0.2, there was no polymerization. BSA started to polymerize when laser gain increased to 0.4 but only the outer part of the hexagon is visible in the picture. With LG0.8/ET8000 and LG 0.8/Exp10000, the structures were stable and clear. But it is obvious that the crown part of the structure showed signs of over-polymerization. We concluded that BSA25/Irga29590.5 was not as good as BSA25/RB0.5.

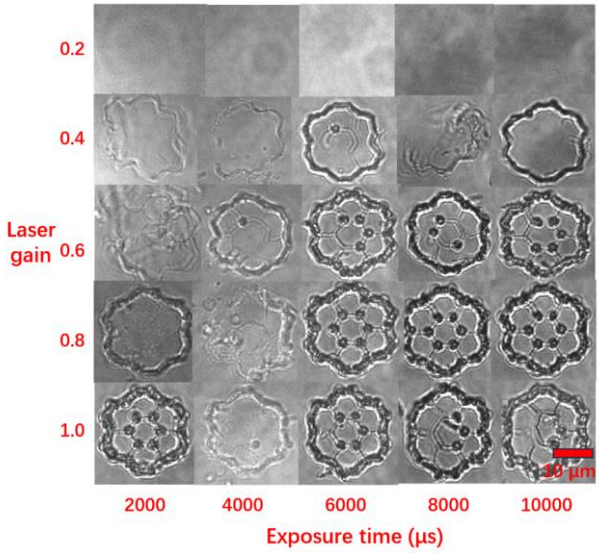

Figure 4.10 Fabrication parameter test of BSA water solution with Irgacure 2959. Images were taken just after fabrication by charged-couple device (CCD) camera of our TPP equipment set-up. Those structures were still in the BSA/Irgacure 2959 solution without washing. Concentrations of formulation, BSA25/Irga2959 0.5. Scale bar 10 µm.

4.2.1.4 Benzophenone derivative

Benzophenone is a very commonly used photoinitiator for both UV curing and two-photon polymerization. Benzophenone has a π-acceptor-π (π-A-π) structure. Based on this basic formula, many benzophenone derivatives were developed to improve the efficiency as a photoinitiator. New formulas with bigger conjugated molecules are explored, such as donor-π-acceptor-π-donor (D-π-A-π-D), D-π-A, D-π-A-π-D.[11,12,13,14] The absorption can also be tuned by conjugation. But almost all of them are not water-soluble. When used together with proteins, we need a water-soluble photoinitiator. The easy and efficient way is to transfer the molecule from water-insoluble organic molecule to a water-soluble salt.[15] Water soluble molecules based on 4-bromomethyl benzophenone are nice targets for our purpose. **Figure 4.11** shows the reaction of the synthesis of our target molecule, *N*-(4-benzoylbenzyl)-*N*,*N*-dimethylethanamine bromide (BDB).

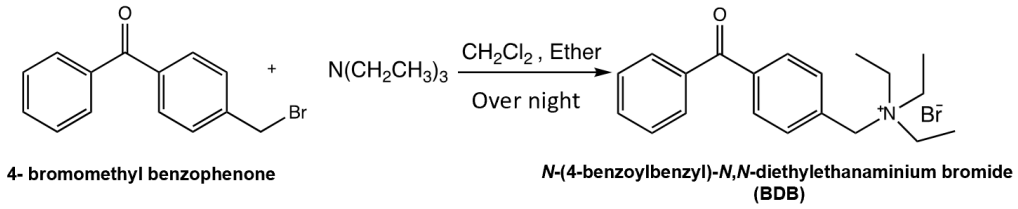

Figure 4.11 Synthesis of water-soluble benzophenone derivative BDB for two-photon polymerization

BDB is the Norrish type II photoinitiator. The photoactivated aldehyde group takes a proton from the tertiary amine to become a hydroxyl group, and the methylene group on the tertiary amine generates a methylene radical, which initiates the subsequent polymerization reaction. **(Figure 4.12)**

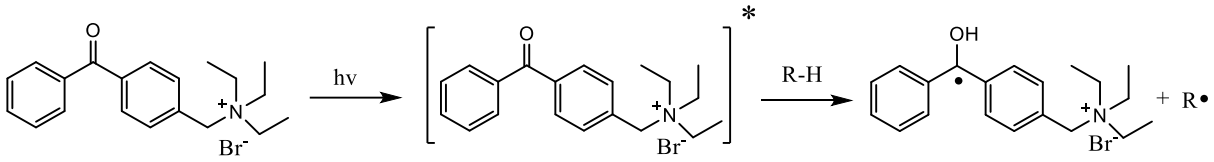

Figure 4.12 Mechanism of BDB as a photoinitiator

Synthesis of BDB

(1) Reaction. 1:1 4-bromomethyl benzophenone and trimethylamine were dissolved in CH_2Cl_2 and ether. After stirring overnight at room temperature, solvent was removed by rotary evaporation.
(2) Recrystallization. As little methanol as possible was added to redissolve the product. Then dimethyl ether was added into the solution. The solution was put into freezer at -26 ^oC for 3 hours.
(3) Solvent was removed by filtration. The resulting white solid was dried in a vacuum oven for 3 hours at 40 ^oC to obtain a white powder and stored in a brown bottle in a refrigerator.

Nuclear Magnetic Resonance (NMR)

^1H NMR was recorded on Brucker Avance III HD 400 MHz spectrometer at 298 k. Deuterated methanol (CD_3OD) was used as the solvent. NMR chemical shifts were recorded in parts per million (ppm) referenced to the residual solvent proton (δ = 3.31 ppm) for ^1H NMR. **Figure 4.13** shows the 1H NMR spectrum of the synthetic photoinitiator BDB.

(4) NMR analysis: CD_3OH was chosen as the solvent.

^{1}H NMR (400 MHz, CD_3OD), δ (ppm), 7.98-7.52 (9H, m), 4.63 (2H, s), 3.41-3.33 (6H, m), 1.60-1.40 (9H, m)

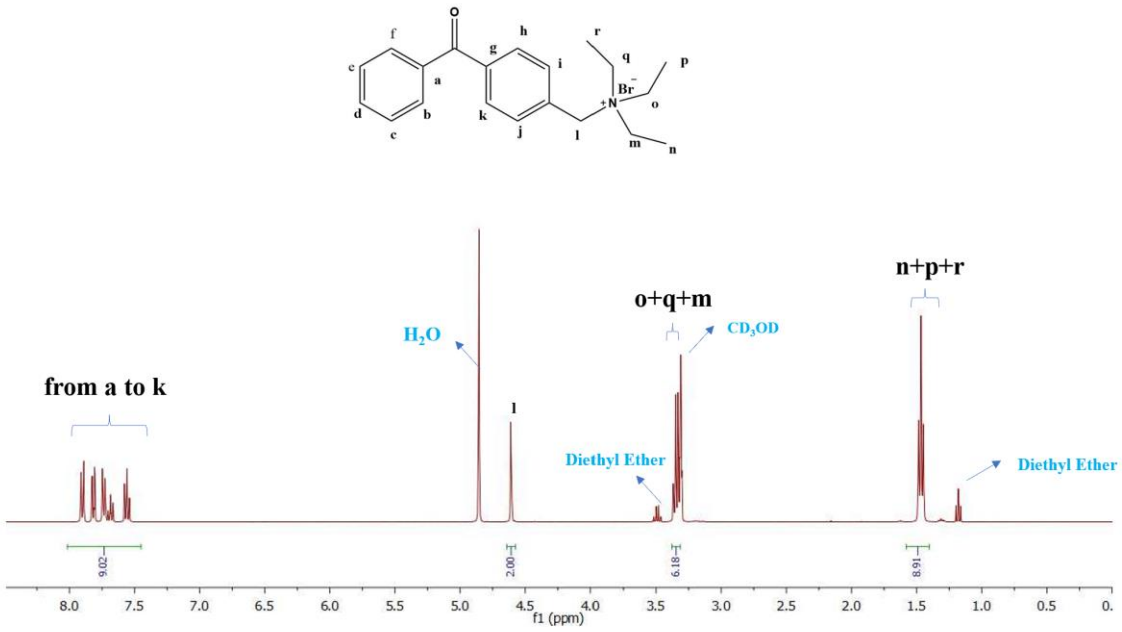

Figure 4.13 ^{1}H NMR spectrum of the synthetic BDB

Yield

The amount of 4-bromomethyl benzophenone was 4 mmol. After recrystallization, 3.35 mmol BDB was obtained. The final yield of the synthesis of BDB was 83.75%.

We tested the new synthetic BDB as a photoinitiator for BSA polymerization, with concentrations of 0.5 and 25 mg/ml respectively (BSA25/BDB0.5). **Figure 4.14** shows the results of the parameter test matrix. Those images were taken by charged-couple device (CCD) camera of our TPP equipment set-up just after fabrication. They were not washed by water. The images clearly show that there was no stable structure with nice resolution at all. Compared to Rose Bengal, BDB did not prove to be an efficient photoinitiator for two-photon polymerization of BSA.

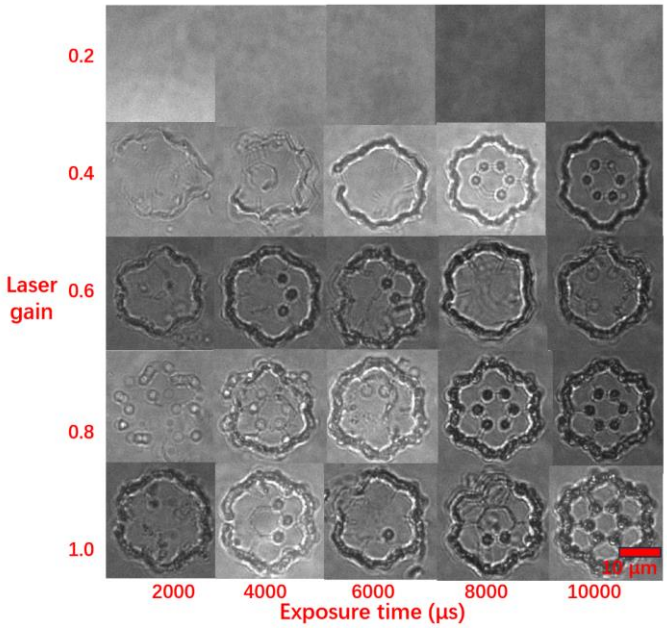

Figure 4.14 Fabrication parameter test of BSA water solution with BDB. Images were taken just after fabrication by charged-couple device (CCD) camera of our TPP equipment set-up. Those structures were still in the BSA/BDB solution without washing. Concentrations of formulation, BSA25/BDB0.5. Scale bar 10 µm.

4.2.1.5 TPO-Li

Phosphine oxide photoinitiators form a large group commonly used in UV and two-photon polymerization. TPO is one of the typical ones, a commercially available photoinitiator which has been widely used in two-photon polymerization. But it is not soluble in water. Then a series of TPO relatives were developed. TPO-Li is one Li salt of the water-soluble form based on TPO (**Figure 4.15**). TPO-Li is a type I photoinitiator. Photoactivated molecular cleave into two free radicals directly (**Figure 4.16**).

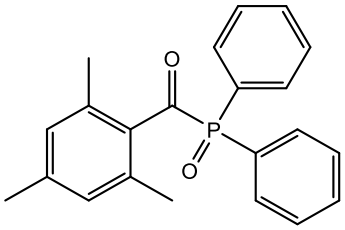

2,4,6-trimethylbenzoyl-diphenylphosphine oxide (TPO)

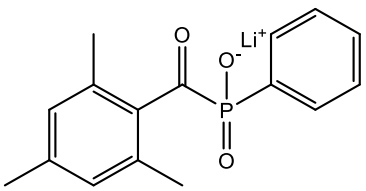

Lithium phenyl-2,4,6-trimethylbenzoylphosphinate (TPO-Li)

Figure 4.15 Chemical structures of TPO and TPO-Li

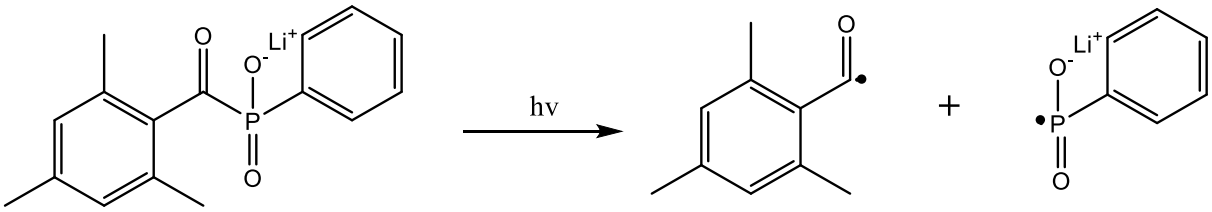

Figure 4.16 Mechanism of TPO-Li as a photoinitiator

We tested BSA25/TPO-Li0.5 the same way as other photoinitiators above, but there was no polymerization. When the concentration of TPO-Li increased to 10 mg/ml and 20 mg/ml, polymerization of proteins began to occur. **Figure 4.17** shows the parameter test with BSA 25/TPO-Li 10 and BSA25/TPO-Li20. It is noticeably clear that there is no complete hexagonal structure. During all the parameter tests, there were no clear structures. These results revealed that the two-photon cross-section of TPO-Li at 532 nm is far lower than that of Rose Bengal.

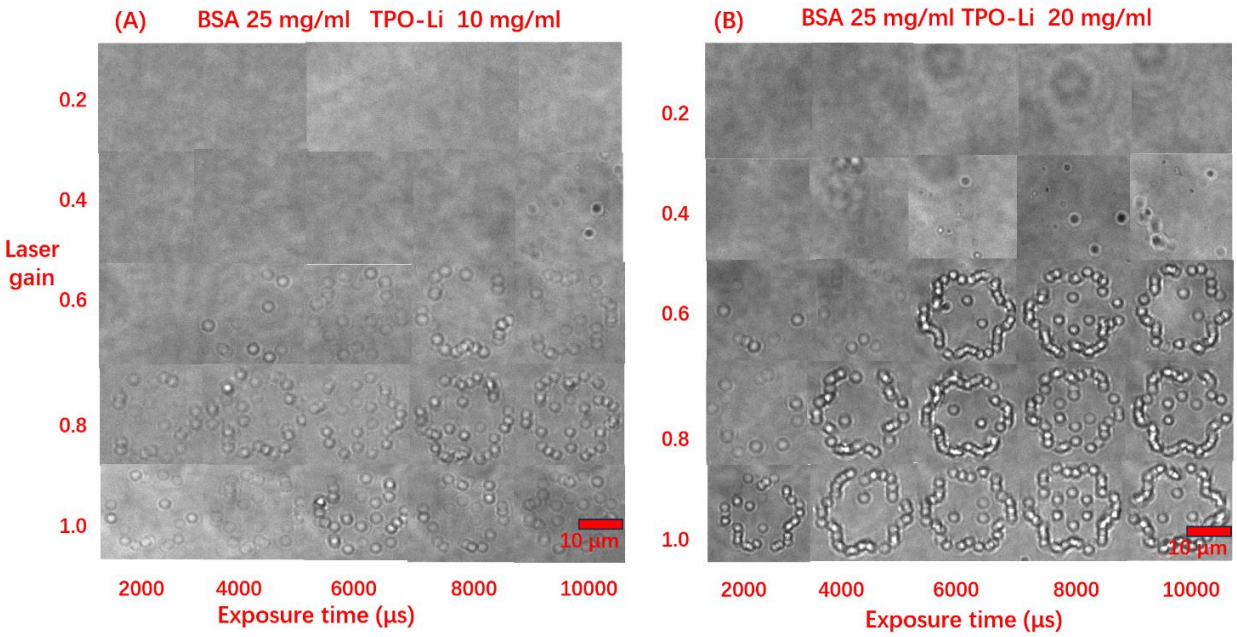

Figure 4.17 Fabrication parameter test of BSA water solution with TPO-Li. Images were taken just after fabrication by charged-couple device (CCD) camera of our TPP equipment set-up. Those structures were still in the BSA/TPO-Li solution without washing. Concentrations of formulation, (A)BSA25/TPO-Li10.(B)BSA25/TPO-Li20. Scale bar 10 µm.

In this section, we tested all five kinds of photoinitiators with BSA. From the results, we concluded that BSA25/RB0.5 was the best formulation.

4.2.2 Stable microstructures with BSA and Rose Bengal.

4.2.2.1 Fine Parameters exploring for two-photon polymerization.

From the parameters test performed above, we found that BSA25/RB0.5 in water was a nice formulation of protein solution for two-photon polymerization. To get the best structure, we narrowed the stepwise of laser gain from 0.3 to 0.4. After fabrication, the structures were put in a pure water bath to be washed and then transferred into a water bath to be viewed. **Figure 4.18** shows the BSA structures in this narrow range. All pictures were taken with Leica fluorescence microscope with a water lens.

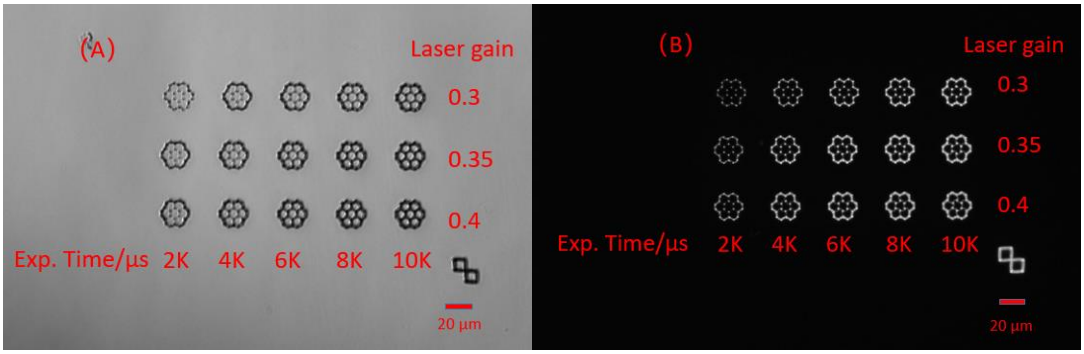

Figure 4.18 TPP structure matrix of BSA25/RB0.5 in water (A) white light channel field image (B) fluorescence images acquired with GFP channel filter. Scale bar 20 μm.

Then the BSA structures were taken out from the water bath and dried in the air directly for SEM. Since BSA is not conductive, the structures were deposited with a layer of gold for SEM observation. **Figure 4.19** shows the SEM images of all the BSA structures. All the structures collapsed because of their low mechanical stability. When we observe with SEM, electron high tension (EHT) voltage will influence the structures and images. When EHT < 3 kV, there was no clear image. When EHT = 3 kV, we got clear image, while 5 kV and 10 kV damaged the 3D BSA structure (**Figure 4.20**). The details of the image were lost at higher EHT conditions. We confirmed that the appropriate EHT for BSA structure is 3 kV. Besides, the mechanical property of raw BSA structure was not strong enough to maintain their shape for SEM. We need post-processing for SEM observation. In the coming section, we tried to maintain the BSA structure by post-processing.

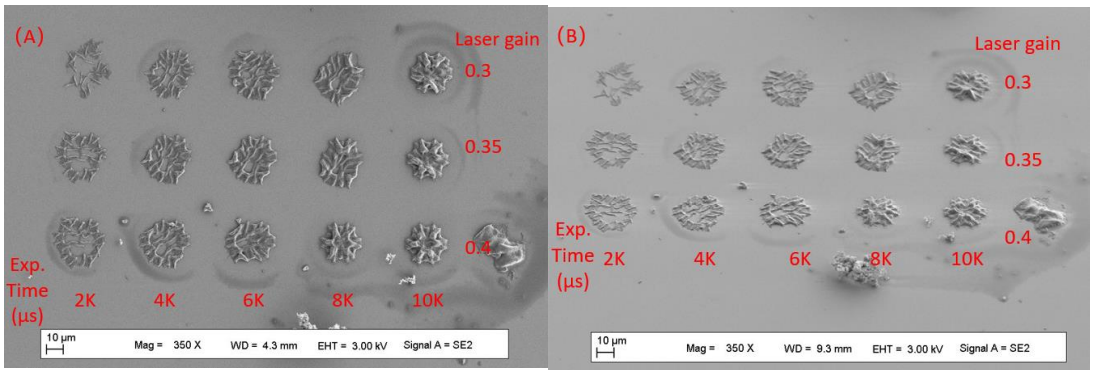

Figure 4.19 SEM image of TPP structure matrix of BSA25/RB0.5 after drying in the air (A) top view (B) tilted 45^0 view. Scale bar 10 μm.

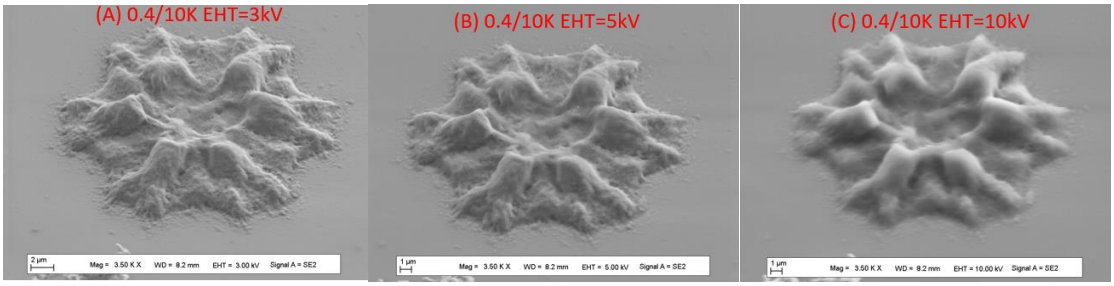

Figure 4.20 Influence of electron high tension (EHT) voltage on SEM image of TPP structure of BSA25/RB0.5 after drying naturally, tilted 45^0 views. (A) EHT= 3kV (B) 5 kV (C) 10 kV. Scale bar 2 μm for (A) and 1 μm for (B) and (C).

4.2.2.2 Effect of glutaraldehyde for the stability of BSA structure.

BSA structures cannot maintain stability after drying directly in the air. We cannot obtain SEM image of stable structures. Glutaraldehyde is a molecule that is commonly used to crosslink proteins. Here we tried to further crosslink our BSA structures to improve stability.

Glutaraldehyde water solution is the form usually used. The possible forms of glutaraldehyde in water solution are shown in **Figure 4.21**. (I) is the formula of glutaraldehyde. There are at least 13 different forms in aqueous solution with varied conditions.[16] In acidic or neutral conditions, free aldehyde form (I), cyclic form (IV) and monomer form (V) are the dominant formulas. In PBS buffer (pH=7.4, basic condition), α, β-unsaturated oligomeric aldehyde (VI) is the dominant form. BSA is a single polypeptide of 67 *kDa* with 59 lysine residues. After two-photon polymerization, lysine residues can react with glutaraldehyde (form VI), forming a Schiff base or Michael addition (**Figure 4.22**). Glutaraldehyde behaves as a crosslinker to strengthen the 3D BSA microstructures.

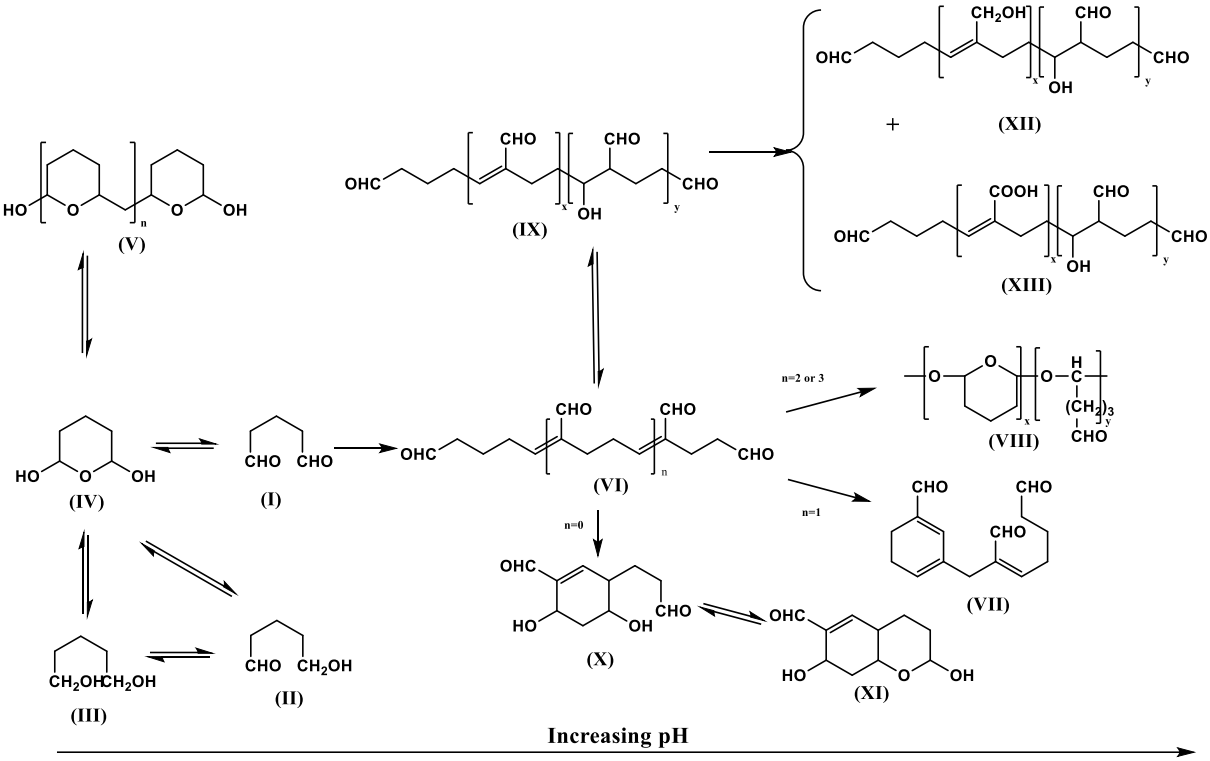

Figure 4.21 Possible forms of glutaraldehyde in water solution[16]

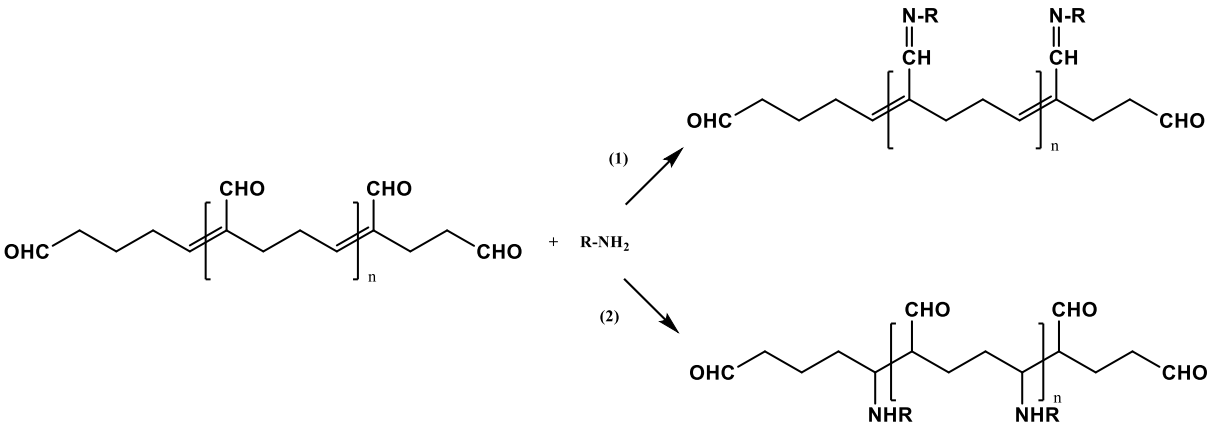

Figure 4.22 Reactions of glutaraldehyde with proteins via (1) Schiff base (2) Michael addition.[16]

We chose the best parameters from the parameter test for elongated open hexagon structures. Laser gain/exposure time (μs) parameters were LG0.35/ET8000, LG0.35/ET10000 and LG0.4/ET10000. After fabrication, the structures were fixed with 4% glutaraldehyde/PBS solution for 30 min and then washed with PBS 3 times, 10 min per time. After washing, the structures were dehydrated according to the following gradient procedure. The first step is to dehydrate the structures in 50% ethanol bath for 10 minutes 2 times. Then, the second step is to dehydrate the structures in 70% ethanol bath for

10 minutes 2 times. Thereafter, the third step is to dehydrate the structures in 95% ethanol bath for 10 minutes 2 times. At last, the fourth step is to dehydrate the structures in 100% ethanol bath for 10 minutes 3 times. After dehydrating, the structures were dried in the air.

Figure 4.23 shows the images of BSA structures with different parameters. The structure with LG0.35/ET8000 had a very thin top part. But it was too weak and was broken during the sample preparation process. The structure with LG 0.35/ET10000 maintained its 3D shape. We concluded that BSA25/RB0.5 was the best formula of the pre-polymerization solution among the solutions tested, and that LG 0.35/ET10000 was the best parameters for their two-photon fabrication.

In the literature, higher concentrations of BSA were tested. Since we already had nice structures with 25 mg/ml BSA, we chose not to test more concentrations.

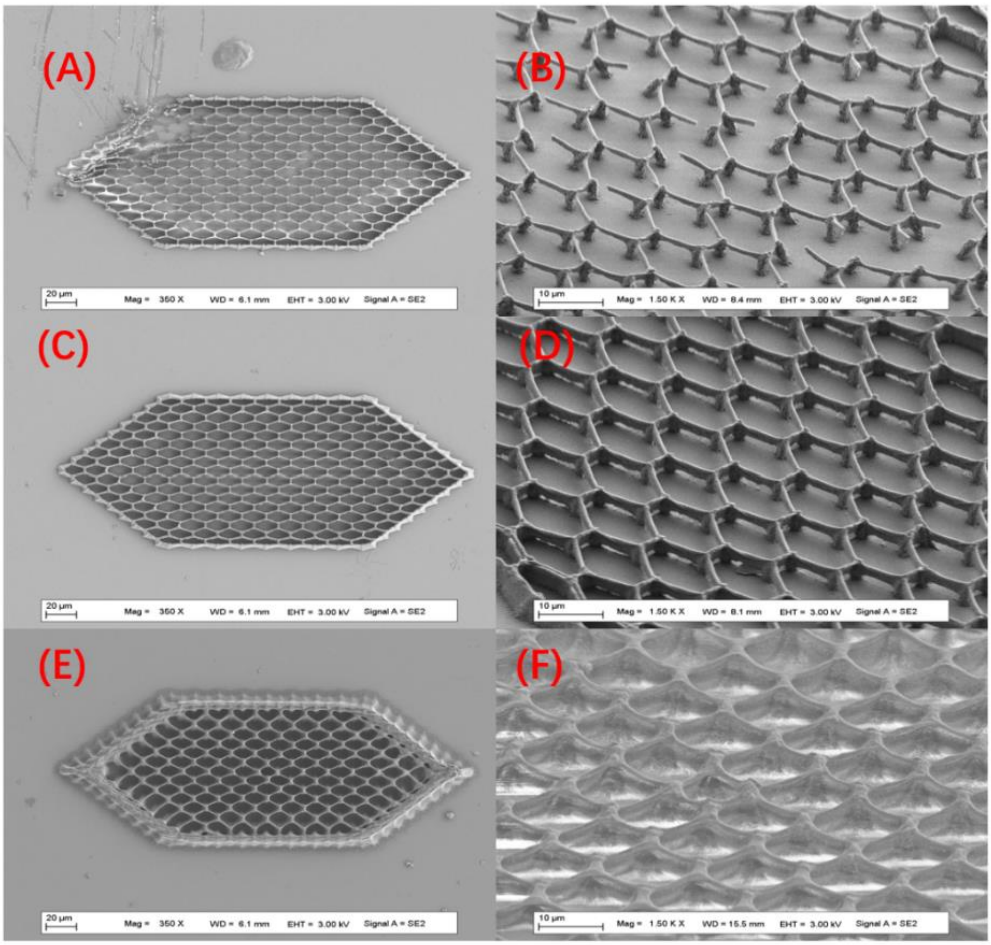

Figure 4.23 SEM images of elongated open hexagon structure with BSA. Parameters of laser gain/exposure time (μs): (A) LG0.35/ET8000, (B) zoom out of (A). (C) LG0.35/ ET8000, (D) zoom out of (C). (E) LG0.35/ ET10000, (F) zoom out of (E). Scale bar, 20 μm for (A), (C) and (E), 10 μm for (B), (D) and (F).

4.3 MDCK cell behaviour on BSA structures

The goal of many cell scaffolds is to mimic the structural support given by the extracellular matrix, to allow cells to settle and proliferate on the scaffold. Here we seeded MDCK cells on elongated open structures (**Figure 4.2** b) for long time incubation to see the stability of the BSA structures and the MDCK cell behavior.

The pre-polymerization solution was BSA25/RB0.5. The fabrication parameters were LG0.35/ET8000, LG0.35/ET10000 and LG0.4/ET8000. Every structure was fabricated separately on one 30 mm round glass slide. After fabrication, slides were put in 35 mm Petri dishes, and the protein scaffold was gently placed in pure water for 5 minutes to allow the unpolymerized BSA/RB solution to diffuse. This rinsing process was repeated three times. After rinsing, BSA structures were stored in pure water in 35 mm Petri dishes.

BSA structures were divided into two groups. Group one corresponded to the unfixed structures. Group two contained BSA structures fixed with 4 % glutaraldehyde for 30 minutes and rinsed with PBS for 3 times, 10 minutes per time. Then we performed the cell experiments three times and got equivalent results. Here we will show the results from the last experiment.

Figure 4.24 (A) shows the evolution of unfixed BSA structures after cell seeding. After 1 day of incubation, cells have settled down on the three structures. From **Figure 4.24 (C)**, we could clearly find that only the MDCK cells colonized area of the structure with LG0.35/ET8000 collapsed. In contrast, no deformation or only minimal was observed in cell-colonized areas of the LG0.35/ET10000 structure. After two days of incubation, MDCK cells partly destroyed all BSA structures. Especially for the structure with LG0.35/ET8000 (**Figure 4.24** (**D**)), the top crown disappeared, and inside pillars and outer wall all collapsed (**Figure 4.24 (E)**). For the structures built with higher exposure times, the pillars of structures with LG0.35/ET10000 (**Figure 4.24 (F)**) and LG0.4/ET8000 collapsed and partly disappeared. After three days of incubation, LG0.35/ET10000 structures almost disappeared while the other two structures only conserved the outer layer. After seven days of incubation, the structure with LG0.35/ET8000 could no more be found. The other two structures only conserved part of the outer wall.

There are two possible reasons to explain the disappearance of BSA structures. One possible reason comes from the mechanical forces and stretching exerting by the cells. The mechanical stability of the BSA structures is relatively low, and MDCK cells attached to them would move in a way that directly pulls off the structure. Another reason, possibly additive, can be biodegradation. Indeed, MDCK cells secrete protein hydrolases (proteases) during growth that could directly break down the protein scaffold.

At the same time, we reinforced the mechanical strength and cross-linked state of the BSA structures by cross-linking them with glutaraldehyde.

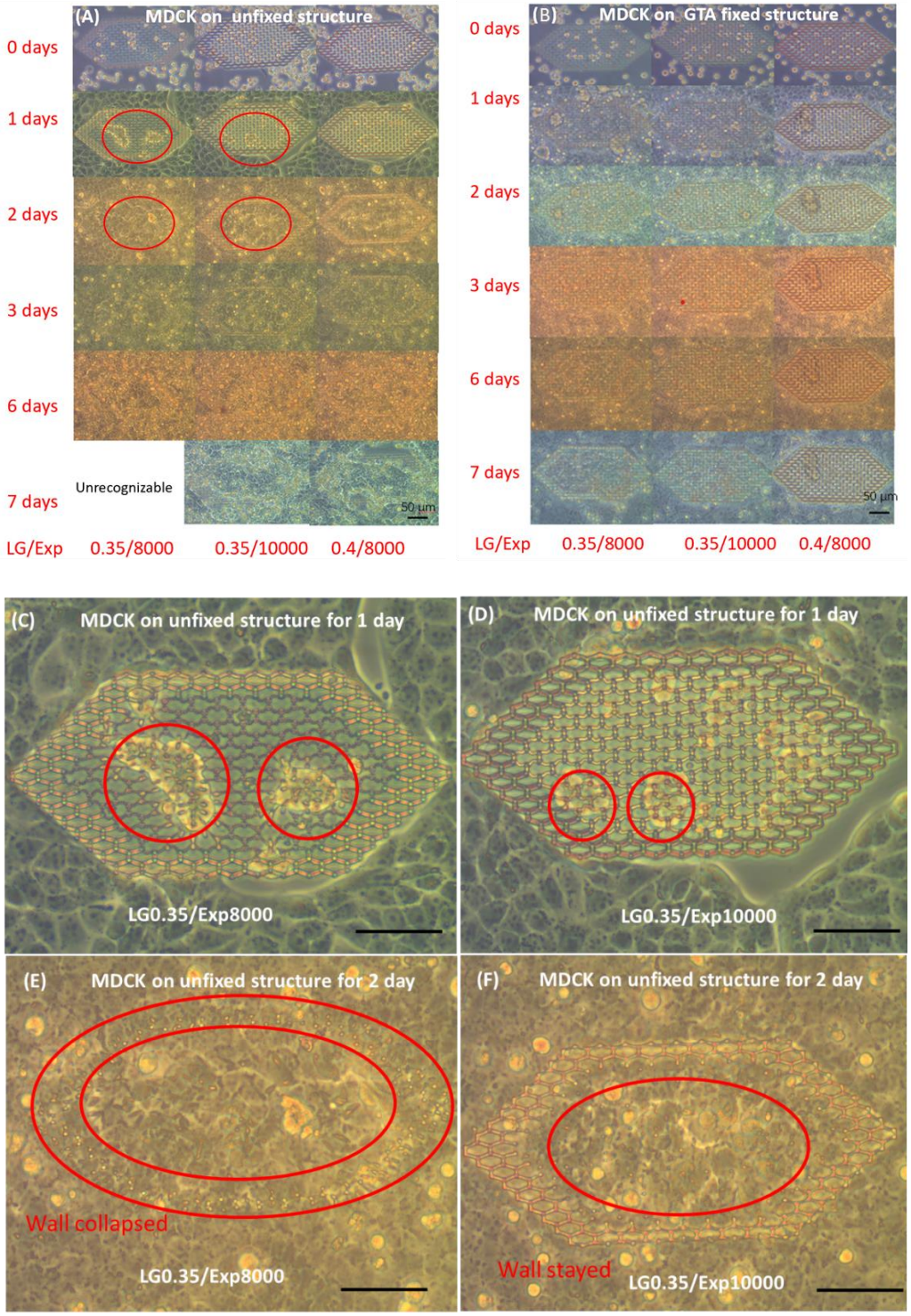

Figure 4.24 MDCK cells on unfixed BSA structures (A) and glutaraldehyde fixed BSA structures (B). (C, D, E, F) zoom out from (A). Scale bar 50 μm. Similar results from three times experiments.

As controls, BSA structures fixed or not with glutaraldehyde kept the same state after 7 days of incubation with cell culture medium alone but without cells (**Figure 4.25**). This excludes the effect of the cell culture medium on the stability of the BSA structures.

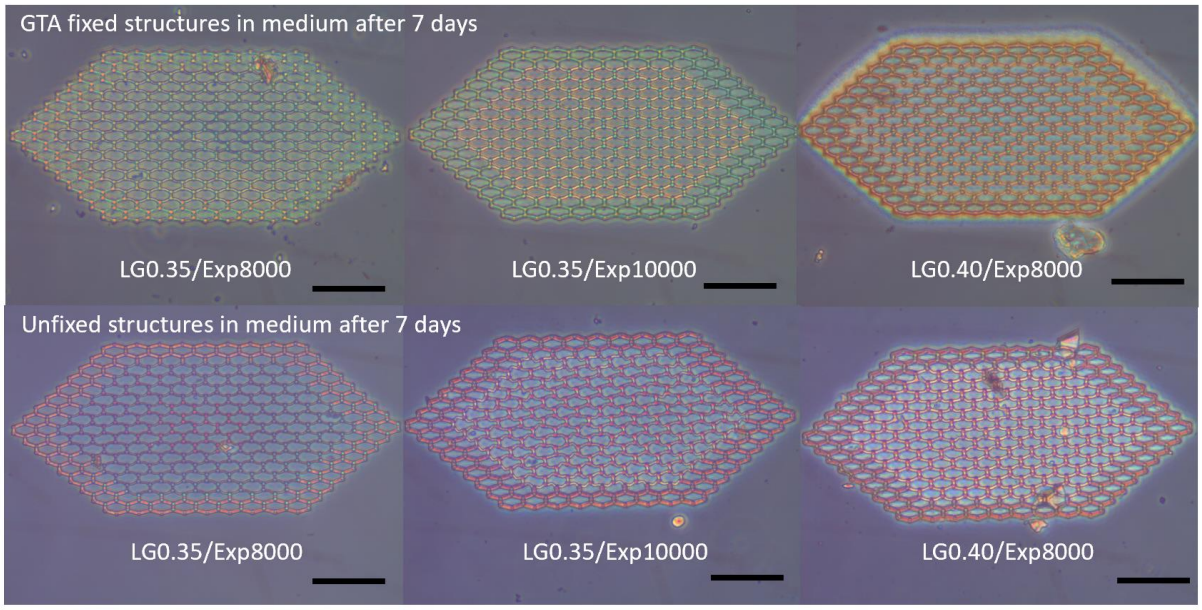

Figure 4.25 glutaraldehyde-fixed BSA structures (up) and unfixed BSA structures (down) in medium without cells for 7 days. Scale bar 50 µm.

4.4 Additional tests on epithelial cell lines

4.4.1 IMCD cell behaviour on unfixed BSA structures

To test the effect of different cell lines on the stability of BSA structures, the same experiment was conducted with another epithelial renal cell line (**Figure 4.26**); m-IMCD3 (IMCD), Inner Medullary Collecting Duct. An attempt was made with control wild-type (WT) and *Pkd1*-KO (model of a renal cystic disease) which may have different protease activities from each other. In this preliminary experiment, we only fabricated structure with one set of parameters, LG 0.35/Exp 8000. After one day of incubation, both IMCD control and IMCD *PKD1*-KO cells spread on the structures. Pillars were destroyed by the cells (**Figure 4.26 (B)** and **(C)**). After 6 days of incubation, BSA structures were partly destroyed by the cells. Pillars collapsed and partly disappeared. We observed a behaviour similar to the one observed with MDCK cells, and we observed no clear difference between the two IMCD cell lines tested.

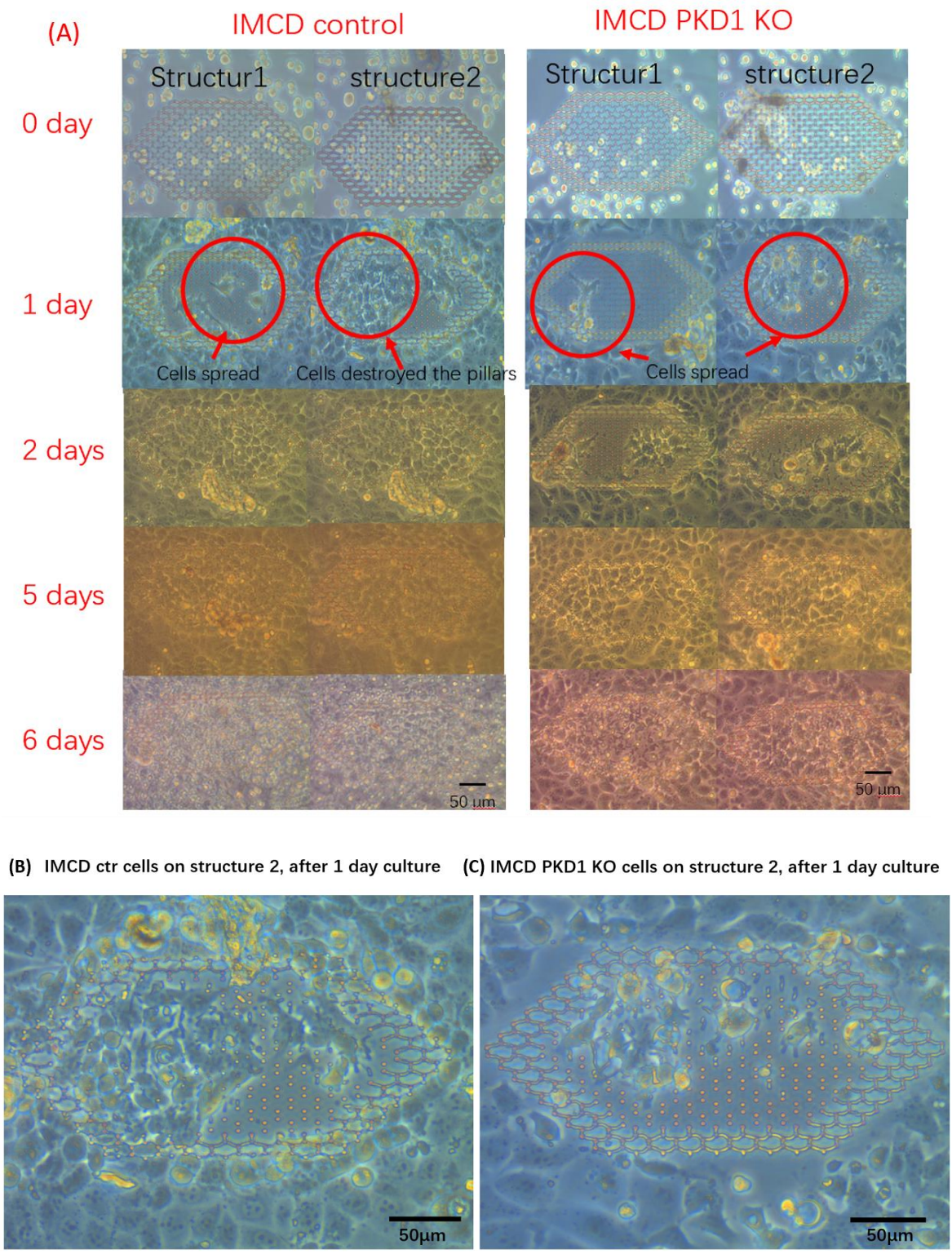

Figure 4.26 (A) IMCD and IMCD *Pkd1*-KO cells on BSA structures. (B), zoom out of IMCD control on structure 2 after 1 day incubation, the second red circle. and (C) zoom out of IMCD *PKD1* KO control on structure 2 after 1 day incubation, the fourth red circle. Fabrication parameters, LG0.35/ET 8000. Scale bar 50 µm. IMCD ctr and *Pkd1*-KO cells were a kind gift of M. Köttgen.

4.4.2 MDA-MB-231 cell and supernatant behaviour on unfixed BSA structures

MDA-MB-231 cells are a well-known cell line used in cancer research, specifically in breast cancer studies. These cells were derived from a metastatic human breast and are commonly used as a model for studying aggressive and invasive breast cancer. We fabricated the same elongated open BSA structures as before, BSA25/RB0.5 with LG0.35/ET8000. Together with our interns Maéva Zawistowski and Juliette Sanchez, a similar test was performed with MDA-MB-231 cells. The preliminary tests showed that MDA-MB-231 partly degraded BSA structures in a few days. In particular, the crowns disappeared on day 2, even before the area was colonized with cells. This suggested in this case an involvement of secreted proteases instead of a direct mechanical action. To strengthen this point, the supernatant of confluent MDA-MB-231 cells was collected and added on some BSA structures: here again, first experiments showed a degradation occurring in 2-3 days. **Figure 4.27** shows the BSA structure incubated with MDA-MB-231 supernatant for 3 days. The top crown disappeared totally. This suggests the importance of secreted factors secreted with cells, very likely proteases, in the degradation of BSA structures, here observed for MDA-MB-231 cells and to be compared in future experiments with the behavior for the other cell types.

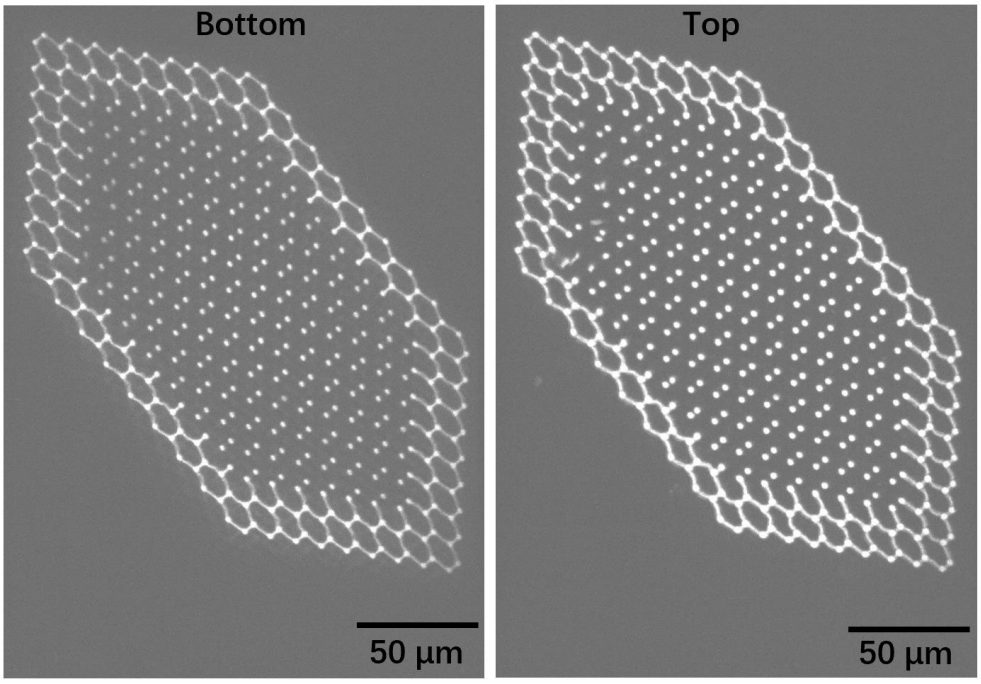

Figure 4.27 Confocal microscope images (DAPI channel) of one BSA structure incubated with MDA-MB-231 (Lifeact-mCherry) cell supernatant for 3 days. The left image is the bottom and the right image the top of the BSA structure. Fabrication parameters, LG 0.35/ET 8000.Scale bar 50 µm. MDA-MB-231 Lifeact-mCherry cells were a kind gift of Philippe Chavrier.

Besides the destruction of the BSA structures, we also note that all three cell types were present on BSA structures. In the literature, BSA has been widely used as anti-fouling coating for bacteria and cell adhesion.[17,18] But the three cell types studied, MDCK cells, IMCD cells and MDA-MB-231 cells, colonized our BSA structures. The isoelectric point (pI) ranges from pH 5.1 to 5.5[19]. In BSA/water solution, the pH of the solution is higher than the pH of BSA pI. BSA coated surface is negatively charged. It is the negative/zwitterionic property of BSA film that prevents the coated surface from bio-adhesion. Whereas our BSA structure has been polymerized. The initial pI was not suitable for the polymerized BSA. A probable reason contributing to the colonization of MDCK cell on BSA structure is that the change of surface charge makes BSA no longer resistant to cell adhesion. Besides, the cells we tested also attached to the glass substrate, which provided a binding site in addition to BSA structure. Another point which should be paid attention to is the concentration of BSA we used for TPP. The concentration of BSA is 25 mg/mL. In the literature, a wide range of concentration of BSA was used from 0 – 1000 mg/mL (See **Table 1.3** in chapter I).[2,20] The final polymerized BSA structure with varied concentrations may have different bio-adhesion effects for cell.

4.5 Summary and perspectives

In this chapter, we explored five kinds of possible photoinitiators for two-photon polymerization of proteins, especially BSA. Among all the photoinitiators, Rose Bengal was the most effective one. The best pre-polymerization solution we found was BSA25/RB0.5. The best fabrication parameters for this solution were LG0.35/ET10000. We achieved elongated hexagonal BSA structure with a nice resolution and nice SEM images with the formular BSA25/RB0.5.

BSA structures obtained by TPP with BSA25/RB0.5 can be used as a nice structure for the culture of different cells (MDCK, IMCD and MDA-MB-231). First experiments with these different epithelial cell lines, cancer-derived or not suggested that cells could destroy in a few days the BSA scaffolds. This was prevented by further cross-linking of BSA scaffolds by glutaraldehyde. The mechanisms involved may imply both the action of cell proteases and the deformation of structures by mechanical forces exerted by cells. Preliminary experiments with digestion of structures by cell supernatant suggested an important contribution of secreted proteases. Future experiments may aim at precising the proteases involved, for example with pharmacological studies with pharmacological inhibitors. In addition to this long-distance action, cells may also locally act on BSA structures, both by membrane-bound proteases and by the exertion of mechanical forces. Concerning the action of mechanical forces exerted by cells, time-lapse experiments should give a first direction of their importance. The quantification of forces exerted by cells, and the forces needed for fiber disruption, could be easier to access on other geometries, like suspended fibers geometries.[21] Such quantification would be performed in line with a methodology currently developed in the group on 3D TPP PEGDA

fibers, and would first imply quantification of the mechanical properties of BSA structures, including their Young's modulus.

In this chapter, we fabricated the same elongated hexagonal structure we used in Chapter II and Chapter III. There are still lots of opportunities for different geometries to try. Concerning the material, many other proteins could be explored for TPP in future developments, like collagen or a mixture of BSA with other proteins. Finally, the development of hybrid structures combining synthetic polymers and proteins is a promising axis.

4.6 References

(1) Francis, G. L. Albumin and Mammalian Cell Culture: Implications for Biotechnology Applications. *Cytotechnology* **2010**, *62* (1), 1–16. https://doi.org/10.1007/s10616-010-9263-3.

(2) Serien, D.; Sugioka, K. Fabrication of Three-Dimensional Proteinaceous Micro- and Nano-Structures by Femtosecond Laser Cross-Linking. *Opto-Electronic Adv.* **2018**, *1* (4), 1–18. https://doi.org/10.29026/oea.2018.180008.

(3) Benveniste, R.; Davies, J. Molecular Mechanisms of Antibiotic Resistance in Bacteria. *Annu. Rev. Biochem.* **1973**, *1*, 471–501. https://doi.org/10.1146/annurev.bi.42.070173.002351.

(4) Iosin, M.; Stephan, O.; Astilean, S.; Dupperay, A.; Baldeck, P. L. Microstructuration of Protein Matrices by Laser-Induced Photochemistry. *J. Optoelectron. Adv. Mater.* **2007**, *9* (3), 716–720.

(5) Lin, C.-Y.; Lien, C.-H.; Cho, K.-C.; Chang, C.-Y.; Chang, N.-S.; Campagnola, P. J.; Dong, C. Y.; Chen, S.-J. Investigation of Two-Photon Excited Fluorescence Increment via Crosslinked Bovine Serum Albumin. *Opt. Express* **2012**, *20* (13), 13669. https://doi.org/10.1364/oe.20.013669.

(6) Turunen, S.; Käpylä, E.; Terzaki, K.; Viitanen, J.; Fotakis, C.; Kellomäki, M.; Farsari, M. Pico- and Femtosecond Laser-Induced Crosslinking of Protein Microstructures: Evaluation of Processability and Bioactivity. *Biofabrication* **2011**, *3* (4), 045002. https://doi.org/10.1088/1758-5082/3/4/045002.

(7) Encinas, M. V.; Rufs, A. M.; Bertolotti, S. G.; Previtali, C. M. Xanthene Dyes/Amine as Photoinitiators of Radical Polymerization: A Comparative and Photochemical Study in Aqueous Medium. *Polymer (Guildf).* **2009**, *50* (13), 2762–2767. https://doi.org/10.1016/j.polymer.2009.04.024.

(8) Tomal, W.; Ortyl, J. Water-Soluble Photoinitiators in Biomedical Applications. *Polymers (Basel).* **2020**, *12* (5), 1–30. https://doi.org/10.3390/POLYM12051073.

(9) Zaborniak, I.; Chmielarz, P. Riboflavin-Mediated Radical Polymerization – Outlook for Eco-Friendly Synthesis of Functional Materials. *Eur. Polym. J.* **2021**, *142* (November), 110152. https://doi.org/10.1016/j.eurpolymj.2020.110152.

(10) Norrish Type I Photoreaction. *IUPAC Compend. Chem. Terminol.* **2008**, *293*, 4219. https://doi.org/10.1351/goldbook.n04219.

(11) Brian H. Cumpston; Sundaravel P. Ananthavel; Stephen Barlow; Daniel L. Dyer; Jeffrey E. Ehrlich; Lael L. Erskine; Ahmed A. Heikal; I.-Y. Sandy Lee; Stephen M. Kuebler; Dianne McCord-Maughon; Jinqui Qin; PErry. Two-Photon Polymerization Initiators for Three-Dimensional Optical Data Storage and Microfabrication. *Nature* **1999**, *398* (March), 51–54.

(12) Zeng, B.; Cai, Z.; Lalevée, J.; Yang, Q.; Lai, H.; Xiao, P.; Liu, J.; Xing, F. Cytotoxic and Cytocompatible Comparison among Seven Photoinitiators-Triggered Polymers in Different Tissue Cells. *Toxicol. Vitr.* **2021**, *72*, 105103. https://doi.org/10.1016/j.tiv.2021.105103.

(13) Li, S.; Liu, X.; Zhang, S.; Zhou, Y.; Wan, X.; Li, N.; Li, J.; Zhang, L. D–π–A–π–D Initiators Based on Benzophenone Conjugate Extension for Two-Photon Polymerization Additive Manufacturing. *Photonics* **2022**, *9* (3), 183. https://doi.org/10.3390/photonics9030183.

(14) Albota, M.; Beljonne, D.; Brédas, J.-L.; Ehrlich, J. E.; Fu, J.-Y.; Heikal, A. A.; Hess, S. E.; Kogej, T.; Levin, M. D.; Marder, S. R.; McCord-Maughon, D.; Perry, J. W.; Röckel, H.; Rumi, M.; Subramaniam, G.; Webb, W. W.; Wu, X.-L.; Xu, C. Design of Organic Molecules with Large Two-Photon Absorption Cross Sections. *Science (80-.).* **1998**, *281* (5383), 1653–1656. https://doi.org/10.1126/science.281.5383.1653.

(15) Le, C. M. Q.; Petitory, T.; Wu, X.; Spangenberg, A.; Ortyl, J.; Galek, M.; Infante, L.; Thérien-Aubin, H.; Chemtob, A. Water-Soluble Photoinitiators from Dimethylamino-Substituted Monoacylphosphine Oxide for Hydrogel and Latex Preparation. *Macromol. Chem. Phys.* **2021**, *222* (19), 1–10. https://doi.org/10.1002/macp.202100217.

(16) Migneault, I.; Dartiguenave, C.; Bertrand, M. J.; Waldron, K. C. Glutaraldehyde: Behavior in Aqueous Solution, Reaction with Proteins, and Application to Enzyme Crosslinking. *Biotechniques* **2004**, *37* (5), 790–802. https://doi.org/10.2144/04375RV01.

(17) Wang, L. S.; Gupta, A.; Duncan, B.; Ramanathan, R.; Yazdani, M.; Rotello, V. M. Biocidal and Antifouling Chlorinated Protein Films. *ACS Biomater. Sci. Eng.* **2016**, *2* (11), 1862–1866. https://doi.org/10.1021/acsbiomaterials.6b00464.

(18) Wang, L. S.; Gopalakrishnan, S.; Luther, D. C.; Rotello, V. M. Protein-Based Films as

Antifouling and Drug-Eluting Antimicrobial Coatings for Medical Implants. *ACS Appl. Mater. Interfaces* **2021**, *13* (40), 48301–48307. https://doi.org/10.1021/acsami.1c15001.

(19) Fologea, D.; Ledden, B.; McNabb, D. S.; Li, J. Electrical Characterization of Protein Molecules by a Solid-State Nanopore. *Appl. Phys. Lett.* **2007**, *91* (5), 053901. https://doi.org/10.1063/1.2767206.

(20) Sun, Y. L.; Hou, Z. S.; Sun, S. M.; Zheng, B. Y.; Ku, J. F.; Dong, W. F.; Chen, Q. D.; Sun, H. B. Protein-Based Three-Dimensional Whispering-Gallery-Mode Micro-Lasers with Stimulus-Responsiveness. *Sci. Rep.* **2015**, *5* (August), 1–14. https://doi.org/10.1038/srep12852.

(21) Greiner, A. M.; Klein, F.; Gudzenko, T.; Richter, B.; Striebel, T.; Wundari, B. G.; Autenrieth, T. J.; Wegener, M.; Franz, C. M.; Bastmeyer, M. Cell Type-Specific Adaptation of Cellular and Nuclear Volume in Micro-Engineered 3D Environments. *Biomaterials* **2015**, *69*, 121–132. https://doi.org/10.1016/j.biomaterials.2015.08.016.

Chapter V. General Conclusions and Perspectives

5.1 General conclusions

This thesis describes the development of bioactive materials by two-photon polymerization with off-stoichiometry thiol-ene (OSTE) resin and with proteins, focusing on bovine serum albumin (BSA). With alkene excess OSTE resin and surface modification, we obtained a cell-repellent substrate at the cell scale. This is an important result, since the technique developed will theoretically allow to perform localized surface grafting or anti-adhesive part in every kind of 3D architecture. OSTE resin could be also used to fabricate three-dimensional (3D) structures and to study the response of cells to microtopographies; here we identified specific geometries that were able to trigger the formation of endothelial filopodia. Concerning protein TPP, we identified conditions yielding nice resolutions for BSA structures and characterized their evolution upon cell seeding, pointing out interesting biodegradation behavior.

5.1.1 OSTE resin and surface modification on 2D surface

In this part, we developed an OSTE resin with four-armed thiol pentaerythritol tetrakis(3-mercatopropionate) and three-armed alkene tris(prop-2-en-1-yloxy)-1,3,5-triazine as the main components and 2,2-dimethoxy-1,2-diphenylethan-1-one (Irgacure 651) as the photoinitiator. To figure out the threshold ratio of the two components in the formulation, we used ATR-FTIR to track the curing possibility of OSTE resin by UV curing. The results show that the ratio of thiol to alkene (functional groups ratio, not molecule ratio) allowing to obtain cured structures ranged from 5:1 to 1:5. We also determined this ratio with the two-photon polymerization technique, the ratio of thiol to alkene also located between 5:1 to 1:5. Based on the UV-visible spectrum analysis and the data from literature, we confirmed that commercial available resin NOA 61 (Norland Products Inc., New Jersey US) is also an OSTE resin and the ratio of thiol to alkene is around 1:1.2.

Our aim was to test the use of OSTE resins for cell biology. First, we tested the cell viability on the 2D surface of OSTE resin. We found that the alkene excess OSTE resin showed excellent cell viability while thiol excess OSTE resin was toxic. The toxicity of the OSTE resin came from the precipitation of unreacted thiols. After a long time of washing, the unreacted thiols were attracted out and the thiol excess OSTE resin was not toxic anymore.

Next, we focused on the alkene excess surface only. We tried to modify the alkene excess surface with different lengths of Me-PEG-SH by click chemistry. Different parameters were tested to get the best anti-adhesive properties. At last, we found that Me-PEG308-SH with Irgacure 651 in glycerol was the best grafting formula.

We modified alkene excess OSTE resin surface with different integer ratio (thiol:ene = 1:2, 1:3, 1:4, 1:5) using Me-PEG308-SH. The results of Madin-Darby canine kidney (MDCK) cells adhesion experiment showed that we obtained a totally cell-repellent surface when the ratio of thiol:ene is higher than 1:2. We also successfully transferred the results from bulk material to small carpet fabricated by two-photon polymerization at the cell scale. By two-photon polymerization, we could fabricate microstructures with our OSTE resin, and two-photon grafting with Me-PEG308-SH enabled the precise control of anti-adhesion at the cell scale.

5.1.2 3D structures of OSTE resin and its application in biology

In this part, we designed a variety of 3D structures for cells, with the aim of studying cell behaviors triggered by microtopography, in particular the formation of cell protrusions. We focused on endothelial blood vessel cells and we were able to identify microstructures inducing endothelial filopodia: these exploratory thin actin-membrane protrusions are not observed in 2D cultures, and are evocative of cell shape changes occurring at the onset of angiogenesis. In more detail, we built regular closed and open hexagonal structures and elongated open structures, with typical dimensions at the cell scale. Those structures were fabricated with NOA 61, a commercial OSTE resin. To explore the role of microtopography, we seeded human umbilical vein endothelial cells (HUVECs) on those structures. HUVECs arranged in monolayers on top of both regular *D10H7-open* (*D* is the diameter of the inscribed circle of the top hexagon, 10 μm. *H* is the height, 7 μm) and elongated *l7L14H7-open* (*l* is the distance from the vertex perpendicular to the direction of elongation, 7 μm. *L* is the distance between the lengths of the two parallel sides in the direction of the elongation of the hexagon, 14 μm) hexagonal structures. We found that the elongation of structures induced an elongation of cells and nuclei in this HUVECs monolayer on top of the structures. When transferring our attention from the horizontal direction to the vertical direction, we found that HUVECs was able to engage vertically from the monolayer only from open structures, and that in that case numerous filopodia were generated in contact with the bottom substrate. As filopodia formation during 3D angiogenesis is triggered by gradients of growth factors, in particular Vascular Endothelial Growth Factor (VEGF), we tested the dependence of filopodia formation on VEGF. Our results suggest that endothelial filopodia can be triggered by microtopography alone.

Beside NOA 61, we managed to fabricate the same elongated hexagonal structures with the OSTE resin we developed in chapter II. MDCK cells we seeded on elongated *l7L14-open* structures fabricated with thiol:ene = 1:5 OSTE resin and fully colonized the structures. After full modification with Me-PEG308-SH, there were no cells anymore on the structure. So, we successfully transferred the anti-adhesive results that we achieved on 2D surface in Chapter II to 3D structures. In addition to hexagonal structures, we also developed the fabrication of suspended fibers with thiol:ene = 1:3, 1:4 and 1:5 OSTE resins. The next step will be to perform local anti-adhesive modifications on suspended fibers, which is not achievable with currently available techniques that are based on sequential fabrication.

5.1.3 Two-photon polymerization of proteins and its application for cell culture

The aim of this part was to optimize TPP for proteins, and to study the behavior of cells on the protein microstructures generated, as well as the temporal evolution of the structures during cell culture. We kept the architecture described previously of elongated open hexagonal structures for this study on protein TPP. Bovine serum albumin (BSA) is a cheap material. We chose BSA as a model protein to test. From the varied photoinitiators for protein polymerization, we chose five typical kinds of photoinitiators to try with BSA. Organic dyes are widely used to polymerize BSA, especially the xanthene series and flavin series. Rose Bengal (RB), one of the best photoinitiators in literature, was tested first to polymerize BSA. Three concentrations of BSA, 10/25/50 mg/ml were tested for TPP with our 532 nm laser. The best formulation here was 25 mg/mL BSA with 0.5 mg/ml Rose Bengal (BSA25/RB0.5). With the fabrication parameters test, we got nice elongated open hexagonal structures *l7L14H7*.

Other photoinitiators, flavin mononucleotide (FMN), Irgacure 2959, self-synthesized *N*-(4-benzoylbenzyl)-*N*,*N*-dimethylethanaminium bromide (BDB), and the commercial Lithium phenyl-2,4,6-trimethylbenzoylphosphinate (TPO-Li) were also tested. But the resolution and stability of the acquired structures were not as nice as the structures we got with RB. So, we kept Rose Bengal as a photoinitiator for subsequent work. In addition, we observed that glutaraldehyde could further crosslink our BSA structures and help improve mechanical stability, allowing us to get nice SEM imaging with minimal mechanical deformation during the preparation process.

At last, we tested the evolution of BSA structures upon cell seeding with different cell lines, renal epithelial and breast cancer cell lines (MDCK, mIMCD3 and MDA-MB-231). BSA structures were degraded a few days after cell seeding, but further cross-linking of BSA structures with glutaraldehyde prevented the degradation observed with MDCK cells. The disassembly of the unfixed BSA structures can be due to a combination of degradation by cell proteases and mechanical actions exerted by the cells.

Our preliminary experiments already showing structure degradation upon addition of MDA-MB-231 cell supernatant suggested the importance of secreted factors, including proteases, secreted by the cells in that process.

5.2 Perspectives

5.2.1 OSTE resin, surface modification and application in biology

We successfully modified alkene excess surfaces with Me-PEG308-SH, obtaining a cell-repellent surface. Thiol excess surface could be also modified with Me-PEG-methacrylate by click chemistry. Here we modified surfaces with PEG, but other functional molecules, for example involved in cell signaling, could also be used to modify the surface of OSTE structures. Surface modification was performed on 2D structures first, and we also achieved full anti-adhesive modification on 3D TPP structures.

In the literature, most of the works to control the cell's adhesion behaviors in 3D were achieved via the combination of different materials. By step two-photon polymerization with different materials, 3D structures were fabricated with spatially distributed multiple components. Step fabrication requires that the structure manufactured in the previous step with the first material is stable when changing materials. The mechanical properties will also change which may have an influence on cell behaviors. When fabricating suspended fibers, we cannot change materials until the whole fiber is finished. It means that step fabrication does not allow for partial functional differentiation of suspension fibers by changing materials. But this kind of spatial control of adhesion and anti-adhesion of cells could be realized by the combination of topography and surface modification. We can fabricate the 3D structures with one material but modify it later. Two-photon modification would represent the only way to our knowledge to do local modification on some complex 3D structures, including suspended fibers.

In the coming step, we could partly modify the surface of elongated open hexagonal structures with Me-PEG308-SH, for example only the crown or only the pillars, to achieve local anti-adhesion of cells. For suspended fibers, the possible direction is to perform anti-adhesive coating of different lengths on the fibers. Indeed, during cell migration along the fiber, the anti-adhesion site would need to be large enough to enable the cell to change the direction of cell migration. We could then probe the length sufficient to stop cell advancement by local two-photon grafting of the fiber with Me-PEG308-SH.

5.2.2 Two-photon polymerization of proteins and its application for cell culture

We fabricated the stable 3D structure with the best formulation BSA25/RB0.5 (25 mg/ml BSA and 0.5 mg/ml Rose Bengal in water). In the literature, the possibility of the BSA concentration ranges 0-1000 mg/ml. Few stable 3D structures were realized with lower concentrations of BSA. We paid more attention to lower concentrations, 10/25/50 mg/ml BSA in our case. In the literature, raw BSA was always used as anti-adhesive coating for cells. But we observed cells grew on BSA structures fabricated with lower concentration (25 mg/ml). It is not clear whether cells were attached to glass or the polymerized BSA. Whether polymerized BSA is still cell-repellent like the raw BSA is also a point to understand. If the answer is yes, the possible reason for cell's attachment to polymerized BSA also needs to be explored in future work.

Another direction of future work can explore the possibility of higher BSA concentrations. We observed a degradation of the structure upon cell addition, and the biodegradation of BSA structures with higher different concentrations could be tested with cells to know whether we can control the biodegradation of BSA structures. The mechanism itself of BSA structure degradation by cells is still to be further characterized, with the possible use of inhibitors targeting specific proteases, and the acquisition of timelapse experiments more spatiotemporally resolved in order to estimate the contribution of cell forces and resulting structure deformations in the process.

BSA is just one of the many proteins that can be used for TPP. There are many more proteins to explore, such as collagen I. Collagen I is the principal component of the extracellular matrix (ECM). It plays an important role in providing support to cells in ECM. The key point of raw collagen I TPP is to find proper collagen concentration and to identify a photoinitiator suitable for an acidic solution. We know that cells can bind to raw collagen I, but whether the binding sites will be modified or destroyed by TPP after polymerization is also an important point to observe. Besides proteins, hybrid structures of proteins and synthetic polymers (e.g., OSTE resin) also represent a promising direction. The synthetic polymer part could provide stable support and the protein part could be biodegradable, which would release more opportunities of scaffolds for cell culture.

Chapter VI. Experimental Part

6.1 Attenuated total reflection Fourier-transform infrared (ATR-FTIR) spectroscopy and ultraviolet-visible (UV-vis) Spectroscopy

ATR-FTIR was performed with a spectrometer Nicolet Magna IR550 (Fisher equipment). For each sample, a 32-times scanning was performed from 500 to 4000 cm^{-1}. Omnic software was used for data analysis. Ultraviolet-visible (UV-vis) Spectroscopy was performed with Milton Ray Spectronic 2000 Array spectrophotometer.

6.2 Water contact angle

Water contact angle was performed by Krüss Drop Shape Analyzer DSA30E. Static contact angle was performed by seat-drop method. 2 µl pure water was dropped on the surface. Static contact angle was performed three times for each sample to have an average value. Advancing contact angle and receding were performed with 10 µl pure water, the speed of drop increasing was 0.1 µl/second. All the surfaces were tested three times and the final values were a mean value with standard deviation.

6.3 X-ray photoelectron spectroscopy (XPS)

XPS analyses were performed with Thermo Scientific™ ESCALAB™ 250Xi X-ray Photoelectron Spectrometer (XPS) Microprobe. A monochromatized focused Al Kα X-ray source (1486.6 eV) was used. The analysis of the data was performed with CasaXPS software. The core level peak decompositions were done with the 285.0 eV as bonding energy of the C1s peak.

6.4 Nuclear Magnetic Resonance (NMR)

1H NMR spectra were recorded on Brucker Avance III HD 400 Hz spectrometer at 298 K. Deuterated methanol (CD3OD) was used as the solvent. NMR chemical shifts were recorded in parts per million (ppm) referenced to the residual solvent proton (δ = 3.31 ppm) for 1H NMR.

6.5 Structure design and Two-photon polymerization

The structures were designed with txt. method. The translation from txt. file to tsk. file was performed with Lithos software. The fabrication processes (focus control of the laser, exposure time, laser gain, fabrication sequence) were also controlled by Lithos software. Two-photon polymerization was performed with a self-organized system. The laser source is a 532 nm green laser from QSwitch Teem Photonics laser (Grenoble, France), 10 kHz, 5 ns pulses. The microscope is an IX70 module from Olympus with a 60X water objective

(*NA* 1.2) LPlanApo or a 100× oil objective (*NA* 1.4). A piezo-z stage and a 3D stage are from Physik Instrumente, Karlsruhe, Germany. A Guppy CCD camera is used during fabrication to monitor the structure.

6.6 Scanning Electron Microscope (SEM)

SEM observation was performed with Zeiss Leo 1530 SEM or Zeiss Supra 40VP SEM. The tilt of the samples was control manually for Zeiss Leo 1530 SEM and by built-in sample stage 3D control system for Zeiss Supra 40VP SEM. The 3D structures were all on 30mm glass slides. Before observation, all the samples were fixed to the sample stage with double-sided conductive adhesive and the edges of the glass sheets were also connected to the sample stage with additional conductive adhesive. Then all samples are gold sprayed. The thickness of the gold layer was controlled to be around 5 nm. Accelerating voltages were controlled at 5 kV for protein structures and 10 kV for OSTE and NOA 61 structures.

6.7 Green Fluorescent Protein (GFP) labelled *E. coli* MG1655 culture and bacteria adhesion

Green Fluorescent Protein (GFP) labelled *E. coli* MG 1655 was frozen from -4 ^{o}C freezer and inoculated into the 10 ml medium with 10 μL kanamycin water solution. *E. coli* MG 1655 was incubated at 37 ^{o}C overnight and then diluted to 10^7 cfu/ml to reactivate the bacteria at 37 ^{o}C inside an incubator. The concentration of E. coli was calculated according to OD600 of 1.0 = 8 x 108 cells/ml.

2.0 ml $1x10^8$ cfu/ml GFP *E. coli* MG1655 was added to OSTE resin covered 35 mm Petri dish, then incubated at 37 ^{o}C with 5% CO_2 for 1 hour. After 1 hour of incubation, floating bacteria were washed with phosphate-buffered saline (PBS) with orbital shaker at the speed of 80 rpm for 5 minutes. Then 75% of the PBS was changed for another round of washing. In total, four washings were performed. Pictures were taken by Leica fluorescence microscope with 470 nm excitation.

6.8 Madin-Darby canine kidney (MDCK) cells culture and adhesion experiment

MDCK wild-type cells were cultured with Dulbecco's modified Eagle's medium with 10% fetal bovine serum (FBS) at 37 ^{o}C with 5% CO_2. Per 50 ml medium, 0.5 ml penicillin-streptomycin (10000 U/ml) was added. Medium was changed every two days. After confluence, cells were washed with PBS and then detached with 2 ml Gibco TrypLE Express (1X) at 37 ^{o}C with 5% CO_2. Then suspended cells were centrifuged at 1000 rpm for 3 minutes. Enriched cells were redispersed in culture medium at 0.2 million/ml.

Before cell seeding, all the surfaces were sterilized with 70% ethanol for 5 minutes and then rinsed three times with phosphate-buffered saline (PBS) containing 1% penicillin-streptomycin (10000 U/ml).

2.5 ml 0.2 million/ml MDCK cells were seeded on OSTE-covered 35 mm Petri dishes then incubated at 37 ^{o}C with 0.5% CO_2 for 2 hours. The surfaces were washed with PBS 3 times to remove the floating cells. The cells were fixed by 1 ml 4% PFA for 5 min, then washed three times with PBS+ (PBS with 1 mM $MgCl_2$ and 1 mM $CaCl_2$). Then cells were permeabilized by 1 ml 0.1% Triton-X 100 for 5 min and rinsed three times with PBS+. For labeling, cells were incubated in PBS+ with 1 ml 1/1000 phalloidin-FITC and 1/1000 Hoechst 34580 (final concentration at 0.05 µg/ml and 0.1 µg/ml, respectively) for 30 min then rinsed three times with PBS+. Cell images were taken by Nikon inverted microscope eclipse Ti-S with Spinning disk CSU-X1 (Yokogawa) integrated in MetaMorph software by Gataca Systems, on 20x dry lens with 0.75 numerical aperture (*NA*) or 60x oil lens and 1.4 NA.

Cell counting was performed automatically by Image J from nuclei labeling. The counting was performed with batch process in Image J. The procedure is as follows.

First step: cell counting background traction and z project.

A first macro-batch process with the following code:

```
run("Median 3D...", "x=2 y=2 z=2");
run("Z Project...", "projection=[Max Intensity]");
run("Subtract Background...", "rolling=50");
setOption("ScaleConversions", true);
run("8-bit");
setAutoThreshold("Default dark no-reset");
```

First input: folder (I)of raw data pictures of cells on the resin acquired by confocal microscopy.
First output: folder (II) (new folder) of all the thresholded pictures

Second step: threshold correction

manually check the threshold of the pictures one by one. Adjust the threshold value from (0, 255)

Second input: folder (II) in the first step
Second output: folder (III) (new folder) of all the corrected thresholded pictures

Third step: Analysis -- particles, cell counting.

A second macro-batch process with the following code:

```
setOption("BlackBackground", true);
run("Convert to Mask");
run("Fill Holes");
run("Watershed");
run("Analyze Particles...", "size=100-Infinity show=Masks clear summarize");
```

Third input: folder (III) (new folder) of all the corrected thresholded pictures

Third output: cell numbers on each image.

Annexes

Ucla, P., Ju, X., Demircioglu, M., Baiz, S., Muller, L., Germain, S., Monnot, C., Semetey, V. and Coscoy, S., 2022. Dynamics of Endothelial Engagement and Filopodia Formation in Complex 3D Microscaffolds. *International Journal of Molecular Sciences*, *23*(5), p.2415.

International Journal of
Molecular Sciences

MDPI

Article

Dynamics of Endothelial Engagement and Filopodia Formation in Complex 3D Microscaffolds

Pierre Ucla [1,2], Xingming Ju [1,2], Melisa Demircioglu [1,2], Sarah Baiz [3], Laurent Muller [4], Stéphane Germain [4], Catherine Monnot [4,†], Vincent Semetey [2,*,†] and Sylvie Coscoy [1,*,†]

1 Institut Curie, Université PSL, Sorbonne Université, CNRS UMR168, Laboratoire Physico Chimie Curie, 75005 Paris, France; pierre.ucla@curie.fr (P.U.); xingming.ju@chimieparistech.psl.eu (X.J.); mdemircioglu@doctors.org.uk (M.D.)
2 Chimie ParisTech, PSL University, CNRS, Institut de Recherche de Chimie Paris, 75005 Paris, France
3 CNRS, CNAM, PIMM, Arts et Metiers Institute of Technology, HESAM Université, 75013 Paris, France; sarah.baiz@ensam.eu
4 Center for Interdisciplinary Research in Biology (CIRB), College de France, Centre National de la Recherche Scientifique, Institut National de la Santé et de la Recherche Médicale (INSERM), Université PSL (Paris Sciences & Lettres), 75005 Paris, France; laurent.muller@college-de-france.fr (L.M.); stephane.germain@college-de-france.fr (S.G.); catherine.monnot@college-de-france.fr (C.M.)
* Correspondence: vincent.semetey@chimieparistech.psl.eu (V.S.); sylvie.coscoy@curie.fr (S.C.)
† These authors have contributed equally to this work.

Abstract: The understanding of endothelium–extracellular matrix interactions during the initiation of new blood vessels is of great medical importance; however, the mechanobiological principles governing endothelial protrusive behaviours in 3D microtopographies remain imperfectly understood. In blood capillaries submitted to angiogenic factors (such as vascular endothelial growth factor, VEGF), endothelial cells can transiently transdifferentiate in filopodia-rich cells, named tip cells, from which angiogenesis processes are locally initiated. This protrusive state based on filopodia dynamics contrasts with the lamellipodia-based endothelial cell migration on 2D substrates. Using two-photon polymerization, we generated 3D microstructures triggering endothelial phenotypes evocative of tip cell behaviour. Hexagonal lattices on pillars ("open"), but not "closed" hexagonal lattices, induced engagement from the endothelial monolayer with the generation of numerous filopodia. The development of image analysis tools for filopodia tracking allowed to probe the influence of the microtopography (pore size, regular vs. elongated structures, role of the pillars) on orientations, engagement and filopodia dynamics, and to identify MLCK (myosin light-chain kinase) as a key player for filopodia-based protrusive mode. Importantly, these events occurred independently of VEGF treatment, suggesting that the observed phenotype was induced through microtopography. These microstructures are proposed as a model research tool for understanding endothelial cell behaviour in 3D fibrillary networks.

Keywords: two-photon polymerization; microtopography; filopodia; endothelial cells; angiogenesis; contractility; mechanotransduction

Citation: Ucla, P.; Ju, X.; Demircioglu, M.; Baiz, S.; Muller, L.; Germain, S.; Monnot, C.; Semetey, V.; Coscoy, S. Dynamics of Endothelial Engagement and Filopodia Formation in Complex 3D Microscaffolds. *Int. J. Mol. Sci.* **2022**, *23*, 2415. https://doi.org/10.3390/ijms23052415

Academic Editor: David Mills

Received: 28 December 2021
Accepted: 16 February 2022
Published: 22 February 2022

1. Introduction

The fundamental understanding of endothelium–extracellular matrix (ECM) interactions during the formation of new blood vessels meets considerable medical needs. The 3D geometrical organization of ECM fibres is complex, and modified in many pathophysiological conditions, such as in tumour microenvironments which favour the formation of tortuous and disorganized vessels. The global ECM stiffness, as well as local 3D fibre geometries, such as bundle size or alignment, are known to exert a central influence on cell fate. Indeed, the geometrical, chemical and mechanical properties of the microenvironment play a crucial role in defining cell behaviours, including morphology, function or

differentiation [1–3]. In particular, the microtopographies of three-dimensional scaffolds surrounding cells, with subcellular sizes in the nanometre to micrometre ranges, have been shown to elicit responses such as contact guidance [4–10], the modulation of migration or invasion [3,4,11–13] or the control of cell fate and differentiation [14–16]. In the field of bioengineering, a comprehensive range of methods has been developed, either to mimic the native microenvironment, or to create innovative microtopographies eliciting cell responses of medical interest. These techniques include photolithography [17], colloidal templating [14], electrospinning [18], moulding [19,20], 3D impression [21] or two-photon polymerization (TPP) [22–24]. To date, TPP allows the largest precision for the creation of 3D microstructures, with typical resolutions of 0.2 µm in the *xy* planes and 1 µm in the *z* plane, making possible the creation of complex microstructures guiding precise migration and invasion [25], or with coupled measurements of 3D mechanical properties [24,26]. Notably, the culture of endothelial cells on microstructures such as microgrooves or micropillars modulates their phenotype and their migratory properties [27–29].

Controlling the sequential steps involved in angiogenesis meets considerable medical needs. Indeed, angiogenesis is deleterious in tumour progression and metastatic dissemination, but beneficial in chronic ischemic diseases, and desired for the vascularisation of bioimplants. The technologies currently developed to trigger angiogenesis rely on growth factors released from bioengineered matrix or cells [30,31] or on an in vitro approach based on spatial patterning with Dll4 ligand [32]. The specific role of microtopography has been poorly characterized. The influence of microgratings and micropillars on endothelial cells was recently reported, using hierarchical nano- and micro-gratings, enhancing the capacity to drive in vitro 3D angiogenesis after cell dissociation from microstructures [33]. However, more complex 3D structures are required in order to trigger specific 3D events characteristic of the initiation of angiogenesis. Early steps in the angiogenic process imply a transitory specialization of some cells into tip cells, which exhibit filopodia [34] involved in the migration and exploration of the microenvironment, and generating extended membrane protrusions named dactylopodia central for tip cell invasion [35]. These cells invade the extracellular matrix, dragging other endothelial cells (stalk cells) with lumen formation, and the balance between tip and stalk cells is ensured by a negative Notch/Dll4 feedback loop; finally, fusion between tip cells emanating from different capillaries gives rise to new vessels (anastomosis) [36]. These angiogenic mechanisms are triggered by chemical gradients of growth factors, in particular VEGF (vascular endothelial growth factor), and by the dynamic interactions with the extracellular microenvironment. It is still unclear which phenotypic characteristics of tip cells are triggered by chemical cues (VEGF) or can be induced by microtopographical cues (ECM geometry).

Here, we describe in detail the interaction between an endothelial monolayer and two types of underlying 3D patterns, «closed» hexagonal lattices and «open» hexagonal lattices on pillars. We observe that, while endothelial monolayers stay at the surface of «closed» hexagonal lattices, their culture on «open» hexagonal lattices on pillars leads to endothelial engagement from the monolayer and to the generation of filopodia, independently of exogenous growth factors (VEGF). This suggests that these behaviours are induced by microtopography. In particular, the protrusive state observed in open structures, based on filopodia dynamics, contrasts with the endothelial cell migratory state on 2D substrates, exclusively based on lamellipodia. Thanks to the development of image quantification tools, we probe the influence of the microtopography (mesh size, regular vs. elongated structures, role of the pillars) on the orientations and engagement of endothelial cells and on filopodia dynamics, and we characterize the mechanisms involved in the interaction of endothelial cells with these 3D substrates, leading to the generation of a phenotype reminiscent of tip cell organization.

2. Results

2.1. Fabrication of Hexagonal Microstructures and Cell Seeding

We investigated the role of complex microtopographies in the control of endothelial protrusive behaviour by using 3D microstructures generated by the two-photon polymerization of NOA resin (Norland Optical Adhesive). We studied cell behaviours in 3D geometries derived from hexagonal patterns. We previously described simple 3D hexagonal lattices for the generation of deep epithelial protrusions strongly increasing cell basal surface area [37], and we were interested in testing the behaviour of endothelial cells on these scaffolds, referred to here as «closed» structures (Figure 1a). However, the physiological microenvironment of endothelial cells is not compact, but composed of extracellular matrix fibres, whose fibrillary characteristics play a key role in their adhesive behaviour, and in particular in guidance events during angiogenesis. So, we performed a systematic comparison between closed microstructures and derived hexagonal lattices on vertical pillars of similar dimensions, which allowed the physical communication of cells in the bottom plane ("open" structures, Figure 1b,c). We focused on 7 µm-high structures, including a typical pillar height of 2–4 µm (Figure 1b,c,f,g). Hexagons were either regular (Figure 1b) or elongated (Figure 1c). Elongated microstructures were considered in the aim to obtain elongated cell shapes, as expected for endothelial cells in capillaries. Our rationale to use elongated structures was to observe if protrusive migratory events were facilitated in this context: indeed, endothelial cells were shown to colonize substrates with grooves faster than flat substrates [27]. We adopted the following nomenclature: regular hexagonal lattices with a horizontal *D* dimension, e.g., of 8 µm, were referred as *D8-open* or *D8-closed* structures, while *l7L14-open* or *l7L14–closed* referred to open or closed structures with elongated hexagons of 7 µm × 14 µm. We built closed structures (Figure 1e) and open structures mechanically stabilized with an external crown of closed hexagons (Figure 1f,g).

HUVECs were seeded on microstructures and fixed after cell coverage of the structures (generally 1–3 days). Unless otherwise specified, a standard VEGF concentration (0.5 ng/mL) of endothelial growth medium was used. We characterized cell coverage on top of the microstructures (Section 2.2) and the topographical requirements for cell engagement into the structures (Section 2.3), and focused in particular on mechanisms for the microtopography-driven formation of endothelial filopodia (Sections 2.4–2.6).

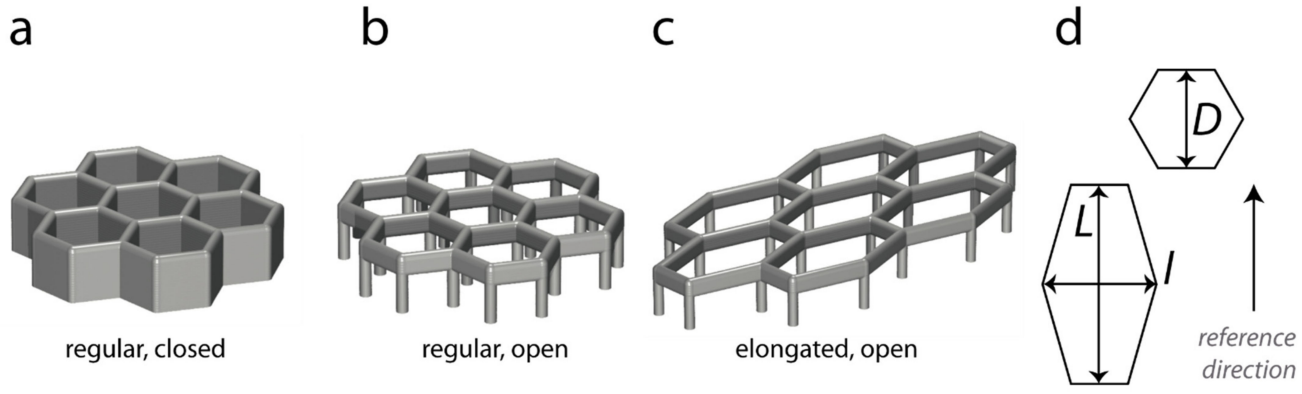

Figure 1. *Cont.*

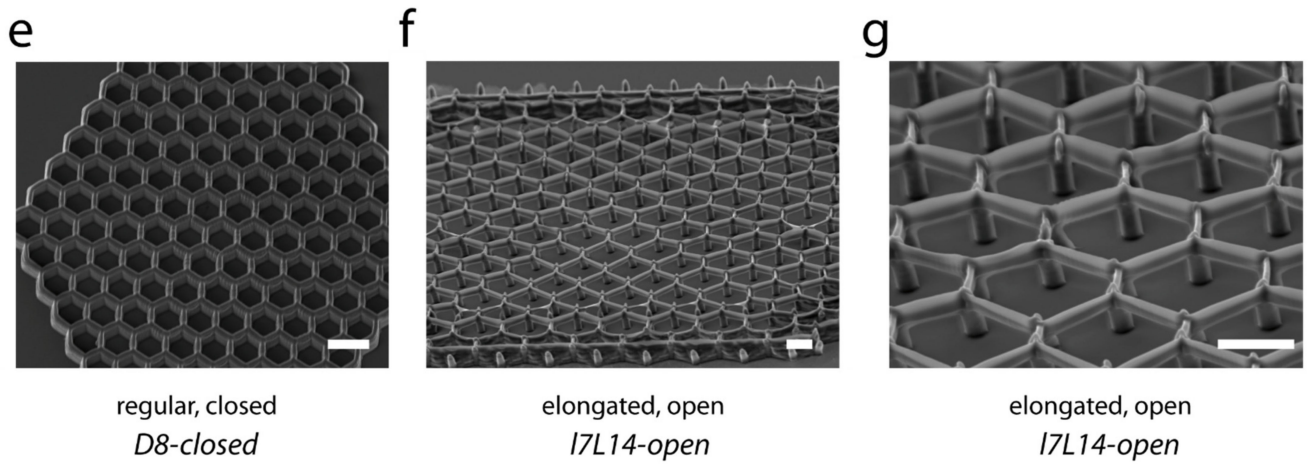

Figure 1. Microfabrication of microstructures. Microstructures were realized with NOA61 (Norland Optical Adhesive) by two-photon polymerization. (**a**) Hexagonal lattices previously described [37] are referred to here as "closed" microstructures. (**b**,**c**) "Open" microstructures were realized by building hexagons on pillars, with a total height H of 7 µm (including the typical pillar height of 2–4 µm), and variable horizontal dimensions. Regular (**b**) and elongated (**c**) hexagons were used. (**d**) Scheme of dimensions measured for regular (D) and elongated (l, L) hexagons. (**e**–**g**) SEM imaging of *D8-closed* (**e**) and *l7L14-open* (**f**,**g**) structures. (**e**) Top view, (**f**,**g**) side views, bars 10 µm.

2.2. Formation of an Endothelial Top Monolayer on Top of the Structures, and its Orientation in the Function of the Geometry of the Underlying Microstructure

A few days after cell seeding, endothelial cells efficiently covered the different microstructures (Figure 2a–d; see Figure A3a for early coverage), and organized in monolayers on top of the structures, in a similar manner on either closed or open. The orientation of cells on the top monolayer, as assessed by nuclei orientation, was compared on elongated hexagons (Figure 2a,c) and on regular hexagons (Figure 2b,d). After the tridimensional segmentation of the nuclei of the top plane (Figure A1a), the angle between the principal nucleus axis in the horizontal plane and the reference axis was determined (Figure 2a,c, vertical arrows). The nuclei in the top plane were oriented in the direction of hexagonal elongation on elongated *l7L14* microstructures, both closed or open; mean angles with the reference direction were, respectively, 30 ± 21°, n = 127, and 29 ± 24°, n = 700) (Figure 2e,f). This preferential orientation appeared to not be affected by the addition or removal of VEGF (Figure A1b,c). On the contrary, nuclei orientation was random on regular *D4.5*, *D6.6*, *D8.8*, *D10*, or *D13.5-open* microstructures (44 ± 26°, n = 1051, with a mean of 45° expected for a random orientation, Figure 2g; see separate similar behaviours in Figure A1d–h). The elongation of cell shape paralleled nuclei orientation from visual observations (Figures 2c, 3 and A3b), as expected from the literature [38–40].

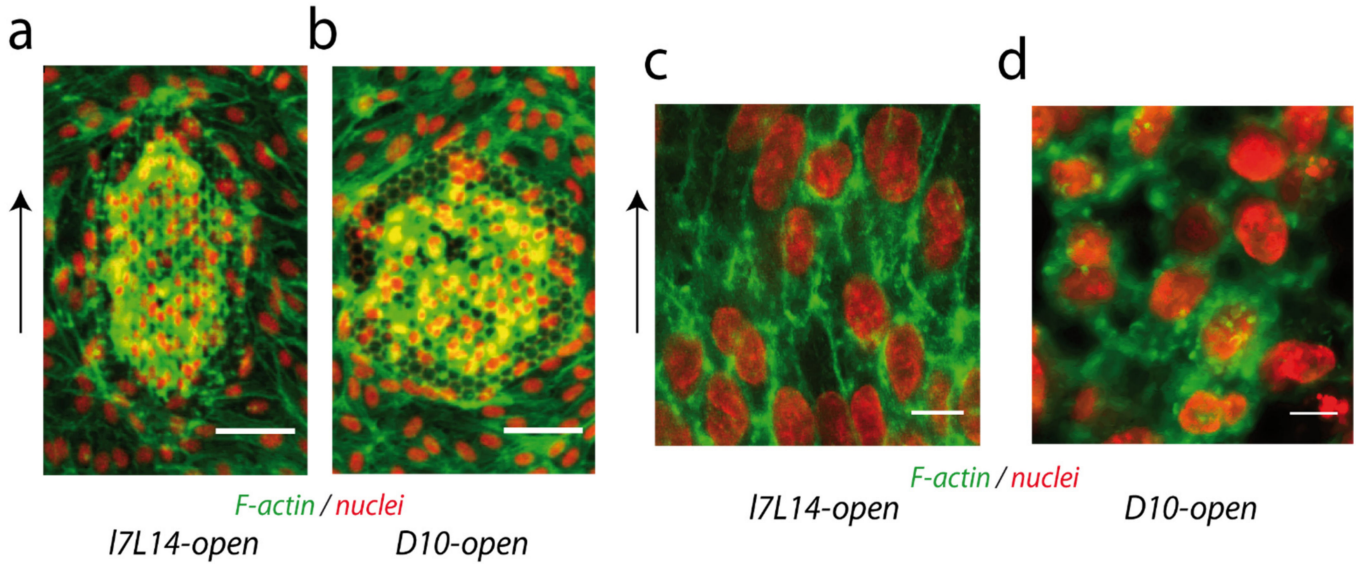

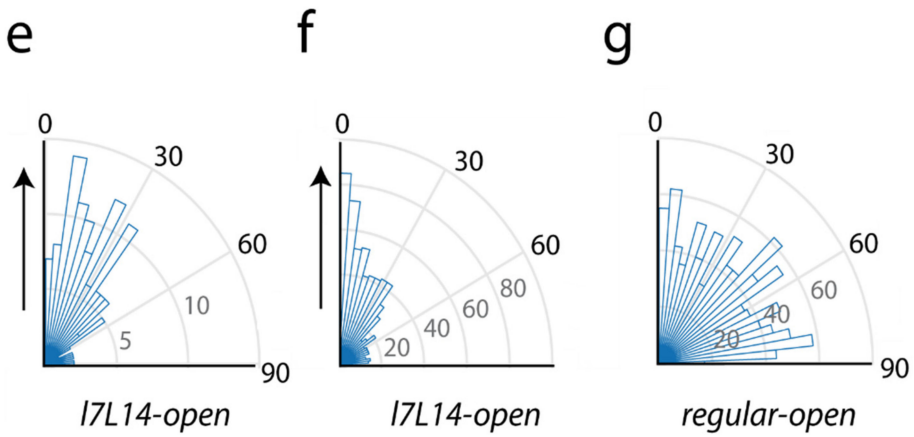

Figure 2. Cellular organization in the top monolayer. (**a**,**b**) Global HUVECs coverage of (**a**) *l7L14-open* and (**b**) *D10-open* microstructures. VEGF 0.5 ng/mL. *z* projection is shown, red: nuclei, green: F-actin, bar 50 µm. (**c**,**d**) Detail of the top monolayer covering (**c**) *l7L14-open*, with the axis of elongation of hexagons represented by a black arrow (top, left), and (**d**) regular *D10-open* microstructures. Red: nuclei, green: F-actin, *z* projection of planes above structures, cells fixed at time of structure colonization (2 (**b**,**d**) or 3 (**a**,**c**) days after cell seeding). Scale bar 10 µm. (**e**–**g**) Histograms of nuclei orientations in the top layer above the microstructures. Only the part of the nuclei above 4 µm height was considered. (**e**) *l7L14-closed* (127 nuclei in 7 structures) (**f**) *l7L14-open* (700 nuclei in 15 structures) (**g**) *D4.5*, *D6.6*, *D8.8*, *D10*, and *D13.5-open* microstructures (1051 nuclei in 23 structures). Vertical arrows in (**a**,**c**,**e**,**f**) represent the reference axis for elongated structures. For regular structures, the reference axis was chosen perpendicular to one size of the hexagon (not shown).

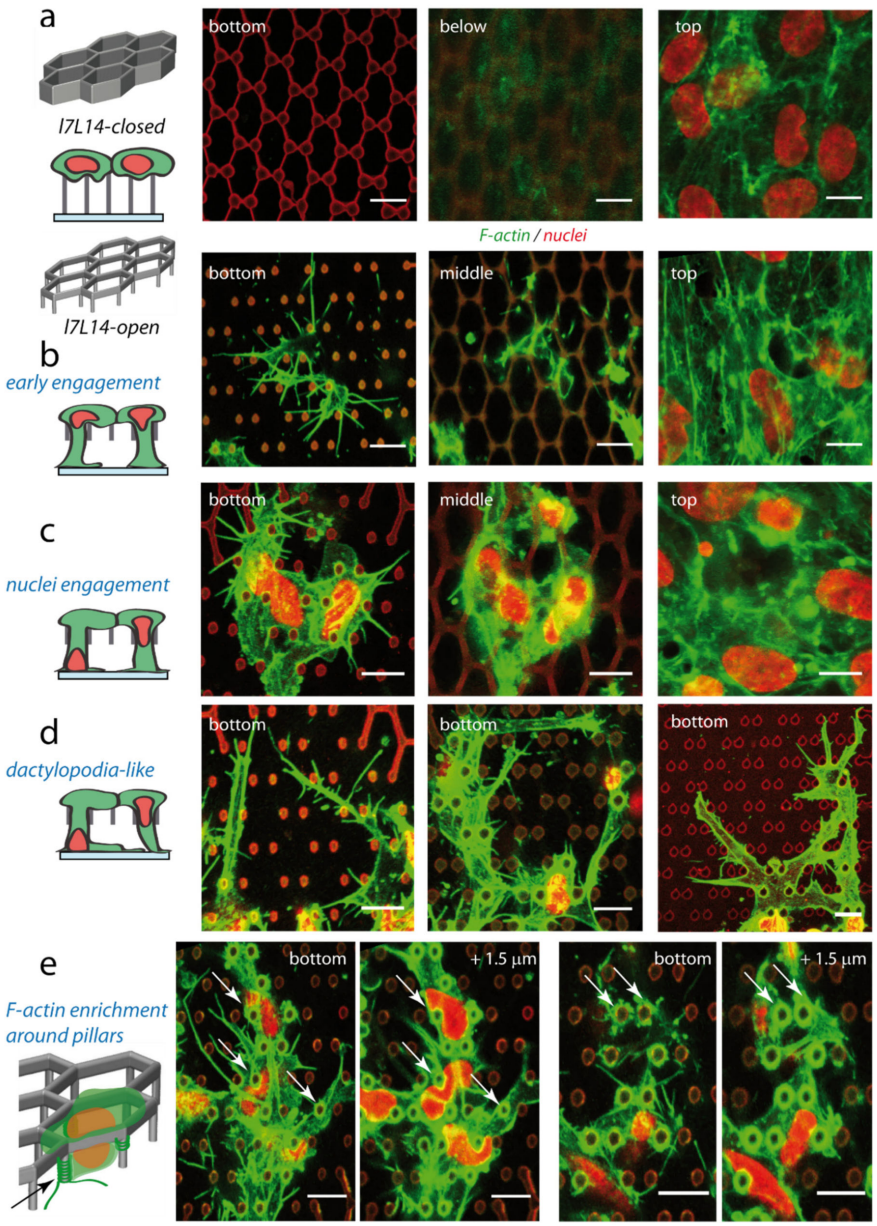

Figure 3. HUVECs organization on closed and open microstructures. Left, schemes of hexagonal lattices, and side or 3D views of typical HUVECs organization after colonization. Right, confocal planes, denoised images, scale bar 10 µm. Red: nuclei and microstructure autofluorescence, green: F-actin. Cells were cultivated in standard conditions (VEGF 0.5 ng/mL) unless otherwise specified. Cells were fixed at time of structure colonization (2 (**b**,**d**-middle, **d**-right), 3 (**d**-left) or 4 (**a**,**c**) days after cell seeding). (**a**) Closed microstructures. Confocal planes on HUVECs on *l7L14-closed* microstructure. Left, bottom plane (contact with the bottom substrate); middle, just below the structure (1.2 µm below the top of the structure); top, above the structure. (**b**–**e**) Typical examples of colonization of open *l7L14-open* structures, with vertical engagement and formation of filopodia in the bottom plane: (**b**) with limited cell area on the basal substrate), (**c**) with larger membrane and nuclei vertical engagement, (**d**) with formation of extended, dactylopodia-like protrusions, and (**e**) typical enrichment observed for F-actin around the micropillars, white arrows. (**b**,**c**) From left to right, bottom plane; middle plane (at the level of the closed part of the structure); top, above the structure. (**d**) Dactylopodia-like protrusions were observed without (**d**-left) or with (**d**-middle,right) VEGF in the media. Bottom planes are shown. For **d**-left, correspondent membrane labelling with bottom, middle and top views is shown in Figure A3c. (**e**) Two examples of bottom and top planes are shown.

Thus, elongated hexagonal geometries induced an elongation of HUVECs nuclei guided by the main direction of hexagons, as expected from the literature on endothelial cells on grooves. Some papers also reported an increased colonization rate for endothelial cells on grooves or elongated structures [27], which could be considered for future bioimplant applications.

2.3. Endothelial Engagement from the Top Monolayer in the "Open" Microstructures Only

2.3.1. Global Observations on Endothelial Cell Engagement

During the first angiogenic step, tip cells polarize, sprout out of the endothelial monolayer and engage in the surrounding microenvironment. In our closed microstructures, there was no cellular vertical engagement from the top monolayer (Figure 3a). The cell cortex was not able to extend further than 1–2 µm below the top of the structure, except in rare occurrences (only 0.6% hexagons filled, and 3% partly filled, on 1105 closed hexagons, with occasionally a few vertical filopodia (see Movie S1a). On the contrary, cells were able to engage vertically in open structures, and to come into contact with the bottom substrate 7 µm underneath, while still maintaining the top monolayer (Figure 3b–e, see Movie S1b). The formation of F-actin-rich vertical protrusions could occur without nucleus engagement, likely corresponding to the early steps of colonization (Figure 3b). However, in most cases a deep nucleus engagement towards the bottom substrate was observed, with some nuclei undergoing strong deformation due to the micropillars (Figure 3c–e). Another striking feature in the open configuration was the formation of endothelial filopodia emerging from the vertically engaged cell body in contact with the bottom substrate (Figure 3b–e). Filopodia were already present at early steps of engagement, where they could either arise directly from cell membrane around pillars (Figure 3b), or in later stages; in particular, they were observed in the extension of elongated protrusions reminiscent of the recently described endothelial dactylopodia (Figure 3d). It is noteworthy that a frequent enrichment in F-actin around pillars was observed (Figure 3e, white arrow). Membrane winding around pillars may provide anchor points to cells beginning to engage vertically, as well as favour focal adhesion maturation and filopodia formation. In addition to this mesenchymal protrusive mode (filopodia + dactylopodia-like), an amoeboid organization with membrane blebs was occasionally observed in open structures; transitions between the two modes will be discussed later (see Section 2.5).

2.3.2. Quantification of Nuclei Engagement in Function of the Microtopography

Endothelial vertical engagement was further quantified by measuring the penetration of nuclei into the structure. After 3D nuclei segmentation, the bottom z position of each nuclei was recorded (Figure 4). Again, the ability to engage nuclei from the top monolayer was dependent on the underlying geometry, closed or open (Figure 4a,b). In closed structures, most nuclei remained on top of the structures or ~2 µm above (*l7L14–closed*, only 2% of nuclei below 5 µm, Figure 4a), even after the addition of VEGF 5 ng/mL (Figure A1i). In contrast, open structures with the same horizontal dimensions induced significant vertical nuclei engagement up to the bottom of the structures (*l7L14–open*, 62% of nuclei below 5 µm, Figure 4b). The same engagement was observed in open structures even without VEGF (Figure A1j).

The vertical engagement is also expected to depend on the horizontal mesh size [37]. Therefore, we studied the engagement of HUVECs on open regular structures of different dimensions D, from 13.5 µm to 4.5 µm (Figure 4c–g). As for *l7L14-open* structures, the majority of nuclei were able to engage vertically and to contact the bottom substrate for *D13.5-open*, *D10-open* and *D8.8-open* structures (Figure 4c–e), in agreement with the fact that *D8.8-10* structures have a surface area close to *l7L14* structures (respectively, 58%, 78% and 64% of nuclei below 5 µm). Nuclei engagement was intermediate for *D6.6-open* structures (44% nuclei below 5 µm, Figure 4f). In contrast, almost no engagement was observed in smaller *D4.5-open* microstructures (6% nuclei below 5 µm, Figure 4g).

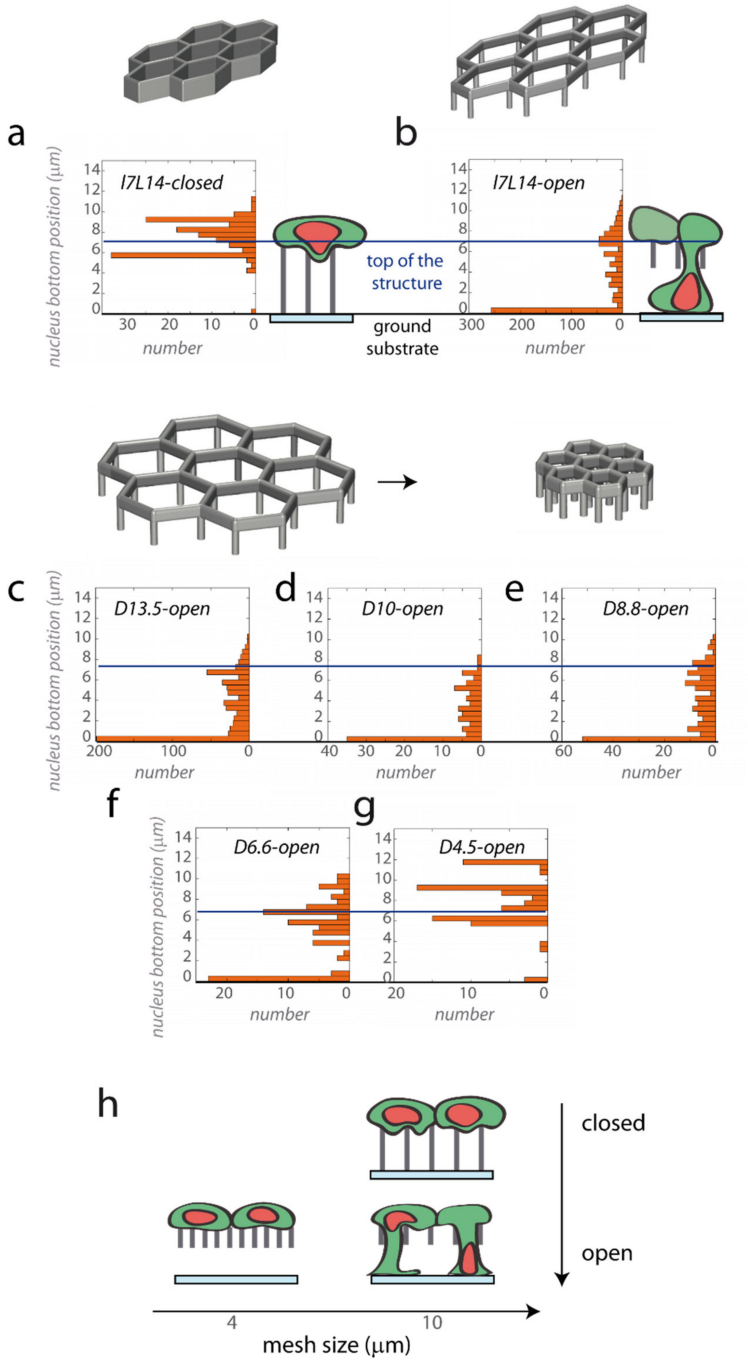

Figure 4. Dependence of geometry and pore size for nuclei engagement. HUVECs were cultivated on elongated (**a**) *l7L14-closed* microstructures (127 nuclei in 7 structures) and (**b**) *l7L14-open* structures (700 nuclei in 15 structures), or on regular open structures with different horizontal dimensions *D*: (**c**) *D13.5-open* (607 nuclei in 6 structures), (**d**) *D10-open* (95 nuclei in 1 structure), (**e**) *D8.8-open*, (178 nuclei in 4 structures), (**f**) *D6.5-open* (94 nuclei in 5 structures), and (**g**) *D4.5-open* (77 nuclei in 7 structures). After the 3D segmentation of nuclei, the position of the bottom of the nuclei was determined, with a position of 0 µm corresponding to the contact with the bottom substrate (black horizontal line) and a position of 7 µm to the top of the microstructures (blue horizontal line). For *D4.5-open* microstructures (**g**), the highest position compared with the expected height of the structure likely reflects an optical deformation when imaging through a densely polymerized structure. (**h**) Recapitulative scheme showing nuclei engagement in the function of the pore size and on the closed or open nature of the microstructure.

To summarize, HUVECs formed a monolayer in the top of every microstructure studied, but was able to engage nuclei vertically from this monolayer only for large enough and open structures (Figure 4h). So, the behaviour of HUVECs was in contrast with that reported for epithelial cells, which were able to engage massive vertical protrusions from dense monolayers on closed hexagonal lattices, as described in our previous work [37].

2.4. Induction of Endothelial Filopodia in Open Microstructures: Development of Automated Detection and Tracking, and Filopodia Characteristics

Filopodia were observed consistently in open structures, emerging horizontally from vertical protrusions in contact with the glass substrate, as visualized from F-actin and membrane labelling (Figures 3b–e and A3c). This contrasted with the lamellipodia-based endothelial organization observed on sparse or confluent 2D substrates, where filopodia have not been observed [35]. Indeed, 2D monolayers of confluent endothelial cells display either continuous, straight and stable or irregular and serrated cell–cell junctions when mature or immature, respectively [41], without displaying protrusive filopodia, and are instead characterized by the formation of large adhesive lamellipodia involved in the migration process [42]. We focused in more detail on filopodia characteristics and dynamics in order to answer the following questions: (1) do filopodia have a protrusive, exploratory behaviour (in opposition to filopodia-like structures that would come from cell retraction [43])? (2) How do their characteristics compare with values found for filopodia in general, and for in vivo endothelial filopodia in particular?

Filopodia characteristics in the standard growth conditions (0.5 ng/mL VEGF) generated in microstructures were quantified using home-made software, with technical challenges being the intricated multicellular organization and the presence of the autofluorescent structure pillars (see Appendix A Figures A2, 5 and 6). First, a semi-automated home-made Matlab script was developed to detect and quantify filopodia on fixed images (Figures A2 and 6a,b). Second, segmented images obtained in the first steps were used to train a convolutional neural network, to perform automated filopodia detection and tracking on timelapse images of HUVECs Lifeact-GFP, in order to quantify filopodia lengths, numbers, orientations, formation/retraction rates, and the percentage of elongating filopodia (Figures 5 and 6c–g, Table 1).

Table 1. Filopodia characteristics in the microstructures. Values extracted from timelapse movies (n = 15, error: S.D.).

Quantity	Extremity	Value
Length (μm)		3.36 ± 0.41
Lifetime (s)		233 ± 58
Elongation speed (nm/s)	(+)-end (−)-end	45.8 ± 5.8 44.3 ± 5.4
Retraction speed (nm/s)	(+)-end (−)-end	48.6 ± 7.0 42.4 ± 5.0
Normalized number (μm^{-1})		0.037 ± 0.020

The length of filopodia could extend to 10–15 μm, with an average length of 4.18 ± 2.97 μm (median 3,43 μm, n = 1651 filopodia, in 21 structures) as assessed from fixed samples (Figure 6a,b). Filopodia orientations compared with structure axes were computed; indeed, the geometry of pillars may be important for filopodia formation, in line with the observation that a significant number of filopodia emerged near pillars and extended preferentially in the direction of other pillars (Figure 3b–e). Indeed, we observed an asymmetry of filopodia orientations in elongated *l7L14-open* hexagonal lattices, due

to the asymmetry of pillar organization, in particular for long filopodia (lengths > 5 µm) (Figure A4), while in regular microstructures filopodia had globally isotropic orientations (Figure A5g,h).

At last, time-lapse imaging allowed the extraction of dynamic values from numerous filopodia (typically, 10–100 filopodia were detected at each time point in a movie, and several thousands in total during the observation time). Lengths, normalized numbers, filopodia lifetimes and rates of formation and retraction of filopodia (−) and (+) extremities were extracted from time-lapse images, and values averaged for each independent movie are shown in Figure 6c–g and Table 1. The mean length value obtained from timelapse samples was 3.36 ± 0.41 µm, the mean lifetime ~230 s, and elongation and retraction rates were of the order of 40–50 nm/s. These values are in the range of typical values described in the literature for filopodia dynamics [35,43,44], in particular filopodia extension rates of 55–87 nm/s reported in different systems [43]. It is noteworthy that filopodia characteristics, such as length, number or dynamic behaviour, exhibited no clear difference between elongated and regular structures (except for filopodia orientations).

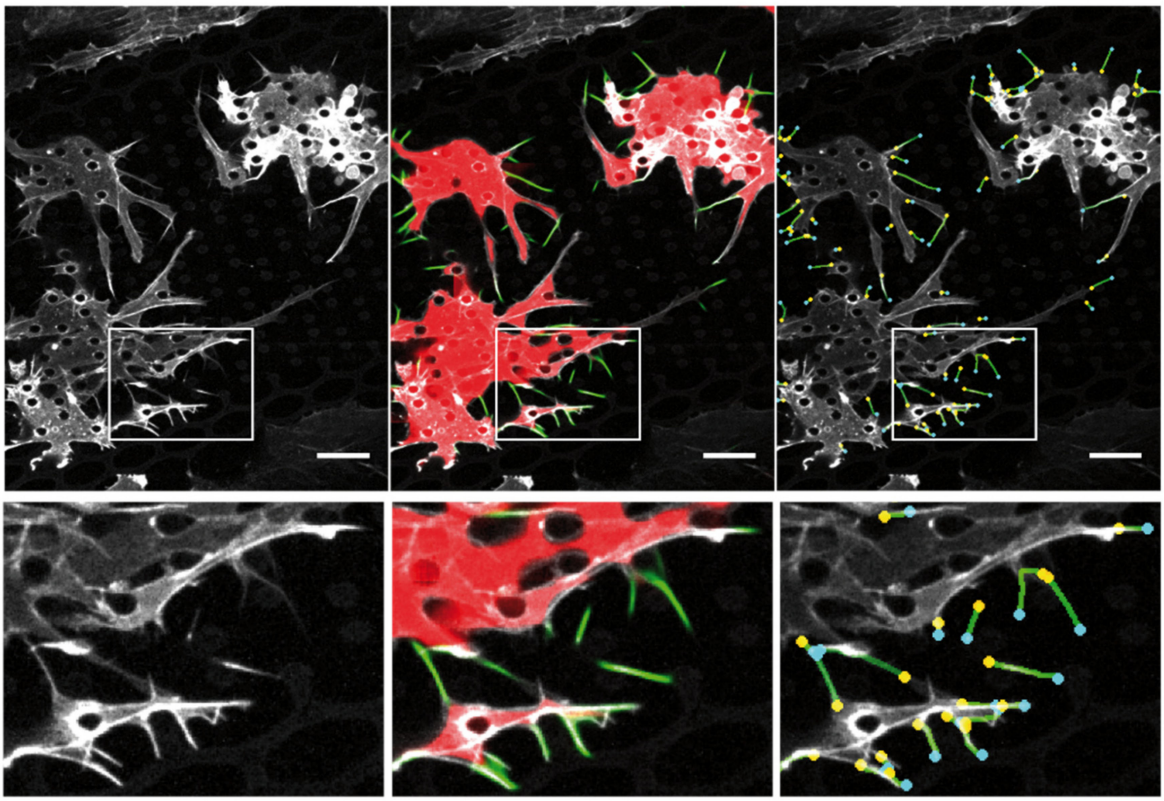

Figure 5. Automated filopodia detection. Left, original image of Lifeact-GFP HUVECs cells in the microstructures. Middle, automatic detection of cell islets (**red**) and filopodia (**green**). Right, detection of (−) and (+) extremities for each individual filopodia, used for filopodia tracking. Bottom, zoom on the image part in the white rectangle on top. Scale bar 15 µm.

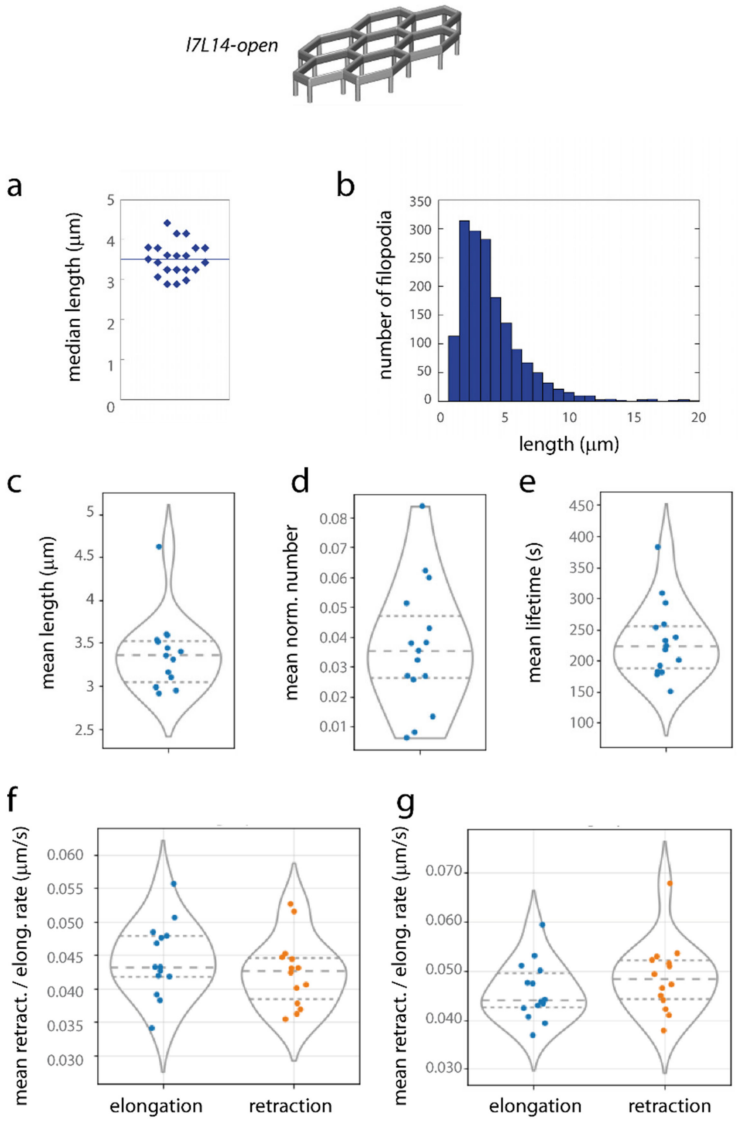

Figure 6. Quantification of filopodia organization. HUVECs were cultivated on *l7L14* microstructures, and filopodia quantified. (**a**) Median filopodia lengths from analyses on fixed samples, one point corresponds to one structure (bar: average value). (**b**) Histogram of filopodia lengths from analyses on fixed samples. (**c**–**g**) Mean values from analyses on timelapse images. Each point of the plot corresponds to the mean filopodia values on one movie (n = 15 independent movies were analysed, with a typical number of 10–100 filopodia detected at a given time point for each movie). Violin plots are shown, with dotted lines representing quartiles (middle line: median). (**c**) filopodia length, (**d**) number of filopodia normalized by the perimeter (in µm) of the cell islets inside the structure, (**e**) filopodia lifetime, (**f**,**g**) elongation (blue) and retraction (orange) rates of the (−) (**f**) and (+) (**g**) filopodia extremities.

2.5. Molecular Mechanisms Governing the Transitions between the Different Protrusive Modes Characteristic for the Microstructures

In addition to filopodia quantification, we studied the interdependence of the different protrusive forms present in the microstructures. First, we observed switches between a mesenchymal phenotype (adherent protrusions) and an amoeboid one (membrane blebs). Second, within the mesenchymal mode, two types of protrusions were seen, filopodia, connected or not to dactylopodia-like extended protrusions; from the literature, dactylopodia-like protrusions may derive from filopodia in a controlled way and may play a central role

during invasion and migration in non-vascular ECM [35]. These two types of switches between modes are here addressed sequentially.

2.5.1. Reversible Switches between Mesenchymal (Filopodia + Dactylopodia-Like) and Amoeboid Modes Are Observed, with ROCK and MLCK Activation of Actomyosin Contractility Favouring Distinct Migration Modes

- Spontaneous mesenchymal–bleb transitions

Movies on Lifeact-GFP cells in the microstructures revealed the existence of transitory membrane blebs in parts of the structures, while other cells in the microstructures retained their adherent protrusive phenotype, and cells outside the structures remained in a lamellipodia-based mode. In the microstructures, interconversions could occur spontaneously between the adherent (mesenchymal-type) mode and the blebbing mode (Figure 7a,b and Movies S2 and S3). Note that blebs were also described in vivo and may contribute to plasticity in sprouting angiogenesis [45]. Since the major difference with cells outside the structures was cell confinement, we assume that reversible membrane blebbing may derive from it [46], with the possible involvement of nuclear confinement during migration between pillars (see Discussion).

- Mesenchymal–bleb reversible transitions in function of ROCK/MLCK balance

In order to understand the molecular players involved in the transition between blebs and adherent states, we targeted ROCK and MLCK pathways. Indeed, in the literature the transition between lamellipodia and membrane blebs was expected to be governed by the degree of non-muscle myosin II activity, with ROCK favouring a blebbing phenotype and MLCK a mesenchymal adherent phenotype [47]. Different contractility levels (higher with ROCK than with MLCK) may be at play [47], as well as a difference in spatial distribution, ROCK activity being higher in the centre of cells and MLCK in their periphery [48].

Inhibiting MLCK with ML-7 (10 µM) induced filopodia retraction and bleb formation into the microstructures, but not outside (Figures 7c and A7a, see Movies S4 and S5). Almost all cell islands exhibited an amoeboid behaviour 30 min after ML-7 addition (on $n = 3$ movies). This was in agreement with a strong decrease in filopodia number observed after quantification (Figures 8b and A7b). The other dynamic parameters of the few remaining filopodia, lengths, rates of elongation and retraction, and lifetime, were not affected (Figures 8a,c and A7b,f). Specific effects of MLCK inhibition on filopodia stability were reported previously, with ML-7 inhibition experiments suggesting that acto-myosin activity was required for the maturation of filopodia shaft adhesions in fibroblasts [49].

On the contrary, ROCK inhibition by Y-27632 (10 µM) inhibited bleb formation (Figure 7d, see Movies S6 and S7), in agreement with [47] and as already observed for endothelial cells [50]. All membrane blebs present before drug addition shifted to an adherent state after Y-27632 treatment (from 5 to 0 blebbing cell islets in three movies). Numerous protrusive filopodia were still observed, and movies visually suggested the formation of a more branched filopodia network upon Y-27632 addition (which would be in agreement with protrusive events linked to LIM kinase 1 (LIMK-1)-mediated phosphorylation of the actin-depolymerizing factor cofilin in that context [51]). Nevertheless, from quantitative data, the dynamic filopodia parameters studied did not significantly differ after Y-27632 treatment (Figures 8a–c and A7c,g). Interestingly, it was also observed in growth cones that Rho kinase inhibition had much smaller effects on growth rate and filopodia numbers than MLCK inhibition [52].

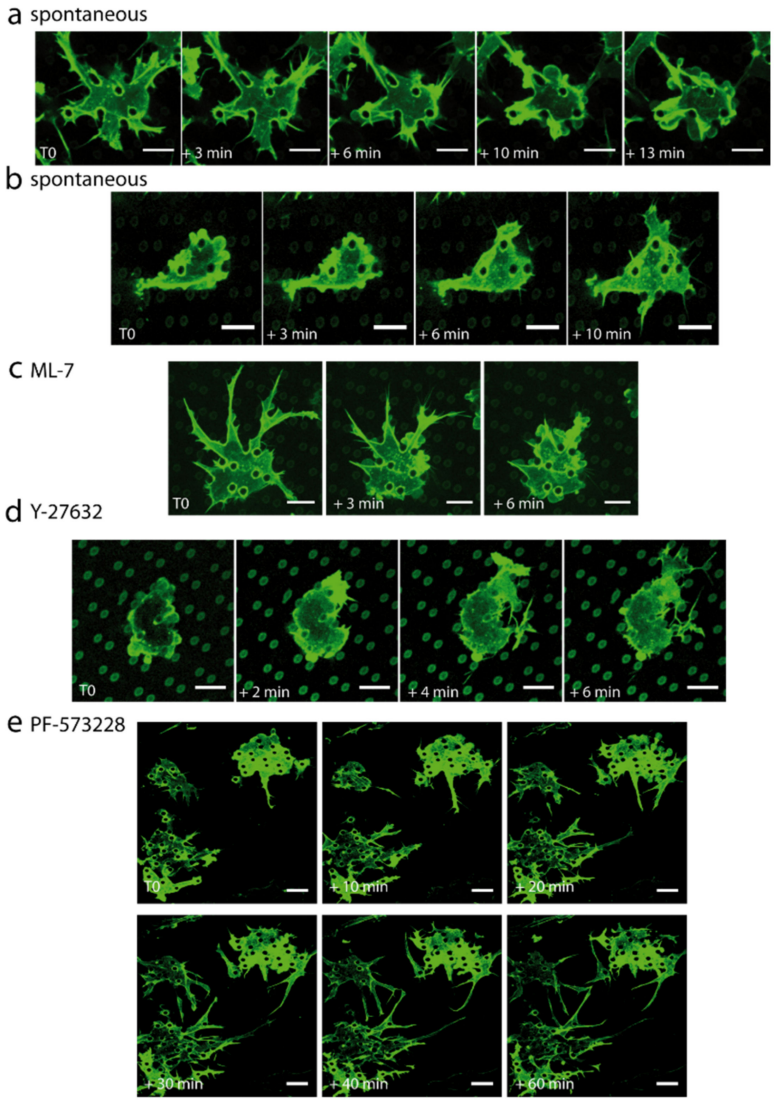

Figure 7. Transition between different protrusive modes in the microstructures, and molecular mechanisms. (**a**,**b**) Spontaneous transitions between an amoeboid state and a mesenchymal state (**a**), and between a mesenchymal and an amoeboid state (**b**). (**c**–**e**) Kinetics of the representative effects of (**c**) ML-7 (10 μM), (**d**) Y-27632 (10 μM), or (**e**) PF-573228 (10 μM) addition on Lifeact-GFP HUVECs cells (green, Lifeact-GFP), *z* projection of the bottom planes. (**a**,**b**) T0 refers to an arbitrary moment chosen as time origin, (**c**–**e**) T0 refers to the time of drug addition. Movies were acquired 1 day after cell seeding. Scale bar 10 μm (**a**–**d**), 15 μm (**e**).

2.5.2. Dactylopodia-Like Protrusions and Their Stabilization by FAK Inhibition

Dactylopodia are finger-like, extended endothelial protrusions proposed to be central for non-vascular ECM invasion. They originate from endothelial filopodia through Arp2/3-dependent membrane ruffling at the base of filopodia. The balance between dactylopodia and filopodia is controlled by NMIIA myosin, which promotes the maturation of focal adhesions (FA), thereby limiting Arp2/3 activation in nascent adhesions [35]. Extended protrusions evocative of dactylopodia were frequently observed in our microstructures and were connected to filopodia. The sizes observed for these protrusions in the microstructures were similar to the ones reported in the literature: typical lengths observed were 25 μm in our system (8–57 μm), for a mean width of 2.8 μm (1–6) (n = 47 dactylopodia-like protrusions on 12 movies), to be compared with reported lengths of 20 μm (5–33) and width 2 μm (0.7–5) found in vivo [35] (Figure 3d). Movies revealed that dactylopodia-like

protrusions were derived from filopodia, with the same triggering mechanism of membrane ruffling at the base of filopodia as the one described in the literature [35] (see Movie S8). In order to study if their formation from filopodia was favoured in the context of non-mature FA, as would be expected, we used the FAK inhibitor PF-573228. We observed that PF-573228 (10 µM) indeed stabilized dactylopodia-like protrusions (Figure 7e, see Movies S9 and S10), with a ~3-fold increase in the number of dactylopodia-like protrusions after treatment (from 8 to 24 dactylopodia-like protrusions in three movies). The quantitative analysis suggested an increase in filopodia lifetime (Figures 8c and A7d), without a major effect on the other dynamic filopodia parameters (Figures 8a,b and A7d,h). Note that PF-573228 also induced an amoeboid–mesenchyme transition by reducing (about 2-fold) the number of blebbing cell islets, in agreement with the fact that FAK inhibition regulates endothelial membrane blebbing by reducing actomyosin contractility [50].

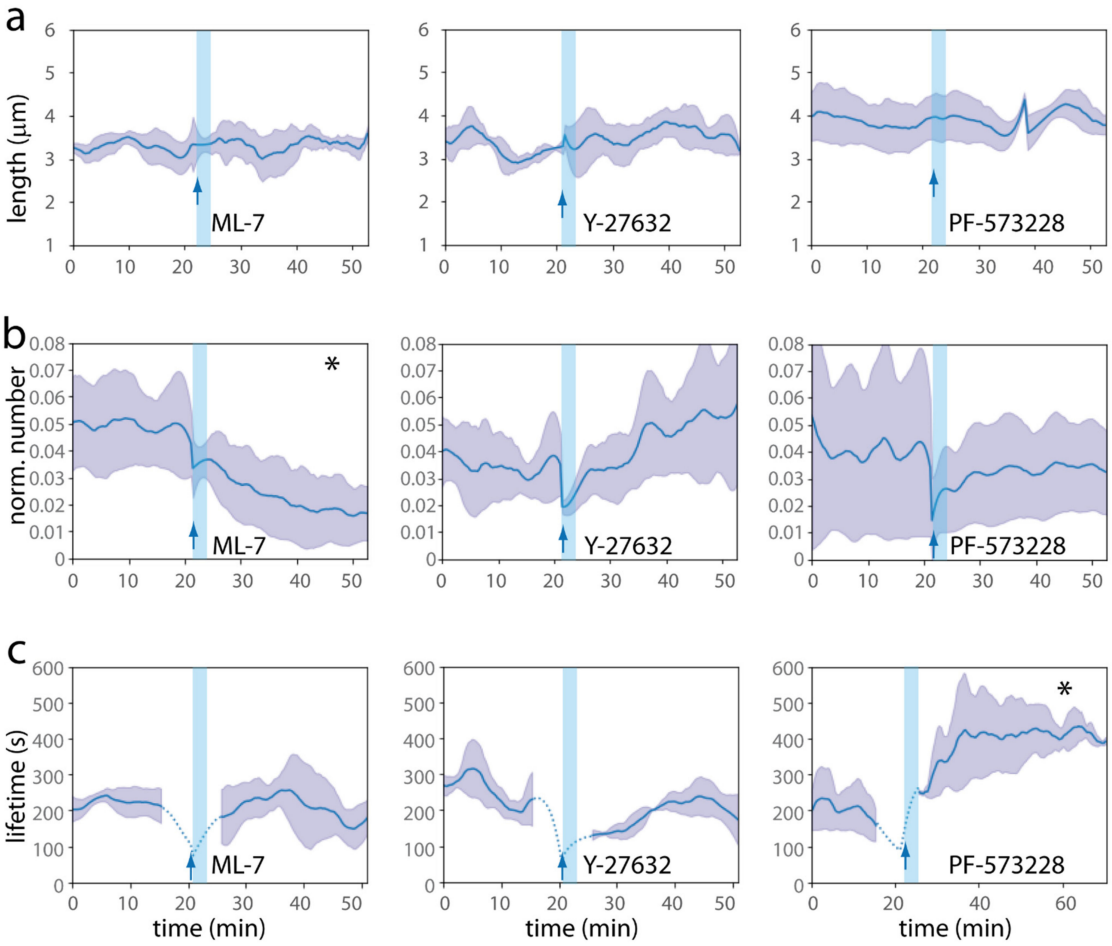

Figure 8. Quantitative analysis of ML-7, Y-27632 and PF-573228 effect on filopodia dynamics. (**a**–**c**) Evolution along time of (**a**) mean filopodia lengths, (**b**) normalized number of filopodia (normalization by the perimeter, in µm, of the cell islets inside the structure), and (**c**) mean lifetimes of filopodia present at this time, for ML-7 (left), Y-27632 (middle) and PF-573228 (right) treatments, $n = 3$ independent experiments per condition. Error: S.D. Pre-treatment and post-treatment graphs are concatenated. The blue arrow indicates the time of drug addition. The light blue vertical bar indicates a state of stabilization of the system after media change (~3 min long). The dotted lines for lifetime (**c**) refer to times where the lifetime cannot be precisely assessed, because of the imaging interruption during media changes (durations, ~1 mean filopodia lifetime before and after drug addition; see Materials and Methods). * in (**b**) ML7, and (**c**) PF-573228, indicates statistically significant differences before and after drug addition, with $p < 0.05$ (see Figure A7b–d).

Then, dactylopodia-like protrusions in our microstructures share common characteristics, not only morphologically but also mechanistically, with dactylopodia that were described as central for endothelial invasion.

2.6. Independence on VEGF

In sprouting angiogenesis, filopodia and dactylopodia formation are induced by VEGF signalling, acting on VEGFR2/3-NRP1, and triggering the CDC42 signalling pathway, regulating formins and thus filopodia formation, and the SRF (Serum Response Factor)/MyosinII pathway, modulating contractility [35]. However, we observed vertical elongation and filopodia formation in the low VEGF concentration present in the basal HUVEC culture media (VEGF 0.5 ng/mL: Figure 3). Such a low concentration is unable to trigger angiogenesis in classical 3D angiogenesis assays [53]. We therefore analysed the VEGF dependence of filopodia formation (Figure 9). We first checked that VEGF was efficiently delivered to subcellular parts in the bottom of the structures, by labelling phosphorylated VEGFR2 after a short VEGF stimulation (Figure A8). We then performed cultures with or without continuous VEGF stimulation. We tested two different culture media without VEGF (Figure 9a,b), standard VEGF concentration (Figure 9c), and higher VEGF concentrations (5, 20 and 50 ng/mL, Figure 9d–f). In classical 3D assays, 5 ng/mL VEGF was sufficient to trigger angiogenesis, and a saturation of the system occurred with 50 ng/mL VEGF [54]. We observed vertical engagement and filopodia formation in all conditions, with similar length and density characteristics (Figure 9g–h). These striking results show that endothelial filopodia are formed independently of exogenous VEGF in our system.

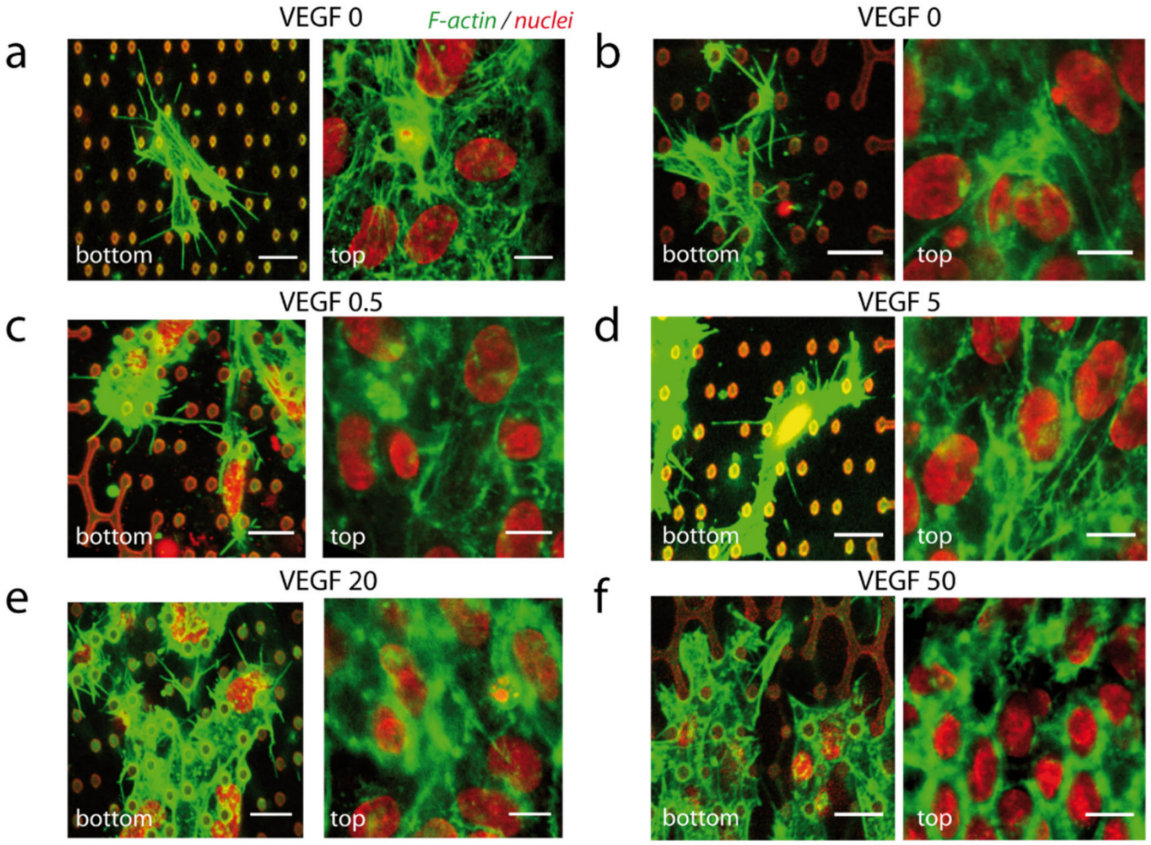

Figure 9. *Cont.*

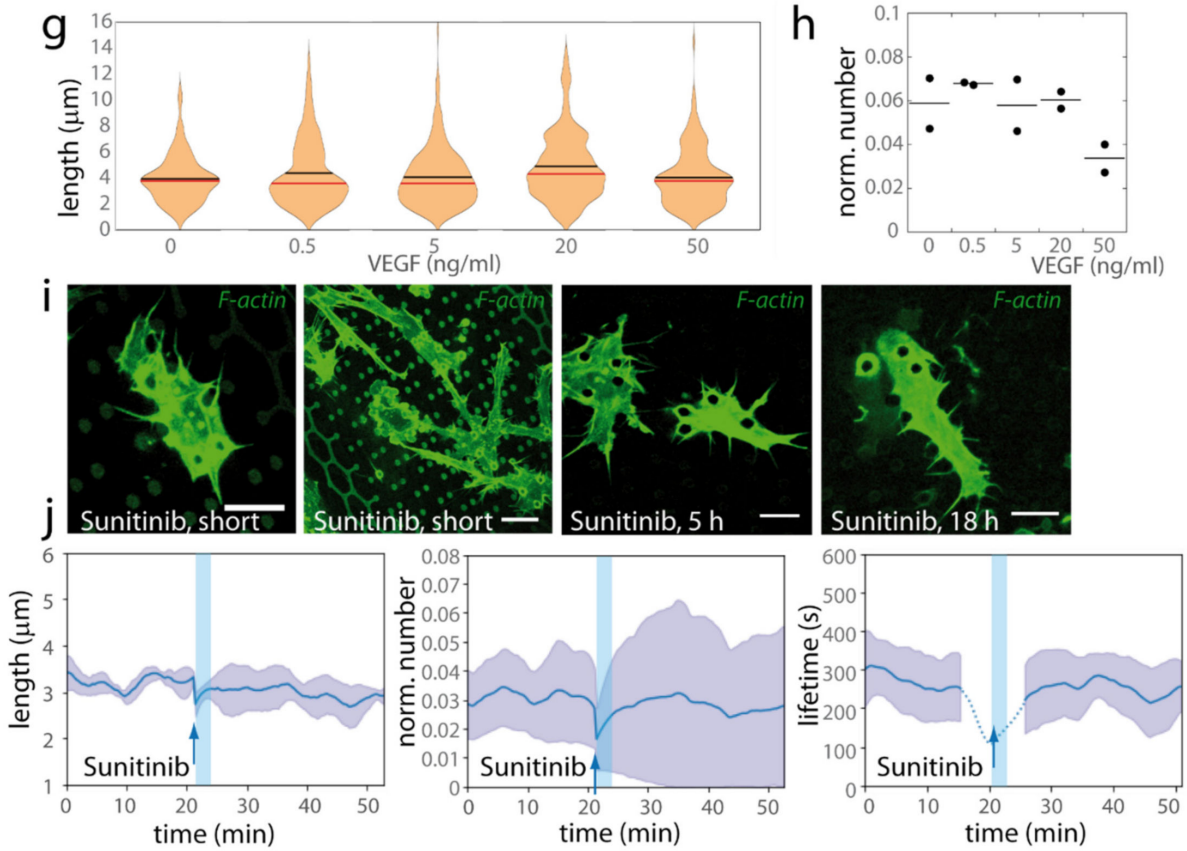

Figure 9. Dependence on VEGF. (**a**–**h**) HUVECs were cultivated on *l7L14-open* microstructures, and long-term cultures were performed in different VEGF concentrations. Cell organization was studied from fixed samples. (**a**,**b**) Culture without VEGF: (**a**) ECGM media (Promocell), which contains no VEGF supplement, (**b**) ECGM2 media without the VEGF supplement. (**b**–**e**) Standard ECGM2 media with (**c**) 0.5 ng/mL VEGF, (**d**) 5 ng/mL, (**e**) 20 ng/mL, and (**f**) 50 ng/mL. (**a**–**f**) Red, nuclei (and structure autofluorescence), green, F-actin. Bottom and top planes are represented. Cells fixed at time of structure colonization (2 (**b**–**f**) or 3 (**a**) days after cell seeding). Denoised images, bar 10 µm. (**g**,**h**) Quantification for experiments realized in parallel in the different VEGF concentrations (2 days after cell seeding). The figure corresponds to an experiment where the five VEGF concentrations were analysed simultaneously, with two structures per condition. The generation of numerous filopodia for the conditions VEGF0 was observed in 3 additional independent microstructures (see raw data). (**g**) Histograms of filopodia lengths (black bar, mean value, red bar, median value). (**h**) Number of filopodia normalized by the perimeter on cell bodies in the bottom part of the structure. One point corresponds to one structure. (**i**,**j**) Effect of sunitinib (300 nM) treatment on HUVECs-Lifeact-GFP cells. Movies were acquired 1 day after cell seeding. (**i**) After sunitinib addition, cells still exhibited filopodia (**left**) and dactylopodia-like protrusions with filopodia (**middle-left**) (26 and 29 min after drug addition, respectively). Dynamic filopodia were still present after longer sunitinib treatments: 5 h (**middle-right**) or 18 h (**right**). Green, Lifeact-GFP, *z* projection of the bottom planes. Scale bars 10 µm (**left**, **middle-right**, **right**), 15 µm (**middle-left**). (**j**) Evolution along time of the mean filopodia length (**left**), of the number of filopodia normalized by the perimeter (in µm) of the cell islets inside the structure (**middle**), and of the mean lifetime of filopodia present at this time, upon sunitinib treatment, $n = 3$ experiments per condition, errors: S.D. ($n = 3$ independent experiments). Pre-treatment and post-treatment graphs are concatenated. The blue arrow indicates the time of drug addition. The light blue vertical bar indicates a state of stabilization of the system after media change (~3 min long). The dotted lines for lifetime (**c**) refer to times where the lifetime cannot be precisely assessed, because of the imaging interruption during media changes (durations, ~1 mean filopodia lifetime before and after drug addition; see Materials and Methods). No statistical difference was detected in filopodia dynamics upon sunitinib treatment (see Figure A7e).

To exclude that an endogenous VEGF secretion by HUVECs may play a role in the observed protrusive phenotype, we performed short treatments with sunitinib, an RTK (receptor tyrosine kinase) inhibitor, in living cell experiments. Sunitinib (300 nM) did not significantly affect the presence of filopodia or dactylopodia-like protrusions, nor did any parameter analysed for filopodia dynamics (Figures 9i,j and A7e, see Movies S11 and S12). Here, we mainly used short treatments with sunitinib targeting the quick cell responses [55,56], which involves the cytoskeleton organization and its upstream signalling pathways. We also checked that numerous protrusive filopodia were still present after longer sunitinib treatments (5 h and 18 h, Figure 9i and Movies S13 and S14).

Therefore, the observed filopodia and filopodia-derived protrusions are likely induced by microtopographies.

3. Discussion

3.1. Summary

In this paper, we report that endothelial cells organize in monolayers at the surface of NOA hexagonal lattices. In open microstructures (hexagonal lattices on pillars), cells were able to engage vertically from the monolayer and to generate endothelial filopodia, two events evocative of a tip-like phenotype. Two-photon polymerization allows a precise 3D control of microstructures, with here an interplay between horizontal elongation and vertical pillars in order to control the endothelial phenotypes, as illustrated in the recapitulative Figure 10, top: (1) On top of the microstructures, the elongation of cells in the monolayer is controlled by the horizontal elongation of hexagons. (2) Endothelial cells are able or not to engage from the monolayer depending on the presence of vertical pillars. (3) In open microstructures, horizontal filopodia are induced as cells engage vertically, with filopodia orientation partly dependent on pillar geometry and thus on horizontal hexagonal elongation.

In open microstructures, we observed interconversions between different protrusive modes characteristic for endothelial organization in 3D substrates (Figure 10, bottom). First, an amoeboid mode, probably due to confinement constraints, was occasionally observed. Second and more systematically, a filopodia-based organization was observed, from which could originate dactylopodia-like elongated protrusions (mesenchymal modes). Dactylopodia were reported to play a central role in non-vascular ECM endothelial invasion [35]. Importantly, filopodia and derived protrusions were observed independently on VEGF, suggesting they may be induced by geometry.

We will now address in more detail the following points: possible mechanisms for vertical engagement, the influence of confinement, the mechanisms for filopodia and dactylopodia-like induction, signalling pathways, and potential applications that may derive from this study.

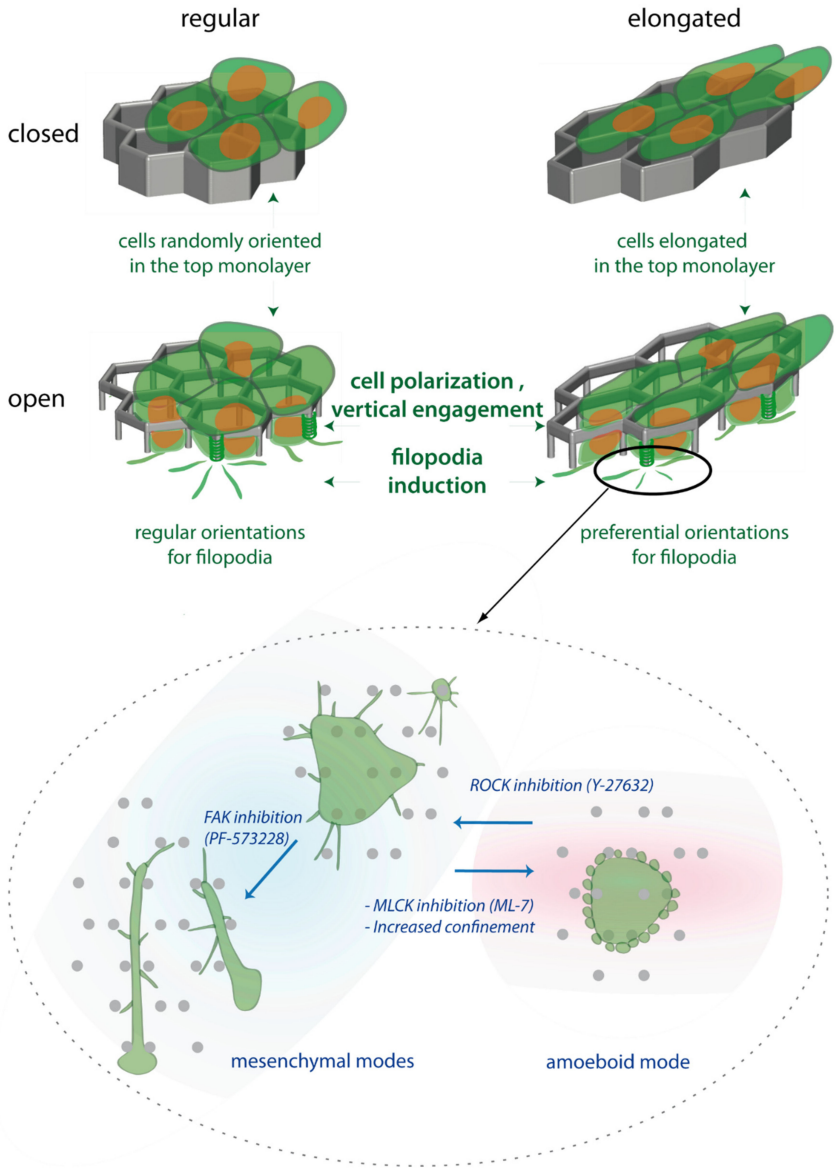

Figure 10. Recapitulative scheme of the global cell behaviour in the microstructures. (**Top**) Organisation of endothelial HUVECs in function of the elongation of hexagons in the horizontal plane, and of the open or closed nature of the microstructure. These two characteristics modulate the orientation of the top monolayer, the vertical engagement and the induction of filopodia, and the orientation of the exploratory filopodia. The vertical cell polarization and the induction of filopodia are hallmarks of tip cell phenotype, but occur independently of VEGF. (**Bottom**) Zoom of the different protrusive modes present in the bottom plane (pillars) of open elongated structures, and transitions between them.

3.2. Vertical Engagement Inside the Microstructures

We found that endothelial cells could only engage vertically from the top monolayer in open microstructures (contrary to epithelial cells, which could form deep basal protrusions even in closed structures [37]). While the precise determination of the mechanisms involved is beyond the scope of this study, we propose a putative mechanism where cells initiating an engagement in vertical open columns would be stabilized by anchor points around pillars in the bottom part, as suggested by the frequent intense F-actin rings (see Figure 3e). Such a mechanism would be in good agreement with the behaviour observed for endothelial cells on micron-sized fibres (such as our pillars), which could form protrusions winding around fibres [57,58]. The formation and 1D migration of protrusions around such fibres was reported for a variety of cell types including endothelial cells [57,58], with

different possible regimes and possible rotations around fibres [57–60]. Cells adopted spindle-shaped morphologies, and long protrusions along the fibre could span up to several hundreds of μm in length and exhibited protrusive waves governed by actomyosin dynamics, according to the balance between Rac1-Arp2/3 and Rho-formins pathways [57]. The protrusive cell activity around 1D fibres has largely been proposed to mimic the 3D ECM microenvironment. It was reported in human carcinomas that an increased ECM alignment provided tracks leading to endothelial activation and capillary morphogenesis, associated with the increased endothelial expression of angiogenesis-related markers and of α1-α3 integrins [61].

3.3. Confinement and the Amoeboid Protrusive Mode

Since the amoeboid mode was mostly observed into the microstructures, and not outside of them, we hypothesized a role for cell confinement. A plausible mechanism was the involvement of nuclear confinement, since cells were proposed to up-regulate their actomyosin contractility in response to confinement via nuclear envelope stretch-sensitive proteins [46]. It is important to note that this mode of blebbing was reported as nonapoptotic [46], and is indeed reversible in our experiments. In our microstructures, cells were subjected to two main types of confinement: the first when engaging into the microstructures in the hexagons; the second only occasionally, depending on the way cells migrated between pillars. The first engagement in hexagons of 14 μm × 7 μm was unlikely to trigger the blebbing phenotype alone, first because in that case blebs would systematically be observed in the structure, and second because in the literature the upregulation of contractility was observed when cell height was restricted to 5 μm, but not 10 μm. So, we hypothesize that the protrusive mode in the microstructures depends partly on the extent of nuclei confinement met at a particular time during cell migration between pillars. Blebs reported in vivo were proposed to contribute to the plasticity in sprouting angiogenesis [45], or could also be caused by confinement events in the ECM.

3.4. Filopodia Generation and Induction of Dactylopodia-Like Protrusions

We found that our microstructures allowed endothelial cells to switch from a 2D lamellipodia-based dynamic behaviour to a filopodia-based morphology characteristic of 3D migration and angiogenesis onset. The role of filopodia in the detection of micro- and nanotopographies has been widely documented for different cell types [62–66]. In particular, endothelial filopodia generated by nanotopography were reported for bacterial pili, silk fibroin films, anodic alumina with surface functionalization and anodized titanium dioxide [62–65,67]. Filopodia induction generally involved guidance along nanotopographical cues, following different passive or active mechanisms. Filopodia originated from 1D membrane wetting in the case of bacterial pili, without active generation by actin polymerization [62,68]. In other studies, cytoskeleton remodelling or differentiation events favouring filopodia formation and induced by the nanotexturation were reported: the activation of VEGFR2 and eNOS (endothelial nitric oxide synthase) [65]; and the upregulation and clustering of αvβ3 or α5β3 integrins, resulting in activity of focal adhesions (FAK phosphorylation) and in the activation of the PI3K/Akt pathway involved in angiogenesis [65,67]. This feature of guidance by nanostructures was not restricted to endothelial cells, but was also described for bone cells [69–72]. These behaviours contrast with the generation of horizontal filopodia in our system, which were not guided along structures; indeed, aside from micron-sized vertical pillars, we do not expect a nanostructuration of our bottom glass substrate, and never observed it in electron microscopy. Filopodia dynamics in our system corresponded to protrusive events, characteristic of an active exploratory behaviour. The detailed dynamic analysis in our system allowed us to quantify filopodia features, which proved to be remarkably stable under the different conditions, with two exceptions, probably pointing to the robustness of their regulation.

We observed that filopodia formation involved transitory contacts with pillars. Mechanisms of stabilization on pillars were reported for fibroblasts near highly flexible hairy

silicon nanowires, allowing us to obtain measurements on traction forces exerted by filopodia (in the range of nN) [66]. Although on a different cell type (fibroblasts spontaneously generate many filopodia, contrary to endothelial cells), it is of interest to note that in this study, filopodia exhibited a clear topographical preference for pillar bundles over a flat substrate, with most filopodia tips in contact with flexible pillars, and unstable filopodia on the flat substrate [66]. In our microstructures, we also distinguished two types of filopodia, with longer ones that had a preferential orientation in the principal direction of hexagons in elongated microstructures. The tips of longer filopodia were usually not in contact with a pillar; rather, pillars were tangential to filopodia. This suggests an intermediate stabilization by pillars, giving a general orientation to filopodia during active exploratory events.

What is the physiological importance of generating endothelial filopodia? While filopodia formation is characteristic for tip cells, in vivo filopodia were described as dispensable for the induction of tip cells and for cell guidance, but modulated the migration speed of the endothelial tube in formation, and were required for anastomosis [73]. More recently, the importance of filopodia for sprouting angiogenesis was proposed to involve their ability to generate the extended dactylopodia protrusions required for endothelial invasion [35]. Indeed, such protrusions were observed in our microstructures, and we observed that they were derived from filopodia from our living experiments, together with the quantification of the dynamic filopodia parameters modulated during this transition. So, the microtopographies presented here allow the generation of filopodia and derived dactylopodia-like protrusions, both expected to play a role in the angiogenic process.

3.5. Signalling Pathways

Although the protrusive phenotypes induced by our microstructures—vertical engagement from a monolayer and the generation of endothelial filopodia—are characteristic for tip cells, the signalling pathways involved differ from the physiological pathway at work in angiogenesis. The canonical pathway for tip cell activation is VEGFR2 activation by VEGF, which triggers several pathways, including PI3K/Akt, leading to cytoskeleton remodelling and filopodia formation; CDC42 and Rac1, which govern endothelial membrane protrusions; and FAK, involved in junction maturation. A fundamental observation of our study is that vertical engagement and the formation of filopodia and derived dactylopodia-like protrusions occur efficiently without exogenous VEGF, or upon RTK inhibition. This suggests the involvement of pathways alternative to VEGFR2 activation. Our preliminary experiments did not allow us to identify an involvement of the known alternative pathway NRP1 (neuropilin 1), a VEGFR2 co-receptor downstream of VEGF signalling, that also participates in ECM-dependent CDC42 recruitment, generating filopodia [74,75], or of the YAP/TAZ pathway [76]. Micro- and nanostructurations are known to modulate the state of maturation of FA [77], which could partly intersect with Src/FAK signalling triggered by VEGF stimulation. It will be of key importance to establish if other characteristics of angiogenic activation will occur in derived microstructures, in the same way as previously reported for nano- and micro-gratings, enhancing the capacity to drive in vitro 3D angiogenesis after cell dissociation [33].

3.6. Perspectives

We describe here hexagonal microstructures promoting protrusive phenotypes characteristic for endothelial tip cells, but without VEGF gradients. On a fundamental point of view, because two-photon polymerization is a versatile way to play on the geometry but also on the local chemistry, including adhesion and stiffness, the system described here provides a convenient way to decipher endothelial filopodia sensing, setting cell migratory properties in 3D fibrillary ECM networks [78]. Furthermore, this study opens paths towards two main applications. First, these open microstructures could be a promising tool for angiogenesis induction and vascularization in the field of bioimplants. Indeed, the success of tissue engineering relies on a rapid and efficient blood supply, therefore requiring the controlled generation of a capillary network inside the implant and its anastomosis within

the host vasculature. While some approaches consist of providing the local production of angiogenic growth factors by co-culturing in the implant endothelial cells with mesenchymal stem cells [79], an alternative approach could consist of the angiogenic activation of the endothelial cells induced by the microstructures, independently of exogenous VEGF treatment. However, such an approach would necessitate further study of the multicellular organization in derived microstructures, which is beyond the scope of this work. Second, the microstructures could be used for screening approaches in the field of VEGF-independent angiogenesis events. Indeed, tumour therapies based on anti-angiogenic (anti-VEGF) drugs often fail because of escaping and resistance processes, involving the emergence of alternative VEGF-independent pathways. Such pathways might partly be governed by geometrical cues and mechanical constraints in the remodelled tumour microenvironment. VEGF-independent tip-like phenotypes observed in our microstructures could constitute a valuable tool to screen drugs targeting these resistant pathways, in the context of a completely controllable system with easy visualization and advanced tools for automated quantification.

4. Materials and Methods

4.1. Two-Photon Polymerization

The two-photon polymerization set-up previously described [37] consisted of a QSwitch Teem Photonics laser (Grenoble, France), 10 kHz, 5 ns pulses, 10 µJ, 532 nm, a IX70 microscope with a water objective 60× (NA 1.2) LPlanApo, Olympus, a piezo-z stage and a 3D stage (Physik Instrumente, Karlsruhe, Germany), and a Guppy CCD camera for monitoring structure formation. It was driven by Lithos software, with an autofocus module [80]. Norland optical adhesive NOA61 (Norland Products, Cranbury, NJ, USA) was used directly on bare glass coverslips for two-photon polymerization. After deposition on a 30 mm silanized or bare circular coverslip of one drop of NOA61 resin, the initial z position of the sample was adjusted so that the focal volume was just above the glass surface, and the microstructure was polymerized by moving the focal volume. Typical parameters used were: laser power at the objective front aperture, 0.5–0.8 mW; exposure time, 6–8 ms. After completion, structures were washed sequentially with acetone and ethanol. The two-photon microfabricated scaffolds were observed using a Scanning Electron Microscope (FEG-SEM LEO 1530, LEO Elektronenskopie GmbH, Oberkochen, Germany) after the samples were gold sputtered. Alternatively, the autofluorescence of microstructures allowed us to visualize them by confocal imaging. Structure autofluorescence was reduced by coating with Sudan Black B (SBB, Sigma Aldrich, Merck, Burlington, MA, USA) for time-lapse experiments. After the washing steps, structures were incubated in SBB at a concentration of 0.1% w/v in 70% ethanol for 1 h. The sample was then rinsed several times with 100% ethanol.

4.2. Cell Culture and Treatments

HUVECs were either from a commercial source with pooled donors or from homemade prepared primary cultures, with similar behaviours. HUVECs used for experiments with labelling on fixed cells were from Lonza, Basel, Switzerland (C2519A, human umbilical vein endothelial cells, pooled). These experiments were realized from three different stocks (amplified in Lonza EGM-2 medium and frozen at their first passage). HUVECs used in live experiments were labelled directly from primary cultures. They were prepared from human umbilical cords provided by AP-HP, Hôpital Saint-Louis, Unité de Thérapie Cellulaire, CRB-Banque de Sang de Cordon, Paris, France. HUVECs Lifeact-GFP cells were obtained from these cells by transduction with rLVUbi–LifeAct®–TagGFP2 (Ibidi, Gräfelfing, Germany). After thawing, cells were maintained for 1–2 passages in endothelial cell growth medium 2 (ECGM2, Promocell GmbH, Heidelberg, Germany), at 37 °C and 5% CO_2, in collagen-coated flasks. Prior to cell seeding, microstructures were first sterilized in ethanol and rinsed three times with PBS. No additional coating was performed, since initial tests with collagen coating of the microstructures did not lead to

clear differences in cell coverage compared with uncoated structures. Cells were seeded at 20,000–30,000 cells/cm^2 in ECGM2 supplemented with penicillin–streptomycin. For some experiments without VEGF, either endothelial cell growth medium (ECGM, Promocell GmbH, Heidelberg, Germany) or ECGM2 without VEGF were used. Cultures were maintained for 1–5 days before fixation; the duration of culture on structures was adjusted with the criteria of having ~1 day of cell coverage on structures before fixation as observed by visual monitoring, and was dependent on the initial local cell surface density. For VEGF treatment, vascular endothelial growth factor (VEGF165, Thermo Fisher Scientific, Waltham, MA, USA) was added a few hours after seeding at different concentrations (see main text), and the medium with VEGF changed every day, including a few hours before fixation. For the assessment of VEGFR2 phosphorylation upon VEGF treatment, cells on microstructures (day 2) were depleted in growth factors for 4 h (endothelial cell basal medium, + 1% bovine serum albumin), incubated 10 min in the same media with or without VEGF (50 ng/mL), and immediately fixed. For pharmacological treatments used in living experiments, first, a movie was realized before drug addition, and second, a movie in the same conditions immediately after drug addition. It was independently checked that DMSO addition at the maximal concentration coming from drug addition (1/1000) did not alter the dynamic behaviour. ML-7 (hexahydro-1-[(5-iodo-1-naphthalenyl)sulfonyl]-1H-1,4-diazepine, Bertin Bioreagent, Montigny le Bretonneux, France), Y-27632 (*4-[(1R)-1-aminoethyl]-N-4-pyridinyl-trans-cyclohexanecarboxamide*, Bertin Bioreagent, Montigny le Bretonneux, France) and FAK inhibitor PF-573228 (*6-[4-(3-Methanesulfonyl-benzylamino)-5-trifluoromethyl-pyrimidin-2-ylamino]-3,4-dihydro-1H-quinolin-2-one*, Sigma Aldrich, Merck, Burlington, MA, USA) were used.

4.3. Cell Labelling

Cells on structures were washed three times with 37 °C PBS+ (phosphate-buffered saline +0.1 mM $CaCl_2$ + 0.1 mM $MgCl_2$), fixed with 4% paraformaldehyde in PBS$^+$ (16% PFA, Electron Microscopy Sciences, diluted in PBS$^+$) and permeabilized with 0.1% Triton-X100. Cells were basically labelled with 1 µg/mL Hoechst 34580 and with 1 µg/mL phalloidin-TRITC (Sigma). For some experiments, membrane was labelled with fluorescent lectins (wheat germ agglutinin, Sigma, 10 µg/mL), or indirect immunofluorescence was performed. For VE-cadherin labelling, an anti-VE-cadherin antibody (Abcam, Cambridge, UK; ab 33168, dilution 1:200) and a secondary anti-rabbit antibody, IgG coupled to Alexa647 (Invitrogen, ThermoFisher Scientific, Waltham, MA, USA, dilution 1:1000) were used. For phosphorylated VEGFR2 labelling, an anti-phosphorylated VEGFR2 (Tyr1175) antibody from Cell Signalling (19A10, dilution 1:200) and a secondary antibody, anti-rabbit IgG coupled to Alexa488 (Invitrogen, ThermoFisher Scientific, Waltham, USA, dilution 1:1000) were used. After labelling, structures with cells were kept in PBS$^+$ and imaging was performed in PBS$^+$ without mounting medium.

4.4. Imaging and Image Analysis

Image acquisitions were performed using: (1) for fixed samples, confocal TCS SP_CSU, with resonant scanner (12 kHz), 63X objective, with *z* compensation (Imaging Facility of Institute Pierre-Gilles de Gennes, Paris, France), and (2) for experiments on living cells, spinning disks from the PICT-IBiSA platform, equipped either with an inverted Eclipse Ti-E (Nikon, Tokyo, Japan) and a spinning disk CSU-X1 (Yokogawa) integrated in Metamorph software by Gataca Systems, with a Prime BSI or QuantEM camera (Photometrics, Tucson, AL, USA) and a *z*-motor Nanoz100 (Mad City Lab, Madison, WI, USA), temperature and CO_2 controllers from Life Imaging Systems, and with a CFI Plan Apo 60X Oil (NA 1.4) objective.

ImageJ was used for rotation, color merging and contrast enhancement. Brightness and contrast were optimized for visual representation. Partial maximal *z* projections are shown for "bottom" representation (contact with glass substrate), middle (closed part of the open structures), "below" (1.2 µm below the top of the structures), and top (above the

structures). z projections were performed on 2–4 confocal planes acquired with 0.3 µm z spacing for bottom and middle/below views, and 4–8 planes (about 2 µm high) for top views. In some cases, denoising was performed using the Safir filter ImageJ plugin [81]. Three-dimensional visualization was performed with the ImageJ 3DViewer plugin (https://imagej.net/3D_Viewer, accessed 1 March 2020) [82]. Alternatively, median filter and background subtraction were used for image presentation from time-lapse experiments. For some images, reconstruction of the whole structure from the different fields was performed with the ImageJ Stitching plugin.

Home-made software was specifically developed for 3D automated detection of nuclei, semi-automatic filopodia detection in fixed samples and automatic filopodia detection and tracking in living experiments in our structures, as detailed in the Appendix A (Figures A1 and A2). Briefly, filopodia were detected using a Convolutional Neural Network (CNN) model trained with semi-automatically labelled images from fixed experiments. The detection map provided by the CNN was then segmented and the resulting objects were tracked along time, with linear assignment performed according to an Intersection over Union (IoU) metric. The barbed (+) and pointed (−) extremities of filopodia were computed based on their distance to the cell body.

The error bars shown correspond to standard deviation. Statistical tests were performed on scipy.stats: paired t-tests were performed after checking the normality of the distributions of the difference between paired conditions with a Shapiro–Wilk test. The violin plots (Figure 5) represent the data distribution and are based on a Gaussian kernel density estimation using the Scott's rule as implemented in matplotlib. For the representation of filopodia length distributions in Figure 9, Matlab (Mathworks, Natick, Massachussetts, USA) violin function was used, with bandwidth 0.5 (Hoffmann H, 2015: violin.m—Simple violin plot using Matlab default kernel density estimation. INRES (University of Bonn), hhoffmann@uni-bonn.de). For smoothing the kinetic curves, a Savitzky–Golay filter was implemented from scipy.signal library, with a window size of 21 time intervals (7 min) and an interpolation with a third-degree polynomial. For the determination of filopodia lifetime, the filopodia that are already present at the beginning or at the end of a movie introduce a bias in the lifetime calculations, since their lifetime cannot be known. In order to remove as much as possible of this effect, first, we did not consider in our interpretation a time interval of a few minutes at the beginning or at the end of the movie (duration corresponding to filopodia lifetime; see dotted areas in the lifetime plots), and second, we discarded all filopodia that we did not see appear and disappear during the movie. For Figure 6 and Table 1, means were performed from intervals of 16.6 min per movie, systematically excluding the beginning and the end of the movies in order to reduce the bias in the estimation of filopodia lifetimes. For Figures 8 and 9, means were performed on time intervals with a constant duration of 10.3 min, defined as follows: for normalized numbers, Ctr (before drug addition), interval immediately before drug addition, and drug, interval beginning 21.3 min after drug addition. For lifetimes, since the 5 last minutes before drug addition could not be considered (see above), the Ctr sampling interval was chosen to end 5 min before drug addition. The Drug treatment was begun 21.3 min after drug addition, except for PF-573228 where the effects fully developed at a longer time (beginning 40 min after drug addition).

Supplementary Materials: The following supporting information can be downloaded at: https://www.mdpi.com/article/10.3390/ijms23052415/s1.

Author Contributions: P.U., Conceptualization, Software, Formal analysis, Investigation, Writing, Visualization. X.J., Investigation. M.D., Investigation. S.B., Investigation. L.M., Investigation. S.G., Conceptualization. C.M., Conceptualization, Resources, Writing, Supervision. V.S., Conceptualization, Methodology, Investigation, Writing, Visualization, Supervision. S.C., Conceptualization, Formal analysis, Investigation, Writing, Visualization, Supervision. All authors have read and agreed to the published version of the manuscript.

Funding: This work was supported by a doctoral grant from the program "Interfaces pour le Vivant", Sorbonne Université (recipient P.U.) and a doctoral grant from the Oversea Study Program of Guangzhou Elite Project (recipient X.J.). This work was supported by the Centre National de la Recherche Scientifique (CNRS), Inserm (Institut National de la Santé et de la Recherche Médicale), Sorbonne Université, Chimie ParisTech and Institut Curie. This work received support from grant ANR-08-PCVI-0012-02.

Institutional Review Board Statement: The study was conducted in accordance with the Declaration of Helsinki, and approved by the French Ethical Committee and the Ministry of Research and Higher Education (authorization number AC-2016-2759).

Informed Consent Statement: Not applicable.

Data Availability Statement: Both the raw data and processed data required to reproduce these findings are available to download from Zenodo, at https://zenodo.org/record/6198946 accessed on 20 December 2021.

Acknowledgments: We are very grateful to Pascal Silberzan, Axel Buguin, Isabelle Bonnet, Nastassia Pricoupenko and all the members of the PBME group (Physico-Biology at Meso-Scales), the group "Matériaux, Interface et Matière Molle", and the group "Role of matrix proteins in hypoxia and angiogenesis". We acknowledge Isabelle Bloch, Pietro Gori, François Amblard, Patricia Bassereau, Matthieu Piel and Stéphanie Lebreton for insightful discussions. We thank members of AP-HP, Hôpital Saint-Louis, Unité de Thérapie Cellulaire, CRB-Banque de Sang de Cordon, Paris, France for providing human umbilical cords. We are grateful to Fanny Tabarin (BMBC) for technical support with cells. This work benefited from the technical contribution of the joint service unit CNRS UAR 3750. The authors would like to thank the engineers of this unit (and in particular Bertrand Cinquin) for their advice during the development of the experiments. The authors greatly acknowledge the Cell and Tissue Imaging core facility (PICT-IBiSA), Institut Curie, member of the French National Research Infractucture France-BioImaging (ANR10-INBS-04). The authors acknowledge the Cytometry Platform of Institut Curie. This work received support from grants ANR-11-LABX-0038 and ANR-10-IDEX-0001-02.

Conflicts of Interest: The authors declare no conflict of interest. The funders had no role in the design of the study; in the collection, analyses, or interpretation of data; in the writing of the manuscript, or in the decision to publish the results.

Appendix A

Appendix A.1. Development of Algorithms for Nuclei Quantification on Fixed Samples

For the 3D automated detection of nuclei, a home-made Matlab script was used. After noise reduction with a median filter, a 3D image was reconstructed by using nearest neighbour interpolation of the original image stack in order to obtain a uniform pixel size in the three dimensions (initial pixel sizes were 0.18 µm on x and y axes, 0.3 µm on z axis, interpolated to 0.18 µm). The image was then binarized with a user-defined intensity threshold (to remove the structure autofluorescence). The binary volume was filled using morphological operations, and the very small elements filtered. Nuclei were separated from each other using a Watershed algorithm. Descriptive information was given by the Matlab regionprops function. The three principal axes of each nucleus were obtained by calculating eigenvectors of the covariance matrix of their coordinates. Projection of the nuclei principal axis on the x-y plane was compared with a manually drawn principal axis of the microstructures, in order to characterize nuclei orientation on top of the structures in the function of microstructure geometry: in that case, only the upper portion of nuclei were chosen (vertical coordinates superior to 4 µm). A typical example of nuclei segmentation on top of a microstructure is depicted in Figure A1a.

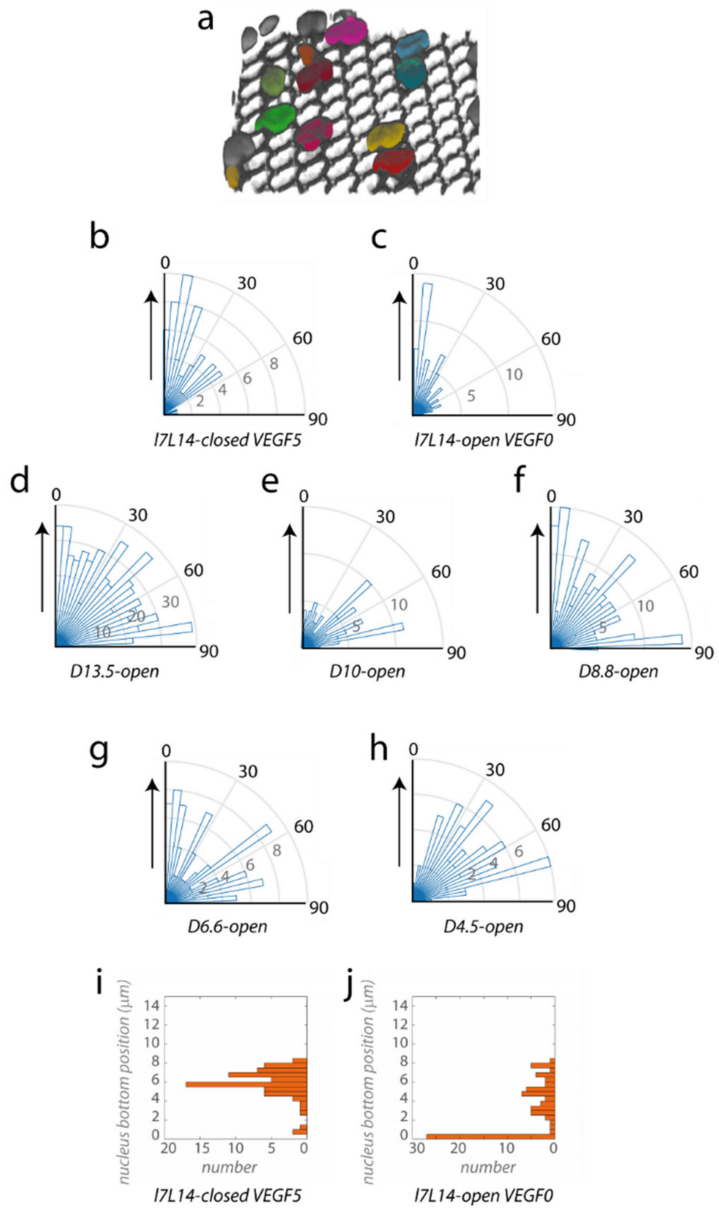

Figure A1. Additional data for nuclei quantification. (**a**) Example of nuclei segmentation on top of a *l7L14* microstructure. (**b**–**h**) Histograms of nuclei orientations in different geometries, in the top layer above the microstructures: (**b**) *l7L14-closed* with 5 ng/mL VEGF (68 nuclei in 3 structures), (**c**) *l7L14-open* without VEGF (1 structure), (**d**) *D13.5-open* structures (607 nuclei in 6 structures), (**e**) *D10-open* structures (95 nuclei in 1 structure), (**f**) *D8.8-open* structures (178 nuclei in 4 structures), (**g**) *D6.6-open* structures (94 nuclei in 5 structures), (**h**) *D4.5-open* structures (77 nuclei in 7 structures). (**i**,**j**) Vertical engagements: position of the bottom of the nuclei for: (**i**) *l7L14-closed* with 5 ng/mL VEGF, (**j**) *l7L14-open* without VEGF.

Appendix A.2. Development of Algorithms for Filopodia Detection, Tracking and Quantifications

Appendix A.2.1. Filopodia Detection on Fixed Samples

Two-dimensioanl semi-automatic detection of filopodia was performed using a home-made Matlab script. Specific challenges were: (1) structure autofluorescence (2) multicellular organization with intricate protrusions. First, an average *z* projection of the 5–10 bottom planes was performed, and the noise was reduced with a median filter. The image was then binarized using thresholds deriving from the user definition of background and cellular

areas. Next, areas with filopodia were selected by the user. This led to the generation of a mask for the cellular area, around which filopodia could form. Normalization of the number of filopodia by perimeter refer to this mask. At last, a Laplacian of Gaussian (LoG) filter was applied to detect edges and strong contrasts. Filopodia were extracted using morphological operations and elements shorter than 0.9 µm were discarded. False detection could be manually eliminated by the user, and/or missing filopodia manually added. Some intricate filopodia, presenting branching points, needed to be separated; this was achieved using a segmentation method taking into account local variations in filopodia orientations. Typical detection results are represented in Figure A2.

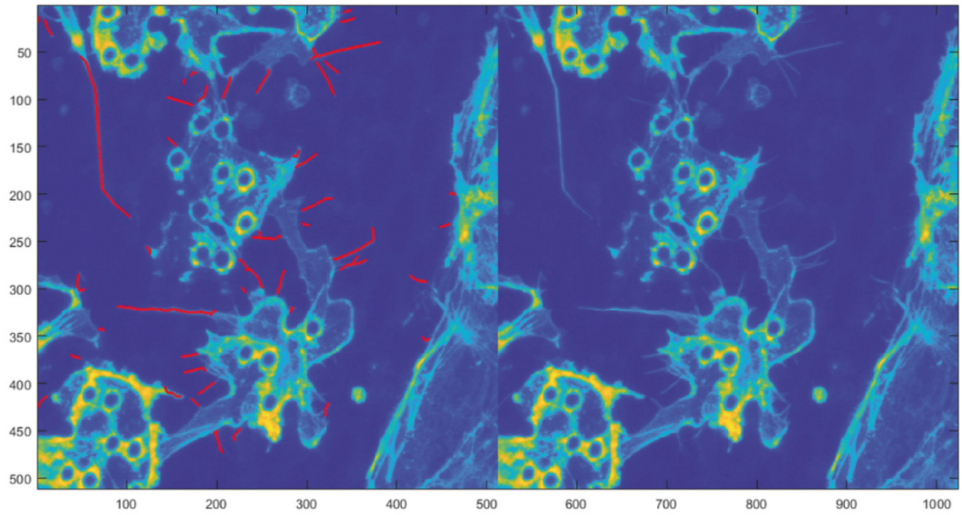

Figure A2. Semi-automatic filopodia detection on fixed samples. Filopodia detection (red) for the right image (average *z* projection of the bottom planes).

Appendix A.2.2. CNN-Based Automated Detection and Tracking on Filopodia in Live Experiments

Although several tools already exist to detect and track filopodia, specific challenges of our setup were: (1) structure autofluorescence and (2) multicellular organization with intricate protrusions. We chose to rely on a convolutional neural network to perform filopodia detection and tracking on timelapse images.

■ Constitution of a training dataset

A training dataset was created using the home-made Matlab script described in A.2.1., detecting candidate filopodia structures and requiring user input to discard false detections and manually draw missing elements. This process helped us to constitute a dataset big enough to train a CNN faster than a fully manual annotation technique. The resulting dataset is constituted of 75 images with 3 labels (background, cell body, filopodia).

■ CNN model

In order to artificially increase the size of our annotated dataset, data augmentation was performed using Keras ImageDataGenerator function to flip and rotate the images. The CNN model chosen was a U-net Xception style model (taken from https://keras.io/examples/vision/oxford_pets_image_segmentation/, accessed 5 October 2020).

The classification problem addressed here is an unbalanced one. Indeed, the number of pixels belonging to the "filopodia" class is always drastically inferior to the number of pixels belonging to the two other classes ("cell body" and "background"). Therefore, using a classical loss function such as the categorical cross-entropy loss to train the network will generate detections that underestimate the quantity of "filopodia" pixels in the image.

To compensate for this effect, we used a weighted categorical cross-entropy loss function, to increase the cost of "filopodia" misclassification.

$$J_{cce} = -\frac{1}{M}\sum_{k=1}^{K}\sum_{m=1}^{M} y_m^k * \log(h_\theta(x_m, k))$$

The classical categorical cross-entropy loss function is defined as: where M is the number of training examples, K is the number of classes, y_m^k is the target label for class k of example m, x_m is the input for training example m and h_θ is the CNN transfer function with weights θ.

The weighted categorical cross-entropy loss is a slightly modified version of this loss, with the addition of a weight vector:

$$J_{wcce} = -\frac{1}{M}\sum_{k=1}^{K}\sum_{m=1}^{M} w_k * y_m^k * \log(h_\theta(x_m, k))$$

where w_k is the weight associated with class k.

In our case, w was empirically found to be optimal with ($w_{background}$ = 1, $w_{filopodia}$ = 20, $w_{cell\ body}$ = 1).

■ Segmentation and tracking

The output of the network is a three-channel probability map corresponding to the three classes ("background", "cell body", "filopodia"). The "filopodia" channel was thresholded and skeletonized before filtering all the elements smaller than 1 micron. The degree of connectivity of the pixels was computed in order to separate branched elements.

The (+) and (−) extremities of each segmented filopodia were determined based on the distance to the closest cell body pixel.

Between each timepoint, the overlap between all filopodia was computed and the intersection over union was used as the objective function to be maximised in order to perform the pairwise assignment of filopodia using the *linear_sum_assignement* function from the *scipy.optimize* library.

Appendix A.3. Additional Information for Nuclei Quantification

We present here additional quantifications of 2D nuclei orientations on top of the microstructures (Figure A1b–h) and of nuclei vertical engagement (Figure A1i,j). Our data suggest that the preferential orientation of nuclei according to the principal axis on elongated hexagons is not altered by the addition of VEGF to a final concentration of 5 ng/mL (Figure A1b) or in its absence (Figure A1c). Separated analysis on regular microstructures of each horizontal dimensions are also presented (Figure A1d–h), illustrating the isotropic orientations in all these conditions, which are pooled in Figure 2g (mean ± S.D.: *D13.5-open*, 44 ± 26°, *D10-open*, 49 ± 24°, *D8.8-open*, 43 ± 27°, *D6.6-open*, 42 ± 28°, *D4.5-open*, 49 ± 22°). At last, we present additional data for vertical engagement, suggesting that the addition of VEGF does not allow a vertical engagement on closed microstructures (Figure A1i), and that the absence of VEGF does not prevent the engagement on open microstructures (Figure A1j).

Appendix A.4. Early Colonization, and Membrane Labelling

We present here a typical multicellular organization at the early steps of microstructure colonization (Figure A3a), the organization of intercellular junctions in the monolayer on the top of the structures as assessed by VE-cadherin labelling, here evocative of dynamic junction rearrangement by junction-associated intermittent lamellipodia (JAIL) [83] (Figure A3b), and typical membrane labelling on a microstructure (Figure A3c).

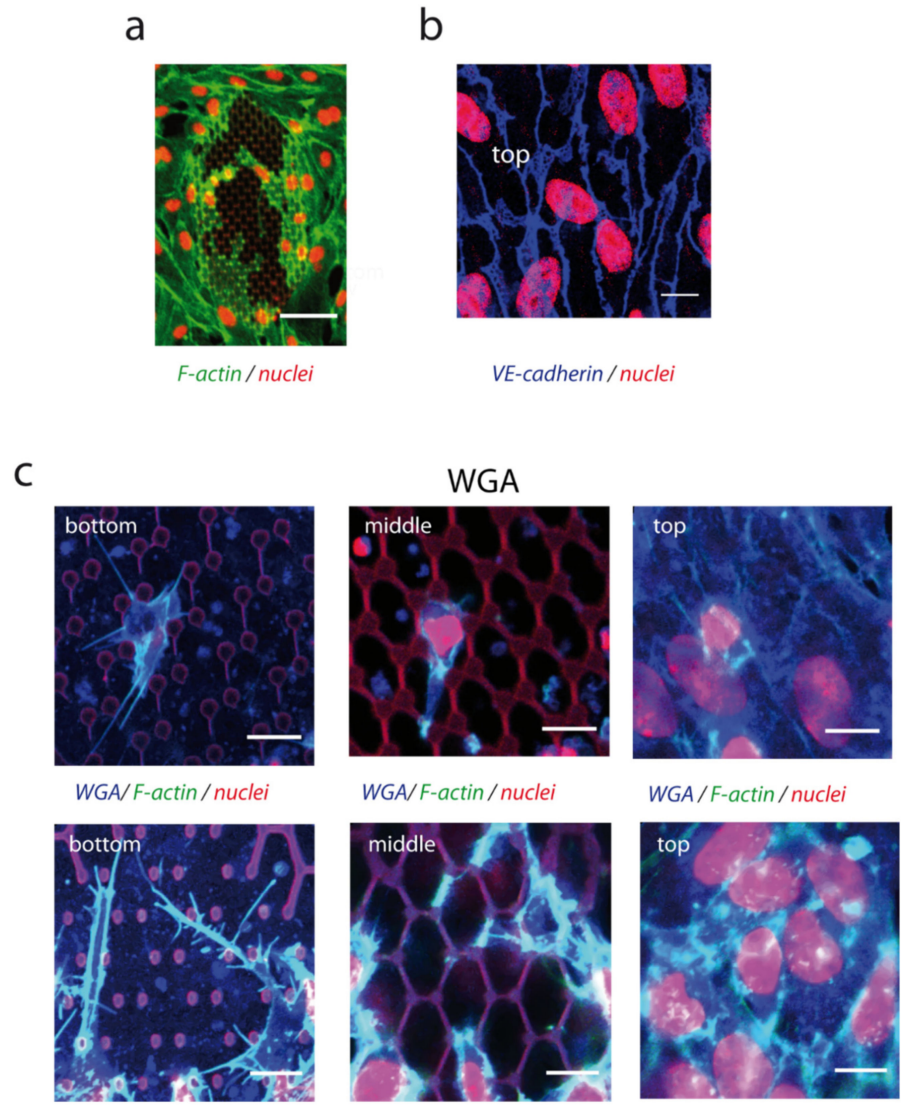

Figure A3. Early colonization and membrane labelling. (**a**) Early cell colonization on a *l7L14-closed* structure, VEGF 5 ng/mL. *z* projection is shown, red: nuclei, green: F-actin, bar 50 µm. (**b**) Monolayer organization on top of a *l7L14-closed* structure: intercellular junctions labelled with VE-cadherin (blue). Nuclei in red. *z* projection of 3 planes above structure. Confocal image acquired from the top, bar 10 µm. (**c**) Membrane labelling with WGA-FITC on a *l7L14-open* microstructure (WGA, blue; nuclei, red; F-actin, green). Top, early colonization (VEGF 5 ng/mL). Bottom, colonization with dactylopodia-like structures, culture in media without VEGF, same image as in Figure 3d, left, with additional WGA labelling. Bar 10 µm. Cells fixed at time of structure colonization (2 (**a**,**b**), 3 (**c** bottom) or 5 (**c** top) days after cell seeding).

Appendix A.5. Filopodia Orientation in Elongated Structures

An asymmetry of filopodia orientation was observed in elongated l7L14-open hexagonal lattices, due to the asymmetry of pillar organization (Figure A4b). When studying the orientation of filopodia compared with the reference direction previously defined, we found that they were preferentially oriented toward this reference direction, although the distribution of orientation was wide (Figure A4a); this preferential orientation was even reinforced when considering only long filopodia, with lengths > 5 µm (Figure A4a), while shorter filopodia had a more isotropic orientation (Figure A6k).

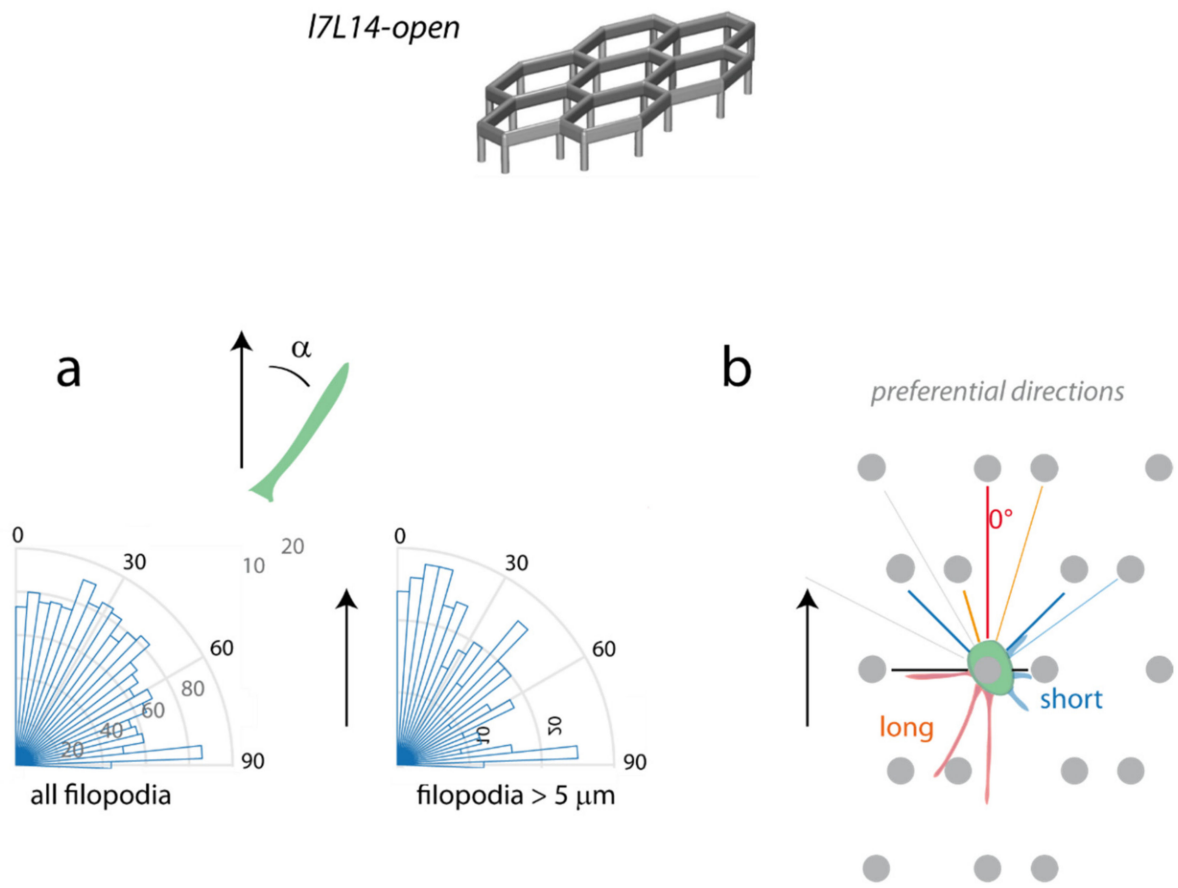

Figure A4. Histograms of filopodia orientations in elongated structures. (**a**) The angle with the reference axis of elongated structures was computed (top). Bottom, left: all filopodia, right: filopodia with lengths > 5 µm. (**b**) Remarkable angles in elongated microstructures (grey circles: pillars). Preferential orientations of short (≤5 µm, blue) and long (>5 µm, red) filopodia.

Appendix A.6. Filopodia Lengths and Orientations in Regular Structures

In regular microstructures, filopodia, induced for a wide range of horizontal D sizes (Figure A5a–d), exhibited more isotropic orientations. Filopodia lengths in regular microstructures were close to the elongated case, with a mean length of 3.58 ± 1.97 µm (Figure A5e,f, median 3.07 µm, n = 1038 filopodia in D13.5-open + D8.8-open microstructures, see Figure A6a–d for separate behaviours). In regular microstructures, filopodia had globally isotropic orientations (Figure A5g), with some peaks likely corresponding to the regular disposition of pillars (0, 30, 60 and 90°, with 30° as the most represented direction, likely due to the presence of two closer pillars with this orientation; Figure A5g,h, see separate behaviours in Figure A6e–j).

Appendix A.7. Additional Information for Filopodia Quantification

We present here separated data for quantifications on *D13.5-open* and *D8.8-open* structures, which are aggregated in Figure A5 because of their similar behaviours (Figure A6a–j). Mean lengths obtained from the whole distribution were 3.56 ± 1.92 µm, median 3.07 µm, in *D13.5-open* structures and 3.64 ± 2.1 µm, median 3.07 µm, in *D8.8-open* structures. We also present the quantification of the orientations of filopodia with lengths ≤ 5 µm on *l7L14-open* and *D13.5-open* + *D8.8-open* structures (Figure A6k, complementary of Figure A5d, and Figure A6l, complementary of Figure A5g).

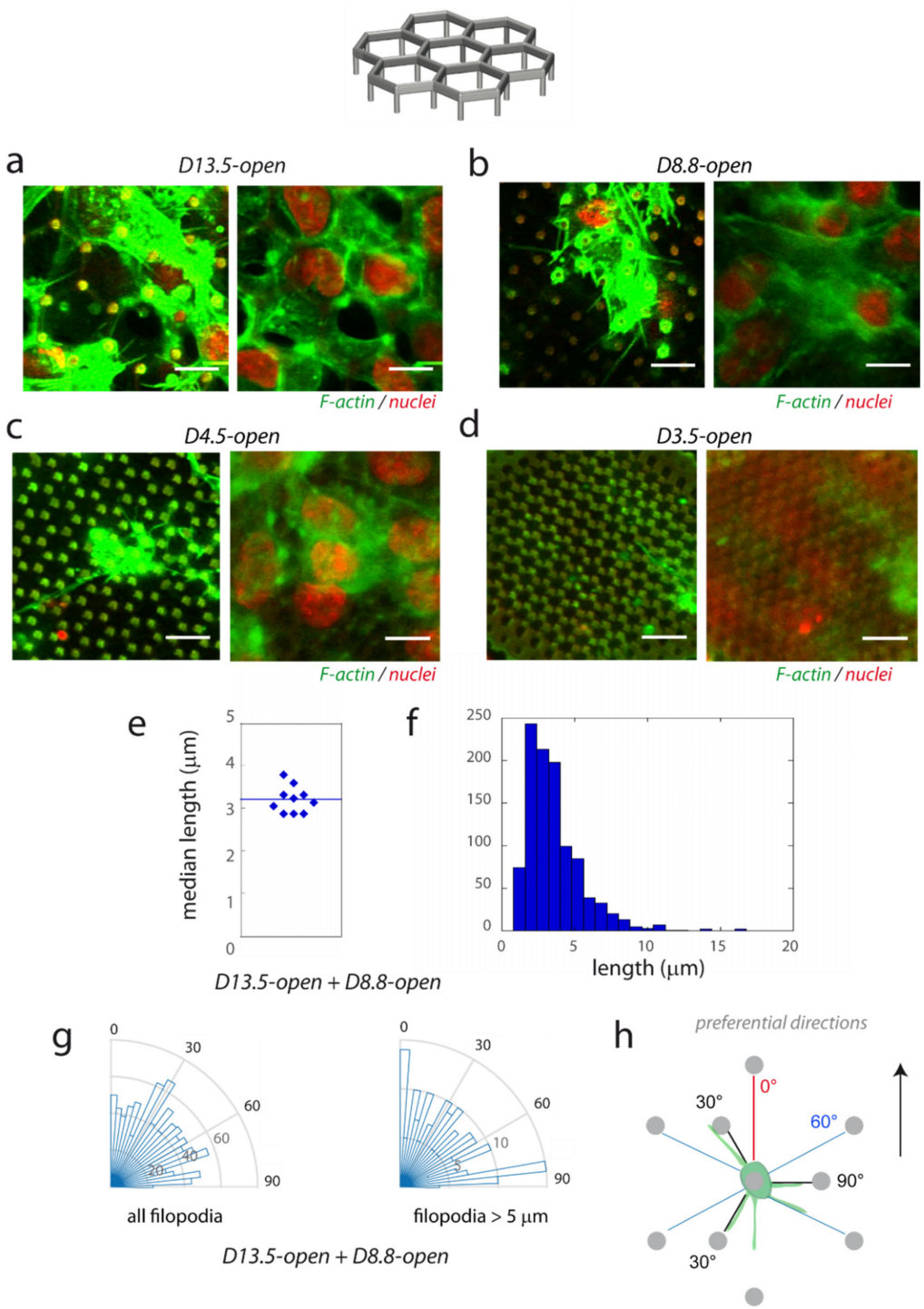

Figure A5. Filopodia characterization on regular microstructures. HUVECs were cultivated on regular open microstructures with different horizontal dimensions *D*: (**a**) *D13.5-open*, (**b**) *D8.8-open*, (**c**) *D4.5-open*, (**d**) *D3.5-open*. Bottom and top planes are represented. Red: nuclei and microstructure autofluorescence, green: F-actin. Cells were fixed at time of structure colonization (2 days after cell seeding). Denoised images, bar 10 µm. (**e**) Median filopodia lengths in *D13.5-open + D8.8-open* microstructures, one point corresponds to one structure (bar: average value). (**f**) Histogram of filopodia lengths in *D13.5-open + D8.8-open* microstructures. (**g**) Histograms of filopodia orientations in *D13.5-open + D8.8-open* structures. The angle with the reference axis of elongated structures was computed. Left: all filopodia, right: filopodia with lengths > 5 µm. (**h**) Remarkable angles.

Appendix A.8. Additional Data on ML-7, Y-27632, PF-573228 and Sunitinib Effects

ML-7 did not significantly affect the morphology of cells outside the microstructure: 1 h 20 min after ML-7 addition, while cells inside the microstructure formed membrane blebs (yellow rectangle), cells outside the microstructure did not display detectable blebs (Figure A7a).

The detail of the statistical analyses performed is shown in Figure A7b–e and in the Materials and Methods. On another side, none of the drugs studied had a detectable effect on filopodia retraction and elongation rates (Figure A7f–i).

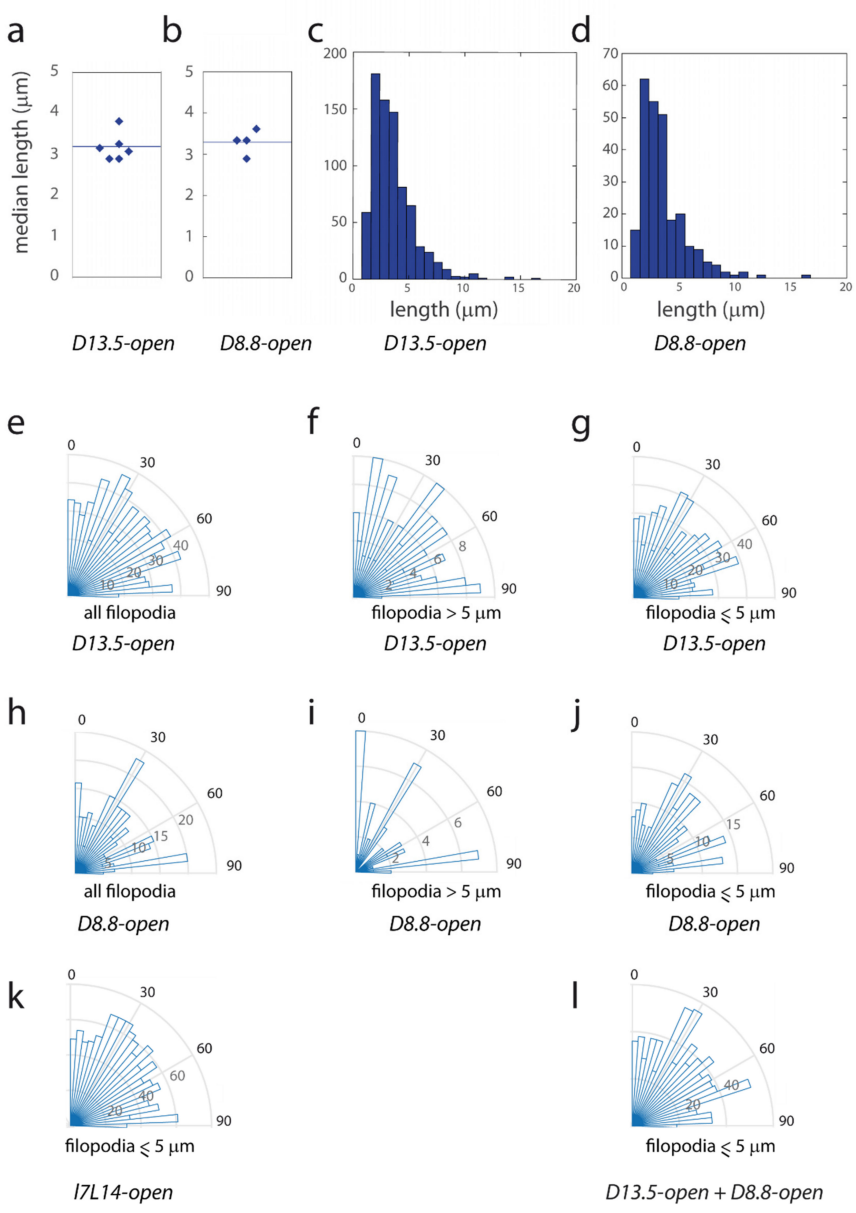

Figure A6. Filopodia orientation on regular lattices of different dimensions. (**a**,**b**) Median filopodia lengths, one point corresponds to one structure (bar: mean value), for *D13.5-open* (**a**) and *D8.8-open* (**b**) structures. (**c**,**d**) Histogram of filopodia lengths, for *D13.5-open* (**c**) and *D8.8-open* (**d**) structures (respectively 782 and 256 filopodia). (**e**–**l**) Histograms of filopodia orientation. The angle with the reference axis of elongated structures was computed. (**e**–**g**) *D13.5-open* structures, (**e**) all filopodia, (**f**) filopodia with length > 5 µm, (**g**) filopodia with lengths ≤ 5 µm. (**h**–**j**) *D8.8-open* structures, (**e**) all filopodia, (**f**) filopodia with length > 5 µm, (**g**) filopodia with lengths ≤ 5 µm. (**k**) *I7L14-open* structures, filopodia with lengths ≤ 5 µm. (**l**) *D13.5-open* + *D8.8-open* structures, filopodia with lengths ≤ 5 µm.

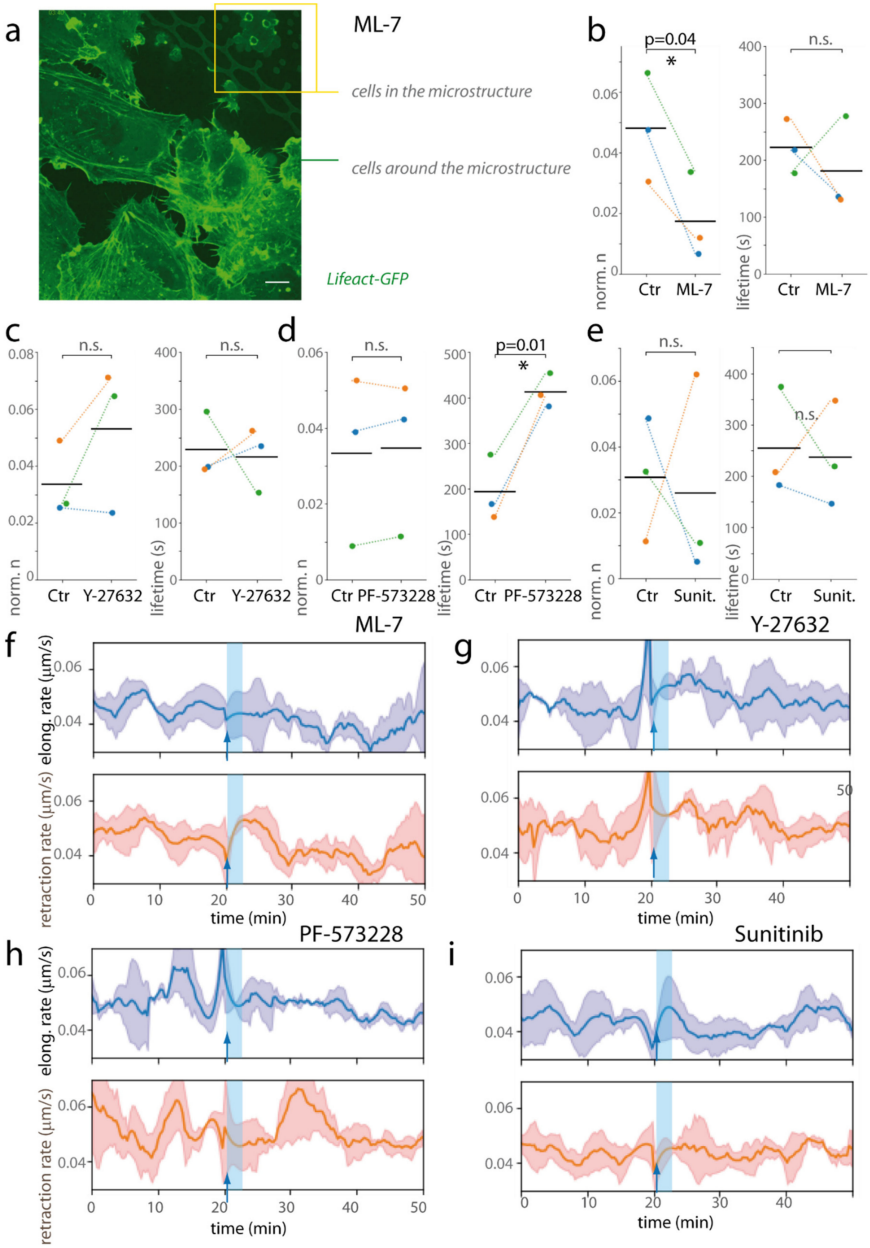

Figure A7. Quantitative analysis of ML-7, Y-27632, PF-573228 and sunitinib effects on filopodia dynamics in the microstructures. (**a**) Cell morphology of HUVECs-Lifeact-GFP cells in and outside the *l7L14-open* microstructure 1 h 20 min after addition of 10 µM ML-7 (1 day after cell seeding) Yellow rectangle: cells formed membrane blebs in the structure. Outside the microstructure, cells displayed no noticeable morphological change. Scale bar, 10 µm. (**b**–**e**) Statistical analyses of the differences in normalized numbers and lifetime upon drug addition. Each point corresponds to the temporal mean in one movie. Three independent experiments (represented with orange, blue and green points) were carried out for each drug, and each experiment is represented by a different colour. Paired *t*-tests were performed to test for statistically significant differences between the values before drug addition (Ctr) and after addition of: 10 µM ML-7 (**b**), 10 µM Y-27632 (**c**), 10 µM PF-573228 (**d**) and 300 nM sunitinib (**e**). * indicates statistically significant differences before and after drug addition with $p < 0.05$, n.s. indicates non statistically significant differences. (**f**–**i**) Kinetics of the mean elongation (blue) and retraction (orange) rates of the (+) filopodia extremities, for 10 µM ML-7 (**f**), 10 µM Y-27632 (**g**), 10 µM PF-573228 (**h**) and 300 nM sunitinib (**i**) treatments. Pre-treatment and post-treatment values are concatenated. Blue arrow, time of drug addition. $n = 3$ independent experiments, errors: S.D. The light blue vertical bar indicates a state of stabilization of the system after media change (~3 min long), which was not considered for analysis.

Appendix A.9. VEGF Accessibility

The accessibility of VEGF to the internal part of the structures, as well as the adequate biological reaction to a VEGF stimulation, were assessed by the labelling of phosphorylated VEGFR2 (VEGF receptor) (Figure A8).

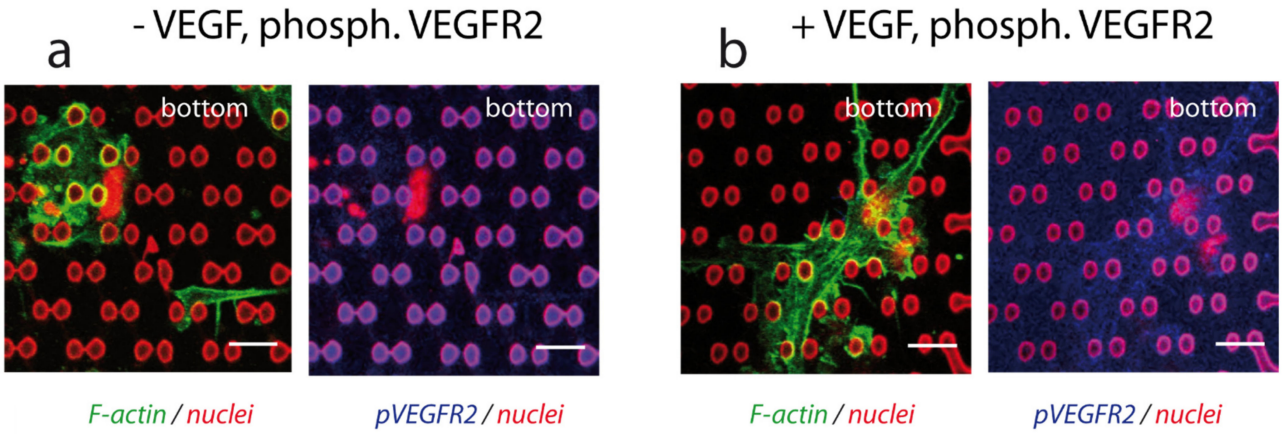

Figure A8. VEGF accessibility. (**a**,**b**) Phosphorylated VEGFR2 labelling, with or without VEGF stimulation. Cells were incubated 10 min without (**a**) or with (**b**) VEGF 50 ng/mL (see Materials and Methods for details), and were immediately fixed and labelled for phosphorylated VEGFR2. Bottom plane. Left, F-actin (green)/nuclei (red). Right, pVEGFR2 (blue)/nuclei (red). Cells were fixed 2 days after cell seeding. Denoised images, bar 10 µm.

References

1. Bettinger, C.J.; Langer, R.; Borenstein, J.T. Engineering Substrate Topography at the Micro- and Nanoscale to Control Cell Function. *Angew. Chem. Int. Ed.* **2009**, *48*, 5406–5415. [CrossRef]
2. Karina Kulangaraa, K.W.L. Substrate topography shapes cell function. *Soft Matter.* **2009**, *5*, 4072–4076. [CrossRef]
3. Flemming, R.; Murphy, C.; Abrams, G.; Goodman, S.; Nealey, P. Effects of synthetic micro- and nano-structured surfaces on cell behavior. *Biomaterials* **1999**, *20*, 573–588. [CrossRef]
4. Teixeira, A.; Abrams, G.A.; Bertics, P.J.; Murphy, C.J.; Nealey, P.F. Epithelial contact guidance on well-defined micro- and nanostructured substrates. *J. Cell Sci.* **2003**, *116*, 1881–1892. [CrossRef]
5. Chen, S.; Jones, J.A.; Xu, Y.; Low, H.-Y.; Anderson, J.M.; Leong, K.W. Characterization of topographical effects on macrophage behavior in a foreign body response model. *Biomaterials* **2010**, *31*, 3479–3491. [CrossRef] [PubMed]
6. Webb, P.; Clark, P.; Skepper, J.; Compston, A.; Wood, A. Guidance of oligodendrocytes and their progenitors by substratum topography. *J. Cell Sci.* **1995**, *108 Part 8*, 2747–2760. [CrossRef]
7. Wood, A. Contact guidance on microfabricated substrata: The response of teleost fin mesenchyme cells to repeating topographical patterns. *J. Cell Sci.* **1988**, *90*, 667–681. [CrossRef] [PubMed]
8. Rajnicek, A.; Britland, S.; McCaig, C. Contact guidance of CNS neurites on grooved quartz: Influence of groove dimensions, neuronal age and cell type. *J. Cell Sci.* **1997**, *110 Part 2*, 2905–2913. [CrossRef]
9. Gomez, N.; Lu, Y.; Chen, S.; Schmidt, C.E. Immobilized nerve growth factor and microtopography have distinct effects on polarization versus axon elongation in hippocampal cells in culture. *Biomaterials* **2007**, *28*, 271–284. [CrossRef]
10. Hanson, J.N.; Motala, M.J.; Heien, M.L.; Gillette, M.; Sweedler, J.; Nuzzo, R.G. Textural guidance cues for controlling process outgrowth of mammalian neurons. *Lab Chip* **2009**, *9*, 122–131. [CrossRef]
11. Dalton, B.A.; Walboomers, X.F.; Dziegielewski, M.; Evans, M.D.; Taylor, S.; Jansen, J.A.; Steele, J.G. Modulation of epithelial tissue and cell migration by microgrooves. *J. Biomed. Mater. Res.* **2001**, *56*, 195–207. [CrossRef]
12. Bettinger, C.J.; Zhang, Z.; Gerecht, S.; Borenstein, J.T.; Langer, R. Enhancement of In Vitro Capillary Tube Formation by Substrate Nanotopography. *Adv. Mater.* **2007**, *20*, 99–103. [CrossRef] [PubMed]
13. Greiner, A.M.; Jäckel, M.; Scheiwe, A.C.; Stamow, D.R.; Autenrieth, T.J.; Lahann, J.; Franz, C.M.; Bastmeyer, M. Multifunctional polymer scaffolds with adjustable pore size and chemoattractant gradients for studying cell matrix invasion. *Biomaterials* **2014**, *35*, 611–619. [CrossRef] [PubMed]
14. Kuo, Y.-C.; Chiu, K.-H. Inverted colloidal crystal scaffolds with laminin-derived peptides for neuronal differentiation of bone marrow stromal cells. *Biomaterials* **2011**, *32*, 819–831. [CrossRef] [PubMed]
15. Koroleva, A.; Deiwick, A.; Nguyen, A.; Schlie-Wolter, S.; Narayan, R.; Timashev, P.; Popov, V.; Bagratashvili, V.N.; Chichkov, B. Osteogenic Differentiation of Human Mesenchymal Stem Cells in 3-D Zr-Si Organic-Inorganic Scaffolds Produced by Two-Photon Polymerization Technique. *PLoS ONE* **2015**, *10*, e0118164. [CrossRef]

16. Yim, E.; Pang, S.; Leong, K.W. Synthetic nanostructures inducing differentiation of human mesenchymal stem cells into neuronal lineage. *Exp. Cell Res.* **2007**, *313*, 1820–1829. [CrossRef]
17. Mata, A.; Kim, E.J.; Boehm, C.A.; Fleischman, A.J.; Muschler, G.F.; Roy, S. A three-dimensional scaffold with precise micro-architecture and surface micro-textures. *Biomaterials* **2009**, *30*, 4610–4617. [CrossRef]
18. Grewal, M.G.; Highley, C.B. Electrospun hydrogels for dynamic culture systems: Advantages, progress, and opportunities. *Biomater. Sci.* **2021**, *9*, 4228–4245. [CrossRef]
19. Dolega, M.E.; Wagh, J.; Gerbaud, S.; Kermarrec, F.; Alcaraz, J.-P.; Martin, D.K.; Gidrol, X.; Picollet-D'hahan, N. Facile Bench-Top Fabrication of Enclosed Circular Microchannels Provides 3D Confined Structure for Growth of Prostate Epithelial Cells. *PLoS ONE* **2014**, *9*, e99416. [CrossRef]
20. Venzac, B.; Madoun, R.; Benarab, T.; Monnier, S.; Cayrac, F.; Myram, S.; Leconte, L.; Amblard, F.; Viovy, J.-L.; Descroix, S.; et al. Engineering small tubes with changes in diameter for the study of kidney cell organization. *Biomicrofluidics* **2018**, *12*, 24114. [CrossRef]
21. Homan, K.A.; Kolesky, D.B.; Skylar-Scott, M.A.; Herrmann, J.; Obuobi, H.; Moisan, A.; Lewis, J.A. Bioprinting of 3D Convoluted Renal Proximal Tubules on Perfusable Chips. *Sci. Rep.* **2016**, *6*, 34845. [CrossRef] [PubMed]
22. Lee, K.S.; Kim, R.H.; Yang, D.Y.; Park, S.H. Advances in 3D nano/microfabrication using two-photon initiated photopolymerization. *Prog. Polym. Sci.* **2008**, *33*, 631–681. [CrossRef]
23. Gittard, S.D.; Narayan, R.J. Laser direct writing of micro- and nano-scale medical devices. *Expert Rev. Med Devices* **2010**, *7*, 343–356. [CrossRef] [PubMed]
24. Hippler, M.; Lemma, E.D.; Bertels, S.; Blasco, E.; Barner-Kowollik, C.; Wegener, M.; Bastmeyer, M. 3D Scaffolds to Study Basic Cell Biology. *Adv. Mater.* **2019**, *31*, e1808110. [CrossRef] [PubMed]
25. Spagnolo, B.; Brunetti, V.; Leménager, G.; De Luca, E.; Sileo, L.; Pellegrino, T.; Pompa, P.P.; De Vittorio, M.; Pisanello, F. Three-dimensional cage-like microscaffolds for cell invasion studies. *Sci. Rep.* **2015**, *5*, srep10531. [CrossRef]
26. Scheiwe, A.C.; Frank, S.C.; Autenrieth, T.J.; Bastmeyer, M.; Wegener, M. Subcellular stretch-induced cytoskeletal response of single fibroblasts within 3D designer scaffolds. *Biomaterials* **2015**, *44*, 186–194. [CrossRef]
27. Sprague, E.A.; Tio, F.; Ahmed, S.H.; Granada, J.F.; Bailey, S.R. Impact of Parallel Micro-Engineered Stent Grooves on Endothelial Cell Migration, Proliferation, and Function. *Circ. Cardiovasc. Interv.* **2012**, *5*, 499–507. [CrossRef]
28. Bedair, T.M.; ElNaggar, M.A.; Joung, Y.K.; Han, D.K. Recent advances to accelerate re-endothelialization for vascular stents. *J. Tissue Eng.* **2017**, *8*, 8. [CrossRef]
29. Lutter, C.; Nothhaft, M.; Rzany, A.; Garlichs, C.D.; Cicha, I. Effect of specific surface microstructures on substrate endothelialisation and thrombogenicity: Importance for stent design. *Clin. Hemorheol. Microcirc.* **2015**, *59*, 219–233. [CrossRef]
30. Deveza, L.; Choi, J.; Yang, F. Therapeutic Angiogenesis for Treating Cardiovascular Diseases. *Theranostics* **2012**, *2*, 801–814. [CrossRef]
31. Gorin, C.; Rochefort, G.Y.; Bascetin, R.; Ying, H.; Lesieur, J.; Sadoine, J.; Beckouche, N.; Berndt, S.; Novais, A.; Lesage, M.; et al. Priming Dental Pulp Stem Cells with Fibroblast Growth Factor-2 Increases Angiogenesis of Implanted Tissue-Engineered Constructs Through Hepatocyte Growth Factor and Vascular Endothelial Growth Factor Secretion. *STEM CELLS Transl. Med.* **2016**, *5*, 392–404. [CrossRef] [PubMed]
32. Tiemeijer, L.A.; Frimat, J.-P.; Stassen, O.; Bouten, C.; Sahlgren, C.M. Spatial patterning of the Notch ligand Dll4 controls endothelial sprouting in vitro. *Sci. Rep.* **2018**, *8*, 6392. [CrossRef] [PubMed]
33. Arora, S.; Lin, S.; Cheung, C.; Yim, E.K.; Toh, Y.-C. Topography elicits distinct phenotypes and functions in human primary and stem cell derived endothelial cells. *Biomaterials* **2020**, *234*, 119747. [CrossRef] [PubMed]
34. Mogilner, A.; Rubinstein, B. The Physics of Filopodial Protrusion. *Biophys. J.* **2005**, *89*, 782–795. [CrossRef]
35. Figueiredo, A.M.; Barbacena, P.; Russo, A.; Vaccaro, S.; Ramalho, D.; Pena, A.; Lima, A.P.; Ferreira, R.R.; Fidalgo, M.A.; El-Marjou, F.; et al. Endothelial cell invasion is controlled by dactylopodia. *Proc. Natl. Acad. Sci. USA* **2021**, *118*, e2023829118. [CrossRef] [PubMed]
36. Germain, S.; Monnot, C.; Muller, L.; Eichmann, A. Hypoxia-driven angiogenesis: Role of tip cells and extracellular matrix scaffolding. *Curr. Opin. Hematol.* **2010**, *17*, 245–251. [CrossRef]
37. Coscoy, S.; Baïz, S.; Octon, J.; Rhoné, B.; Perquis, L.; Tseng, Q.; Amblard, F.; Semetey, V. Microtopographies control the development of basal protrusions in epithelial sheets. *Biointerphases* **2018**, *13*, 41003. [CrossRef]
38. Bray, M.-A.P.; Adams, W.J.; Geisse, N.A.; Feinberg, A.W.; Sheehy, S.P.; Parker, K.K. Nuclear morphology and deformation in engineered cardiac myocytes and tissues. *Biomaterials* **2010**, *31*, 5143–5150. [CrossRef]
39. Caille, N.; Tardy, Y.; Meister, J.J. Assessment of Strain Field in Endothelial Cells Subjected to Uniaxial Deformation of Their Substrate. *Ann. Biomed. Eng.* **1998**, *26*, 409–416. [CrossRef]
40. Maniotis, A.J.; Chen, C.; Ingber, D.E. Demonstration of mechanical connections between integrins, cytoskeletal filaments, and nucleoplasm that stabilize nuclear structure. *Proc. Natl. Acad. Sci. USA* **1997**, *94*, 849–854. [CrossRef]
41. Angulo-Urarte, A.; van der Wal, T.; Huveneers, S. Cell-cell junctions as sensors and transducers of mechanical forces. *Biochim. Biophys. Acta (BBA)—Biomembr.* **2020**, *1862*, 183316. [CrossRef] [PubMed]
42. Cazes, A.; Galaup, A.; Chomel, C.; Bignon, M.; Bréchot, N.; Le Jan, S.; Weber, H.; Corvol, P.; Muller, L.; Germain, S.; et al. Extracellular Matrix–Bound Angiopoietin-Like 4 Inhibits Endothelial Cell Adhesion, Migration, and Sprouting and Alters Actin Cytoskeleton. *Circ. Res.* **2006**, *99*, 1207–1215. [CrossRef] [PubMed]

43. Urbančič, V.; Butler, R.; Richier, B.; Peter, M.; Mason, J.; Livesey, F.J.; Holt, C.E.; Gallop, J.L. Filopodyan: An open-source pipeline for the analysis of filopodia. *J. Cell Biol.* **2017**, *216*, 3405–3422. [CrossRef] [PubMed]
44. Jacquemet, G.; Paatero, I.; Carisey, A.F.; Padzik, A.; Orange, J.S.; Hamidi, H.; Ivaska, J. FiloQuant reveals increased filopodia density during DCIS progression. *bioRxiv* **2017**. [CrossRef]
45. Ma, X.; Uchida, Y.; Wei, T.; Liu, C.; Adams, R.H.; Kubota, Y.; Gutkind, J.S.; Mukouyama, Y.-S.; Adelstein, R.S. Nonmuscle myosin 2 regulates cortical stability during sprouting angiogenesis. *Mol. Biol. Cell* **2020**, *31*, 1974–1987. [CrossRef]
46. Lomakin, A.J.; Cattin, C.J.; Cuvelier, D.; Alraies, Z.; Molina, M.; Nader, G.P.F.; Srivastava, N.; Sáez, P.J.; Garcia-Arcos, J.M.; Zhitnyak, I.Y.; et al. The nucleus acts as a ruler tailoring cell responses to spatial constraints. *Science* **2020**, *370*, eaba2894. [CrossRef]
47. Ghosh, I.; Singh, R.K.; Mishra, M.; Kapoor, S.; Jana, S.S. Switching between blebbing and lamellipodia depends on the degree of non-muscle myosin II activity. *J. Cell Sci.* **2021**, *134*, jcs248732. [CrossRef]
48. Totsukawa, G.; Wu, Y.; Sasaki, Y.; Hartshorne, D.J.; Yamakita, Y.; Yamashiro, S.; Matsumura, F. Distinct roles of MLCK and ROCK in the regulation of membrane protrusions and focal adhesion dynamics during cell migration of fibroblasts. *J. Cell Biol.* **2004**, *164*, 427–439. [CrossRef]
49. Hu, W.; Wehrle-Haller, B.; Vogel, V. Maturation of Filopodia Shaft Adhesions Is Upregulated by Local Cycles of Lamellipodia Advancements and Retractions. *PLoS ONE* **2014**, *9*, e107097. [CrossRef]
50. Zheng, Y.; Gong, J.; Zhen, Y. Focal adhesion kinase is activated by microtubule-depolymerizing agents and regulates membrane blebbing in human endothelial cells. *J. Cell. Mol. Med.* **2020**, *24*, 7228–7238. [CrossRef]
51. Hopkins, A.M.; Pineda, A.A.; Winfree, L.M.; Brown, G.T.; Laukoetter, M.G.; Nusrat, A. Organized migration of epithelial cells requires control of adhesion and protrusion through Rho kinase effectors. *Am. J. Physiol. Liver Physiol.* **2007**, *292*, G806–G817. [CrossRef] [PubMed]
52. Schmidt, J.T.; Morgan, P.; Dowell, N.; Leu, B. Myosin light chain phosphorylation and growth cone motility. *J. Neurobiol.* **2002**, *52*, 175–188. [CrossRef] [PubMed]
53. Nakatsu, M.; Sainson, R.C.A.; Pérez-Del-Pulgar, S.; Aoto, J.N.; Aitkenhead, M.; Taylor, K.L.; Carpenter, P.M.; Hughes, C.C.W. VEGF121 and VEGF165 Regulate Blood Vessel Diameter Through Vascular Endothelial Growth Factor Receptor 2 in an in vitro Angiogenesis Model. *Lab. Investig.* **2003**, *83*, 1873–1885. [CrossRef]
54. Beckouche, N.; Bignon, M.; Lelarge, V.; Mathivet, T.; Pichol-Thievend, C.; Berndt, S.; Hardouin, J.; Garand, M.; Ardidie-Robouant, C.; Barret, A.; et al. The interaction of heparan sulfate proteoglycans with endothelial transglutaminase-2 limits VEGF 165 -induced angiogenesis. *Sci. Signal.* **2015**, *8*, ra70. [CrossRef]
55. Labots, M.; Gotink, K.J.; Dekker, H.; Azijli, K.; Van Der Mijn, J.C.; Huijts, C.M.; Piersma, S.R.; Jiménez, C.R.; Verheul, H.M.W. Evaluation of a tyrosine kinase peptide microarray for tyrosine kinase inhibitor therapy selection in cancer. *Exp. Mol. Med.* **2016**, *48*, e279. [CrossRef] [PubMed]
56. Van der Mijn, J.C.; Broxterman, H.J.; Knol, J.C.; Piersma, S.R.; De Haas, R.R.; Dekker, H.; Pham, T.V.; Van Beusechem, V.W.; Halmos, B.; Mier, J.W.; et al. Sunitinib activates Axl signaling in renal cell cancer. *Int. J. Cancer* **2016**, *138*, 3002–3010. [CrossRef]
57. Guetta-Terrier, C.; Monzo, P.; Zhu, J.; Long, H.; Venkatraman, L.; Zhou, Y.; Wang, P.; Chew, S.Y.; Mogilner, A.; Ladoux, B.; et al. Protrusive waves guide 3D cell migration along nanofibers. *J. Cell Biol.* **2015**, *211*, 683–701. [CrossRef] [PubMed]
58. Xue, N.; Bertulli, C.; Sadok, A.; Huang, Y.Y.S. Dynamics of filopodium-like protrusion and endothelial cellular motility on one-dimensional extracellular matrix fibrils. *Interface Focus* **2014**, *4*, 20130060. [CrossRef]
59. Doyle, A.D.; Wang, F.W.; Matsumoto, K.; Yamada, K.M. One-dimensional topography underlies three-dimensional fibrillar cell migration. *J. Cell Biol.* **2009**, *184*, 481–490. [CrossRef]
60. Yevick, H.G.; Duclos, G.; Bonnet, I.; Silberzan, P. Architecture and migration of an epithelium on a cylindrical wire. *Proc. Natl. Acad. Sci. USA* **2015**, *112*, 5944–5949. [CrossRef]
61. Herrera, A.; Herrera, M.; Guerra-Perez, N.; Galindo-Pumariño, C.; Larriba, M.J.; García-Barberán, V.; Gil, B.; Giménez-Moyano, S.; Ferreiro-Monteagudo, R.; Veguillas, P.; et al. Endothelial cell activation on 3D-matrices derived from PDGF-BB-stimulated fibroblasts is mediated by Snail1. *Oncogenesis* **2018**, *7*, 76. [CrossRef] [PubMed]
62. Charles-Orszag, A.; Tsai, F.-C.; Bonazzi, D.; Manriquez, V.; Sachse, M.; Mallet, A.; Salles, A.; Melican, K.; Staneva, R.; Bertin, A.; et al. Adhesion to nanofibers drives cell membrane remodeling through one-dimensional wetting. *Nat. Commun* **2018**, *9*, 4450–4463. [CrossRef]
63. Du, X.; Wang, Y.; Yuan, L.; Weng, Y.; Chen, G.; Hu, Z. Guiding the behaviors of human umbilical vein endothelial cells with patterned silk fibroin films. *Colloids Surf. B Biointerfaces* **2014**, *122*, 79–84. [CrossRef] [PubMed]
64. Formentín, P.; Catalán, Ú.; Pol, L.; Fernández-Castillejo, S.; Solà, R.; Marsal, L.F. Collagen and fibronectin surface modification of nanoporous anodic alumina and macroporous silicon for endothelial cell cultures. *J. Biol. Eng.* **2018**, *12*, 21. [CrossRef]
65. Beltrán-Partida, E.; Valdéz-Salas, B.; Moreno-Ulloa, A.; Escamilla, A.; Curiel, M.A.; Rosales-Ibáñez, R.; Villarreal, F.; Bastidas, D.M.; Bastidas, J.M. Improved in vitro angiogenic behavior on anodized titanium dioxide nanotubes. *J. Nanobiotechnol.* **2017**, *15*, 10. [CrossRef] [PubMed]
66. Albuschies, J.; Vogel, V. The role of filopodia in the recognition of nanotopographies. *Sci. Rep.* **2013**, *3*, srep01658. [CrossRef] [PubMed]
67. Chaudhuri, P.; Harfouche, R.; Soni, S.; Hentschel, D.M.; Sengupta, S. Shape Effect of Carbon Nanovectors on Angiogenesis. *ACS Nano* **2010**, *4*, 574–582. [CrossRef] [PubMed]

68. Borghi, N.; Alias, K.; De Gennes, P.-G.; Brochard-Wyart, F. Wetting fibers with liposomes. *J. Colloid Interface Sci.* **2005**, *285*, 61–66. [CrossRef] [PubMed]
69. Zhu, Y.; Liu, X.; Wu, J.; Wong, T.M.; Feng, X.; Yang, C.; Wu, S.; Zheng, Y.; Liu, X.; Cheung, K.M.C.; et al. Micro- and Nanohemispherical 3D Imprints Modulate the Osteogenic Differentiation and Mineralization Tendency of Bone Cells. *ACS Appl. Mater. Interfaces* **2019**, *11*, 35513–35524. [CrossRef]
70. Li, J.-R.; Shi, L.; Deng, Z.; Lo, S.H.; Liu, G.-Y. Nanostructures of Designed Geometry and Functionality Enable Regulation of Cellular Signaling Processes. *Biochemistry* **2012**, *51*, 5876–5893. [CrossRef]
71. Nune, K.C.; Misra, R.; Gai, X.; Li, S.J.; Hao, Y.L. Surface nanotopography-induced favorable modulation of bioactivity and osteoconductive potential of anodized 3D printed Ti-6Al-4V alloy mesh structure. *J. Biomater. Appl.* **2017**, *32*, 1032–1048. [CrossRef] [PubMed]
72. Zhu, L.; Luo, D.; Liu, Y. Effect of the nano/microscale structure of biomaterial scaffolds on bone regeneration. *Int. J. Oral Sci.* **2020**, *12*, 6. [CrossRef] [PubMed]
73. Phng, L.-K.; Stanchi, F.; Gerhardt, H. Filopodia are dispensable for endothelial tip cell guidance. *Development* **2013**, *140*, 4031–4040. [CrossRef] [PubMed]
74. Fantin, A.; Lampropoulou, A.; Gestri, G.; Raimondi, C.; Senatore, V.; Zachary, I.; Ruhrberg, C. NRP1 Regulates CDC42 Activation to Promote Filopodia Formation in Endothelial Tip Cells. *Cell Rep.* **2015**, *11*, 1577–1590. [CrossRef] [PubMed]
75. Lamalice, L.; Houle, F.; Jourdan, G.; Huot, J. Phosphorylation of tyrosine 1214 on VEGFR2 is required for VEGF-induced activation of Cdc42 upstream of SAPK2/p38. *Oncogene* **2004**, *23*, 434–445. [CrossRef] [PubMed]
76. Hansen, C.G.; Moroishi, T.; Guan, K.-L. YAP and TAZ: A nexus for Hippo signaling and beyond. *Trends Cell Biol.* **2015**, *25*, 499–513. [CrossRef]
77. Yang, Y.; Wang, K.; Gu, X.; Leong, K.W. Biophysical Regulation of Cell Behavior—Cross Talk between Substrate Stiffness and Nanotopography. *Engineering* **2017**, *3*, 36–54. [CrossRef]
78. Kim, M.-C.; Silberberg, Y.R.; Abeyaratne, R.; Kamm, R.D.; Asada, H.H. Computational modeling of three-dimensional ECM-rigidity sensing to guide directed cell migration. *Proc. Natl. Acad. Sci. USA* **2018**, *115*, E390–E399. [CrossRef]
79. Atlas, Y.; Gorin, C.; Novais, A.; Marchand, M.F.; Chatzopoulou, E.; Lesieur, J.; Bascetin, R.; Binet-Moussy, C.; Sadoine, J.; Lesage, M.; et al. Microvascular maturation by mesenchymal stem cells in vitro improves blood perfusion in implanted tissue constructs. *Biomaterials* **2020**, *268*, 120594. [CrossRef]
80. Wang, I.; Bouriau, M.; Baldeck, P.; Martineau, C.; Andraud, C. Three-dimensional microfabrication by two-photon-initiated polymerization with a low-cost microlaser. *Opt. Lett.* **2002**, *27*, 1348–1350. [CrossRef]
81. Kervrann, C.; Boulanger, J. Optimal Spatial Adaptation for Patch-Based Image Denoising. *IEEE Trans. Image Process.* **2006**, *15*, 2866–2878. [CrossRef] [PubMed]
82. Schmid, B.; Schindelin, J.; Cardona, A.; Longair, M.; Heisenberg, M. A high-level 3D visualization API for Java and ImageJ. *BMC Bioinform.* **2010**, *11*, 274. [CrossRef] [PubMed]
83. Cao, J.; Ehling, M.; März, S.; Seebach, J.; Tarbashevich, K.; Sixta, T.; Pitulescu, M.E.; Werner, A.-C.; Flach, B.; Montanez, E.; et al. Polarized actin and VE-cadherin dynamics regulate junctional remodelling and cell migration during sprouting angiogenesis. *Nat. Commun.* **2017**, *8*, 2210. [CrossRef] [PubMed]

RÉSUMÉ

La polymérisation à deux photons est un outil de choix pour fabriquer des microstructures 3D à l'échelle cellulaire. Ce travail a permis de développer un système de polymères synthétiques (thiol-ène hors ratio stœchiométrique, résine OSTE) et un système de polymères naturels (protéines) pour la polymérisation à deux photons. Ces deux systèmes de polymères ont été explorés afin de développer des outils pour la biologie cellulaire fondamentale. Pour la résine OSTE, nous avons obtenu différents niveaux d'excès de groupes alcènes à la surface. Le Me-PEG-SH a été greffé avec succès sur la surface avec excès d'alcènes par greffage à un et deux photons. Grâce à des techniques d'analyse chimique de la surface (FTIR, angle de contact et XPS) et à des expériences d'anti-bioadhésion (E. coli et cellules), les meilleures conditions de greffage ont été sélectionnées pour la modification de la surface 2D à l'échelle microscopique. En étudiant le rapport entre les thiols et les alcènes ainsi que le type et la concentration des photo-initiateurs, nous avons systématiquement développé des prépolymères de résine OSTE qui peuvent être utilisés pour la polymérisation à deux photons. En s'appuyant sur les résultats obtenus pour l'anti-adhésion 2D, le greffage de Me-PEG-SH a été appliqué à la modification de surface en 3D, ce qui permet une anti-adhésion locale à l'échelle de la cellule. En ce qui concerne les protéines, nous avons testé de manière approfondie le potentiel de divers photo-initiateurs hydrosolubles pour polymériser différentes concentrations d'albumine sérique bovine (BSA) en vue de leur utilisation dans des formulations de polymérisation à deux photons. Nous avons observé une biodégradation rapide de la microstructure de la BSA par les cellules et avons effectué une première caractérisation de ce phénomène. Les différents systèmes développés dans ce travail pour la polymérisation à deux photons apportent de nouveaux outils pour les applications biomédicales, y compris pour les études de biologie cellulaire et le contrôle local de l'adhésion dans les dispositifs médicaux.

MOTS CLÉS

Polymérisation à deux photons, Stœchiométrie hors ratio, Résine thiol-ène, Chimie click thiol-ène, Greffage de surface anti-adhésives, Polymérisation de protéines, Albumine de sérum bovin

ABSTRACT

Two-photon polymerization is a crucial tool to fabricate 3D microstructures at the cell scale. This work developed a synthetic polymer system (off-ratio stoichiometry thiol-ene, OSTE resin) and natural polymer system (proteins) for two-photon polymerization, in order to develop tools for basic cell biology. For OSTE resin, we obtained different levels of excess of alkene groups on the surface. Me-PEG-SH was successfully grafted onto the alkene excess surface by one-photon and two-photon grafting. By surface chemical analysis techniques (FTIR, contact angle and XPS) and anti-bioadhesion (*E. coli* and cells) experiments, the best grafting conditions were selected for 2D surface modification at the microscale. By investigating the ratio of thiols to alkenes and the type and concentration of photoinitiators, we have systematically developed prepolymers OSTE resin that can be used for two-photon polymerization. Based on the 2D anti-adhesion results, Me-PEG-SH grafting was transferred to 3D surface modification, which gives us a chance for localize anti-adhesion at the cell scale. For proteins, we comprehensively tested the potential of various water-soluble photoinitiators for polymerizing different concentrations of bovine serum albumin (BSA) for use as two-photon polymerization formulations. We observed a fast biodegradation of the BSA microstructures by cells and performed an initial characterization of this phenomenon. The different systems developed in this work for two-photon polymerization bring more tools for biomedical applications, including cell biology studies and locally controlled anti-adhesive surfaces in medical devices.

KEYWORDS

Two-photon polymerization, Off-ratio stoichiometry thiol-ene resin, Thiol-ene click chemistry, Anti-adhesive surface grafting, Protein polymerization, Bovine serum albumin